

# AIRBORNE CCN MEASUREMENTS

A THESIS

SUBMITTED TO THE UNIVERSITY OF MANCHESTER

FOR THE DEGREE OF

DOCTOR OF PHILOSOPHY (PHD)

IN THE FACULTY OF THE FACULTY OF ENGINEERING AND  
PHYSICAL SCIENCES

**2013**

**James Alexander Trembath**

SCHOOL OF EARTH, ATMOSPHERIC AND ENVIRONMENTAL SCIENCE

# Contents

<b>Abstract</b>	<b>23</b>
<b>Declaration</b>	<b>25</b>
<b>Copyright</b>	<b>26</b>
<b>Acknowledgements</b>	<b>28</b>
<b>Expected Publications</b>	<b>29</b>
<b>1 Introduction</b>	<b>30</b>
<b>2 Cloud Condensation Nuclei Counter: Instrument Behaviour, Characterisation and Operation</b>	<b>44</b>
2.1 CCNc Instrument . . . . .	44
2.1.1 Principle of Operation . . . . .	44
2.1.2 Instrument Behaviour . . . . .	48
2.1.3 CCNc Calibrations . . . . .	49
2.1.4 Reduced Pressure Inlet . . . . .	58

2.1.5	Pressure and Supersaturation . . . . .	67
2.1.6	CCNc Instrument Warm Up Requirements . . . . .	72
2.2	<i>In situ</i> Sampling . . . . .	77
2.2.1	Instrument Deployment . . . . .	77
2.2.2	Sampling Architecture . . . . .	81
2.2.3	Rosemount Inlet Characterisation . . . . .	98
2.3	Flying operations . . . . .	122
<b>3</b>	<b>Results and Discussion</b>	<b>126</b>
3.1	Characterisation of Aerosol and Cloud Properties in the South Equatorial Pacific . . . . .	126
3.1.1	Longitudinal Structure . . . . .	132
3.1.2	Vertical Structure . . . . .	158
3.2	Kappa Analysis . . . . .	176
3.3	CCN Closure . . . . .	198
3.3.1	Sensitivity Analysis of Externally Mixed Model . . . . .	213
3.4	Threshold Droplet Growth Analysis . . . . .	239
<b>4</b>	<b>Further Work</b>	<b>247</b>
<b>5</b>	<b>Conclusions</b>	<b>251</b>
<b>6</b>	<b>Appendices</b>	<b>267</b>

**Final word count: 50,719**

# List of Figures

1.1	Global average radiative forcing (RF) in 2005 (best estimates and 5 to 95 % uncertainty ranges) with respect to 1750 for CO <sub>2</sub> , CH <sub>4</sub> , N <sub>2</sub> O and other important agents and mechanisms, together with the typical geographical extent (spatial scale) of the forcing and the assessed level of scientific understanding (LOSU). Aerosols from explosive volcanic eruptions contribute an additional episodic cooling term for a few years following an eruption. The range for linear contrails does not include other possible effects of aviation on cloudiness. . . . .	34
1.2	Köhler curves for two ammonium sulphate and sodium chloride of an initial 0.5 $\mu$ m dry size. Both the competing Kelvin and solute terms are show. With the critical supersaturation, $S_c$ and critical diameters, $d_c$ , picked out. . . . .	36



2.1	Picture of a single column CCNc, courtesy of DMT Inc. Boulder, Co. The dual column CCNc used in this work has the same footprint as this instrument. The deionised water and waste water reservoirs can be seen through the viewing window. The lab view software that controls and stores the CCN data can be seen running on the front mounted touch screen. . . . .	45
2.2	Cross section representation of the CCNc column turned on its side. . . . .	47
2.3	CCNc calibration experiment set up. . . . .	50
2.4	Panels a to e show Sigmoid fits from a CCNc calibration experiment showing $S_c(D_0)$ as calculated in Equation 2.4. Panel f shows the fit between the measured set point $S_c(D_0)$ and ADDEM output for all sizes. . . . .	54
2.5	Long term calibrations using ammonium sulphate as described in the calibration procedure. The data marked with crosses from 2 <sup>nd</sup> April 2012 are from a single calibration set up with five replicate calibration points. These data are for equivalent particle diameters as the on going calibrations but have been shifted up from 0.04, 0.065 and 0.085 $\mu\text{m}$ to 0.042, 0.067 and 0.087 $\mu\text{m}$ to allow comparison. The dashed line represents the theoretical critical supersaturation from ADDEM. The open symbols the dates of the calibrations, see the legend. . . . .	57
2.6	Design of the reduced pressure inlet, dimensions are given in Table 2.1. . . . .	59

2.7	Reduced pressure inlet characterisation experimental set up. Note all T-pieces shown in this experimental set up are in fact Y-pieces with an angle of $33^\circ$ . . . . .	62
2.8	Experimental data from the reduced pressure inlet characterisation study showing the ambient total particle concentration $N_{CN}$ against the simple density corrected aerosol as sampled through the reduced pressure inlet. The error bars express 1 standard deviation of the mean. Closed symbols represent the different PSL bead diameters, their exact diameter and error in this diameter measurement can be seen in the Figure legend. . . . .	65
2.9	Modeled losses for the reduced pressure inlet operating at 650 hPa for PSL beads with density of $1050 \text{ kg m}^{-3}$ as compared to the experimental data, the error bars show the propagated relative uncertainty in the measurements of both the control, ambient sample and the test sample at reduced pressure. The open circles represent the measured data, the solid line the total particle penetration, the dashed line the loss on the front face of the critical orifice, the dotted line the losses to the rear of the orifice and the dotted and dashed line the losses to the wall of the inlet post orifice. . . . .	66
2.10	Experimental set up to test instrument effective supersaturation sensitivity to pressure. . . . .	68
2.11	Column A activation curves for $(\text{NH}_4)_2\text{SO}_4$ showing reduced $d_c$ with decreasing pressure. Sigmoid fit lines for each curve are shown, the error bars reflect one standard deviation of the measurement. The open symbols represent the different pressures, each pressure has a distinct line type for each sigmoid fit. The pressure for each test can be seen in the legend. . . . .	69

2.12	Activation curves for $(\text{NH}_4)_2\text{SO}_4$ at five different pressures for column B, each curve is fitted with sigmoid. The sigmoid fit to the lowest pressure is in red as the fit returned a value of a $y$ max over 1.0 and as such the estimation of $x$ half is inaccurate. The error bars reflect one standard deviation of the measurement. The open symbols represent the different pressures, each pressure has a distinct line type for each sigmoid fit. The pressure for each test can be seen in the legend . . . . .	70
2.13	Comparison of the estimated effective supersaturation from AD-DEM for the activation curves in Figures 2.11 and Figures 2.12, the digitised data from Rose et al. (2008) (open triangles) and the model from Roberts et al. (2010) (dotted line with 10 % error the shaded area). The CCNc column A and B are represented by open circles and squares, respectively. The red filled square is the erroneous $SS_{eff}$ estimated from the final activation curve in column B. . . . .	71
2.14	Mean $F_A$ for seven scans of $0.05\text{ }\mu\text{m}$ $(\text{NH}_4)_2\text{SO}_4$ particles for column A. The error bars represent $1\sigma$ of the mean. Each scan is represented by a different shading as seen in the legend. . . . .	73
2.15	Mean $F_A$ for seven scans of $0.05\text{ }\mu\text{m}$ $(\text{NH}_4)_2\text{SO}_4$ particles for column B. The error bars represent $1\sigma$ of the mean. Each scan is represented by a different shading as seen in the legend. . . . .	73
2.16	Activation curves for column A for all seven scans with fitted sigmoid curves. Inset bar chart shows the percentage range of $S_c$ as a function of scans included in the analysis. The data for each scan is represented by open symbols and each sigmoid by a line, both of which can be seen in the legend. . . . .	75

2.17	Activation curves for column B for all seven scans with fitted sigmoid curves. Inset bar chart shows the percentage range of $S_c$ as a function of scans included in the analysis. The data for each scan is represented by open symbols and each sigmoid by a line, both of which can be seen in the legend. . . . .	76
2.18	Internal plan and front elevation of FAAM BAe-146 Certificate of Conformity (CofC) showing the location of the instrument rack containing the CCNc and TSI 3786, three racks from the front of the aircraft on the port side, labelled CCN/CPC/FWVS. . . . .	79
2.19	External elevation of FAAM Bae-146 CofC, Showing the position of the aft port Rosemount inlet pair used by the CCNc and TSI 3786, Port hardpoint PW5 above bay 1 on the large radiation blister. . . . .	80
2.20	Schematic of both the on rack and off rack plumbing for the CCNc and CPC. The red denotes the reduced pressure section and the blue the ambient. . . . .	82
2.21	Model (dashed line) and measured data (closed circles) from flight B599 for reduced pressure inlet variable flow with changing ambient pressure (colour array), $P_2$ . The grey shaded area shows $\pm 2.5\%$ of the model estimate. . . . .	83

2.22	The solid line is an empirical model to describe the pressure in the sample line behind a Rosemount inlet compared to the static ambient pressure. The relationship is based on five flights of data (open symbols) using the pressure transducer in the TSI, 3786 CPC and a validity set of data recorded using a Digitron manometer from flight B599. No error bars are shown as the values of at one standard deviation are too small to be represented on the plot, ranging from 1.05 to 4.24 hPa across all flights. These data fit well to ram pressure theory, depicted by the checked line. . . . .	84
2.23	System $C_v$ plotted against pressure ratio. The colour array represents the positive relationship between $C_v$ and system flow. The dashed line represents the linear relationship between the system $C_v$ and pressure ratio. . . . .	86
2.24	Plumbing architecture for the CCNc instrument rack, from the Rosemount to the rack. The dimensions for these numbered sections are in Table 2.3. . . . .	87
2.26	Example of the composite function, $\eta_{transport}$ (solid line), of loss mechanisms for inertial losses in bends ( $\eta_{bend,inert}$ , short dashed line) and contractions ( $\eta_{cont,inert}$ , medium dashed line), gravimetric losses ( $\eta_{grav}$ , long dashed line) and diffusion ( $\eta_{diff}$ , dotted line) in the CCNc sample line. From the first right angle of the Rosemount inlet to the instrument at a line pressure of 1013.25 hPa with a particle density of $1000 \text{ kg m}^{-3}$ , $\eta_{diff}$ underlies $n_{transport}$ below $0.3 \mu\text{m}$ . . . . .	94

2.27	Total particle transmission calculated for both the CCNc (black lines) and CPC (red lines) for three different pressure altitudes, 1013.25 hPa (solid lines), 845.6 hPa (dotted lines) and 701.2 hPa (dashed lines). . . . .	95
2.28	Model estimates of the total particle losses, $\eta_{transport}$ (solid line) and the contributory mechanisms for inertial losses in bends ( $\eta_{bend,inert}$ , short dashed line) and contractions ( $\eta_{cont,inert}$ , medium dashed line), gravimetric losses ( $\eta_{grav}$ , long dashed line) and diffusion ( $\eta_{diff}$ , dotted line) in the Grimm-SkyOPC sample line. The open circles represent the measured data using PSL beads as the aerosol source. The error bars represent one standard deviation of the measurements. . . . .	97
2.29	Schematics showing the unmodified Rosemount 102E housing with the usual PRT embedded on the left hand side with the modified version used for aerosol sampling on the BAe-146 to the right. . .	98
2.30	Images of the Aft Rosemount pair on the BAe-146. The upper of the two inlets provides the sample for the Aerosol Mass Spectrometer and the lower the CCNc. . . . .	99
2.31	Position of the aft Rosemount pair with respect to the BAe-146 boundary layer depth taken from James (2003). The Thickness lines show the thickness of the velocity boundary layer, defined as the distance from the solid body at which the viscous flow velocity is at 95 and 99 % (open triangles and squares, respectively) of the free stream velocity. . . . .	100

2.32	Panel showing the lab comparison results from the three Grimm Technik Sky-OPC instruments (black CCN inlet, red LTI and blue AMS inlet) used for the inlet analysis flights during the Fennec campaign, 2011. The error bars in each plot represent one standard deviations of the measurement. . . . .	102
2.33	Aerosol distributions measured by the three Grimm Sky-OPCs (CCN red, LTI black and AMS blue), all corrected for both refractive index (real and imaginary 1.53 and 0.001 respectively). The dashed lines represent data that has not been and the solid lines data that has been corrected for loss functions. The data is averaged over 64 minutes from a single straight and level run (SLR) at 343m above the Sahara in N. Mali. <sup>1</sup> These data are not the raw OPC data but data that has been corrected for the enhancement and loss functions of the LTI as per Wilson et al. (2004). . . . .	107
2.34	CCN Rosemount inlet enhancement for all the flights during the Fennec campaign over the Sahara in 2011 where the LTI was operating isokinetically ( $1.0 \pm 0.25\%$ ) The optical diameters have been RI corrected using 1.53n and 0.001i. The coloured blocks represent the descriptive statistics of the inlet efficiency. With solid line the median, the light grey the interquartile range, the medium shading the interdecile range and the black shading the maximum range. The dashed line represents an inlet operating isokinetically and sampling representatively. . . . .	109

2.35	AMS Rosemount inlet enhancement for all the flights during the Fennec campaign over the Sahara in 2011 where the LTI was operating isokinetically ( $1.0 \pm 0.25\%$ ). The optical diameters have been RI corrected using 1.53n and 0.001i. The coloured blocks represent the descriptive statistics of the inlet efficiency. With solid line the median, the light grey the interquartile range, the medium shading the interdecile range and the black shading the maximum range. The dashed line represents an inlet operating isokinetically and sampling representatively. . . . .	110
2.36	The mean inlet enhancements for the two Rosemount inlets (AMS in blue and CCN in red) and the difference between them (open circles) for all flights during the Fennec campaign over the Sahara in 2011 where the LTI was operating isokinetically ( $1.0 \pm 0.25\%$ ). . . . .	112
2.37	Comparison of two different aerosol compositions and the CCN inlet sampling efficiency for each. The black represents the data taken during the Fennec project, the blue represents data taken from one instrument test flight over the North Sea on June 14 2011. Both traces represent the median and the interquartile ranges of the RI corrected data collected. The dashed line represents an inlet operating isokinetically and sampling representatively. . . . .	114
3.1	VOCALS flight tracks for the sorties in Table 3.1 used in the analysis. The operating base Arica can be seen on the Peru, Chile border. The grey lines are the political boundaries, the black the flight tracks and the blue closed circles those points where data was included in the $\kappa$ analysis. . . . .	129



3.2	A schematic of the vertical and longitudinal extent of each flight from the VOCALS subset of sorties used in this analysis. Data is also shown in Table 3.1 and Figure 3.1. Each flight is given a different coloured line, B410 red, B412 black, B414 blue and B417 green. . . . .	130
3.3	Longitudinal gridded descriptive statistics for aerosol and cloud microphysics parameters. Whiskers represent the interdecile range, the box extremities the interquartile range, the middle bar the median and the crosses the mean. The numbers above each box are the number of samples. . . . .	133
3.4	Longitudinal gridded descriptive statistics for sulphate and nitrate ions and non-refractory organic mass fractions from the VOCALS data set. These mass fractions ignore any contribution from ammonia, and chloride ions, on average these components make up a mean value of 4.5 % ( $\sigma$ 2.8 %) of the total mass fraction. Graph 3.4(d) shows the longitudinal trend in organics to sulphate ratio an aerosol characteristic used to highlight differences in source. . . . .	139
3.5	Relationship between organic to sulphate ratio and carbon monoxide concentration for all flights included in the longitudinal survey. Flights that co-sampled with the RH Brown are picked out with crosses as well as open circles. Colours of open circles represent individual flights. . . . .	141
3.6	Longitudinal plot of the mole mass ratio with a line of best fit denoting an increase in acidification with distance from the coast, the $y = 0.5$ and $y = 2.0$ lines showing the ratio at which $\text{H}_2\text{SO}_4$ and $(\text{NH}_4)_2\text{SO}_4$ dominate respectively. . . . .	143

3.7	Scatter plot of CN as measured by the TSI modified 3786 WCPC against integrated CN as measured by the SMPS, highlighting the rejection criteria used in the SMPS data stratification procedures. Flight numbers are represented by closed shapes and colours represent the failure criteria and ‘good data’.	148
3.9	dN/dlog(Dp) log-normal fits for the mean SMPS distribution measured in the MBL between 70° and 80° West. The traces represent the high (red), falling (green) and low (blue) sulphate zones, respectively. The reduction in concentration can be seen along with a shift in dominant mode from the accumulation to the nucleation with distance from the South American continent. The count median diameter ( $D_{pg}$ ) and the geometric standard deviation ( $\sigma_g$ ) for these fits can be found in Table 3.3.	154
3.10	Describes the altitude response of important aerosol parameters used in this analysis. Whiskers represent the interdecile range and the limits of the box the interquartile range. The median is represented by the line bisecting the box and the mean represented by the black crosses.	159
3.11	Co-located measurements for AMS, CPC and SMPS using the same QA procedure for all data which has been averaged to match the same time sequence as the SMPS so data are co-located to the same altitude zone, longitude, flight and time. In Figures 3.11(a) and 3.11(b) the colour array represents altitude. In Figures 3.11(c) and 3.11(d) the red represents the SMPS data whilst the black is AMS and CPC, respectively	162

3.12	Describes the altitude response of AMS mass fractions parameters from the sub set of flights used in this analysis. Again these fractions ignore the contribution from chloride and ammonium ions. Whiskers represent the interdecile range and the limits of the box the interquartile range. The median is represented by the line bisecting the box, the mean is represented by the black crosses.	165
3.13	Mean SMPS distributions for each longitudinal and altitude zone, solid lines and dashed lines representing the mean measurement and the log normal distribution fit respectively.	167
3.14	(a), (b) and (c) Show the cloud parameters represented in both longitudinal and altitude space. White grids represent bins with no data.	169
3.15	GOES 10 1 km resolution. The most northerly and southerly lines of latitude represent 15° and 25° S. The most easterly line of longitude is 70° and westerly 85° W. Both longitude and latitude cells are 5° by 5°.	170
3.16	Graphical representation of the methodology of Equation 3.2 from data collected during the VOCALS campaign. The cumulative SMPS concentration is cumulated from the large to the small diameters.	177
3.17	Relationship between $\kappa$ and SMPS derived critical diameter. The error bars express the propagated standard deviation in the averaging of the CCN to match the SMPS measurement frequency. Bound and filled squares represent the mean $\kappa$ and are colour filled by effective supersaturation. The larger box represents one standard deviation of this mean.	179

3.18	Variation in $\kappa$ with longitude and altitude. . . . .	179
3.19	AMS and CCNc derived $\kappa$ compared with mean SMPS distributions for each zone. The data for this figure can also be seen in Table 3.6. Filled squares represent the CCNc derived and filled diamonds represent the AMS derived $\kappa$ . The colour array for both represent the supersaturation. . . . .	183
3.20	CCNc derived $\kappa$ of differing levels of instrument undercounting (circle at 0 %, squares 2 %, up triangles 4 %, down triangles 6 % and left triangles 10 %) compared with mean SMPS distributions (solid black line) for each zone. The colour array is the supersaturation. . . . .	191
3.21	Five physiochemical schemes of the simplified Köhler equation compared to CCN measurements from the VOCALS campaign. Only data from the lowest 400 m are used. The shaded are a is the $y = x \pm 50\%$ . The colour array represent the supersaturation, circles column A and squares column B of the CCNc. . . . .	206
3.22	Effects on the EXMIX model of stabilising both the chemistry and the particle size distributions to investigate which of the aerosol characteristics have a first order effect on CCN concentrations. The colour array represents supersaturation and the dotted line the $x = y$ line. . . . .	213
3.23	Sensitivity of the EXMIX Köhler model to an increase and decrease of 50%, 30% and 10% in sulphate, nitrate and organic mass loadings. This analysis was conducted only on data from the lowest 400 m of the MBL. Right hand side panels show the $y = x$ as a dashed line. All data have been sorted in ascending order with respect to CCNc measured CCN concentrations. . . . .	217

3.24	Sensitivity of the EXMIX Köhler model to an increase and decrease of 50%, 30% and 10% in critical supersaturation, surface tension and van't Hoffs number, this analysis was conducted only on data from the lowest 400 m of the MBL. All right hand side panels show the $y = x$ as a dashed line. All data have been sorted in ascending order with respect to CCNc measured CCN concentrations. . . .	219
3.25	Sensitivity of the EXMIX Köhler model to an increase and decrease of 50%, 30% and 10% in aerosol number concentration and particle diameter, this analysis was conducted only on data from the lowest 400 m of the MBL. All right hand side panels show the $y = x$ as a dashed line. All data have been sorted in ascending order with respect to CCNc measured CCN concentrations. . . . .	222
3.26	Sensitivity of the CCNc instrument to an increase and decrease of 50%, 30% and 10% in CCN number concentration to the baseline EXMIX Köhler model, this analysis was conducted only on data from the lowest 400 m of the MBL. All right hand side panels show the $y = x$ as a dashed line. All data have been sorted in ascending order with respect to the model. . . . .	229
3.27	The fraction of less hygroscopic aerosol as a function of particle diameter as calculated from the maximum overestimation model shown in Wex et al. (2010). Data points are coloured by CCNc derived $\kappa$ for all effective supersaturations, the error bars represent one standard deviation of the critical diameter mean values. The linear model fit used to extrapolate to larger diameters is also shown as are the estimated ranges for three environment types from McFiggans et al. (2006). . . . .	231

3.28	Mean SMPS distributions and less hygroscopic modes for each sulphate zone. The $f_{less}$ model critical diameter estimates have solid bisecting lines, the AMS, the CCNc and the critical diameter of the less hygroscopic mode itself use dashed lines. All measurements are for an effective supersaturation of 0.17 % . . . . .	232
3.29	$f_{less}$ models compared to CCNc measured CCN concentrations, colour coded by effective supersaturation. The black closed circles represent the EXMIX baseline model. . . . .	234
3.30	Example of the output distribution from the CCNc OPC and model estimates of the Normal probability distribution function for each, used to estimate mean droplet diameter and the standard deviation of that mean in Figures 3.32 and 3.33. The dotted line represents the $x = y$ and the red and black crosses the column A and column B of the CCNc respectively. . . . .	241
3.31	Example of the output distribution from the CCNc OPC and model estimates of the normal probability distribution function for each, used to estimate mean droplet diameter and the standard deviation of that mean in Figures 3.32 and 3.33. Black represents 0.085 , red 0.05 and blue 0.04 $\mu\text{m}$ $(\text{NH}_4)_2\text{SO}_4$ dry particle diameters. . . . .	242
3.32	Calibration salt TDG analysis for column A. The closed symbols are calibration salt diameters. The open symbols represent the modelled data at 650 hPa. The lines represent different power laws, dashed for measured, dotted for 700 and solid for 650 hPa, respectively. . . . .	243

3.33	Calibration salt TDG analysis for column B. The closed symbols are calibration salt diameters. The open symbols represent the modelled data at 650 hPa. The lines represent different power laws, dashed for measured, dotted for 700 and solid for 650 hPa, respectively. . . . .	244
3.34	Threshold droplet growth analysis for the data collected throughout the VOCALS campaign with both columns compared to ammonium sulphate calibration salts. Shaded area represents the standard deviation of the calibrated model as estimated in the previous section of this work. . . . .	245

# List of Tables

2.1	Dimensions of the reduced pressure inlet, the flow rate under choked conditions. . . . .	59
2.2	Dynamic heating of sample in the Rosemount inlet calculated assuming an adiabatic process. . . . .	85
2.3	Dimensions of the plumbing between the first right angle of the modified Rosemount inlet and the CCN rack, section numbers relate to labels in Figure 2.24, orientation is with respect to gravity and angle is the angle of the bend in radians. . . . .	88
2.4	Dimensions of the plumbing between the point A and the CCNc inlet, section numbers relate to labels in Figure 2.25(a), orientation is with respect to gravity and angle is the angle of the bend in radians. . . . .	89
2.5	Dimensions of the plumbing between the point A and the CCNc inlet, section numbers relate to labels in Figure 2.25(a), orientation is with respect to gravity and angle is the angle of the bend in radians. . . . .	89



3.1	Details of the VOCALS sorties as flown by the BAe-146 and the flights whose data are used in this analysis. Comment is given on those flights where data is not included and the reason for exclusion. 'No CCN data' refers to one or more columns being operated below the minimum threshold after pressure corrections. . . . .	131
3.2	SMPS data rejection criteria and the number of data points rejected by each or included by each method. It should be noted that the erroneous data are not mutually exclusive, a data point with an inversion error is more than likely to also be rejected on grounds of inlet shattering. . . . .	149
3.3	Descriptive statistics for aerosol measurements and lognormal parameters for the coarse MBL zonal data stratifications; high, falling and low sulphate regions. It should be noted that the difference between the number of points in each analysis will be different as each instrument has their own criteria for data rejection. . . . .	155
3.4	Descriptive statistics for aerosol measurements and log-normal parameters for the coarse zonal and altitude data stratifications; high, falling and low sulphate zones in the longitudinal axis, 0-400 m, 400-800 m and 800 -1200 m in the vertical. All data including or derived from the CCN concentration, CCN and $F_A$ are for instrument measurements when the supersaturations were between 0.09 and 0.13% . . . . .	174
3.5	Kappa and critical diameter calculations binned by longitudinal for SPMS scans from the lowest 400 m. The maximum and minimum values are calculated from the propagation of the errors associated with the variability in the CCN measured during each SMPS scan.	181

3.6	Mean and relative standard deviation measurements for the data plotted in Figure 3.19. . . . .	184
3.7	$\kappa$ values taken from the literature. It should be noted that all these measurements are made in the boundary layer unless specifically stated otherwise. Again unless otherwise stated these data are derived from CCNc measurements and not other methodologies. . . . .	195
3.8	Table showing the speciation of ammonium and sulphate ions referenced to the value of $R_{so4}$ . . . . .	199
3.9	Closure analysis for the VOCALS CCN data set and the five particle physio-chemical models. The table shows the slope of the fit of the data, and the correlation coefficient, $R^2$ . The normal mean error, NME, indicates the degree of scatter, and normal mean bias, NMB, reflects the degree of systematic errors from perfect closure. The mean, standard deviation, minimum and maximum predicted to observed ratio ( $N_p/N_o$ ) are also shown. . . . .	207
3.10	CCN closure experiments from the literature. . . . .	211
3.11	Various parameterisations and measurement errors from this work and the literature for the initialisation parameters used in Equation 3.5 under the EXMIX scheme. . . . .	214
3.12	Sensitivity analysis metrics of the EXMIX model. . . . .	225
3.13	Fit statistics for $f_{less}$ models compared to the simple EXMIX model. . . . .	234
6.1	List of principle symbols . . . . .	268
6.2	List of principle symbols cont. . . . .	269

# Abstract

This work tests the validity of using a commercial cloud condensation nuclei (CCN) counter (CCNc) on the Facility for Airborne Atmospheric Measurements (FAAM) research aircraft. The CCNc was suitable for aircraft work with stable and repeatable supersaturation, temperature and pressure relationships. The sample architecture of the aircraft fitted CCNc was found to transmit particles with acceptable losses in the diameter range of interest as was a pressure control device designed for airborne work. Rosemount inlets, used to sample aerosol, were found to be sensitive to particle density resulting in disparate aerosol being sampled with different efficiencies. In dust dominated aerosol inlet efficiency peaks at 10.24 at an optical diameter of  $2.91\text{ }\mu\text{m}$ , with a minimum inlet efficiency between 1.78 and 1.51 at  $0.28\text{ }\mu\text{m}$ . In less dense aerosol inlets sample representatively below  $0.6\text{ }\mu\text{m}$  and comparably below  $1.0\text{ }\mu\text{m}$ .

The thorough testing of the CCNc, associated sampling architecture and measurement strategies, enabled vertical and horizontal CCN to be investigated along with other aerosol and cloud microphysical properties in the Southern Equatorial Pacific (SEP). The primary source of particulates was the South American continent, with sulphate dominating composition. There were strong gradients in aerosol and gas phase chemistry concentration with distance from the coast and in the cloud microphysics measurements where highest droplet numbers and smallest diameters were close to the coast. These data represent an important validating and parameterisation data set for models of all scales. CCN data were used to calculate the aerosol hygroscopicity parameter, the mean project value,  $\kappa$ , was  $0.21 \pm 0.18$ . There was no evident variation in hygroscopicity with distance from the Chilean coastline suggesting a single dominant source and a well mixed boundary layer up to 907 km to the west. CCN measurements were also compared to predictions from multiple models of different composition and mixing state assumptions. The best CCN closure used an external mixture of inorganic and organic aerosol components, with a modelled to observed ratio of  $1.37 \pm 0.32$ . It was hypothesised that this large ratio and the relatively low bulk hygroscopicity was influenced by an external mixture. Incorporating this external mixture is imperative if CCN are to be accurately modelled and any subsequent cloud processes accurately captured.

# Declaration

**The University of Manchester**

***PhD Candidate Declaration***

**Candidate Name: James Alexander Trembath**

**Faculty: School of Earth, Atmospheric and Environmental Science**

**Thesis Title: Airborne CCN Measurements**

**Declaration to be completed by the candidate:**

I declare that no portion of this work referred to in this thesis has been submitted in support of an application for another degree or qualification of this or any other university or other institute of learning.

Signed:

Date: November 4, 2013

# Copyright

The author of this thesis (including any appendices and/or schedules to this thesis) owns any copyright in it (the "Copyright")<sup>1</sup> and s/he has given The University of Manchester the right to use such Copyright for any administrative, promotional, educational and/or teaching purposes.

Copies of this thesis, either in full or in extracts, may be made only in accordance with the regulations of the John Rylands University Library of Manchester. Details of these regulations may be obtained from the Librarian. This page must form part of any such copies made.

The ownership of any patents, designs, trade marks and any and all other intellectual property rights except for the Copyright (the "Intellectual Property Rights") and any reproductions of copyright works, for example graphs and tables ("Reproductions"), which may be described in this thesis, may not be owned by the author and may be owned by third parties. Such Intellectual Property Rights and Reproductions cannot and must not be made available for use without the prior written permission of the owner(s) of the relevant Intellectual Property Rights and/or Reproductions.

---

<sup>1</sup>This excludes material already printed in academic journals, for which the copyright belongs to said journal and publisher. Pages for which the author does not own the copyright are numbered differently from the rest of the thesis.

Further information on the conditions under which disclosure, publication and commercialisation of this thesis, the Copyright and any Intellectual Property and/or Reproductions described in it may take place is available in the University IP Policy (see <http://documents.manchester.ac.uk/DocuInfo.aspx?DocID=487>), in any relevant Thesis restriction declarations deposited in the University Library, The University Library's regulations (see <http://www.manchester.ac.uk/library/aboutus/regulations>) and in The University's policy on Presentation of Theses

# Acknowledgements

I dedicate this work to my family, in particular my wife Beth and though it is of little comfort to them my daughters Eve, Maya and Lily. I can only apologise for all the times I have not been around in the last year whilst writing up. I would like to thank all those in the School of Earth, Atmospheric and Environmental Science at Manchester University who have helped me produce this work, particularly Hugh Coe and Paul Williams. I would also like to thank everyone I have worked with at the Facility for Airborne Atmospheric Measurements, and in particular Phil Rosenburg, Greame Nott and Axel Wellpot, better sounding boards would be hard to find and I apologise after the fact for boring you all senseless. Finally I would like to thank Alan Woolley who has been understanding and supportive as both a friend and a manager.

# Expected Publications

From this thesis I expect to produce the following publications. A paper detailing the limitations of using modified Rosemount housings as aerosol inlets. A paper continuing the closure analysis of the CCNc data from the SEP to include cloud droplet number closure utilising the Aerosol-Cloud-Precipitation Interaction Model (ACPIM). Finally the  $\kappa$  analysis from this work will be included in a data synthesis of all the CCNc data collected from the BAe-146 using the CCNc instrument tested here.



# Introduction

The origin of the word *aerosol* is an analogue of the word *hydrosol*, the accepted definition being of a particle suspension in a gaseous medium (Hinds, 1999). Developments in aerosol science have historically been propelled by two main drivers, health and air quality. In recent decades the profound effect aerosols exert on the global thermodynamic and energy budgets has come to the fore (Hudson, 1993; Andreae, 2009). Aerosols interact with the global radiation by both scattering and absorbing incoming shortwave radiation and absorbing outgoing longwave radiation (Haywood and Boucher, 2000). The effect an aerosol has on the radiative balance of the planet can be split into three distinct groups; direct, semi-direct and indirect effects, discussed below. The addition to the aerosol burden by man’s activity necessarily affects all of these processes (Haywood and Boucher, 2000; Haywood et al., 2003; Roberts et al., 2006; Andreae, 2009; Roberts et al., 2010; Lance et al., 2009).

The direct effect dictates how aerosols scatter and absorb solar and thermal infrared radiation altering the radiative balance of the planet, essentially modifying the planetary albedo (Haywood and Boucher, 2000; Haywood et al., 2003; Osborne et al., 2000), the overall effect is one of cooling the atmosphere by re-

ducing the input of energy to the surface. The magnitude of the direct effect is a function not only of aerosol concentrations and dry diameter but of relative humidity in the subsaturated regime. The effective radius of many atmospheric aerosols can be increased by absorption of water, the extent of this growth is a function of the aerosol’s hygroscopicity and the ambient relative humidity (Haywood and Boucher, 2000). The semi-direct effect is concerned only with radiative absorption, where an aerosol can decrease low cloud cover by heating the air and reducing the relative humidity, this process can also modify low level heat fluxes as less energy reaches the surface. This in turn can reduce cloud cover or reduce the likelihood of cloud cover forming (Johnson et al., 2004).

When the atmosphere becomes supersaturated, primarily in updrafts, some aerosol particles in an ambient population grow in size, via a process of water vapour condensation to form droplets. This growth initially occurs in equilibrium with the environmental saturation ratio until the droplet reaches a tipping point at a critical diameter. At this point the droplet can be considered to be activated and forms a cloud droplet. Once activated the droplet is no longer in equilibrium with its environment. If the ambient saturation ratio is greater than the droplet equilibrium vapour pressure then the droplet will grow unchecked. These aerosol particles that activate to form cloud droplets are known as cloud condensation nuclei (CCN). They are not a fixed proportion of the aerosol population but a variable subset, dependent on the number of soluble molecules contained in a particle, which is consequently a function of the particle’s characteristic size and chemistry (Andreae and Rosenfeld, 2008). As such not all particles are equally efficient as CCN. It is the measurement of aerosol composition that poses a challenge in predicting an aerosol’s ability to act as a CCN, particularly as an aerosol ages (Seinfeld and Pandis, 2006; Dusek et al., 2006; Lance et al., 2009).

Historically interest in CCN was confined to the effects on both warm and cold

precipitation in addition to aerosol scavenging processes (Hudson, 1993). These interests continue today with increased CCN concentrations due to anthropogenic activities playing a role in increased convective precipitation, redistribution of water resources and the possibility of increasing severity of hurricanes by redistributing moisture from low to higher levels in storm systems (Hudson, 1993; Cotton et al., 2007; Andreae, 2009). The Intergovernmental Panel on Climate Change (IPCC) in its most recent report puts emphasis on increasing the understanding of the effects of aerosol, namely CCN, on the cloud radiative properties through modification of the microphysics (Forster et al., 2007). This is known as the cloud albedo or indirect effect.

The indirect effect can be described in the broadest manner as the processes by which aerosols affect the global radiation budget through their interaction with clouds, which of all the planetary surfaces contribute the most to the total reflection of incoming radiation, through modifying cloud fraction, their life time and albedo (Twomey, 1974). Of all the bulked-averaged quantities that cloud albedo depends on, optical thickness is by far the most important and has the most dominant role in determining the amount of light scattered by clouds. Assuming that the liquid water content (LWC) and the vertical velocities are constant, a cloud's optical thickness is determined by the size of the cloud drop, this characteristic in turn is very much controlled by the number and composition of the aerosol and therefore by extension can be perturbed by anthropogenic aerosol (Twomey, 1974; Hudson, 1993; Haywood and Boucher, 2000; Andreae, 2009). This effect is often called the first indirect or Twomey effect. The number of CCN in an aerosol population can also modify the lifetime of clouds. Assuming uniformity in the conditions under which a cloud forms, an increase in the number of CCN decreases the size of each droplet which subsequently reduces the drizzle production.

In warm clouds, cloud droplet spectral broadening is required for raindrops to form. This is controlled by the collision- coalescence process (Rogers and Yau, 1996). Unlike condensational growth which takes too long to grow particles in excess of  $20\text{ }\mu\text{m}$  the collision- coalescence process is exponential in nature (Wood, 2012). Where larger particles, often called collector drops, fall due to gravity within the cloud colliding with smaller cloud drops. In some instances these collisions result in coalescence and a larger drop is formed. This process is an accelerating growth process as the collector drops falls its adds to its mass therefore falling faster with a larger surface area reducing the chance of smaller cloud droplets being diverted around the drop. High concentrations of CCN have been shown to inhibit this collision-coalescence precipitation process leading to the suppression of warm rain, this has been dubbed pluvial constipation (Hudson, 1993). This reduction in precipitation in turn increases the cloud liquid water content and the fractional cloudiness and in the end the lifetime of the cloud itself (Albrecht, 1989; Hudson, 1993; Haywood and Boucher, 2000; Osborne et al., 2000; VanReken et al., 2003).

The current understanding of the magnitude and uncertainty associated with each of the total aerosol effects (both direct and indirect) has been published by the IPCC (Forster et al., 2007) and can be seen in Figure 1.1. Of major interest here is the sign and the magnitude of the uncertainty associated with the aerosol effects. Anthropogenic aerosols cool the planet, however the estimate of the uncertainty associated with the indirect effect alone is close in magnitude to the entire positive radiative forcing term associated with the greenhouse effect of  $\text{CO}_2$ . The processes associated with the indirect effect have been defined, by the IPCC, as having a low level of scientific understanding (LOSU), implying that more research effort is required in this area. These large uncertainties are primarily a function of the complexity of aerosol cloud interactions and the strong influence

clouds have on the planetary radiative balance. The sub grid nature of the cloud processes can cause errors when upscaled to estimate global radiative forcing. These scale issues are often compounded by poorly constrained parameters and assumptions regarding cloud aerosol interactions (Lance et al., 2009; Pringle et al., 2010; Snider et al., 2003; Wood et al., 2011).

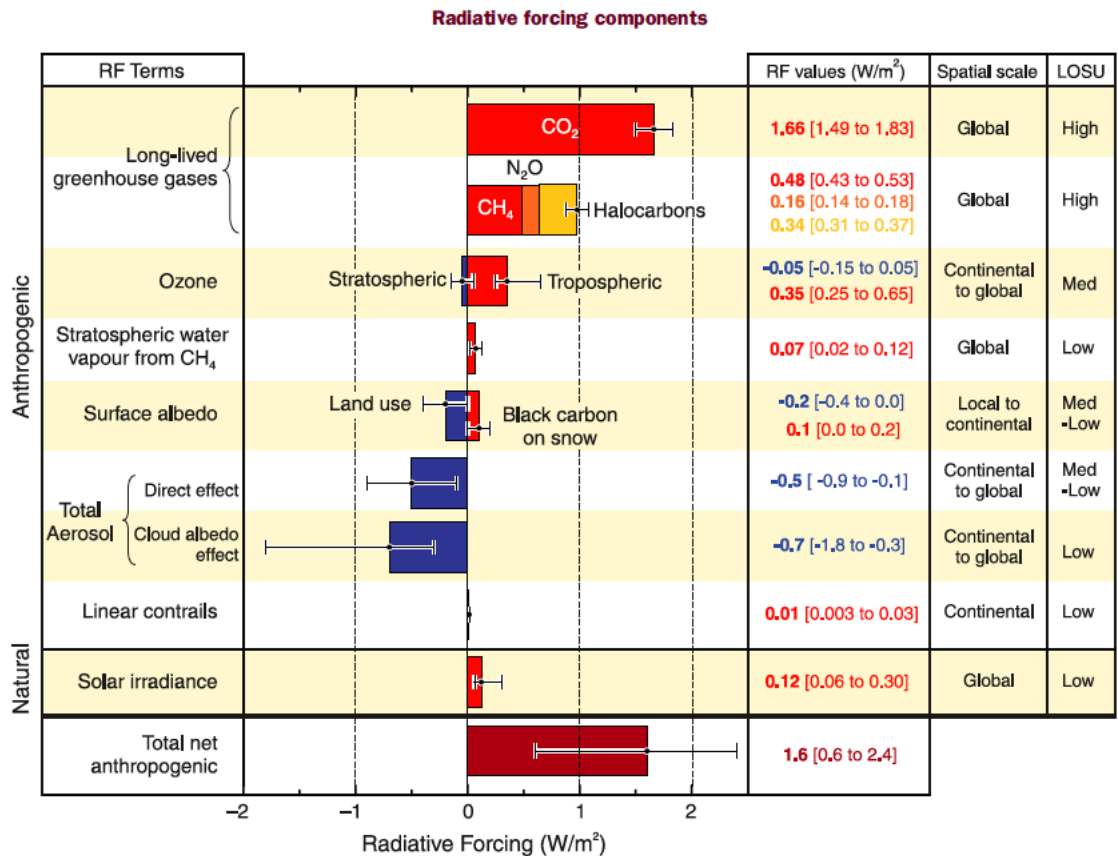


Figure 1.1: Global average radiative forcing (RF) in 2005 (best estimates and 5 to 95 % uncertainty ranges) with respect to 1750 for CO<sub>2</sub>, CH<sub>4</sub>, N<sub>2</sub>O and other important agents and mechanisms, together with the typical geographical extent (spatial scale) of the forcing and the assessed level of scientific understanding (LOSU). Aerosols from explosive volcanic eruptions contribute an additional episodic cooling term for a few years following an eruption. The range for linear contrails does not include other possible effects of aviation on cloudiness.

One challenge therefore is to accurately estimate the ability of an aerosol particle to act as a CCN under atmospherically relevant conditions (Rose et al., 2010)

and thereby reduce the level of uncertainty in the estimate of radiative forcing due to the indirect effect. The ability of an aerosol particle to form a cloud drop can be modelled using the simplified Köhler equation which gives an equilibrium relationship between an aqueous salt solution droplet and water vapour, derived from the Clausius-Clapeyron equation which describes the change in saturation vapour pressure with temperature (Seinfeld and Pandis, 2006). Where the saturation ratio

$$\ln\left(\frac{p_w(D_p)}{p^0}\right) = \frac{4M_w\sigma_w}{RT\rho_w D_p} - \frac{6n_s M_w}{\pi\rho_w D_p^3}, \quad (1.1)$$

$p_w(D_p)$  and  $p^0$  are the water vapour pressures over a droplet and over a flat surface respectively,  $D_p$  is the droplet diameter  $M_w$  the molecular weight of water,  $\sigma_w$  the surface tension of water,  $R$  the universal gas constant,  $T$  the ambient temperature,  $\rho_w$  the density of water and  $n_s$  the number of moles of the solute. It is however, customary to write

$$A = \frac{4M_w\sigma_w}{RT\rho_w} \quad B = \frac{6n_s M_w}{\pi\rho_w}, \quad (1.2)$$

where  $A$  is known as the curvature or Kelvin term and  $B$  the solute or Raoult term, so

$$\ln\left(\frac{p_w(D_p)}{p^0}\right) = \frac{A}{D_p} - \frac{B}{D_p^3}. \quad (1.3)$$

Figure 1.2 shows the Köhler curves for two inorganic salts  $(\text{NH}_4)_2\text{SO}_4$  and  $\text{NaCl}$  both of the same initial dry size of  $0.5\mu\text{m}$ . As discussed previously an aerosols ability to activate is dependent on the number of soluble molecules contained in a particle which is consequently a function of the particles characteristic size and chemistry. This dependency on the number of soluble molecules can be

seen in the different saturation ratio maxima of the curves for the two salts of the same original dry diameter. With a critical supersaturation of 0.3 % for NaCl and 0.4 % for  $(\text{NH}_4)_2\text{SO}_4$ .

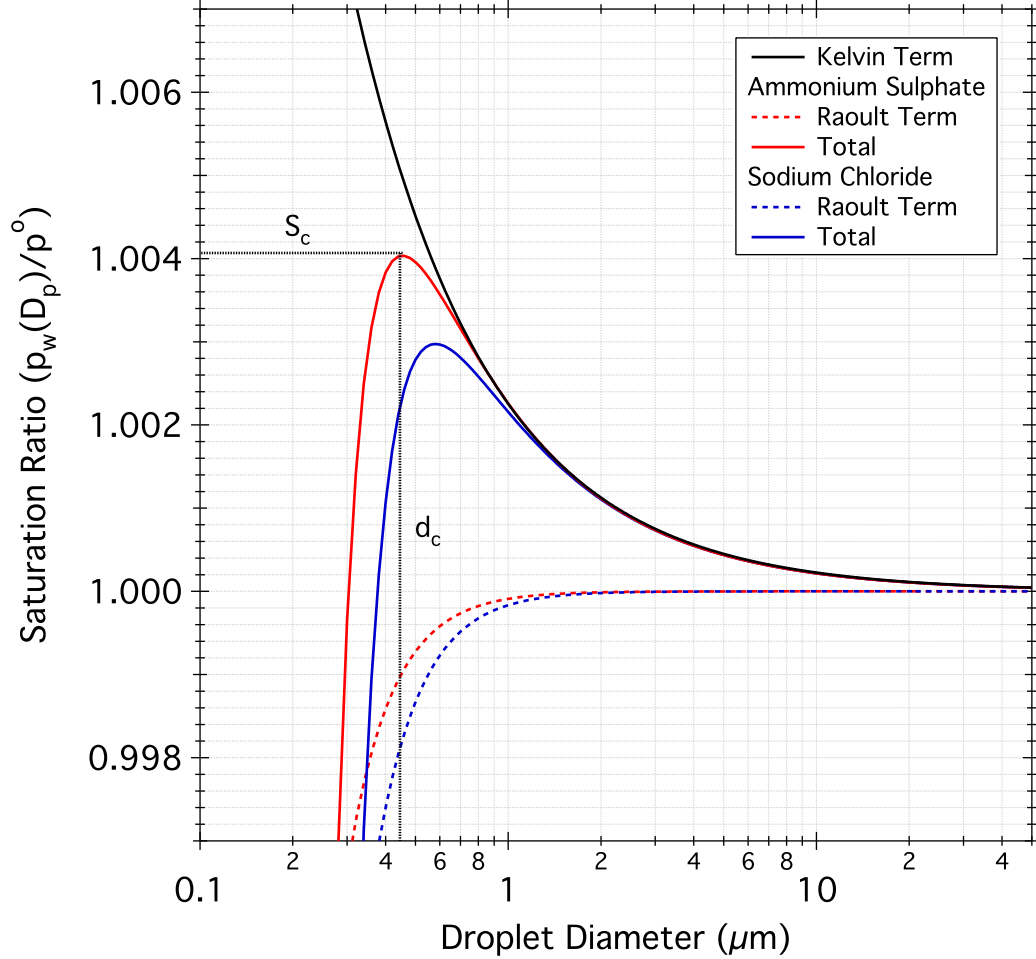


Figure 1.2: Köhler curves for two ammonium sulphate and sodium chloride of an initial  $0.5 \mu\text{m}$  dry size. Both the competing Kelvin and solute terms are shown. With the critical supersaturation,  $S_c$  and critical diameters,  $d_c$ , picked out.

Supersaturation can be calculated from the saturation ratio as the percentage of the fraction above 1.0. There is a single maxima in supersaturation for any given initial dry particle size and composition, this is known as the critical supersaturation ( $S_c$ ). So the  $S_c$  of a droplet formed from a  $0.05 \mu\text{m}$  ammonium sulphate particle, where the saturation ratio is 1.004 is 0.4 %. Consequently the diameter

of the droplet at which this maxima is reached is called the critical diameter ( $d_c$ ). To the left hand side of this maxima, in Figure 1.2, the droplet is in equilibrium with the environment. Its size being dependent on the atmospheric saturation ratio. If the environment dries out water molecules are lost from the surface of the droplet causing it to shrink and *vica versa*. Once the ambient supersaturation exceeds the critical supersaturation water molecules will continue to condense onto the droplet as long as the ambient supersaturation remains above the equilibrium vapour pressure as dictated by the Kelvin equation, solid black line in Figure 1.2. So for any give ambient supersaturation there can be two droplet diameters, only one of which is in equilibrium and stable.

At droplet diameters less than the critical diameter the solute term which is dependent on the the number of solute molecules and the level to which those molecules disassociate in water dominates. Droplets are assumed to be dilute enough to act as ideal solutions. The addition of an inorganic salt such as ammonium sulphate reduces the vapour pressure of that of pure water by action of ensuring that not all the molecules at the surface are water molecules and available for evaporation.

At supersaturations above the critical diameter the Kelvin term dominates. The Kelvin equation dictates that the vapour pressure over a curved surface is always more than over a plane surface. On a curved surface there are fewer molecules adjacent to any molecule that is at the liquid gas interface than in a flat surface. This reduction in molecules produces a reduction in the attractive Van der Waals forces on each surface molecule causing a reduction in the amount of energy required to separate this molecule from surface liquid to the gas phase. As with the equilibrium vapour pressure of a plane surface the Kelvin effect is temperature dependent. The colder the droplet the lower the equilibrium vapour pressure. The most important point is that for a water droplet to be



in equilibrium with its environment the air needs to be supersaturated as the equilibrium vapour pressure of a droplet is greater than that of flat surface. It is also important to note that the equilibrium of a pure water droplet is unstable. Consider the Kelvin term in Figure 1.2 on page 36 the addition of a few water molecules by collision will increase the diameter of the droplet. The loss of a few water molecules from the atmosphere will have no apparent effect on the ambient supersaturation. Now the equilibrium vapour pressure for that droplet will have fallen causing more water vapour to condense on to the particle and the droplet to continue to grow. The converse of this scenario is also true, the smallest nudge to this system can cause complete evaporation or uncontrolled growth.

This instability is tempered in reality as there are no homogeneously or self-nucleated cloud droplets containing only pure water. This form of nucleation requires supersaturations in excess of 250 % at standard temperature pressure (STP). In reality droplets are all aqueous solutions and are formed by heterogeneous condensation. This is a process of droplet formation that is promoted by the presence of a cloud condensation nuclei as described by the Köhler equation. Because of these nuclei activation can occur at saturation ratios that are atmospherically relevant (below 1 %) due to the Raoult term in Equation 1.3. This form of nucleation is the primary mechanism for cloud droplet formation (Hinds, 1999; Rogers and Yau, 1996; Seinfeld and Pandis, 2006). Condensation nuclei can be both soluble and insoluble and can take up water at relative humidities below 100 % to form haze. The importance of which has been discussed with regard to the increase in direct effects as a response to an aerosol's increased effective radius.

Single salt parameterisations of the Köhler equation, historically ammonium sulphate was used as it is the most atmospherically relevant, often lead to over-predictions of modelled CCN number when compared to measurements (Van-

Reken et al., 2003; Roberts et al., 2006; Rissman et al., 2006; Roberts et al., 2010). These parameterisations, however, are simple to initialise as the thermodynamic characteristics of the aerosol are well known. Even more complex multi-component parameterisations which increase the representative nature of the models can lead to errors in predicted CCN number for numerous reasons. As yet no single measurement technique is capable of measuring the full array of compounds in an ambient aerosol population (McFiggans et al., 2006; Andreae and Rosenfeld, 2008; Lance et al., 2009) so accurate solute parameterisation is often impossible. The complexity of aerosol organics and the sheer magnitude of possible compounds, many with unknown characteristics, often leads to assumptions being made with regard to their solubility, density, molecular weight, surfactant properties and their interaction with inorganic components (Prisle et al., 2008, 2011; Lance et al., 2009; Asa-Awuku et al., 2011). As the prevalence of organics increases in an aerosol’s mass so the importance of understanding the exact composition of the organics also increases (Wang et al., 2008). Most of these more complex solute schemes work on a volume mixing rule so it stands to reason the more of something in solution, ideality assumed, the more effect it has on the activation properties. An aerosol’s composition is more often than not complex. This complexity can be compounded when considering an aerosol population’s mixing state, particularly when close to source in newly formed aerosol particles. The best estimates of CCN number are achieved where there is knowledge of the size-resolved chemistry of the aerosol population (Murphy et al., 2009; Moore et al., 2012). Mixing state is strongly correlated to aerosol age; the further an aerosol is from source the easier it becomes to model. As an aerosol is advected away from source it ages. The ageing processes of condensation, oxidation and oligomerization generally act to increase the aerosol hygroscopicity. (Andreae, 2009; Roberts et al., 2010; Juranyi et al., 2010). A more detailed discourse on sources of error involved with using the simplified Köhler equation can be found

in Section 3.3.

The need for detailed thermodynamic characteristics, molecular weight, density and activity coefficient (a factor used to account for deviations away from ideal behaviour in a mixture), required to parameterise Köhler models, can be absolved by using single parameterisations. These parameters capture the characteristics of the solute term, that term of the Köhler equation that describes an aerosol’s hygroscopicity. A parameter that is widely used in the literature is  $\kappa$  (Petters and Kreidenweis, 2007),

$$\kappa = \frac{4A^3}{27d_c^3 \ln^2 S_c} \quad (1.4)$$

where  $d_c$  is the critical diameter,  $S_c$  the critical supersaturation.  $A$  is given by

$$A = \frac{4\sigma M_w}{RT\rho_w} \quad (1.5)$$

where  $M_w$  the molecular weight of water,  $\sigma$  the surface tension of the droplet,  $R$  the universal gas constant,  $T$  the ambient temperature,  $\rho_w$  the density of water.

This parameter can be used to directly compare aerosol hygroscopicity from different sources, understand the spatio-temporal variability in aerosol hygroscopicity and reduce the computational requirement and compositional informational requirement to predict the CCN number of an ambient aerosol. The single most striking feature of the spatial variability in aerosol hygroscopicity is that seen between the great oceans and continents. This difference is also reflected in cloud droplet number (Wood, 2012). These differences have been known for some time and is related to differing major sources and source strengths over oceans and continents (Squires, 1958; Hudson, 1993), and is reflected in the the mean  $\kappa$  values for each aerosol type. Most continental aerosol  $\kappa$  values fall within a narrow

range of around  $0.3 \pm 0.1$  and for marine aerosol the mean value is  $0.7 \pm 0.1$  (Andreae, 2009). Rose et al. (2010) showed that a  $\kappa$  value of 0.3, the mean measured in the Pearl River Delta, China during the summer of 2006, appears to capture the majority of variability in measured CCN, but fails to capture the full extent of the variability in time when used to model CCN. This suggests that the mean value for continental aerosol should not be used for models with short time scales. This fits with the findings of Dusek et al. (2006) that size is the primary driver of an aerosol's ability to be a CCN and that chemistry is a second-order driver. The application of  $\kappa$  to a range of aerosols in climate models is as yet not well characterised (Roberts et al., 2010), and therefore more data is required to underpin these generalisations.

Knowledge of the spatio-temporal distribution of CCN is a requirement to be able to accurately parameterise aerosol cloud interactions in models of all scales. This can only be achieved by adding to the current data set of CCN measurements taken from many regions of the world (Andreae, 2009; Bougiatioti et al., 2009; Dusek et al., 2006; Ervens et al., 2005; Gunthe et al., 2009; Lance et al., 2009; Roberts et al., 2006, 2010; Moore et al., 2011, 2012; Wang et al., 2008; Asa-Awuku et al., 2011). Until recently few data were available for the Southern Equatorial Pacific (SEP) region. This region is characterised by a persistent large subtropical stratocumulus deck, a common feature of coastal regions where cold water upwelling reaches the surface (Wood et al., 2011; Allen et al., 2011; Zheng et al., 2011; Bretherton et al., 2010). Stratus clouds are important for climatic considerations for a number of reasons. Globally they cover more area and have longer lifetimes than other cloud types. Since they are predominantly a maritime feature they provide a greater albedo contrast with the underlying ocean surface and being persistent they ensure continued albedo contrast. They are optically thinner so when perturbed their optical properties are more sensitive to micro-

physical alterations. Finally these low level clouds have a greater cooling effect than high level clouds as their energy balance is skewed in favour of shortwave reflection over absorption due to their higher cloud top temperatures (Hudson, 1993).

There are five major science questions posed at the start of this work. These goals form the basis of the following two chapters and are explicitly discussed below with some reference to their importance and relation to previous topics discussed in this chapter. All subsequent questions in this work are reliant on the completion of the first goal.

Can an ‘off the shelf’ CCNc be used on a fast research jet, such as the BAe-146, to produce viable data sets? CCN are, as has already been discussed, important in understanding the link between aerosols and cloud microphysics and therefore the indirect effect. These aerosol cloud interactions are not currently well understood and more data is needed to further the process understanding. It is also incredibly important that these measurements are made in the portion of the atmosphere that is most relevant to warm rain cloud formation. Namely the top of the boundary layer, which is only readily reachable by powered aircraft. The CCNc instrument used here is tested and validated in Section 2.1 on page 44.

Given the importance of stratocumulus cloud decks in the global albedo of the planet. What are the characteristics of the aerosol and gas phase chemistry in the SEP? A region of the planet that has the largest and most persistent stratocumulus deck. This information is of importance as a validity and parameterisation data set for models of all scales. Section 3.1 on page 126 deals with these data in great depth.

Thirdly, can the CCNc data be used to derive a value for  $\kappa$  in the SEP, what are the characteristics of this parameter in respect to any trends born out of the SEP characterisation? How do values in this hygroscopicity parameter compare to

values derived from AMS composition data and what are the possible limitations of the methodologies used? This parameter as discussed can be of great use in comparing the hygroscopicity of aerosol between different environments. It is also routinely used in determining CCN concentration and therefore CDN in modelling studies. This analysis can be found in Sections 3.2 and 3.3.

The fourth goal is linked to the third, what does the derived  $\kappa$  tell us about the aerosol of the SEP? Is it what the composition measurements suggest it should be if not what source of error could cause a discrepancy? This is important as both the CCNc derived hygroscopicity or the composition derived value can be used in modelling studies. If there is discrepancies, they can be carried through to estimations of CCN, CDN and other cloud processes. Can it be used to inform on source locations, long range transport and mixing state? How does it compare to other studies from the literature? These questions are discussed in Section 3.3 on page 198

The final goal is to use the CCNc data to investigate if there are any kinetic limitations to water uptake of the aerosol in the SEP? Is the activation of the aerosol retarded in anyway when compared to a ‘rapid growth’ model. This retardation is usually a function of insoluble organics creating a kinetic barrier that delays growth. In the CCNc this could result in particles of smaller diameters, that would have activated if there was no delay in growth, not being counted as CCN. In the atmosphere these kinetic limitations can cause suppression of drizzle by inhibiting the growth of giant CCN and limiting the activation and growth of other subsets of the aerosol population. (Asa-Awuku et al., 2009; McFiggans et al., 2006). The analysis of the aerosol activation kinetics can be found in Section 3.4 on page 239.

# Cloud Condensation Nuclei Counter: Instrument Behaviour, Characterisation and Operation

## 2.1 CCNc Instrument

### 2.1.1 Principle of Operation

The Cloud Condensation Nuclei counter (CCNc) used here is the Droplet Measurement Technologies Inc. (DMT) dual column (column A and B) continuous-flow stream-wise thermal gradient chamber (CFSTGC) instrument: see Figure 2.1. It is designed to operate on both the ground and in airborne applications. The principles of its design are outlined in Roberts and Nenes (2005); Rose et al. (2008) and Lance et al. (2006). At the core of the instrument is a 0.5 m long vertical cylindrical aluminium column with an internal diameter of 0.02 m the inner surface of which is coated with a 2.5 mm deep bisque ceramic layer. This is kept saturated by pumping up to 72.0 ml per hour of distilled water onto the



Figure 2.1: Picture of a single column CCNc, courtesy of DMT Inc. Boulder, Co. The dual column CCNc used in this work has the same footprint as this instrument. The deionised water and waste water reservoirs can be seen through the viewing window. The lab view software that controls and stores the CCN data can be seen running on the front mounted touch screen.



liner. An aerosol sample is drawn into the instrument at 1.0 liters per minute (lpm), 0.5 lpm per column. This flow is initially split 0.45 lpm to sheath flow and 0.05 lpm to sample flow for each column. The sheath flow is conditioned to be particle free, humidified to near-saturation and heated ( $T_{\text{inlet}}$ ). Both the sheath and aerosol flows are input at the top of the column. The sample flow is drawn down the centre line enveloped in the sheath flow. Each column has a near linear temperature gradient in the stream-wise direction, controlled by three regions of thermoelectric cooler (TEC) plates. These TEC plates are mounted on the outer wall of the column at the top middle and bottom, with temperatures  $T_1$ ,  $T_2$ ,  $T_3$ , respectively; see Figure 2.2.

As the air propagates down the column, under a laminar regime, water vapour and heat diffuse from the inner surface of the column towards the centre line. Because water diffuses through air quicker than heat a supersaturation is maintained. The mechanism for this relies on the difference between heat ( $\alpha$ ) and mass (diffusivity of water,  $D_v$ ) diffusion (e.g  $0.21 \text{ cm}^2\text{s}^{-1}$  versus  $0.25 \text{ cm}^2\text{s}^{-1}$  at 294 K and 1013 hPa, respectively). The timescale needed for mass ( $\tau_C$ ) and heat ( $\tau_T$ ) to reach the centre line can be described as

$$\tau_c = R_{ccn}^2/\alpha \quad (2.1)$$

and

$$\tau_T = R_{ccn}^2/D_v, \quad (2.2)$$

where  $R_{can}$  is the radius of the column. Water molecules have a lower molecular mass than air (primarily  $\text{N}_2$  and  $\text{O}_2$ ) and as such can diffuse quicker through the air than heat which is governed by the collisions between the air molecules themselves (Roberts and Nenes, 2005; Lance et al., 2006; Rose et al., 2008; Moore

and Nenes, 2009; Bougiatioti et al., 2009; Good et al., 2010). Using Figure 2.2 as a reference, at any point  $(0, z)$  along the centreline of the CCNc column the heat has transferred from point  $(R, z - x_t)$  and the water vapour from point  $(R, z - x_c)$ . The actual partial pressure of water at point  $(0, z)$  is equal to the partial pressure of water at point  $(R, z - x_c)$  whilst the temperature is lower equal to that at point  $(R, z - x_t)$ , than at point  $(R, z - x_c)$ . This results in a supersaturated environment. The instrument has a supersaturation range between 0.07 % and 2 %. This upper value is primarily constrained by buoyancy flows that develop with larger temperature gradients  $(\Delta T)$ , the lower end by the non-linearities that pervade at low  $\Delta T$  (Roberts and Nenes, 2005).

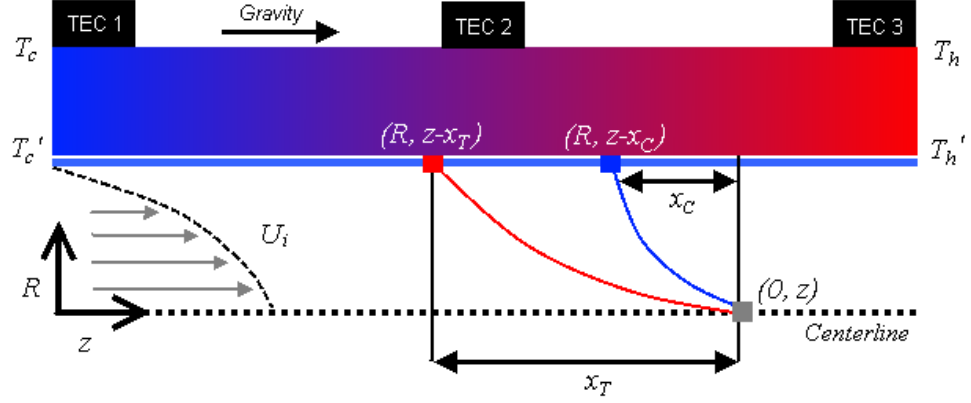


Figure 2.2: Cross section representation of the CCNc column turned on its side.

The aerosol particles are subjected to a constant supersaturation as they flows down the centre line of the CCNc column. Those particles with a critical supersaturation less than that maintained at the centreline will activate to form droplets. The residence time in the column is sufficient for activated droplets to grow to diameters larger than  $1 \mu\text{m}$ ; those particles with a diameter of less than  $1 \mu\text{m}$  are assumed to be unactivated interstitial particles. An optical particle counter (OPC) at the base of the column measures the size distribution of the droplets in the range of  $0.75 \mu\text{m}$  to  $10 \mu\text{m}$  in 20 bins. The particle data from the OPC is

recorded along with multiple diagnostic and housekeeping parameters at 1 Hz on an integrated PC.

### 2.1.2 Instrument Behaviour

The relationship between effective supersaturation ( $SS_{eff}$ ), the true centreline supersaturation as opposed to the modelled, and the column  $\Delta T$  of the CCNc centre line depends on the temperature at the top of the column ( $T_1$ ), the pressure ( $P$ ) and flow rate ( $Q$ ) (Roberts and Nenes, 2005; Rose et al., 2008). Using models and experimental data Rose et al. (2008) showed a dependence of  $\Delta SS_{eff} / \Delta T_1 = -0.0057 \% \text{ K}$  and  $\Delta SS_{eff} / \Delta T_1 = -0.0048 \% \text{ K}$  respectively. It is also noted that the experimental variability of  $SS_{eff}$  at  $T_1$  of  $\approx 299 \text{ K}$  was of a similar magnitude in both the observed and modelled data at 296 K and 303 K. Roberts and Nenes (2005) calculated a value of  $0.0034 \% \text{ K}^{-1}$  for this dependence. Roberts and Nenes (2005) showed a decrease in  $SS_{eff}$  of  $0.031 \%$  with every 100 hPa reduction in pressure. This compares well to the findings of Rose et al. (2008) where the relationship was experimentally shown to be  $0.037 \%$  and a model value of  $0.031 \%$  was estimated. Further work on calibrating a DMT CCNc at different pressures is shown in Roberts et al. (2010). At high atmospheric pressure, 1020 hPa, the observed increase in  $SS_{eff}$  is  $0.029 \%$  per 0.1 lpm of volumetric flow. This increases to  $0.042 \%$  per 0.1 lpm at lower pressure, 650 hPa. The model slopes were  $0.061 \%$  and  $0.038 \%$  per 0.1 lpm at 1020 and 650 hPa, respectively. Throughout the operation of the CCNc, volumetric flow rate was always set at 0.5 lpm per column and monitored. Pressure was controlled externally to the CCNc and  $T_1$  was allowed to vary to enable the instrument to operate at various aircraft cabin temperatures (Rose et al., 2008). The variability in these parameters is taken into account in both the experimental design and the data corrections discussed here.

It must be considered that the linear relationship between theoretical supersaturation and estimated temperature gradient (Roberts and Nenes, 2005) may not be a true representation of the actual  $SS_{eff}$  in the CCNc. This is because the thermal diffusivity of individual columns will differ subtly. The temperature measured on the outer surface of the column is not the true temperature of the inner surface. There may also be inaccuracies in the temperature measurements used to calculate  $\Delta T$  (Lance et al., 2006). These effects on  $SS_{eff}$  can be characterised as a whole by directly calibrating the instrument supersaturation against the theoretical critical supersaturation of a known inorganic salt, usually ammonium sulphate  $(\text{NH}_4)_2\text{SO}_4$ , used due to its high level of sphericity and subsequently its low shape factor correction (1.02). A variable used to describe the effect of shape of a non-spherical particle. It is defined as the ratio of the resistive forces of an irregular particle to that of a spherical particle with the same volume and velocity. As such a shape factor of unity describes a sphere.

### 2.1.3 CCNc Calibrations

CCNc calibration exercises are carried out routinely during aircraft role changes, a period during which the scientific instrument suite is changed. These occur on average twice a year, calibrations are also undertaken before and after field campaigns where the CCNc is a highly desired instrument. Currently all calibrations take place in the laboratory at FAAM. Historically they were conducted wherever a differential mobility analyser (DMA) was available. A sample  $(\text{NH}_4)_2\text{SO}_4$  solution is nebulised using a standard medical nebulising cup (Allied Health Care, Aerosmist Model SA-BF61403) and dried using a diffusional drier (TSI, model 3062). The relative humidity (RH) is constantly monitored using a laser-trimmed capacitive sensor (Honeywell, HIH-4000) after drying to ensure RH is below the efflorescence point for  $(\text{NH}_4)_2\text{SO}_4$ , between 30 to 33 % (Martin, 2000). The aerosol

is then charge equilibrated, or neutralised, using a Krypton-85 radioactive source (TSI, Model 3077 Aerosol Neutralizer), where particles receive either a positive, negative or zero charge. These particles then enter the DMA (TSI, Model 3080L DMA) and are separated according to their electrostatic mobility, which is inversely proportional to diameter - to give a monodisperse aerosol of a known diameter.

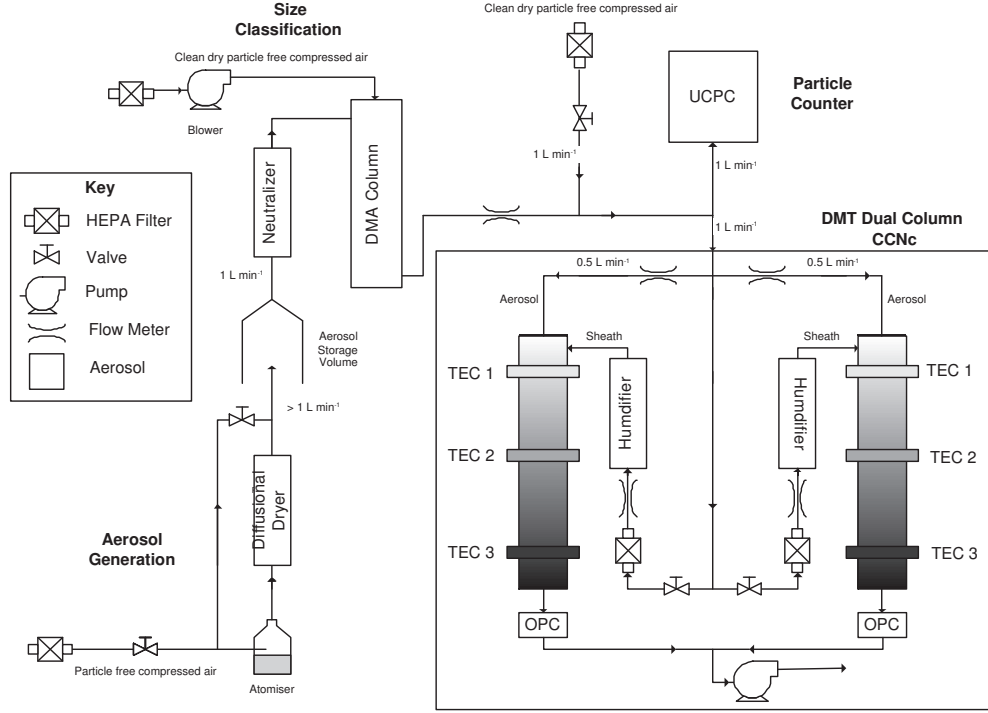


Figure 2.3: CCNc calibration experiment set up.

When using the CCNc in conjunction with a DMA, particles with more than one charge may be sampled, since not all the particles of a given electrical mobility selected are singly charged. Multiply charged particles, mostly doubly charged, have the same mobility as singlets but are larger in diameter. Due to this larger diameter these doubly charged particles are activated at a lower supersaturation than those with a single charge due to their lower critical supersaturation,  $S_c$  (Rose et al., 2008; Good et al., 2010). These multiply charged particles can be seen in activated fraction plots as small plateaus at supersaturations below the

critical supersaturation for the given calibration salt size selected, see Figure 2.4 on page 54. Rose et al. (2008) showed where the fraction of doubly charged particles is less than 0.1 of the activated fraction,  $F_A$ , the overall deviation of the  $SS_{eff}$  is less than 1 %. Using an example distribution from a nebuliser, Good et al. (2010) showed that a charge distribution is composed mostly of singlets ( $> 90\%$ ) and that the fraction of doubly charged particles increases with particle diameter up to a maximum of  $\approx 10\%$  at  $0.2\ \mu\text{m}$ . The largest size used routinely in CCNc calibrations here is  $0.1\ \mu\text{m}$ , therefore no correction for doubly charged particles is used.

After the particle diameter has been selected using the DMA the calibrant flow has a particle free dried air, zero air, added. This added volume ensures a constant sample flow demand on the DMA of 1 lpm, maintaining a sample to sheath flow ratio of 10:1. This ratio is kept tight to ensure a narrow DMA transfer function, ensuring the output distribution is as monodisperse as possible. The sample flow is then separated using a polypropylene y-piece (Cole-Parmer, WZ-06295-30) to both the CCNc and a CN counter, the model of CN counter may change depending on availability. If the CN counter flow is less than 1 lpm then a volumetric flow controller (MC5SLP-D/10M, Alicat) and lab pump (VTE 3, Rietschle) are used to make up any shortfall. The experimental set up for the calibrations can be seen in Figure 2.3.

The CCN and CN concentrations are then used to calculate the activated fraction ( $F_A(S, D_0)$ ) as

$$F_A(S, D_0) = \frac{N_{CCN}(S, D_0)}{N_{CN}(D_0)}, \quad (2.3)$$

where  $N_{CCN}(S, D_0)$  is the CCN measured at a set supersaturation  $S$  and a diameter selected by the DMA  $D_0$  and  $N_{CN}(D_0)$  is the number concentration of

CN as measured by the CPC at the same selected size (Good et al., 2010).  $F_A$  is used to calculate the critical supersaturation  $S_c$  for the particle diameter selected  $D_0$ .  $S_c(D_0)$  is usually defined as the point at which  $F_A(S, D_0)$  is equal 0.5. In order to find the point at which  $F_A(S, D_0) = 0.5$  the instrument set point  $S$  is increased over a range that ideally returns  $F_A(S, D_0)$  values between 0 and 1. A minimum  $F_A(S, D_0)$  of zero ensures that the calibration set up has no leaks. However, there may well be a discrepancy between the maximum  $N_{CCN}(S, D_0)$  and  $N_{CN}(D_0)$ . This could be a function of leaks, flow imbalances or systematic counting errors in the CN counter used. Leaks are tested for prior to each calibration and y-pieces are used in conjunction with flow and sample tube matching to counter any possible flow imbalances. Good et al. (2010) showed that these discrepancies could be up to 15 % and that this discrepancy was eliminated using a constant correction to ensure a maximum  $F_A$  of 1.0. For a discrepancy of 4.5 % there was no significant difference to the calculated  $S_c(D_0)$ . A discrepancy of 15 % from (Good et al., 2010) was taken as an upper limit and any calibrations with  $F_A$  less than 0.85 were not used. A further criterion, that the maximum  $F_A$  is stable across a whole calibration exercise, was used to ensure an accurate estimate of  $SS_{eff}$ . As no systematic  $F_A$  correction is used here  $S_c(D_0)$  is not equal to a  $F_A(S, D_0)$  of 0.5,

$$S_c(D_0) = ((F_A(S, D_0)_{max} - (F_A(S, D_0)_{min}) * 0.5. \quad (2.4)$$

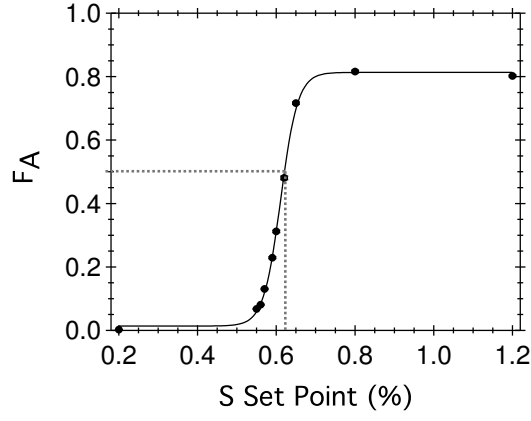
Five particle diameters ( $D_0$ ) of  $(\text{NH}_4)_2\text{SO}_4$  are used in each calibration, nominally 0.04, 0.05, 0.065, 0.085 and  $0.1 \mu\text{m}$ . Each diameter is subjected to a minimum of ten supersaturation set points. These set points are spread in a non-linearly fashion with the majority falling around a known pre-existing  $S_c(D_0)$  calibration point, see Figure 2.4. Each set point is held for ten minutes to allow for settling time, and data only used for calculating  $F_A(S, D_0)$  when the

$N_{CCN}(S, D_0)$  and the column temperatures have stabilised. The concentrations of particles were kept below  $1000 \text{ cm}^{-3}$  to ensure there is no coincidence in the CCNc OPC and ensure there is no water vapour competition.

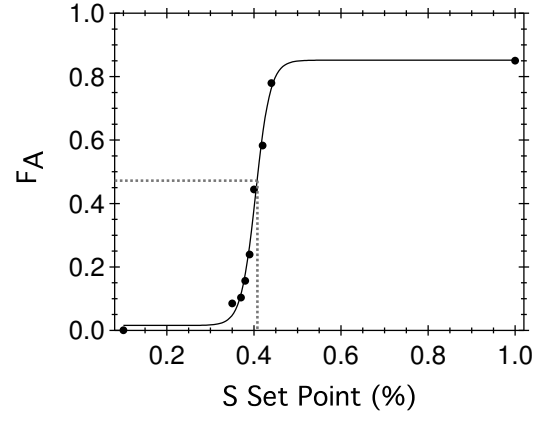
Water vapour competition causes a reduction in the midline supersaturation. When high concentrations of CCN are present there is condensational loss of water vapour to the CCN. This process necessarily reduces the size of the activated particles leaving the column. Lathem and Nenes (2011) showed with both models and measurements that at concentrations below  $5000 \text{ cm}^{-3}$  water depletion had less than 10 % effect on both midline supersaturation and activated droplet size. This concentration limit is dependent not the activation kinetics of the aerosol used. In their study Lathem and Nenes (2011) used  $(\text{NH}_4)_2\text{SO}_4$ . However, if a compound were less hygroscopic the threshold concentration would be greater than  $5000 \text{ cm}^{-3}$  and *visa versa*.

When particle concentrations are high there is an increase possibility of two particles passing through the detection beam of an OPC at one time and being miscounted and often mis-sized. This coincidence has not been reported in the literature at concentrations below  $8000 \text{ cm}^{-3}$  (Roberts and Nenes, 2005) though both Rose et al. (2008) and Good et al. (2010) ensure concentrations during calibrations are kept below  $3000 \text{ cm}^{-3}$ .

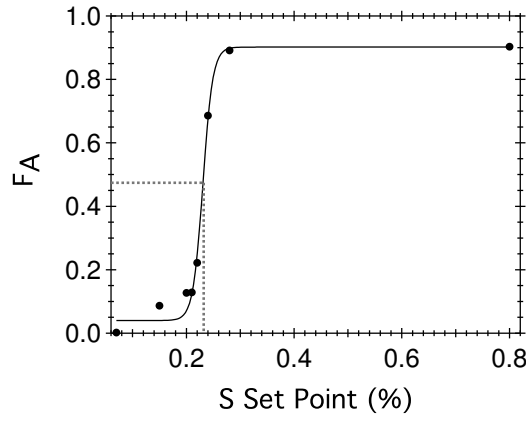




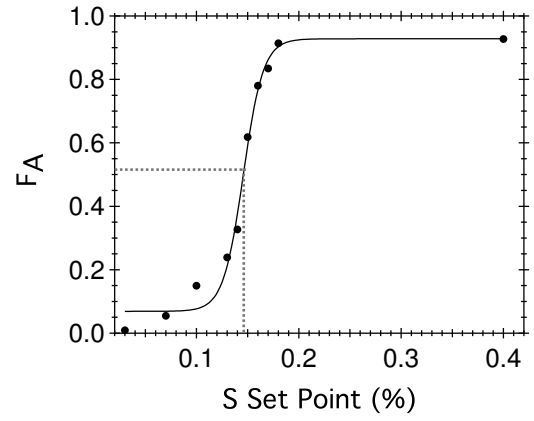
(a) 40 nm  $(\text{NH}_4)_2\text{SO}_4$



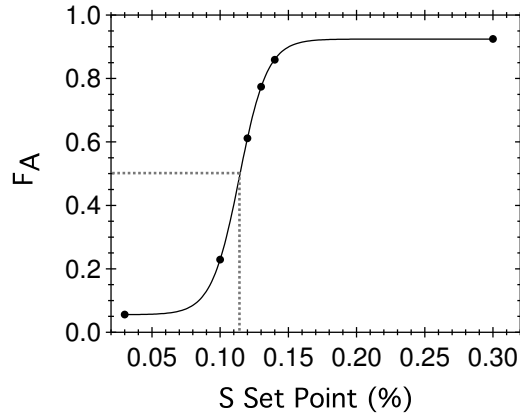
(b) 50 nm  $(\text{NH}_4)_2\text{SO}_4$



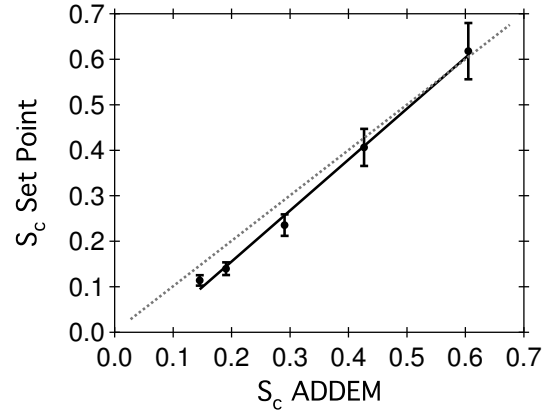
(c) 65 nm  $(\text{NH}_4)_2\text{SO}_4$



(d) 85 nm  $(\text{NH}_4)_2\text{SO}_4$



(e) 100 nm  $(\text{NH}_4)_2\text{SO}_4$



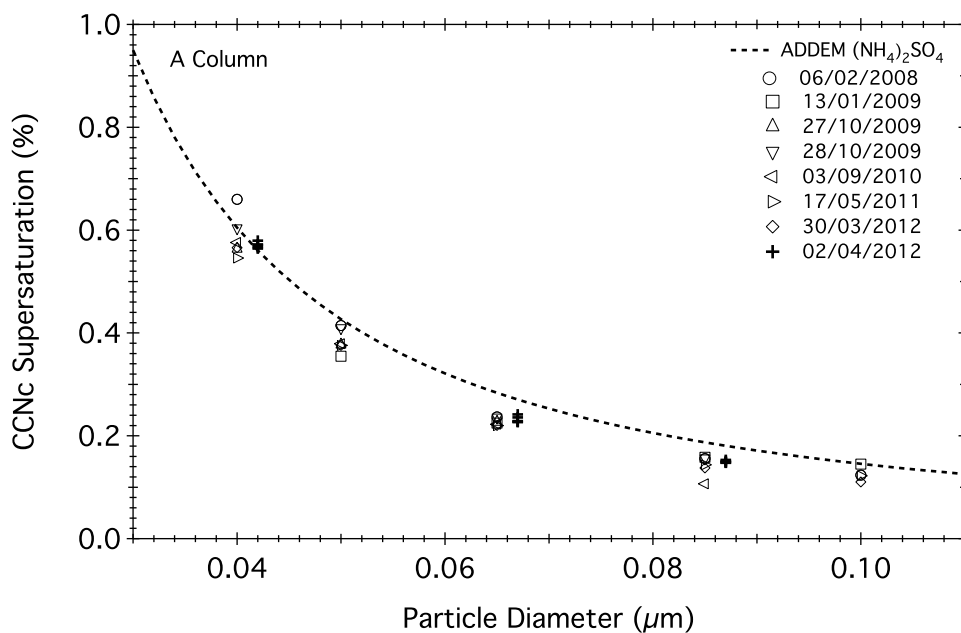
(f) ADDEM  $S_c$  and Set Point  $S_c$

Figure 2.4: Panels a to e show Sigmoid fits from a CCNc calibration experiment showing  $S_c(D_0)$  as calculated in Equation 2.4. Panel f shows the fit between the measured set point  $S_c(D_0)$  and ADDEM output for all sizes.

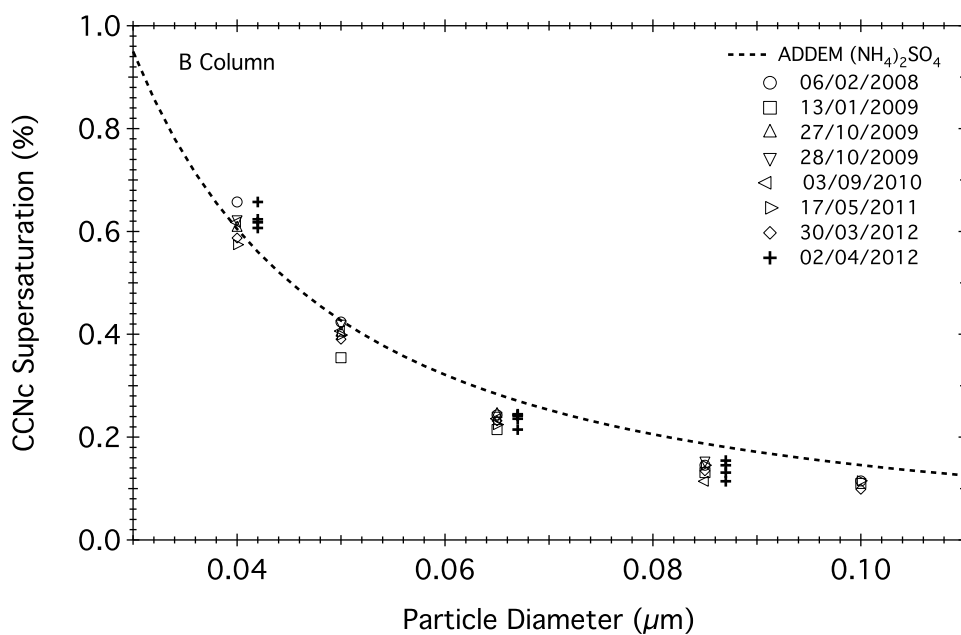
A sigmoid function is then fitted around this activation spectrum from which the  $S_c(D_0)$  is determined using Equation 2.4. Figures 2.4(a) to 2.4(e) show individual scans for DMA sized diameters,  $D_0$ . An increasing particle diameter is a concomitant decrease in the critical supersaturation from just above 0.6 % to 0.11 % for all sizes tested. The results of the sigmoid fit are then compared to their theoretical  $S_c(D_0)$  values estimated using the aerosol diameter dependent equilibrium model (ADDEM) (Topping et al., 2005a,b) to produce a linear correction for  $SS_{eff}$  for both CCNc columns: see Figure 2.4(f). This model is a diameter dependent hygroscopic aerosol model that uses a thermodynamic framework, chemical equilibria is met by minimising the Gibbs free energy, to predict the equilibrium behaviour of an aerosol. The model inputs are composition, dry size, relative humidity and temperature. Figure 2.4(f) shows the improvement in estimating the centreline supersaturation by undertaking these calibrations rather than using the factory settings. The factory settings have reduced accuracy, though greater precision, at larger supersaturations.

The long term calibration record in Figure 2.5 shows how repeatable the results of instrument calibration are. Not only are measurements with the CCNc repeatable but the precision is very good with the maximum relative standard deviation of 7 % across experiments spanning more than four years. It is noticeable that the accuracy of the measurements falls with decreasing instrument supersaturation. This reduction in accuracy is accounted for and corrected by the calibration procedures. Plotted on these figures are also the results of multi iteration calibration undertaken in an attempt to remove systematic errors induced by using a different nebulisers, driers, DMAs, CN counters and plumbing that naturally occur over multiple calibration dates and locations. These data were collected using the same solution source, nebuliser, driers, DMA, CPC and plumbing all in one sixteen hour period. The data are clearly part of the same

population as the long term calibration record showing that the variation between calibrations is associated with the instrument itself and not the experimental set up.



(a) Long term calibration record from the CCNc column A.



(b) Long term calibration record from the CCNc column B.

Figure 2.5: Long term calibrations using ammonium sulphate as described in the calibration procedure. The data marked with crosses from 2<sup>nd</sup> April 2012 are from a single calibration set up with five replicate calibration points. These data are for equivalent particle diameters as the on going calibrations but have been shifted up from 0.04, 0.065 and 0.085  $\mu\text{m}$  to 0.042, 0.067 and 0.087  $\mu\text{m}$  to allow comparison. The dashed line represents the theoretical critical supersaturation from ADDEM. The open symbols the dates of the calibrations, see the legend.

The CCNc sample and sheath flows are calibrated using a primary flow standard (Sensidyne, Gilibrator). The effect of pressure, as previously discussed, is of particular importance in maintaining a stable  $SS_{eff}$ . Most scientific instrumentation is ground based and will be subject to pressure fluctuations of tens of hPa over a period of hours. However, on an aircraft platform the pressure can range over an order of magnitude with a rate of change in the region 100 hPa per 1000 m (ISA) during a low level procedural climb at a rate  $5.0 \text{ ms}^{-1}$ . A climb from the ground to the ceiling altitude of the BAe-146 would result in a decrease in  $SS_{eff}$  of approximately 0.25% simply due to the reduction in pressure. This is an equivalent change in critical diameter,  $d_c$ , from  $0.048 \mu\text{m}$  to  $0.076 \mu\text{m}$  for  $(\text{NH}_4)_2\text{SO}_4$ . This variation in  $SS_{eff}$  would make direct comparison of CCN number or activated fraction between flights, or even between pressure altitudes during a single flight unachievable and in some cases could drive the  $SS_{eff}$  below the minimum value of, 0.07% (Roberts and Nenes, 2005).

#### 2.1.4 Reduced Pressure Inlet

The variability in  $SS_{eff}$  in response to fluctuations in pressure can be overcome by stabilising the CCNc inlet pressure during operation using a constant or reduced pressure inlet (Bahreini et al., 2008; Chen et al., 2007; Pui et al., 1988, 1990). This is a simple concept where a valve, regulator, capillary or critical orifice is used to restrict flow, creating a pressure drop down stream of this restriction. This pressure drop can be manipulated to two ends; one to produce a constant flow, commonly called choked flow (when the upstream to downstream pressure ratio is greater than 0.54), or secondly to maintain a constant pressure. In the latter the flow can be manipulated downstream of the orifice to vary the inlet pressure. A critical orifice is used here as previous studies show that regulators and valves tend to trap particles in sharp turns and dead spaces whilst capillary

tubes showed greater losses and intermittent particle re-entrainment from the walls (Lee et al., 1993; Pui et al., 1990). The dimensions of the device used can be seen in Figure 2.6 and Table 2.1. Three critical orifices diameters (O’Keefe Controls Co., CT, USA) were initially tested: 0.43, 0.51 and 0.73 mm. These tests simply measured the CCNc total flow whilst setting the reduced pressure inlet to different low pressures. Each orifice had a different pressure differential (ambient to reduced) range that they operated over before the flow of the CCNc was compromised. 0.73 mm operated ideally between a pressure differential of 17 to 187 hPa, 0.51 mm orifice operated between 60 and 412 hPa and the 0.43 mm orifice operated without deleterious effect on the CCNc flow between 111 and 512 hPa. Based on these results the smallest of the orifices was chosen to be the most suitable for airborne applications, though the 0.73 mm could be useful for stabilising inlet pressures for ground based applications.

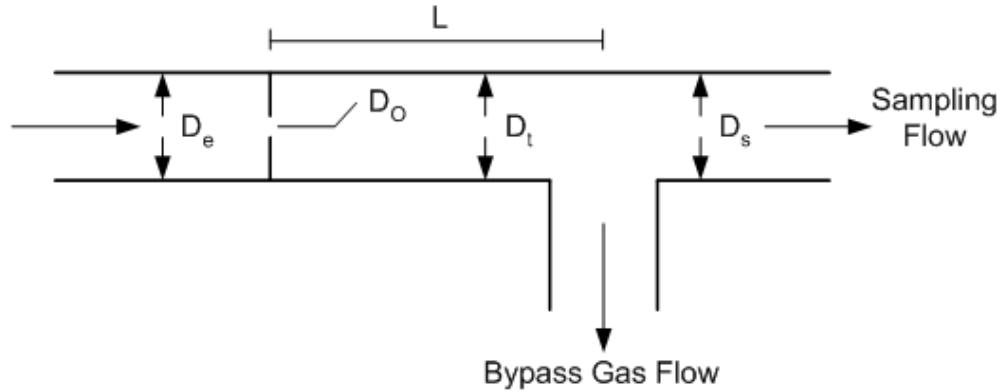


Figure 2.6: Design of the reduced pressure inlet, dimensions are given in Table 2.1.

$D_e$	$D_{or}$	$D_t$	$D_s$	$L$	$Q$
mm	mm	mm	mm	mm	lpm
4.82	0.43	4.5	4.5	47.7	1.55

Table 2.1: Dimensions of the reduced pressure inlet, the flow rate under choked conditions.

In this inlet sample gas is transported to the reduced pressure chamber by a

pneumatic line with an internal diameter of 4.82 mm ( $D_e$ ). The sample pressure is then reduced by expansion through the critical orifice of diameter ( $D_{or}$ ). This expanded sample gas enters the chamber with an internal diameter of ( $D_t$ ). Particles are sampled through the extraction tube ( $D_s$ ) at a distance  $L$  downstream of the critical orifice and the bypass flow exits through a 90° bend to the pressure control valve (Alicat PC-15PSIA-D/ M RIN) and pump (KNF N86KNDC B). In the designs of Bahreni et al (2007) and Lee et al (1993) the bypass, or excess flow path is downstream of the sample extraction point. To keep engineering costs down and ensure certification an 'off the shelf' Swagelok stainless steel T-piece (SS-400-3) was used as the main body. The critical orifice size and pressure were chosen to give as wide an operating envelope through out the planetary boundary layer whilst still maintaining a flow ratio of sample to bypass above 1.0. Though it was not investigated here it is proposed that a ratio below 1.0 may result in the reduced pressure inlet acting as a virtual impactor with larger particles being enhanced in the sample stream as those particles with low inertia follow the majority of the flow round the bend into the bypass flow.

For aerosol research purposes it is ideal that any sample conditioning device neither removes or adds particles to the sample and that if the sample is modified that this modification is both measurable and repeatable. To this end particle transmission through the reduced pressure inlet was investigated. Such devices are subject to a number of different loss mechanisms; impaction on the front face and rear faces of the critical orifice and loss of particles caught in the expansion jet that are impacted in to the walls of the reduced pressure system downstream of the critical orifice (Pich, 1964; Bahreini et al., 2008; Chen et al., 2007; Pui et al., 1988, 1990) The experimental design to investigate these losses was similar to the CCNc calibration procedure. However the CCNc was replaced with a second CN counter (3010 CPC, TSI) as seen in Figure 2.7 on page 62. Polystyrene

Latex Spheres (PSL) beads (Duke scientific) with diameters of  $102 \pm 3$  nm,  $198 \pm 5$  nm,  $300 \pm 3$  nm,  $500 \pm 4$  nm,  $595 \pm 6$  nm and  $705 \pm 6$  nm were used as the sample aerosol. These sizes represent a large proportion of the accumulation mode in which most atmospheric CCN are found and therefore the size range across which the inlet would ideally transmit particles. A DMA (3080L, TSI) was used to size select the mean PSL diameter so the sample aerosol was monodisperse being free from agglomerates and residuals often associated with PSLs. Once size selected this sample was split, half passing thorough the reduced pressure inlet to the TSI 3010 and half through the ambient pressure line to the second CN counter (3025a CPC, TSI). The TSI 3010 was chosen for the reduced pressure partition as the instrument flow is controlled using a critical orifice and therefore if enough vacuum is supplied the flow can be maintained over a wide pressure range. The experiment was run for nine different inlet pressures; an ambient control with no reduced pressure inlet, the inlet and no bypass flow (approx. 870 hPa), and the inlet controlled to 850, 800, 750, 700, 650, 600 and 550 hPa. Since the reduced pressure inlet has a variable volumetric flow a make up flow, equal to the bypass flow at each pressure, was used to ensure a constant demand on the DMA, maintaining a 10:1 sheath to sample flow ratio. Each PSL size was run for approximately ten minutes to allow for the system to stabilise. These experimental data were compared to equations and experimental data from the literature for the loss mechanisms discussed (Pich, 1964; Bahreini et al., 2008; Chen et al., 2007; Pui et al., 1988, 1990). The equations used and their references are shown in Equations 2.5, 2.10 and 2.11. All the equations were incorporated into a model written in IGOR Pro (Wavemetrics, Inc.). When initialised with pressure, temperature, particle density and a particle diameter array the model output the loss functions as in Figure 2.9.



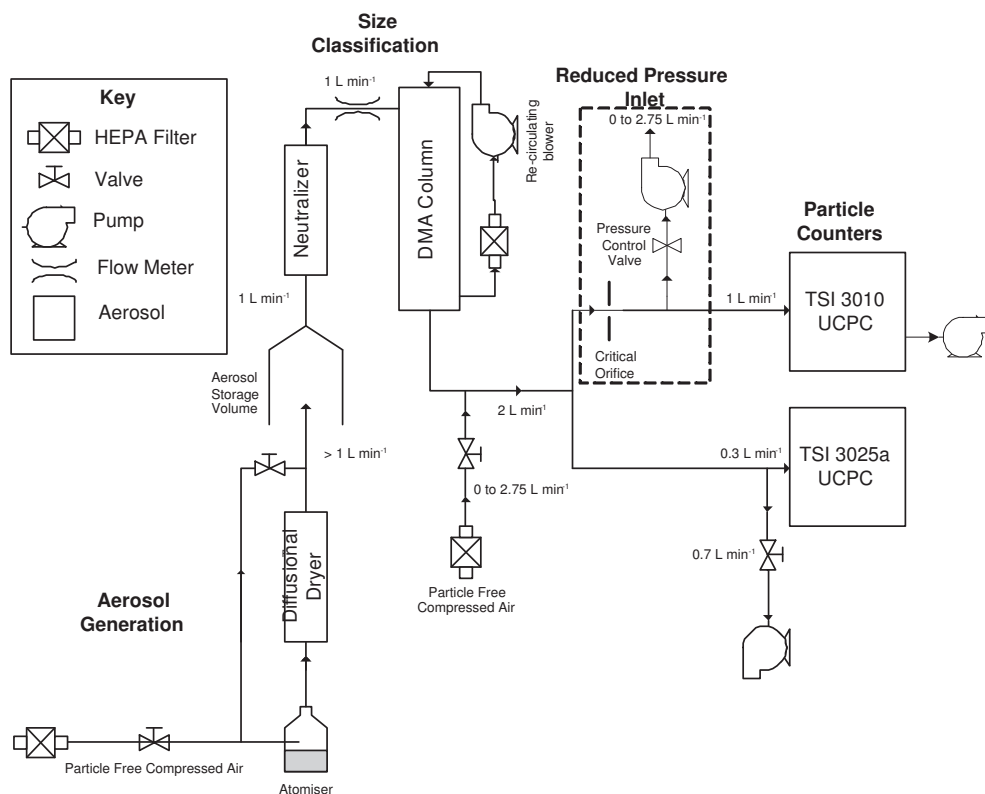


Figure 2.7: Reduced pressure inlet characterisation experimental set up. Note all T-pieces shown in this experimental set up are in fact Y-pieces with an angle of 33°.

$$\eta_{ff} = \frac{2E}{1 + \alpha} - \frac{E^2}{(1 + \alpha)^2}, \quad (2.5)$$

where,  $\eta_{ff}$  are the losses to the front face of the critical orifice as described in Pich (1964) where

$$E = 2A + 2A^2[\exp(-1/A) - 1] \quad (2.6)$$

$$A = St_0 \sqrt{\alpha} \quad (2.7)$$

$$\alpha = \sqrt{A_0/A_i}(1 - \sqrt{A_0/A_i}), \quad (2.8)$$

here  $A_0$  and  $A_i$  are the area of the orifice and inlet tube (m) and the  $St_0$  is the Stokes number which is defined here as

$$St_0 = \frac{\rho_p D_p^2 U_i C_c}{9\mu D_{or}}, \quad (2.9)$$

where  $\rho_p$  is the particle density ( $\text{kg m}^{-3}$ ),  $D_p$  the particle diameter (m),  $U_i$  is the average velocity at the inlet tube ( $\text{m s}^{-1}$ ),  $C_c$  the Cunningham slip correction factor,  $\mu$  the air dynamic viscosity ( $\text{N s m}^{-1}$ ) and  $D_{or}$  is orifice diameter (m).

The deposition losses for the rear face of the orifice plate and the tube wall after the orifice,  $\eta_{rf}$  and  $\eta_{tao}$  respectively have been estimated from digitised data in the original reference Pui et al. (1988). The models used are

$$\eta_{rf} = \frac{36.36}{1 + \exp^{\frac{(0.393 - \sqrt{Stk'})}{0.047}}} \quad (2.10)$$

and

$$\eta_{tao} = \frac{91.65}{1 + \exp^{\frac{(0/389 - \sqrt{Stk'})}{0.049}}} \quad (2.11)$$

where

$$Stk' = \frac{\rho_p D_p^2 U_{or} C_c}{18\mu D_{or}} / (D_t/D_{or})^{0.58} \quad (2.12)$$

and  $U_{or}$  is the average velocity at the orifice ( $\text{m s}^{-1}$ ) and  $D_t$  is the inlet internal diameter (m).

To enable a comparison between the ambient and reduced pressure sampling techniques, and any associated losses, a simple density correction was employed to ensure measurement compatibility. The results in Figure 2.8 demonstrate that for the range of particle diameters tested the inlet has an acceptable transmission efficiency with a slope of 1.002 and a coefficient of determination of 0.99.

The modelled data in Figure 2.9 suggest that this transmission efficiency shouldn't fall below 90 % until a diameter of  $1.2 \mu\text{m}$  at 650 hPa. However, the experimental data shows a reduction in transmission efficiency below 90 % at a much smaller diameter, somewhere between  $0.6$  and  $0.7 \mu\text{m}$ . PSL beads with diameters greater than  $0.5 \mu\text{m}$  in diameter all have concentrations below  $100 \text{ cm}^{-3}$ , at 650 hPa the concentration of  $0.705 \mu\text{m}$  beads is less than  $5 \text{ cm}^{-3}$ . The error bars in Figure 2.9 on page 66 describe the propagated relative uncertainty of both the control and test measurements. These errors increase drastically at diameters greater than  $0.5 \mu\text{m}$  as such little significance should be given to the larger PSL bead penetration efficiency. Pui et al. (1988, 1990) experimentally showed that the larger the orifice the smaller the effect of the recirculating jets have in transporting particles to the rear surface of the orifice plate. Their work used orifices between the sizes of 0.05 and 0.16 mm compared to a relatively large orifice 0.432 mm used here. As such the losses to the rear face plate should be

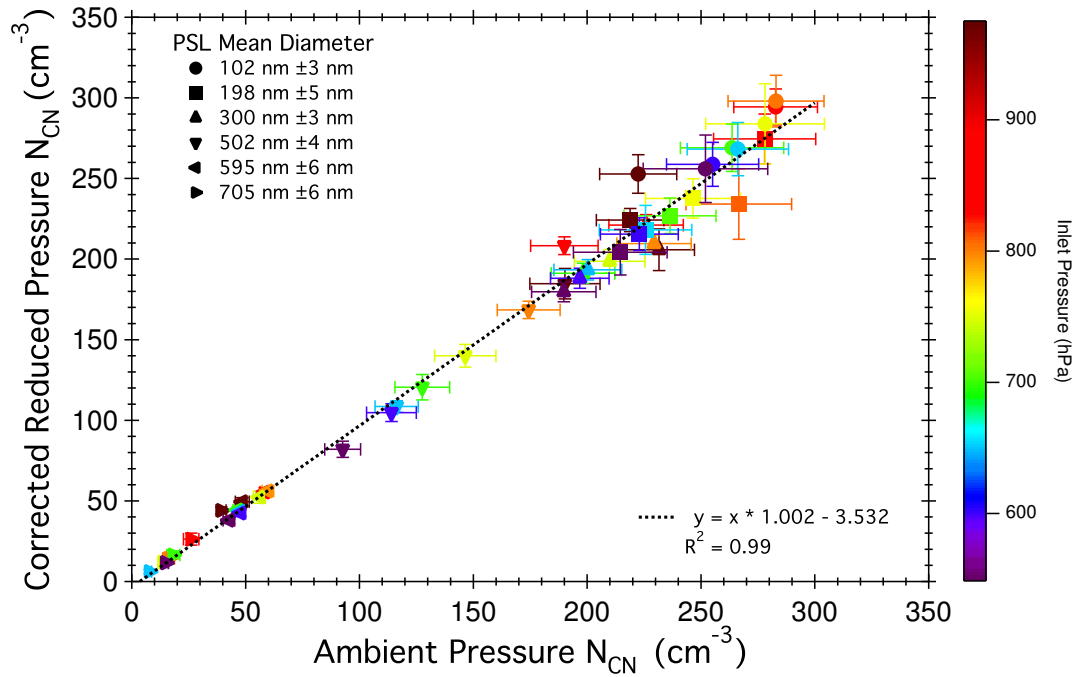


Figure 2.8: Experimental data from the reduced pressure inlet characterisation study showing the ambient total particle concentration  $N_{CN}$  against the simple density corrected aerosol as sampled through the reduced pressure inlet. The error bars express 1 standard deviation of the mean. Closed symbols represent the different PSL bead diameters, their exact diameter and error in this diameter measurement can be seen in the Figure legend.

considered to be over estimates.

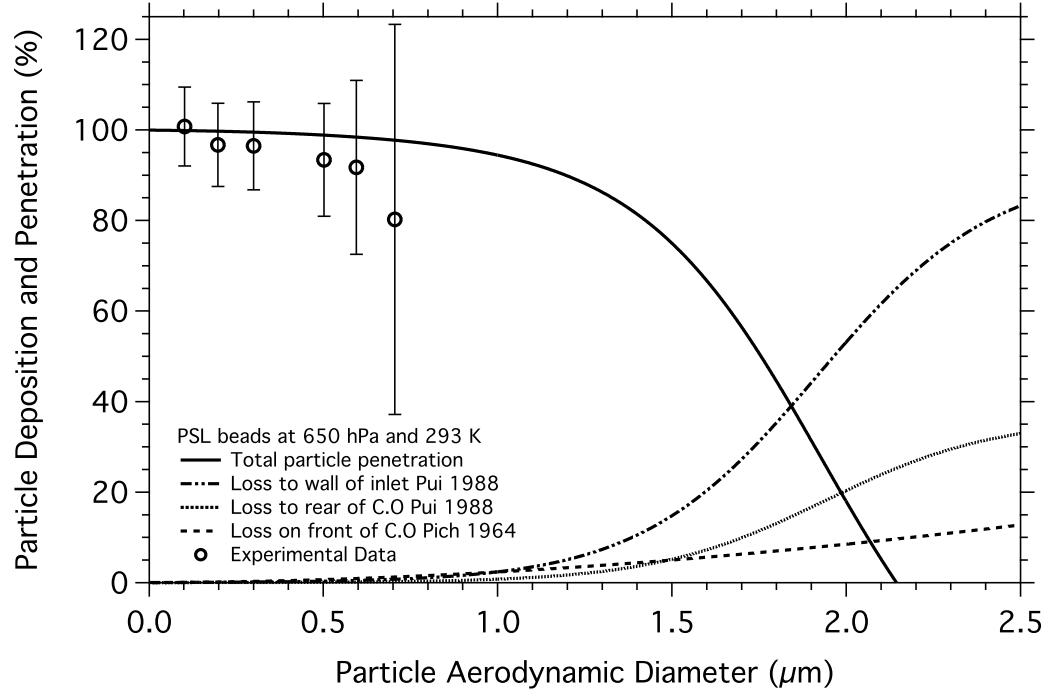


Figure 2.9: Modeled losses for the reduced pressure inlet operating at 650 hPa for PSL beads with density of  $1050 \text{ kg m}^{-3}$  as compared to the experimental data, the error bars show the propagated relative uncertainty in the measurements of both the control, ambient sample and the test sample at reduced pressure. The open circles represent the measured data, the solid line the total particle penetration, the dashed line the loss on the front face of the critical orifice, the dotted line the losses to the rear of the orifice and the dotted and dashed line the losses to the wall of the inlet post orifice.

The diffusive loss of particles in this device were not included in this experiment as the particle diameters of interest for CCN active aerosol occur in the accumulation mode, *i.e.* those particles greater than  $0.1 \mu\text{m}$ . However, Chen et al. (2007) showed at 260 Torr (under critical conditions) the diffusive losses behind a critical orifice are zero at diameters greater than  $0.04 \mu\text{m}$ . These diffusive losses do increase from 0 to 25 % as diameters are decreased from  $0.1 \mu\text{m}$  to  $0.015 \mu\text{m}$  when the pressure is increased further to 620 Torr (non-critical conditions). It was considered that these losses were not significant for the particle sizes of in-

terest. Under the weight of the arguments and the relationship in Figure 2.8 the reduced pressure inlet was deemed fit for purpose.

### 2.1.5 Pressure and Supersaturation

The reduced pressure inlet was used to stabilise the CCNc inlet pressure routinely on all flights and to explore the instrument specific pressure effects on  $SS_{eff}$ . The dependence of  $SS_{eff}$  on pressure of the CCNc instrument used here was shown to be very similar to other instruments investigated in the literature. The experimental set up used to investigate this can be seen in Figure 2.10. To enable five different pressure settings two different critical orifices were used, for the lower pressures the standard 0.043 mm diameter unit was used but for the higher pressures a second orifice of 0.73 mm diameter was used. At the diameters investigated no losses are expected. Unlike the CCNc calibrations the instrument was held at a constant  $\Delta T$  of 5 K with a flow of 0.5 lpm per column. The  $(\text{NH}_4)_2\text{SO}_4$  aerosol diameter was scanned using the DMA instead of scanning the supersaturation. Not only does this make comparison with the literature easier but it highlights how the instrument is both sensitive to variations in the temperature gradient as well as particle diameter.

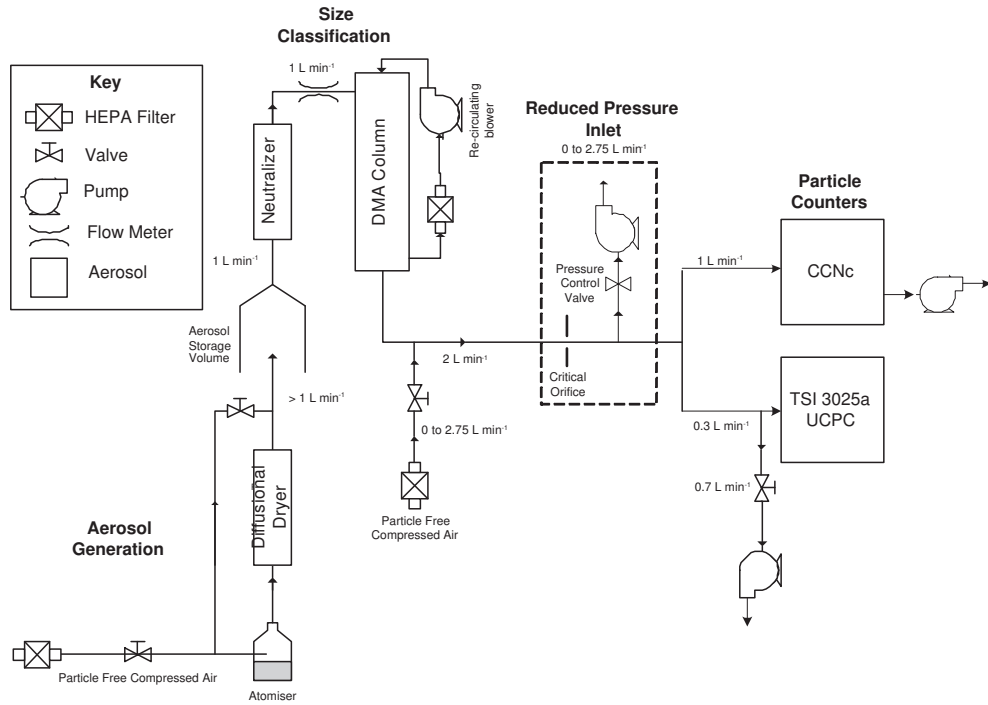


Figure 2.10: Experimental set up to test instrument effective supersaturation sensitivity to pressure.

The activation curves for the experiment can be seen in Figures 2.11 and 2.12. As with the routine calibrations, each curve has a sigmoid fitted. The critical dry diameter ( $d_c$ ), that diameter at which half the sample is activated, is defined as half the difference between  $F_{Amax}$  and  $F_{Amin}$ . ADDEM is used to estimate the  $SS_{eff}$  from the  $d_c$  values measured.

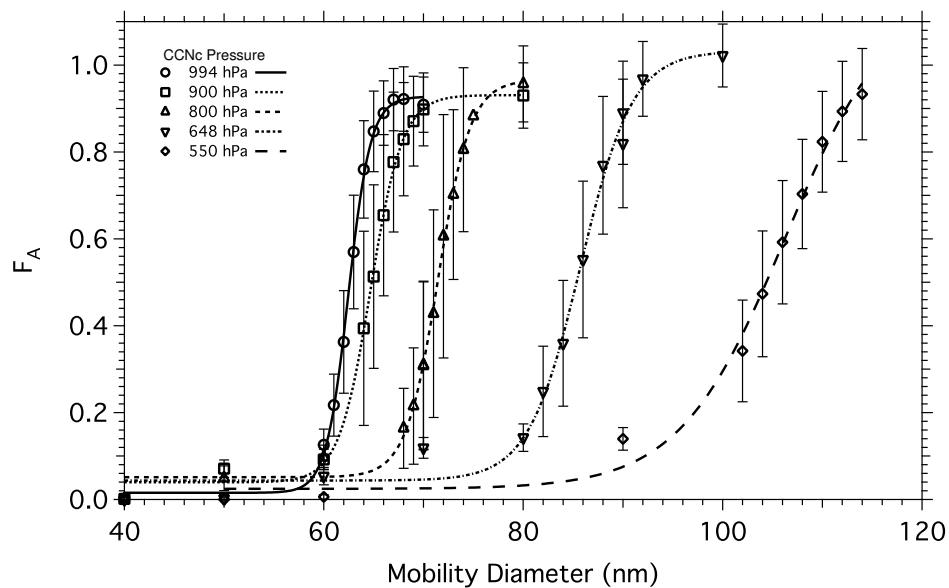


Figure 2.11: Column A activation curves for  $(\text{NH}_4)_2\text{SO}_4$  showing reduced  $d_c$  with decreasing pressure. Sigmoid fit lines for each curve are shown, the error bars reflect one standard deviation of the measurement. The open symbols represent the different pressures, each pressure has a distinct line type for each sigmoid fit. The pressure for each test can be seen in the legend.



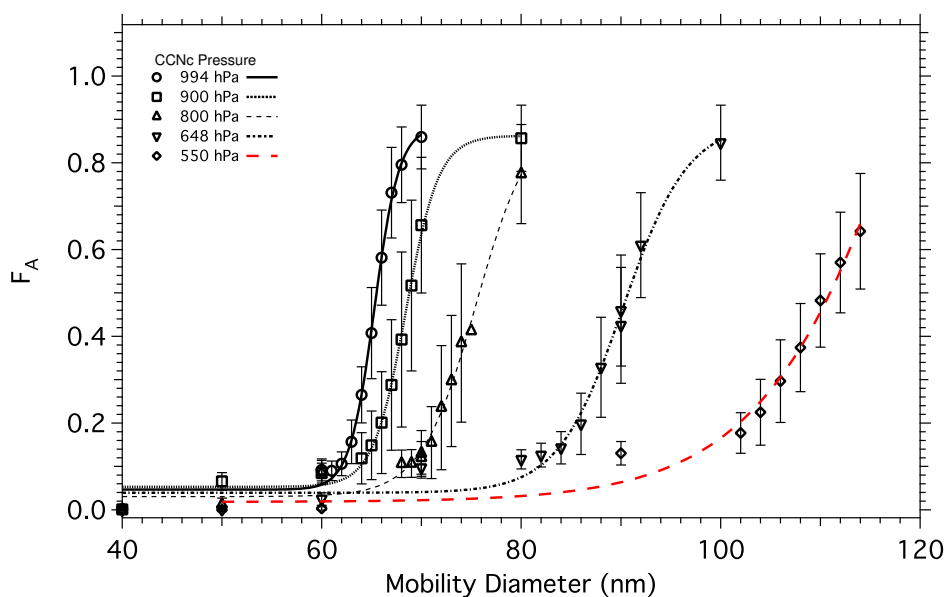


Figure 2.12: Activation curves for  $(\text{NH}_4)_2\text{SO}_4$  at five different pressures for column B, each curve is fitted with sigmoid. The sigmoid fit to the lowest pressure is in red as the fit returned a value of a  $y$  max over 1.0 and as such the estimation of  $x$  half is inaccurate. The error bars reflect one standard deviation of the measurement. The open symbols represent the different pressures, each pressure has a distinct line type for each sigmoid fit. The pressure for each test can be seen in the legend

Both columns compare well to those data previously published by Rose et al. (2008); Roberts et al. (2010). As such the model, Equation 2.15, from Roberts et al. (2010), is used to correct the instrument supersaturation for reduced pressure operations, this equation is accurate to 10% for all DMT CCNc columns run at 0.5 lpm. This holds for the columns used here.

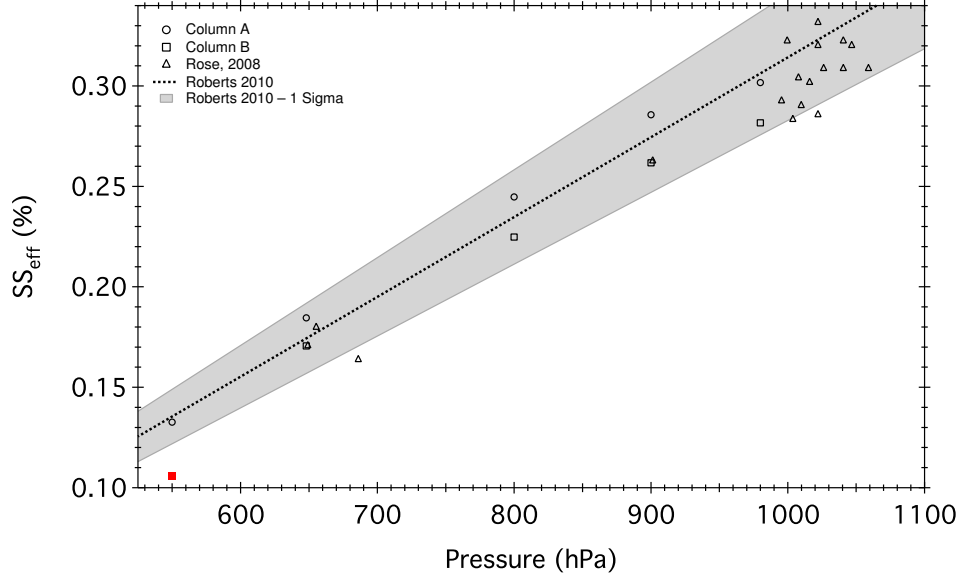


Figure 2.13: Comparison of the estimated effective supersaturation from ADDEM for the activation curves in Figures 2.11 and Figures 2.12, the digitised data from Rose et al. (2008) (open triangles) and the model from Roberts et al. (2010) (dotted line with 10 % error the shaded area). The CCNc column A and B are represented by open circles and squares, respectively. The red filled square is the erroneous  $SS_{eff}$  estimated from the final activation curve in column B.

$$m_p = 5.087e^{-5}P + 1.833e^{-2} \quad (2.13)$$

$$y_p = 1.429^{-4}P - 0.1747^{-2} \quad (2.14)$$

$$SS_{eff} = m_p\Delta T + y_p, \quad (2.15)$$

where  $P$  is the CCNc inlet pressure (hPa) and  $\Delta T$  is the temperature ( $^{\circ}C$ ) differential between the top (T1) and bottom (T3) of the CCNc column.

### 2.1.6 CCNc Instrument Warm Up Requirements

An extra consideration in the suitability of the CCNc to airborne deployment is the time it takes for the instrument to ‘warm up’ from a cold, wet start to a state where all the instrument set points are reached and CCN measurements are repeatable and reliable. A cold wet start can be defined as any instance where the instrument is turned on after period of time where the instrument has been left powered down long enough for the temperature gradient in the column to collapse completely. Unlike a ground-based instrument that can be powered 24 hours a day, aircraft are not allowed by law to be left powered whilst unattended. Too short a warm up period and the instrument will not reach a stable state until the in-flight measurement period has started. This stability period was investigated using the experimental set up in Figure 2.3 on page 50.

A single diameter,  $0.05\ \mu\text{m}$  monodisperse  $(\text{NH}_4)_2\text{SO}_4$  aerosol was fed into the instrument from the DMA and the same six supersaturation set points, cycled for ten minutes once an hour. This was repeated over an eight hour period. The final three minutes of data from each ten minutes was then stratified by supersaturation and by scan number (a proxy for running time), from 1 to 7. The CN counter logging timed out on the eighth scan, so was not included in the analysis. Each sub-population of the data was checked to ensure equality of variance, homoscedasticity, and that the residuals were normally distributed. All sub populations met these criteria so an analysis of variance (ANOVA) test was used to test if the sub-sample means were equal for each supersaturation and scan. These sample means can be seen in Figure 2.14 and 2.15. Only the second group of supersaturations (0.3 and 0.33 % for columns A and B, respectively) show any statistical significance in the equality of their means. This would suggest that neither column is stabilised across the seven hours. This definitely appears to be the case for column A where each subsequent scan, excluding the fifth, has a

higher mean  $F_A$  than the last.

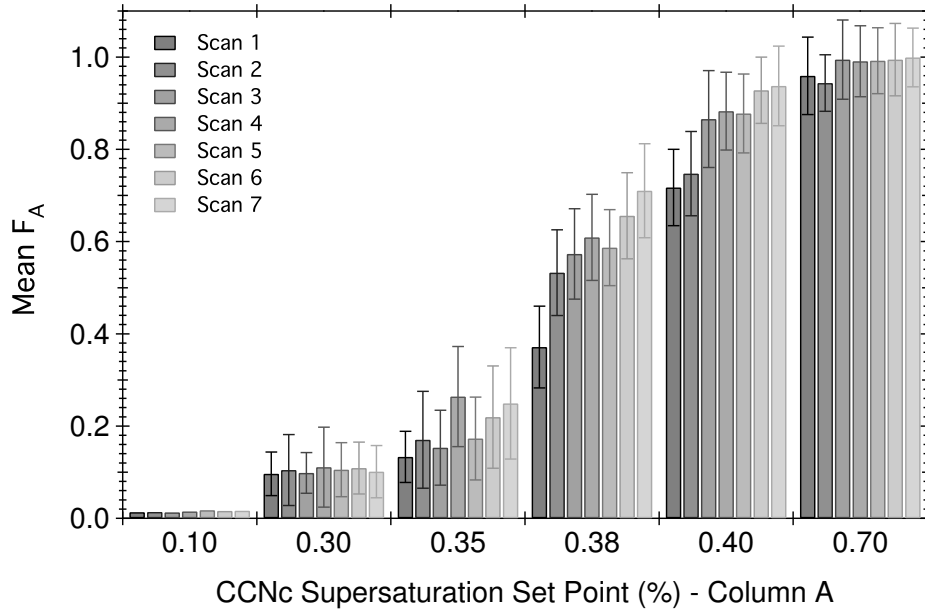


Figure 2.14: Mean  $F_A$  for seven scans of  $0.05 \mu\text{m}$   $(\text{NH}_4)_2\text{SO}_4$  particles for column A. The error bars represent  $1\sigma$  of the mean. Each scan is represented by a different shading as seen in the legend.

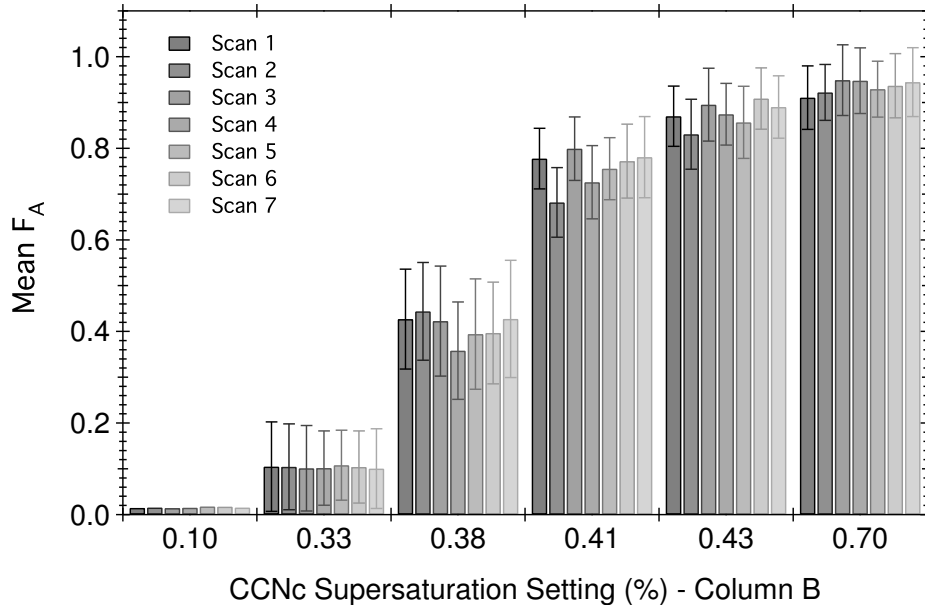


Figure 2.15: Mean  $F_A$  for seven scans of  $0.05 \mu\text{m}$   $(\text{NH}_4)_2\text{SO}_4$  particles for column B. The error bars represent  $1\sigma$  of the mean. Each scan is represented by a different shading as seen in the legend.

It is not however, the mean of value  $F_A$  that is of interest in the operation of the CCNc, but the value of  $SS_{eff}$ . Figures 2.16 and 2.17 show the activation curves for all scans from both columns. Those regions in which the mean value of  $F_A$  appears most variable are in the region of  $F_A$  being equal to 0.5 (supersaturation set points of 0.38 and 0.41 % for columns A and B). During this inflection zone any small variation in the supersaturation or particle diameter can have a large effect on  $F_A$ . However, the converse is also true, a large change in the  $F_A$ , as seen in both histograms, actually results in a very small change in the  $S_c$  as shown in the insert graphs in Figures 2.16 and 2.17. With the total variation in  $F_A$  causing a percentage maximum in  $S_c$  of less than 2.5 % after 2 hours in both columns. It is however, noticeable that column B stabilises faster and results in a more stable state. These very small percentage effects on  $S_c$  are evidence that though there is natural variability in the instrument it is suited to a two hour warm up associated with a standard flight.

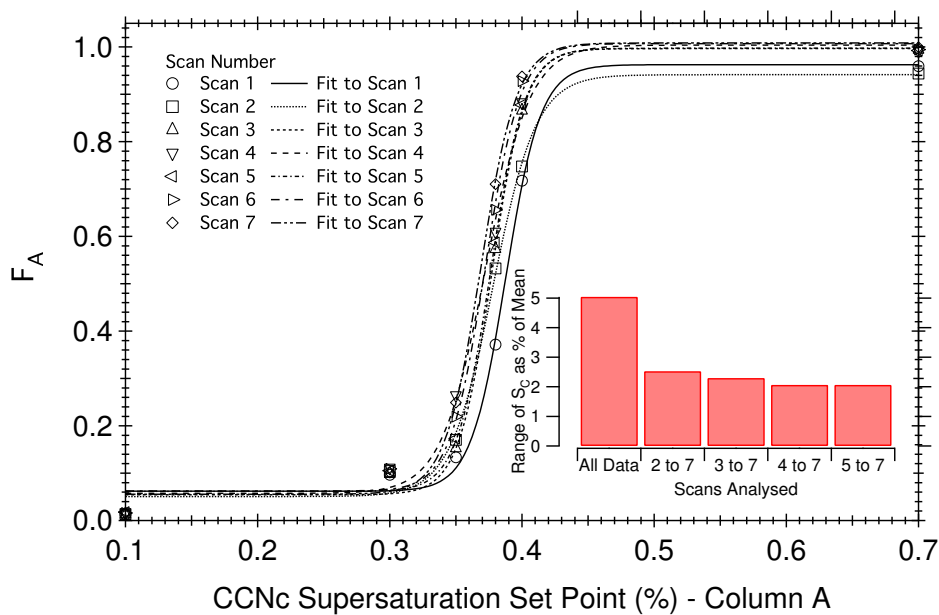


Figure 2.16: Activation curves for column A for all seven scans with fitted sigmoid curves. Inset bar chart shows the percentage range of  $S_c$  as a function of scans included in the analysis. The data for each scan is represented by open symbols and each sigmoid by a line, both of which can be seen in the legend.

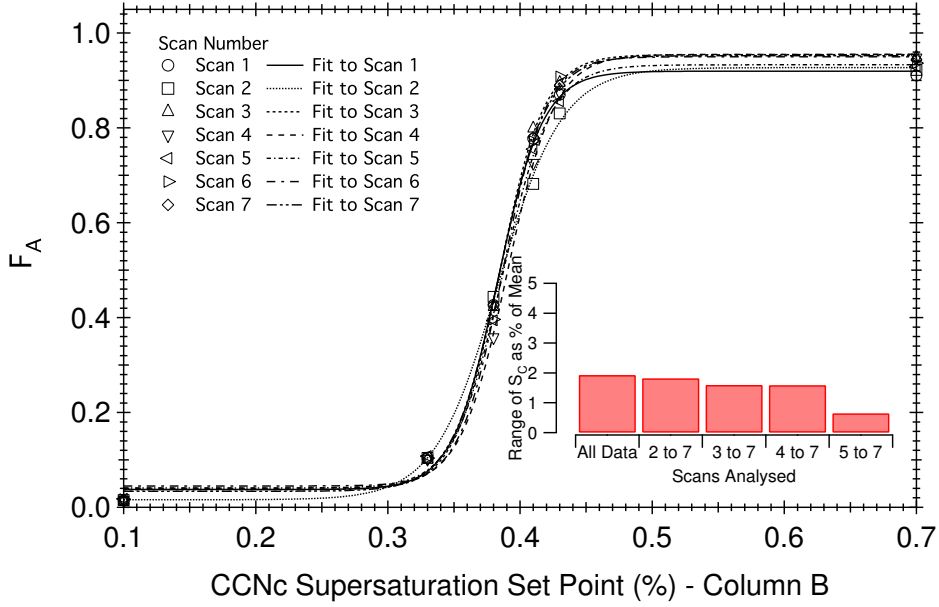


Figure 2.17: Activation curves for column B for all seven scans with fitted sigmoid curves. Inset bar chart shows the percentage range of  $S_c$  as a function of scans included in the analysis. The data for each scan is represented by open symbols and each sigmoid by a line, both of which can be seen in the legend.

In summary of Section 2.1. The CCN measurements are repeatable with a high level of precision as shown by the multiple calibrations across multiple years. The accuracy of the calibrations is variable across the instrument operating supersaturation, with reduced accuracy at lower supersaturations. These errors are absolved when correcting the supersaturation to theoretical values. This is important information for this specific CCNc but has been shown in many previous studies (Roberts and Nenes, 2005; Rose et al., 2008; Good et al., 2010). This work has also added to the information in the literature on the relationship between effective supersaturation and pressure (Roberts and Nenes, 2005; Rose et al., 2008; Roberts et al., 2010). Data produced here has verified the model of Roberts et al. (2010) in another instrument for the first time. Though constant pressure inlets have been used in conjunction with CCNc instrument before no information exists regarding their operational pressure envelope or particle trans-

mission. The constant pressure inlet design used here is unique and transmits particles across the diameters of interest with less than 10 % losses. No work has ever been published on CCNc warm up times and instrument stability. This is crucial in understanding if the instrument is suited to the rigours of aircraft use. The variation in column effective supersaturation is below 2.5 % after the first two hours of running from a cold, wet start. This variation is less than the inter-calibration variation of 7 %.

In conjunction all of the findings from this Section form the bedrock of all further analyses contained in this work. Without understanding the instruments operation and having faith in the accuracy and repeatability of the measurements in the laboratory there would be little utility in making airborne measurements.

## **2.2 *In situ* Sampling**

### **2.2.1 Instrument Deployment**

The CCNc is fitted to a double 19" rack as are the majority of the instruments flown on the BAe-146. Each of these racks has to undertake a rigorous BAe Systems Plc. safety analysis before being certified to be fitted to the aircraft. This analysis is centred on a documentation process known as a Technical Specification of Scientific Equipment (TSSE) this document outlines the fit, form and function of the instrumentation housed on each rack. Once certified the racks are fitted to the aircraft by locating spigots on the seat rails, this attachment method can be seen in Figure 2.18. This provides a safe system that also allows for certain level of plug and play modularity. It does mean that a rack may not always be near an appropriate inlet. This is the case for the CCNc rack (Rack ID CCN/CPC/FWVS third from the front port side in Figure 2.18). The inlet designated for the CCNc



is the aft inlet of a modified Rosemount pair, PW5. This hard point can be seen above the large radiation blister in Figure 2.19. This inlet is 2.63 m from the rack position (the inlet is shown as the blue coloured blanked window adjacent to the AMS rack in Figure 2.18) and as such the CCNc requires extended sample lines to transport the sample from the inlet to the instrumentation. This sample line architecture is designed to be as unobtrusive and safe as possible with particle transmission being only a second order driver.

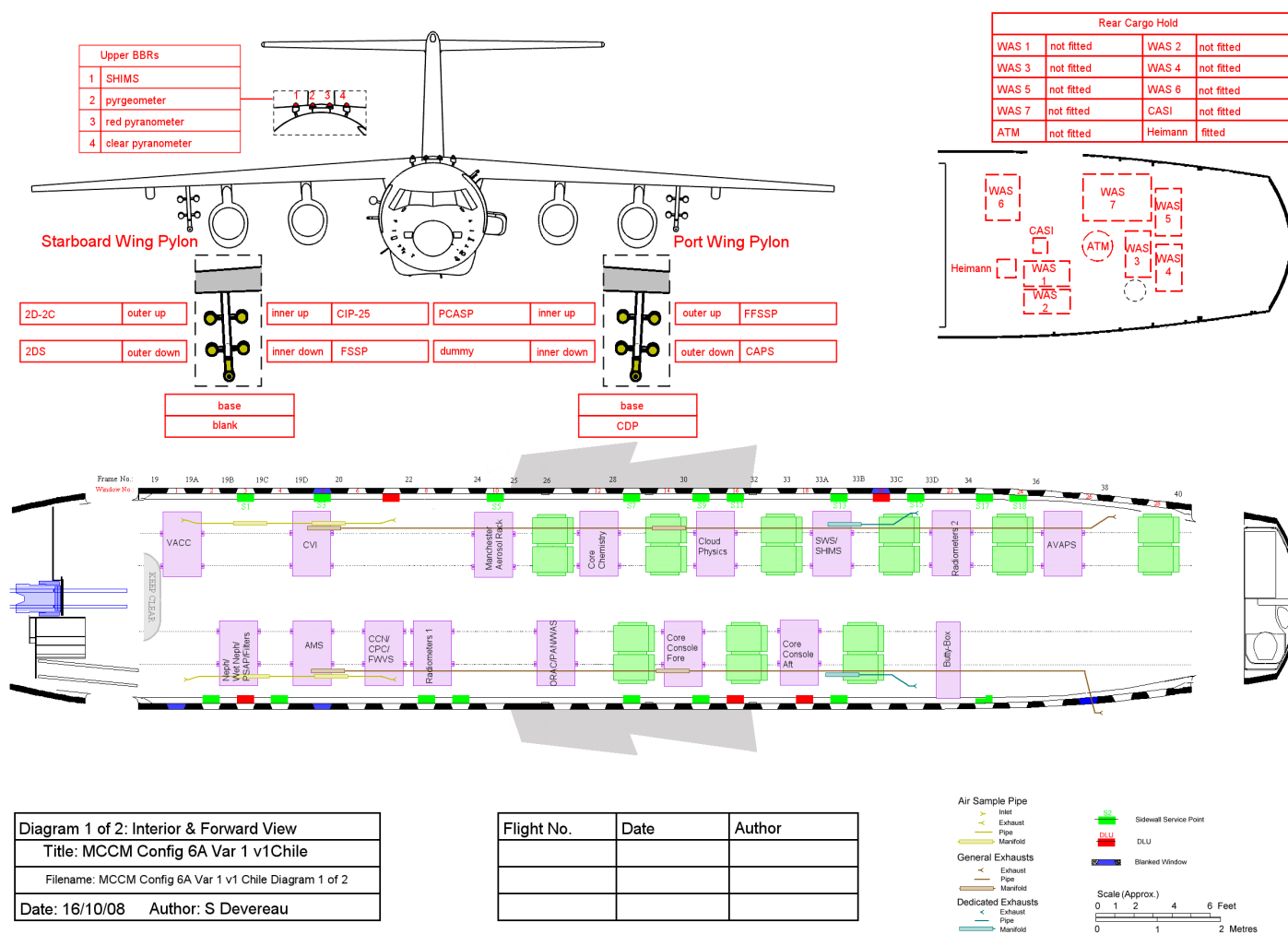


Figure 2.18: Internal plan and front elevation of FAAM BAe-146 Certificate of Conformity (CofC) showing the location of the instrument rack containing the CCNc and TSI 3786, three racks from the front of the aircraft on the port side, labelled CCN/CPC/FWVS.

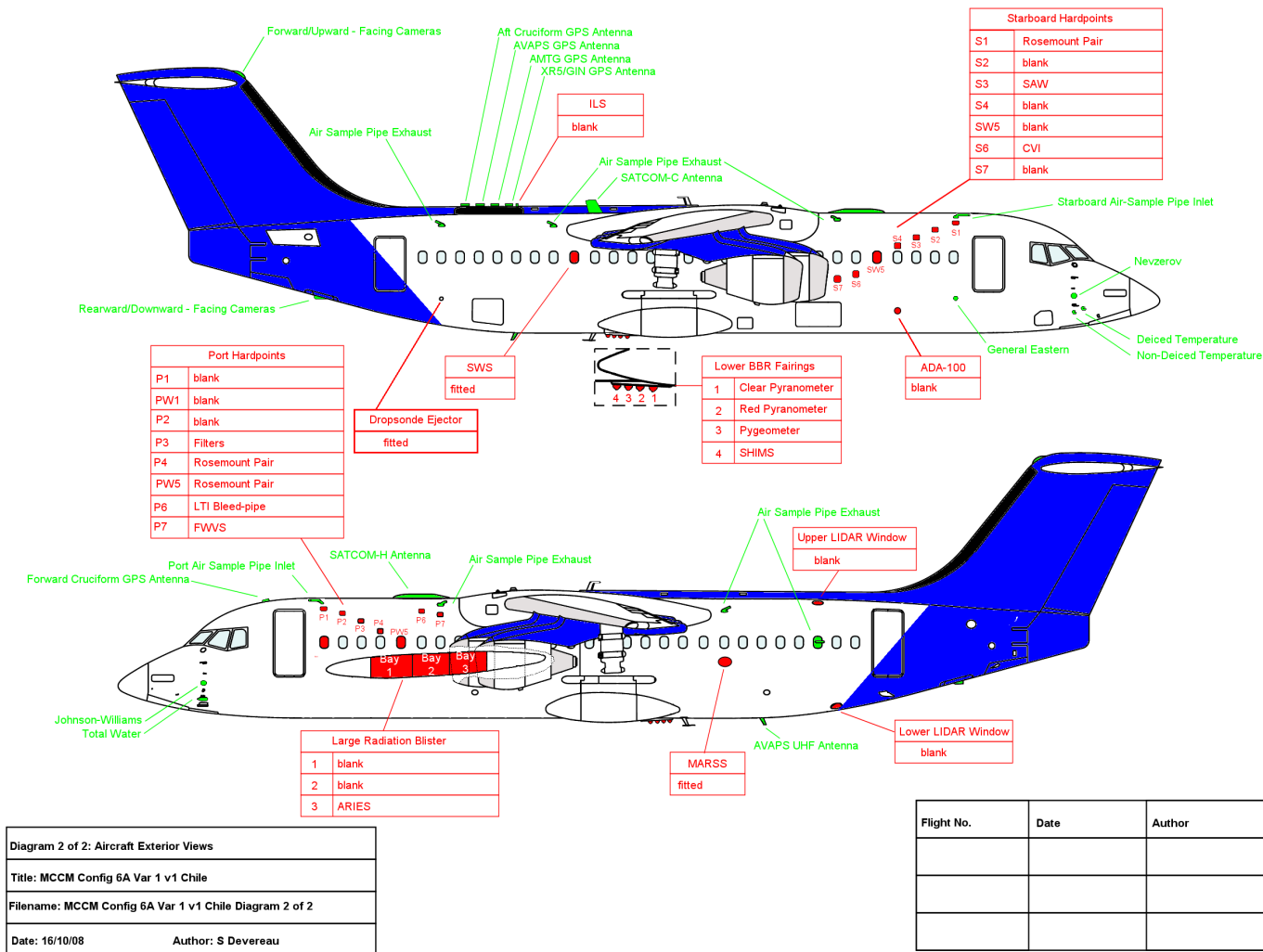


Figure 2.19: External elevation of FAAM Bae-146 CofC, Showing the position of the aft port Rosemount inlet pair used by the CCNc and TSI 3786, Port hardpoint PW5 above bay 1 on the large radiation blister.

### 2.2.2 Sampling Architecture

A schematic of the plumbing can be seen in Figure 2.20. The system has been designed to be operated through the reduced pressure inlet. However, if this were to fail or ambient conditions were desirable the two quarter turn on/off valves can be switched connecting the CCNc to ambient pressure conditions. The detailed plumbing to the CCN rack and within the CCN rack for both instruments of interest, CCNc and CN counter (modified 3786 UCPC, Quant), can be seen in Figures 2.24, 2.25(a) and 2.25(b) on page 88. The specific dimensions of which are in Tables 2.3 on page 88, 2.4 on page 89 and 2.5 on page 89. This detailed plumbing information is required for two reasons, firstly to calculate the lag time for the CCNc and the CPC and secondly to model particle transport losses. Estimation of the lag time is important as the BAe-146 uses a central time server to which all instrument parameters are cross referenced. The response time of these instruments can vary from the near instantaneous, e.g. GPS altitude, to tens of seconds for some aerosol and chemical species, to understand the atmosphere being sampled each instrument's lag time needs to be estimated so comparison is possible. As for modelled sample losses, it is important to understand what part of the aerosol distribution penetrates to the measurement system and which sizes are lost. This information allied with accurate distribution measurements are needed to reconstruct the true characteristics of the ambient aerosol. Both reasons require an accurate estimate of volumetric flow rate in their calculations. This is a key estimate as the reduced pressure inlet is designed to control pressure by varying flow. The following Bernoulli's equation can be used to model the CCNc system flow,  $Q$

$$Q = C_v A \sqrt{2 \frac{ZRT_s}{M} \left( \frac{k}{k-1} \right) \left( \frac{P_2}{P_1} \right)^{\frac{2}{k}} - \left( \frac{P_2}{P_1} \right)^{\frac{(k+1)}{k}}}, \quad (2.16)$$

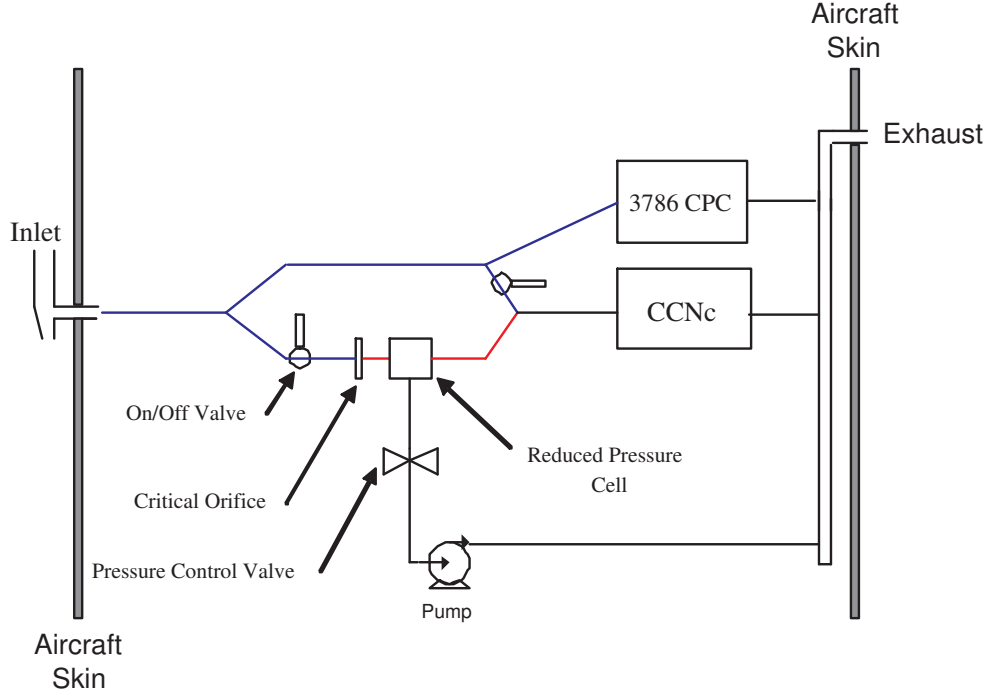


Figure 2.20: Schematic of both the on rack and off rack plumbing for the CCNc and CPC. The red denotes the reduced pressure section and the blue the ambient.

where  $C_v$  is the total system flow coefficient, a measure of a devices efficiency at allowing fluid flow, is calculated experimentally.  $A$  is the cross-sectional area of the critical orifice,  $1.464 \times 10^{-7} \text{ m}^2$ .  $Z$  the mean gas compressibility factor calculated here to be 0.9998 and considered to be stable across the operating envelope of the system.  $R$  the universal gas constant,  $8.3145 \text{ J K}^{-1} \text{ mol}^{-1}$ .  $T_s$  should ideally be the upstream temperature (K), but since this is not measured in the system the downstream sample temperature from the CCN instrument is used.  $M$  is the molar mass of air, estimated at  $0.02896 \text{ kg mol}^{-1}$ . The specific heat ratio  $k$  much like the compressibility factor, can be treated as a constant of 1.4 across the operating envelope of the aircraft.  $P_1$  and  $P_2$  are the upstream and downstream pressures in Pa. The downstream pressure is measured in the CCNc, the upstream pressure, like the temperature, is not measured.

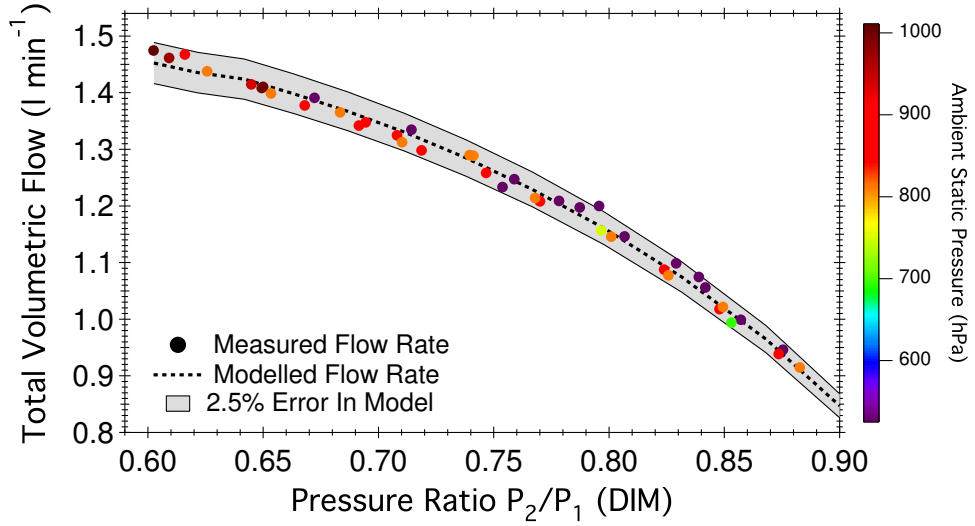


Figure 2.21: Model (dashed line) and measured data (closed circles) from flight B599 for reduced pressure inlet variable flow with changing ambient pressure (colour array),  $P_2$ . The grey shaded area shows  $\pm 2.5\%$  of the model estimate.

To estimate this upstream pressure, and collect a validatory data set of flow, both pressure and flow were measured at multiple pressure altitudes using an absolute pressure transducer (2025P, Digitron) and a mass flow meter (GCM-B58A-BW00, Vögtlyn) on a single test flight (B599). To add to this pressure data set new logging software was written in LabView to record the absolute inlet pressure from the TSI 3786 CPC. Figure 2.22 shows the relationship between the ambient static pressure and the line pressure, the pressure in the sampling system. The solid line represents an empirical linear model of the data and the dashed line the relationship as predicted from first principles with ram pressure theory for an ideal gas assuming no losses or exchange of heat or momentum with the inlet walls. This can be calculated using Equation 2.17.

$$dP = \frac{\rho v^2}{2}, \quad (2.17)$$

where  $dP$  is the pressure increase,  $\rho$  is the air density and  $v$  the velocity of the

body, in this case the aircraft velocity or true air speed (TAS).

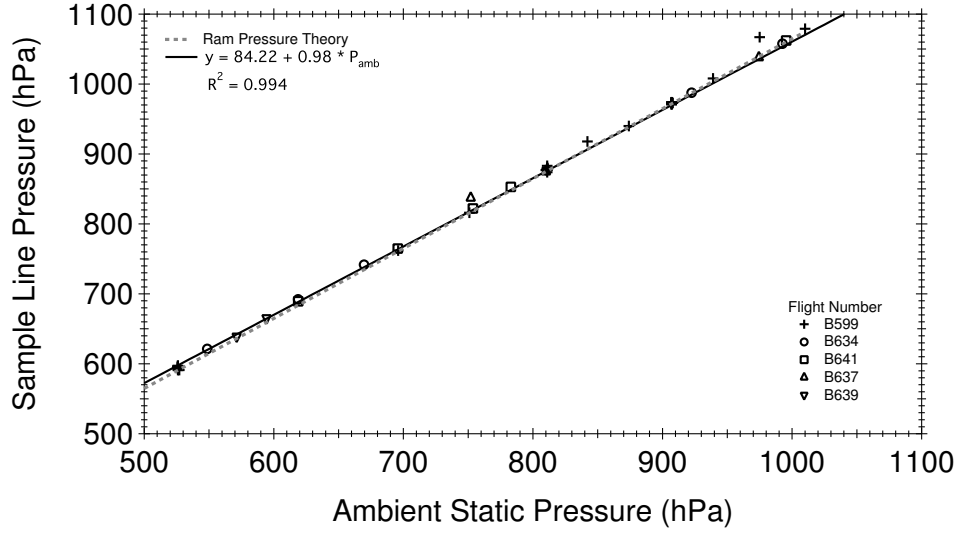


Figure 2.22: The solid line is an empirical model to describe the pressure in the sample line behind a Rosemount inlet compared to the static ambient pressure. The relationship is based on five flights of data (open symbols) using the pressure transducer in the TSI, 3786 CPC and a validatory set of data recorded using a Digitron manometer from flight B599. No error bars are shown as the values of at one standard deviation are too small to be represented on the plot, ranging from 1.05 to 4.24 hPa across all flights. These data fit well to ram pressure theory, depicted by the checked line.

The increase in pressure in the inlet also causes dynamic adiabatic heating due to compression. This heating can be calculated using Equation 2.18. The estimates of inlet heating can be seen in Table 2.2 these values should be treated as theoretical maxima as this calculation implies no removal of heat by the flow.

$$\frac{T_2}{T_1} = \left( \frac{P_2}{P_1} \right)^{\frac{R_s}{C_P}}, \quad (2.18)$$

where  $T_2$  and  $T_1$  are the temperature of the compressed and the ambient uncompressed air respectively and  $P_2$  and  $P_1$  are the pressures of each.  $R_s$  is the specific gas constant for dry air,  $287.04 \text{ J kg}^{-1} \text{ K}^{-1}$  and the heat capacity for air

at constant pressure  $C_p$  is  $1.005 \text{ J kg}^{-1} \text{ K}^{-1}$ .

Altitude	Static	Ambient	TAS	Denstiy	Dynamic
	Pressure	Temperature			Heating
m	hPa	°K	ms <sup>-1</sup>	kg m <sup>-3</sup>	°K
30	1009.6	288.0	103.0	1.22	5.1
305	977.2	286.2	104.4	1.19	5.3
1524	843.1	278.2	110.8	1.06	6.2
3048	696.8	268.3	119.7	0.91	7.5
6096	465.6	248.5	140.9	0.65	10.8
9144	300.1	228.7	168.2	0.46	15.6

Table 2.2: Dynamic heating of sample in the Rosemount inlet calculated assuming an adiabatic process.

$C_v$  in Equation 2.16 on page 81 is also an unknown but can be estimated by reordering Equation 2.16. Equation 2.19 can be solved as  $Q$  was also measured during the test flight. So  $C_v$  is a function of the velocity and the change in temperature and pressure across the critical orifice.  $C_v$  is calculated from Equation 2.16 using the measured flow rate,  $Q$ . A linear model was then developed to describe the relationship between pressure drop across the critical orifice and  $C_v$  that is carried forward in this section.

$$C_v = \frac{Q}{Af(\Delta PT)} \quad (2.19)$$



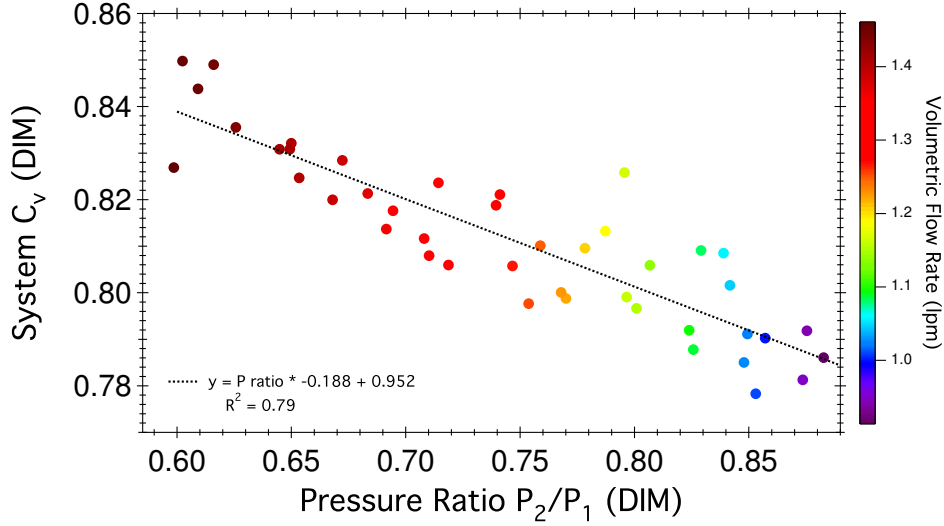


Figure 2.23: System  $C_v$  plotted against pressure ratio. The colour array represents the positive relationship between  $C_v$  and system flow. The dashed line represents the linear relationship between the system  $C_v$  and pressure ratio.

When an aerosol sample is transported down a sample tube, losses occur; diffusion of small particles to the wall of the sampling tubes, inertial loss of particles in bends and contractions and the losses due to gravimetric settling. The first of these mechanisms affects the Aitken and nucleation modes, the latter two mechanisms are associated with the upper accumulation and coarse modes (Willeke and Baron, 2005; Hinds, 1999; Foltescu et al., 1995; von der Weiden et al., 2009). Electrophoretic and thermophoretic losses are not considered here as the sample line material is either stainless steel or conductive tubing and the temperature in the sample lines is considered to be in thermal equilibrium once inside the aircraft cabin. The fraction of particles lost in the sample system is expressed using the transport efficiency, Equation 2.20.

$$\eta_{transport} = \prod_{tubesections} \left( \prod_{mechanism} \eta_{tubesection,mechanism} \right), \quad (2.20)$$

to calculate  $\eta_{transport}$  the detailed measurements of the sample lines are needed;

length of sample tube section, internal diameter (ID), orientation of the tubing with respect to gravity and the angle of each bend in radians. This information can be seen in Figures 2.24, 2.25(a) and 2.25(b) and the information in Tables 2.3, 2.4 and 2.5 for both off rack plumbing and the instrument specific CCNc and CPC plumbing.

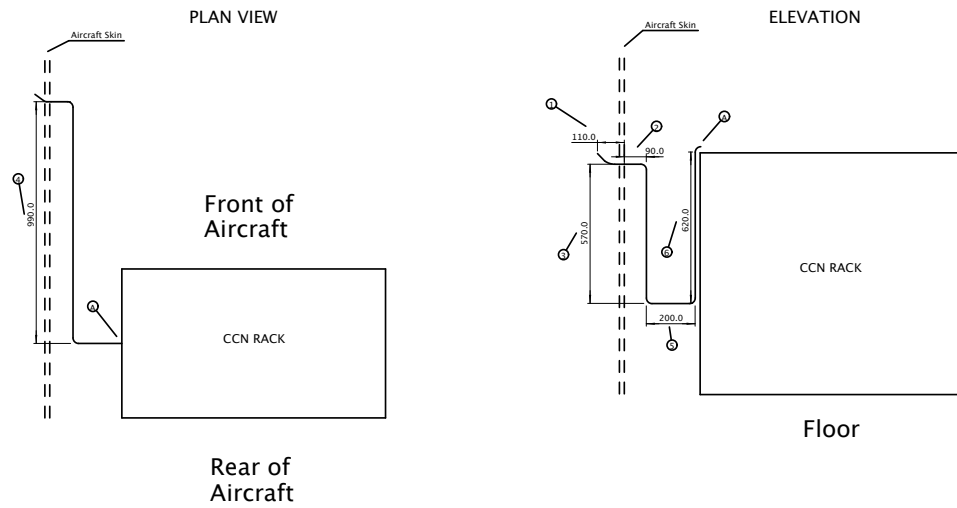
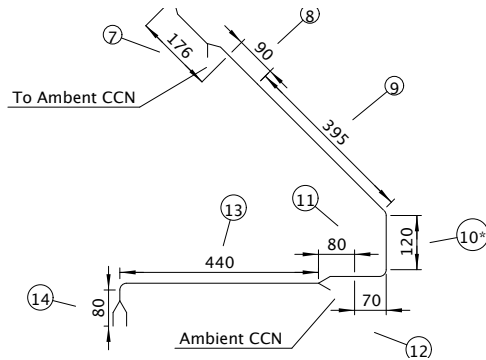


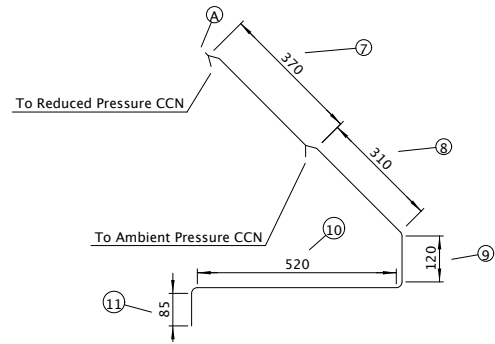
Figure 2.24: Plumbing architecture for the CCNc instrument rack, from the Roseount to the rack. The dimensions for these numbered sections are in Table 2.3.

Section	Length	ID	Orientation	Material	Angle
	mm	mm			radians
1	110	8.3	horizontal	stainless steel	0.63
2	90	7.9	horizontal	conductive	1.57
3	570	7.9	vertical	conductive	1.57
4	990	7.9	horizontal	conductive	0
5	200	7.9	horizontal	conductive	1.57
6	670	7.9	vertical	conductive	1.57
Total	2630				

Table 2.3: Dimensions of the plumbing between the first right angle of the modified Rosemount inlet and the CCN rack, section numbers relate to labels in Figure 2.24, orientation is with respect to gravity and angle is the angle of the bend in radians.



(a) CCNc on rack plumbing.



(b) CPC on rack plumbing.

Figure 2.25: On rack plumbing for CCNc and CPC. The dimensions for these numbered sections can be seen in Tables 2.4 and 2.5.

Section	Length	ID	Orientation	Material	Angle
	mm	mm			radians
7	175	4.8	horizontal	conductive	0
8	90	4.5	horizontal	stainless steel	0
9	395	4.8	horizontal	conductive	0.79
10	120	4.5	horizontal	stainless steel	1.57
11	70	4.5	vertical	stainless steel	0
12	80	4.8	vertical	conductive	0
13	440	4.8	vertical	conductive	1.57
14	80	4.8	horizontal	conductive	0
Total	1450				

Table 2.4: Dimensions of the plumbing between the point A and the CCNc inlet, section numbers relate to labels in Figure 2.25(a), orientation is with respect to gravity and angle is the angle of the bend in radians.

Section	Length	ID	Orientation	Material	Angle
	mm	mm			radians
7	370	4.8	horizontal	conductive	0
8	310	4.8	horizontal	conductive	0.79
9	120	4.8	horizontal	conductive	1.57
10	520	4.8	vertical	conductive	1.57
11	85	4.5	horizontal	stainless steel	0
Total	1405				

Table 2.5: Dimensions of the plumbing between the point A and the CCNc inlet, section numbers relate to labels in Figure 2.25(a), orientation is with respect to gravity and angle is the angle of the bend in radians.

The Equations 2.24 to 2.33 have been chosen from the literature, matching

where possible the operating conditions to calculate  $\eta_{tube\,section,mechanism}$  in Equation 2.20. The equations have been coded into IGOR Pro (Wavemetrics Inc.) to create a model that is initialised with temperature, pressure and an array of particle diameters of interest. The model outputs are estimates of the individual loss mechanisms as seen in Figure 2.26. The model was run for three International Standard Atmosphere (ISA) pressure altitudes, 0, 1500 and 3000 m, 1013.25, 845.6 and 701.2 hPa respectively to assess the suitability of the plumbing and understand the losses associated in the transport of aerosol from the inlet to the instruments.

To calculate the losses associated with sampling some basic parameters must be defined, one of these is the terminal settling velocity of a particle,  $V_{ts}$

$$V_{ts} = \tau g \quad (2.21)$$

where  $\tau$  the particle relaxation time (s) and  $g$  the gravitational acceleration,  $9.81 \text{ m s}^{-2}$ .

$$\tau = \frac{\rho_p D_p^2 C_c}{18\eta}, \quad (2.22)$$

the parameters in Equation 2.22 are the same as Equation 2.9 on page 63 with the exception of  $\eta$ , the gas absolute viscosity ( $\text{N s m}^{-2}$ ).

$$Stk = \frac{\tau U}{d}, \quad (2.23)$$

where  $U$  is the characteristic gas velocity ( $\text{m s}^{-1}$ ) and  $d$  is the characteristic system dimension.

During sampling particles settle out of pipes due to the force of gravity. The

rate of settling is a function of particle size, residence time, tube diameter and angle of incline. These gravimetric settling losses ( $\eta_{grav}$ ) can be estimated using Equation 2.24 (Fuchs, 1964) below for horizontal and Equation 2.26 non-horizontal flows (Heyder and Gebhart, 1977).

$$\eta_{grav} = 1 - \frac{2}{\pi} [2\varepsilon \sqrt{1 - \varepsilon^{2/3}} - \varepsilon^{2/3} \sqrt{1 - \varepsilon^{2/3}} + \arcsin(\varepsilon^{1/3})], \quad (2.24)$$

where

$$\varepsilon = \frac{3}{4} Z_{grav} = \frac{3}{4} \frac{L}{d} \frac{V_{ts}}{U}, \quad (2.25)$$

and  $Z_{grav}$  is the gravitational deposition parameter,  $L$  the length of the tube section,  $d$  the internal diameter of the sample tube and  $V_{ts}$  is the terminal settling velocity.

$$\eta_{grav} = 1 - \frac{2}{\pi} [2\kappa \sqrt{1 - \kappa^{2/3}} - \kappa^{2/3} \sqrt{1 - \kappa^{2/3}} + \arcsin(\kappa^{1/3})] \quad (2.26)$$

where

$$\kappa = \varepsilon \cos \theta, \quad (2.27)$$

$\theta$  being the angle of the sample line with respect to gravity. Equation 2.26 only holds if the axial component of a particles settling velocity is small in comparison to the average gas velocity in the tube. The magnitude of diffusional losses depend on residence time, which in a plumbed system is a function of tube length, cross sectional area and volumetric flow rate. Diffusional losses in a laminar flow regime

can be calculated using Equations 2.29 and 2.30 (Willeke and Baron, 2005).

$$\xi = \frac{\pi DL}{Q} \quad (2.28)$$

$\xi$  is used to define two regimes under which diffusion occurs, where  $D$  is the particle diffusion coefficient,  $L$  the tube length and  $Q$  the volumetric flow rate through the tube. For  $\xi < 0.02$

$$\eta_{diff} = 1 - 2.56\xi^{2/3} + 1.2\xi + 0.177\xi^{4/3}, \quad (2.29)$$

and for  $\xi > 0.02$

$$\eta_{diff} = 0.819\exp(-3.657\xi) + 0.097\exp(-22.3\xi) + 0.032\exp(-57\xi). \quad (2.30)$$

The inertial losses in the bends of the sampling system ( $\eta_{bend,inert}$ ) can be calculated from the empirical relationship in Equation 2.31. The empirical equation of for inertial losses in bends from Pui and Liu (1987) was for systems with Reynolds number of 1000, curvature ratios (quotient of the radius of the bend and radius of the tube) of 5.6 and 5.7 for tubing with internal diameters between 4 and 8.5 mm. The Reynolds numbers of the CCN arrangement investigated here never exceeded 815, the tube diameters ranged from 4.5 to 8.3 mm and the tightest curve gives a curvature ratio of 6.35.

$$\eta_{bend,inert} = \left[ 1 + \left[ \frac{Stk}{0.171} \right]^{0.452 \frac{Stk}{0.171} + 2.242} \right]^{-\frac{2}{\pi} \varphi}, \quad (2.31)$$

where  $\varphi$  is the angle of the bend in radians. Particles are also lost at points where sharp contractions occur in the sample tubing ( $\eta_{cont,inert}$ ), as discussed in

Section 2.1.4 on the use of critical orifices in reduced pressure devices. Where contractions could not be designed out of the system the inertial losses were calculated using Equation 2.32 (Muyshondt and Anand, 1996).

$$\eta_{cont,inert} = 1 - \frac{1}{1 + \left\{ \frac{2Stk \left[ 1 - \left( \frac{d_0}{d_i} \right)^2 \right]}{3.14 \exp(-0.0185\theta_{cont})}, \right\}^{-1.24}} \quad (2.32)$$

where  $d_0$  and  $d_i$  are the diameter of the smaller tube and the larger tube, respectively, and  $\theta_{cont}$  is the angle of contraction. Minimising both this angle and  $\frac{d_0}{d_i}$  can reduce the losses associated with contractions. The efficiency of sampling particles around the first right angle in the sampling system ( $\eta_{asp,90^\circ}$ ), the point at which the horizontal streamlines in Figure 2.29 on page 98 are drawn into the vertical, can be estimated by using Equation 2.33 (Brixey et al., 2005).

$$\eta_{asp,90^\circ} = \frac{1}{1 + 4GStk \left( \frac{U_0}{U} \right)^{0.25}}, \quad (2.33)$$

where

$$G = 2 + \left( \frac{0.62}{\left( \frac{U_0}{U} \right)} \right) - 0.9 \left( \frac{U_0}{U} \right)^{0.1} \quad (2.34)$$

and  $\frac{U_0}{U}$  is the ratio of free stream velocity to sampling velocity (velocity ratio). Ideally the stream flow in the Rosemount inlet head should be used here but as this is not known the value for true air speed is used as proxy. Brixey et al. (2005) has extended previous work by investigating aspiration efficiency at high velocity ratios, up to 50. This makes this model ideally suited to aircraft sampling.

These modelled losses as a function of particle diameter can be seen in Figures 2.26 and 2.27. Figure 2.26 depicts all of the loss functions calculated for particle sizes between 0.001 and 20  $\mu\text{m}$  assuming a temperature of 293.15 K, pressure



of 1013.25 hPa and a particle density of  $1000 \text{ kg m}^{-3}$ . Where Figure 2.27 depicts only the composite of all losses,  $\eta_{transport}$  for three different ISA conditions, again assuming a particle density of  $1000 \text{ kg m}^{-3}$ .

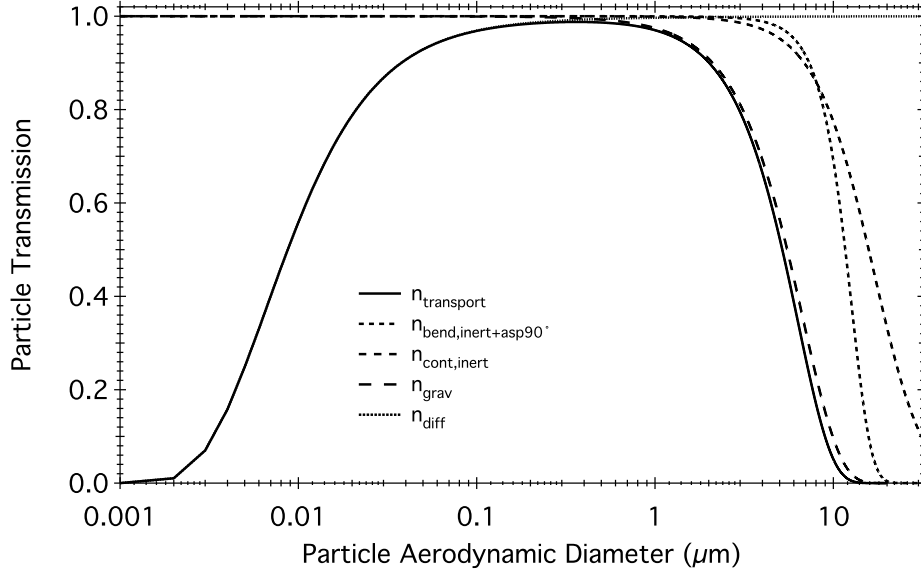


Figure 2.26: Example of the composite function,  $\eta_{transport}$  (solid line), of loss mechanisms for inertial losses in bends ( $\eta_{bend,inert}$ , short dashed line) and contractions ( $\eta_{cont,inert}$ , medium dashed line), gravimetric losses ( $\eta_{grav}$ , long dashed line) and diffusion ( $\eta_{diff}$ , dotted line) in the CCNc sample line. From the first right angle of the Rosemount inlet to the instrument at a line pressure of 1013.25 hPa with a particle density of  $1000 \text{ kg m}^{-3}$ ,  $\eta_{diff}$  underlies  $\eta_{transport}$  below  $0.3 \mu\text{m}$ .

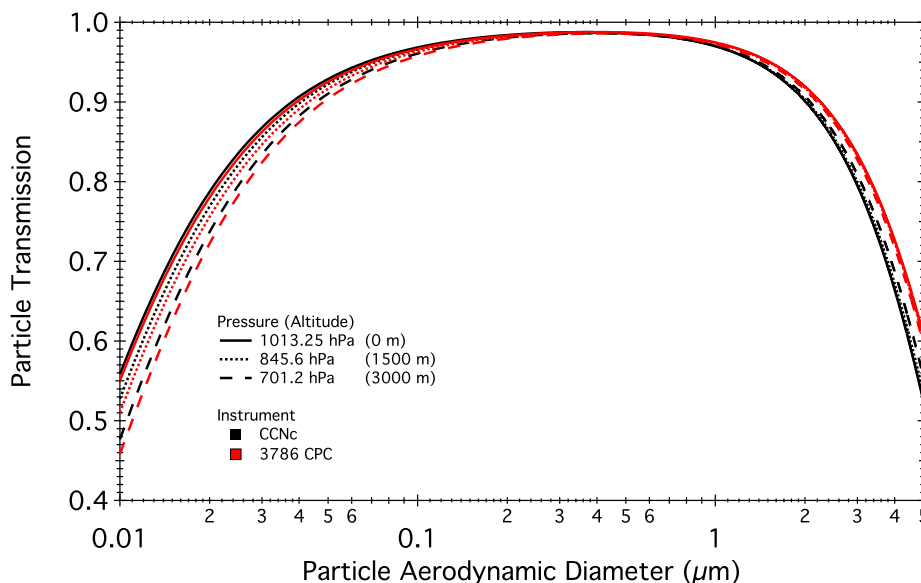


Figure 2.27: Total particle transmission calculated for both the CCNc (black lines) and CPC (red lines) for three different pressure altitudes, 1013.25 hPa (solid lines), 845.6 hPa (dotted lines) and 701.2 hPa (dashed lines).

Modelled diffusive losses can be seen to extend into the accumulation mode. The lower the pressure, the greater the diffusive losses; see Figure 2.27. This is both a function of the increased mean free path and therefore greater diffusion coefficient and an increased residence time in the sample line at lower pressures. The increased residence time is a function of lower bypass flows in the reduced pressure inlet needed to maintain the set point pressure. At 701.2 hPa the residence time is 6.02 s compared to 4.98 s at 1013.25 hPa. The diffusive losses drop to less than 1 % by  $0.286 \mu\text{m}$  in Figure 2.27. The increased flow at high pressures increases the losses due to inertia. This interplay between these two loss functions can be seen in Figure 2.27, where higher inertial losses occur at higher pressures. However, inertial losses have little or no contribution until  $3.86 \mu\text{m}$  and  $2.6 \mu\text{m}$  for losses in bends and contractions respectively, by which time they contribute 1 % to the total loss. The gravimetric losses also extend well into the accumulation mode at  $0.594 \mu\text{m}$ ; they contribute 1 % to the total loss. In total

the losses across the accumulation mode in the CCNc and CPC plumbing are low. Where possible the CCNc uses electrically conductive tubing internally and all tube runs are minimised to reduce the diffusive losses. Roberts and Nenes (2005) calculated the diffusive losses in the instrument plumbing to be less than 3 % for  $0.027\ \mu\text{m}$  particles and impaction losses are negligible for particles less than  $10\ \mu\text{m}$  in diameter. Across all pressure altitudes the maximum loss modelled at  $0.1\ \mu\text{m}$  is 4 % (701.2 hPa CPC run), dropping to a maximum of 3 % (1013.25 hPa) at  $1\ \mu\text{m}$ . As the losses are minimal in the accumulation mode and there is no apparent distinction between the losses from either instrument activated fraction measurements can be considered to have no bias.

All the losses are calculated from the point referred to as the ‘first right angle’ (the start of section 1 in Figure 2.24 on page 87 also shown in Figure 2.29 at the intersection of the horizontal and vertical parts of the Rosemount inlet) of the system and ignore any non-representative sampling resulting from non-isoaxial or non-isokinetic conditions related to movement of the air entering the Rosemount inlet as in Foltescu et al. (1995). This is remiss as with the high speed of incident air flow on airborne platforms any particle enhancement or denudation could cause disparities by orders of magnitude in inlet aspiration efficiency (Petzold, 2009). To investigate the suitability of using a modified 102E Rosemount as an aerosol inlet a series of experiments were undertaken on flights in the UK and Northern Mali during the Fennec project, 2011.

The model outputs must be validated with measurements as in Section 2.1.4 on page 58 for the reduced pressure inlet losses. This was not done at the time of writing but since that time a laboratory experiment was run to test the same loss equations in the same model for a different instrument’s sampling architecture. The model was run to describe the losses in the following Section 2.2.3 on page 98 for the Sky-OPC (Grimm Technik, Model 1.129 essentially a replumbed model

1.109 (Heim et al., 2008)) sample lines. The losses were also estimated from laboratory comparisons undertaken in June 2013. The experimental set up as exactly the same as for the reduced pressure inlet in Figure 2.7 on page 62 though the reduced pressure inlet was replaced as the treatment by the sample line from the Sky-OPC. PSL beads were used as the test aerosol. The system flow was provided by the Sky-OPC at 1.2 lpm. The comparison between the model and the measurements can be seen in Figure 2.28.

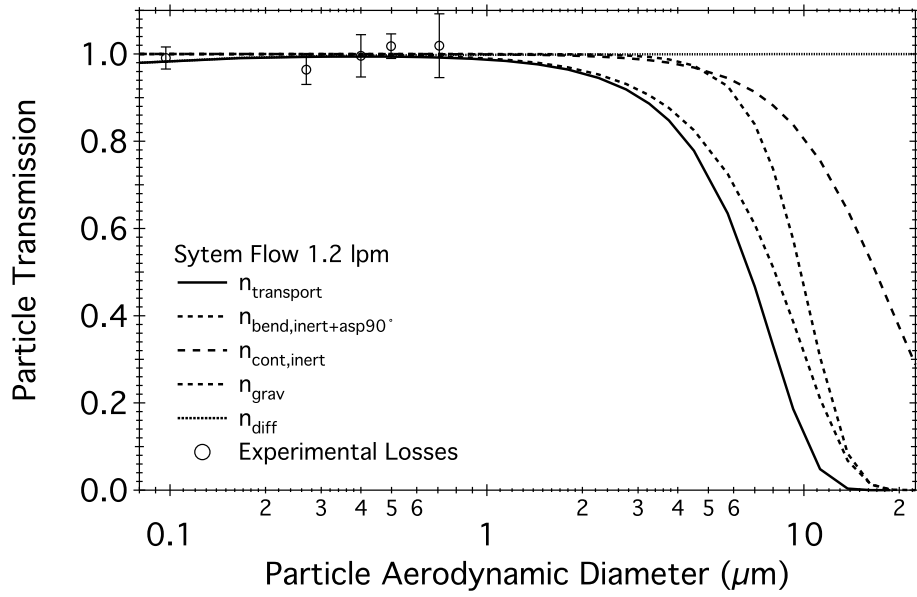


Figure 2.28: Model estimates of the total particle losses,  $\eta_{transport}$  (solid line) and the contributory mechanisms for inertial losses in bends ( $\eta_{bend,inert}$ , short dashed line) and contractions ( $\eta_{cont,inert}$ , medium dashed line), gravitational losses ( $\eta_{grav}$ , long dashed line) and diffusion ( $\eta_{diff}$ , dotted line) in the Grimm-SkyOPC sample line. The open circles represent the measured data using PSL beads as the aerosol source. The error bars represent one standard deviation of the measurements.

The loss measurements and the loss models used in this Section and the proceeding compare well. The maximum deviation between the two is 3% at an aerodynamic particle diameter of  $0.269 \mu\text{m}$ .

### 2.2.3 Rosemount Inlet Characterisation

The standard aerosol inlet used on the BAe-146 is a 102E modified Rosemount housing. These inlets are certified for all aircraft and usually house platinum resistance thermometers (PRT). They have been modified for use on the BAe-146 by passing a  $\frac{3}{8}$ " tube up the centre of the inlet. This insert stops just short of horizontal section end, as seen in Figure 2.29.

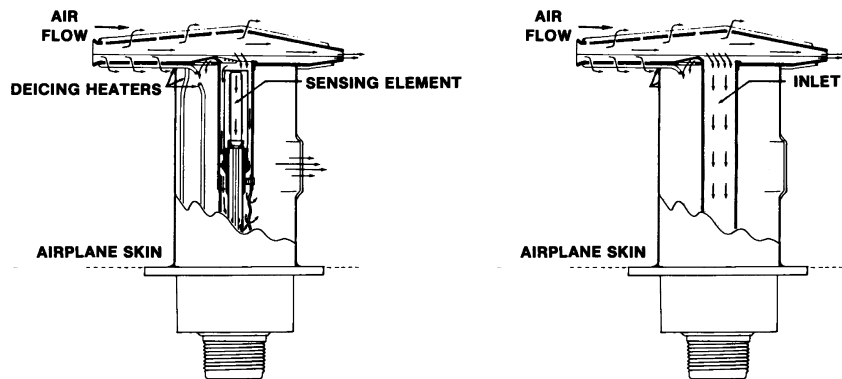


Figure 2.29: Schematics showing the unmodified Rosemount 102E housing with the usual PRT embedded on the left hand side with the modified version used for aerosol sampling on the BAe-146 to the right.

The Rosemount inlets are mounted on a window blank (Figure 2.19 on page 80) and the middle of each inlet extends 103 mm beyond the skin. This distance puts the inlet just into the free stream outside of the aircraft boundary layer as modelled by BAe Systems (James, 2003); see Figure 2.31. Since these inlets have not been designed with transmission of aerosol as the driving criterion it is important to understand how they sample an ambient aerosol population. Two previous studies have investigated this problem. Foltescu et al. (1995) assumed the aspiration efficiency was unity and simply modelled the losses from the first right angle. Petzold (2009), however, showed that Rosemount inlets enhance aerosol across the distribution measured, from a factor of 1.5 to just over 6 between  $0.25$  to  $0.8 \mu\text{m}$  at pressure altitudes between 350 and 900 hPa at a true air speed of



(a) View of modified Rosemount 102E housing from the front looking towards the rear of the aircraft. (b) View of modified Rosemount 102E housing from the rear looking towards the nose of the BAE-146.

Figure 2.30: Images of the Aft Rosemount pair on the BAE-146. The upper of the two inlets provides the sample for the Aerosol Mass Spectrometer and the lower the CCNc.

$137 \text{ m s}^{-1}$ .

To test the modified Rosemount housing's utility as an aerosol inlet a control inlet was needed, one where the aspiration and transmission efficiencies are known and with which aerosol spectra gathered from a Rosemount could be compared. A University of Denver Low Turbulence Inlet (LTI) is operated on the BAE-146. This inlet is designed to sample supermicron particles from aircraft traveling at velocities in excess of  $100 \text{ m s}^{-1}$  in a characterised manner. It operates isokinetically and has enhancement factors of 1.0 for submicron aerosol, particles with a greater diameter are enhanced, up to four times at  $15 \mu\text{m}$ . These enhancements, however, are well characterised and can be corrected for (Wilson et al., 2004). The LTI has been shown to sample representatively, after corrections were applied, in a comparison between the University of Denver's focused cavity aerosol spectrometer derived extinction coefficients, measuring particles between  $0.09$  to  $2.0 \mu\text{m}$ , and the Stratospheric Aerosol and Gas Experiment (SAGE) II version 6.20 data product (Reeves et al., 2008). During the Fennec project of 2011 three Sky-OPCs were used to sample aerosol from both the LTI and two Rosemount inlets. Two of the three Sky-OPCs were operated simultaneously behind both

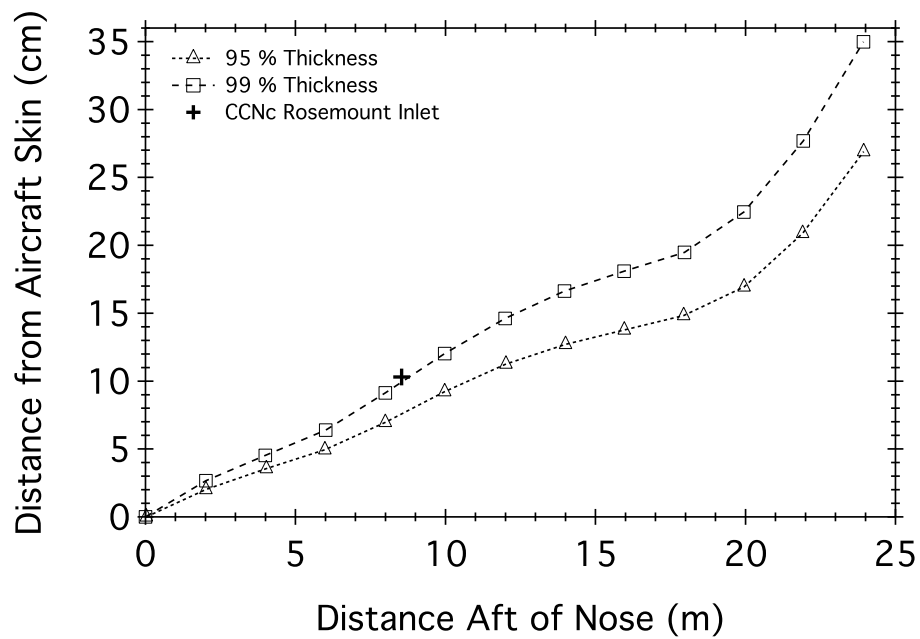
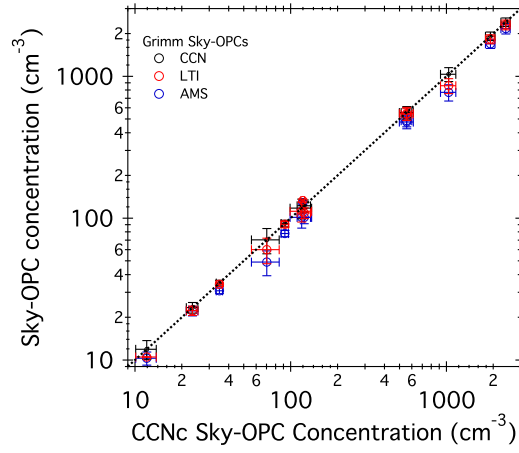


Figure 2.31: Position of the aft Rosemount pair with respect to the BAe-146 boundary layer depth taken from James (2003). The Thickness lines show the thickness of the velocity boundary layer, defined as the distance from the solid body at which the viscous flow velocity is at 95 and 99 % (open triangles and squares, respectively) of the free stream velocity.

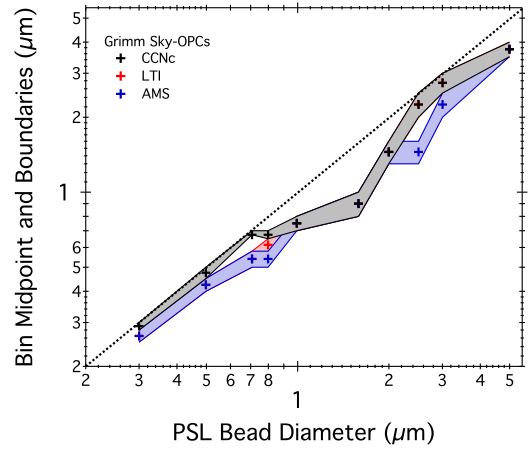
the CCNc and the AMS Rosemount inlets. These OPCs are designed specifically for low pressure airborne applications and measure an aerosol spectrum between 0.3 and 32  $\mu\text{m}$ . The third Sky-OPC was connected to a bespoke sub-sampling rig, designed to sample isokinetically in extracting a sample from the main LTI sample flow (Belyaev and Levin, 1974).

Three experiments were conducted to check the counting and sizing characteristics of the Sky-OPCs used. The results of this laboratory based comparison can be seen in Figure 2.32.

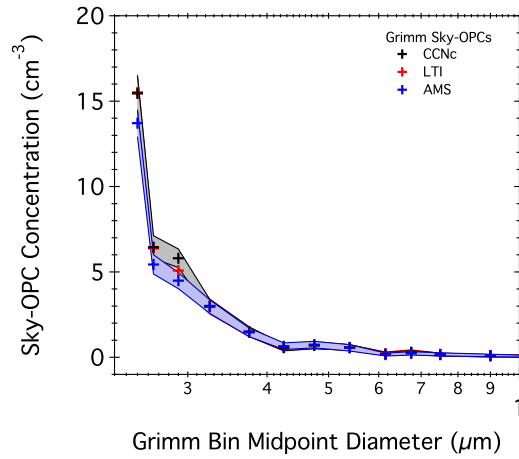




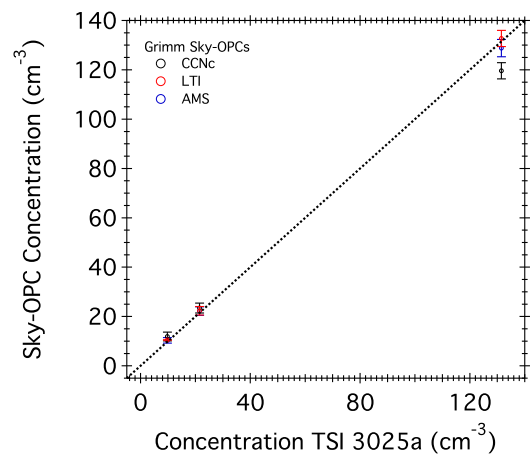
(a) Sky-OPC counting comparison



(b) Sky-OPC sizing comparison



(c) Sky-OPC ambient air comparison



(d) Sky-OPC counting comparison with a TSI 3025a CPC

Figure 2.32: Panel showing the lab comparison results from the three Grimm Technik Sky-OPC instruments (black CCN inlet, red LTI and blue AMS inlet) used for the inlet analysis flights during the Fennec campaign, 2011. The error bars in each plot represent one standard deviations of the measurement.

The first experiment used ten different PSL bead diameters between  $0.3 \pm 0.006 \mu\text{m}$  and  $4.99 \pm 0.04 \mu\text{m}$ . The beads were nebulised, dried and passed through a DMA to remove any conglomerates or surfactant residues associated with the medium. In the same manner as aerosol production in previous experiments; see Figures 2.3 on page 50, 2.7 on page 62 and 2.10 on page 68. The

flow was then split equally to the three OPCs. Figure 2.32(a) compares the counting ability of all three instruments against the instrument used on the CCN Rosemount inlet. This instrument was chosen for the control as it was a brand new instrument that had been calibrated at the factory less than a month before these experiments were conducted. As such the black open circles, the CCN OPC expresses the  $x=y$  line. Both the AMS and LTI OPCs undercount the CCN instrument across the entire size range. The undercount ranges between 5 % and 30 % with a mean undercount of  $13 \% \pm 9 \%$  for the AMS and 1 % and 17 % with an average of  $5 \% \pm 7 \%$  for the LTI. These data were also used to investigate the sizing of the instruments. Figure 2.32(b) shows the comparison of factory bin midpoints compared to the mean PSL bead diameter. The shaded background for each colour trace reflects the total bin width for the associated OPC midpoint. There are two main features of this plot. Firstly all three instruments size within one bin of one another at six of the ten diameters investigated. The diameters where divergence appears are 0.7, 0.79, 2.54 and  $3.0 \mu\text{m}$ . At two of those diameters 2.54 and  $3.0 \mu\text{m}$  it is only the AMS OPC that sizes the particles into a different bin. Overall the sizing comparison is good. The second primary feature of Figure 2.32(b) is the divergence of all three instruments from the  $x=y$  line at  $1.6 \mu\text{m}$ . This is a function of the Grimm calibration procedure and Mie-Lorenz oscillations at this scattering cross section derived diameter. The second experiment connected all three OPCs to a shared inlet measuring ambient air. All three OPCs produced similar distributions shapes. Again the AMS OPC undercounted on average  $12 \% \pm 8 \%$  across the first three bins and that the AMS and LTI instruments diverged by 22 and 12 %, respectively, from the CCN instrument in the bin centred at  $0.265 \mu\text{m}$ . In Figure 2.32(d) the counting efficiency of the three OPCs was tested against a control CN counter, a TSI 3025a. This was done for three different PSL bead sizes,  $0.3 \pm 0.006$ ,  $0.498 \pm 0.005$  and  $0.707 \pm 0.006 \mu\text{m}$ . All three instruments are within 9 % of the CN counter except in one instance

where the CCN OPC is 21 % lower than expected. In summary the instruments compare well in the laboratory experiments with all mean counting efficiencies within 10 % and of a possible 30 bin allocations (3 instruments and 10 particle diameters) only five are more than one bin apart.

Using three identical instruments has advantages, there is no need to resample the spectra or cumulate the data to undertake a comparison of the inlet efficiencies. All the data collected by the Rosemount inlet sampling Sky-OPCs were corrected for transport losses in the same model as in the previous section (Equations 2.24 on page 91 to 2.33 on page 93), again up to the first right angle of the Rosemount inlet. A model was also written in IGOR Pro to correct the Sky-OPC subsampling from the LTI for aspiration and transport losses (Equations 2.35 to 2.37) as well as enhancements associated with the LTI (Wilson et al., 2004). A particle density of  $2695 \text{ kg m}^{-3}$  (C.Ryder, personal communication, 2011) was used for all dust dominated aerosol and  $1769 \text{ kg m}^{-3}$  for the data collected over the North Sea, shown in Figure 2.37. The aspiration of the subsampler ( $\eta_{asp,subsampler}$ ) can be calculated as

$$\eta_{asp,subsampler} = 1 + \left( \frac{U_0}{U} - 1 \right) \left( 1 - \frac{1}{1 + (2 + 0.617(\frac{U_0}{U}))Stk} \right), \quad (2.35)$$

where  $U$  is the velocity in the subsampler,  $U_0$  the velocity in the parent flow, in this scenario the LTI sample line velocity, the flow that is subsampled and  $Stk$  is the Stokes Number from Equation 2.23 on page 90. As the ratio  $\frac{U_0}{U}$  increases the inlet becomes more subisokinetic and the maximum enhancement increases and occurs at smaller Stokes numbers and *visa versa*.

If flow is subisokinetic,  $U_0 > U$  then the inertial losses in the subsampler ( $\eta_{inert,subsampler}$ ) can be calculated using the equation from Liu et al. (1989) below

$$\eta_{inert, subsampler} = \frac{1 + [\frac{U_0}{U} - 1]/[1 + \frac{2.66}{Stk^{\frac{2}{3}}}]}{1 + [\frac{U_0}{U} - 1]/[1 + \frac{0.418}{Stk}]} \quad (2.36)$$

Liu et al. (1989) maintain that in superisokinetic sampling,  $U_0 < U$ , particles are not directed towards the walls of the inlet and subsequently the inertial transmission efficiency is unity. Hangal and Willeke (1990) however, assert that there is a region of loss in the *vena contracta* of the inlet and as such the inertial losses can be estimated using Equation 2.37

$$\eta_{inert, subsampler} = \exp[-75(I_v)^2], \quad (2.37)$$

where

$$I_v = 0.09 \left[ Stk \frac{U - U_0}{U_0} \right]^{0.3}, \quad (2.38)$$

$I_v$  describes the inertial losses in the *vena contracta*. Gravimetric losses in the subsampler inlet can be hard to conceptualise as the inlet itself is indistinct from the sampling tube behind it, making it hard to discriminate between the inlet and the sample line gravimetric losses. As such the gravimetric losses have been ignored here. The assumption being they are captured in the application of Equation 2.24 and 2.26 to the remainder of the sampling architecture.

The aspiration efficiency of an individual Rosemount can be calculated as the quotient of the corrected distribution measured behind the Rosemount inlet and the LTI for a given particle diameter ( $\eta_{Rosemount}(D_o)$ ) from Equation 2.39. Understanding the aspiration efficiency of these Rosemount inlets is very important to understand how representative an aerosol measurement is. It is also important to know if two Rosemount inlets sample equally across a distribution as inferences in atmospheric science can be gleaned from derived measurements whose data

may have been collected from different inlets on the same aircraft, such as single scattering albedo or  $\kappa$  the hygroscopicity parameter.

$$\eta_{Rosemount}(D_o) = \frac{N_{Rosemount}(D_o)}{N_{LTI}(D_o)} \quad (2.39)$$

Data for this analysis were primarily collected in mineral dust-dominated aerosol over the northern Sahara during the Fennec project of 2011. The findings published here are not representative of all aerosol types sampled using the BAe-146. Figure 2.33 shows a distribution of mean Sky-OPC measured distributions from a single one hour long low level run above northern Mali. The plot shows transmission loss corrected and uncorrected data for all three inlets. The dashed lines are the uncorrected and solid, transmission corrected data. The difference between the two give some idea of the efficiency of each sampling architecture.

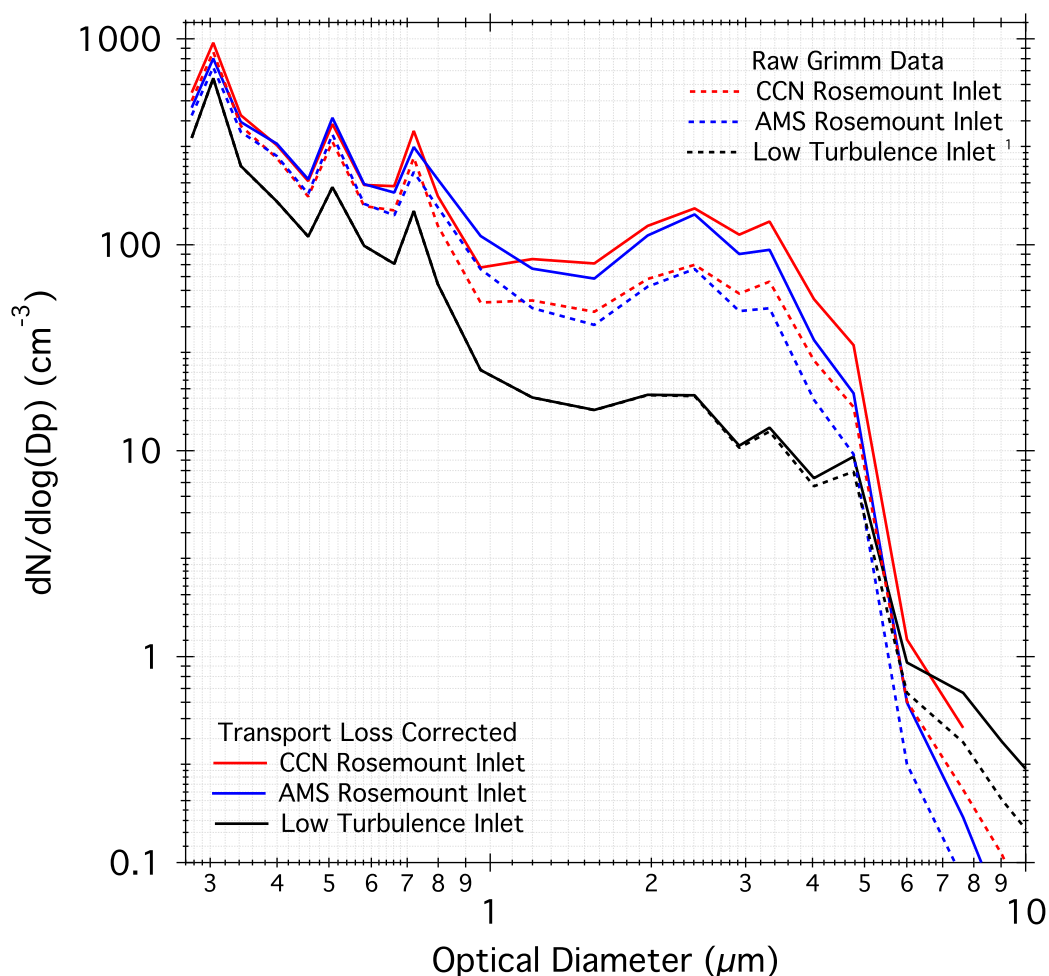


Figure 2.33: Aerosol distributions measured by the three Grimm Sky-OPCs (CCN red, LTI black and AMS blue), all corrected for both refractive index (real and imaginary 1.53 and 0.001 respectively). The dashed lines represent data that has not been and the solid lines data that has been corrected for loss functions. The data is averaged over 64 minutes from a single straight and level run (SLR) at 343 m above the Sahara in N. Mali. <sup>1</sup> These data are not the raw OPC data but data that has been corrected for the enhancement and loss functions of the LTI as per Wilson et al. (2004).

The Grimm Sky-OPC like all OPCs collects aerosol scattered light at an angle, specifically 90°. The amount of light collected is a function of the particle size, shape and composition of the aerosol and the architecture of the sample volume. This light is measured by the detector where it is collated in discrete time and pulse height bins, these bins are related to particle diameters defined

during a manufacturer’s calibration using PSL beads. As such the scattering cross sections, the true measurand of an OPC detector voltage, is for PSL beads not for the ambient aerosol in question, dust. This can be corrected for using the Mie-Lorenz theory and is done here using the correction methods described by Rosenberg et al. (2012). In this work, a complex refractive index (RI) correction of 1.53 for the scattering portion and 0.001 for the imaginary absorbing sections has been used to correct the OPC bin midpoints (Ryder et al., 2013).

Once the data have been refractive index corrected the diameters are fed into loss correction model assuming a particle density of  $2695 \text{ kg m}^{-3}$ . These diameters have not been corrected for dynamic shape factor as no specific data for this parameter are available for this project. The power law relationship between dynamic shape factor and particle diameter measured during the SAMUM project in Southern Morocco was deemed inappropriate as the measurements only spanned a  $0.24 \mu\text{m}$  range between  $0.72$  and  $0.96 \mu\text{m}$  (Kaaden et al., 2009). As such the diameters are considered spherical, the outcome of which will be a slight over estimation of both the inertial and gravimetric losses. In all 19 SLR were flown between  $325$  and  $4628 \text{ m}$  to estimate these Rosemount inlet efficiencies.

Figures 2.34 and 2.35 both use Stokes number calculated at the inlet plane assuming a TAS of  $115 \text{ ms}^{-1}$  and the density quoted above as the independent variable. Figure 2.34 shows the descriptive stats of the calculated enhancements for the CCN Rosemount inlet during the Fennec project. For representative sampling the inlet efficiency should be unity, picked out with a dashed line. Values greater than one indicate the inlet is enhancing the ambient aerosol population. Values lower than one indicate a reduction in the aerosol sampled when compared to the ambient concentrations.

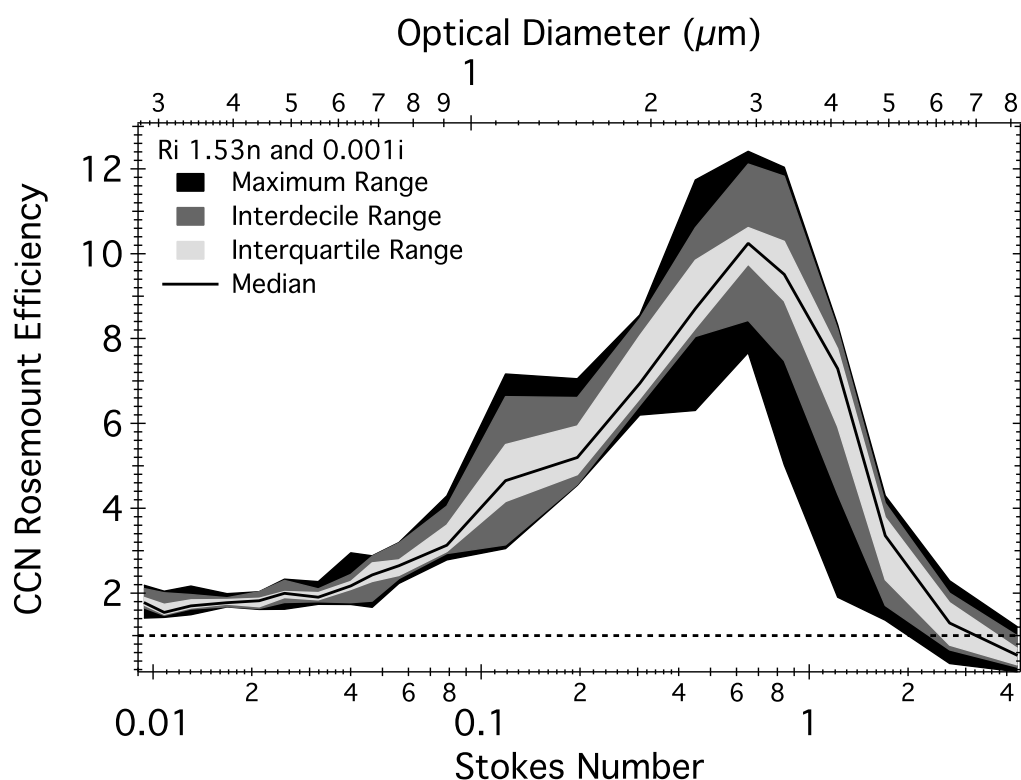


Figure 2.34: CCN Rosemount inlet enhancement for all the flights during the Fennec campaign over the Sahara in 2011 where the LTI was operating isokinetically ( $1.0 \pm 0.25\%$ ). The optical diameters have been RI corrected using 1.53n and 0.001i. The coloured blocks represent the descriptive statistics of the inlet efficiency. With solid line the median, the light grey the interquartile range, the medium shading the interdecile range and the black shading the maximum range. The dashed line represents an inlet operating isokinetically and sampling representatively.

Figure 2.35 shows the same inlet efficiency curves as described for Figure 2.34 but for the Rosemount employed by the AMS.



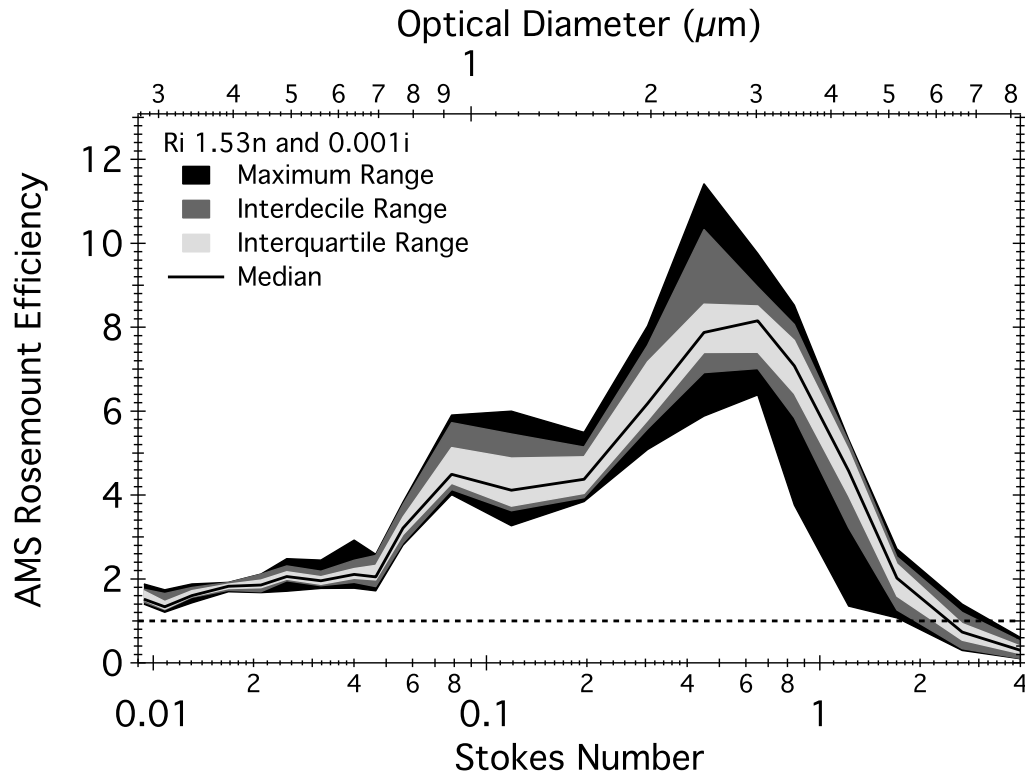


Figure 2.35: AMS Rosemount inlet enhancement for all the flights during the Fennec campaign over the Sahara in 2011 where the LTI was operating isokinetically ( $1.0 \pm 0.25\%$ ). The optical diameters have been RI corrected using 1.53n and 0.001i. The coloured blocks represent the descriptive statistics of the inlet efficiency. With solid line the median, the light grey the interquartile range, the medium shading the interdecile range and the black shading the maximum range. The dashed line represents an inlet operating isokinetically and sampling representatively.

The two Rosemount efficiency curves compare well across the entire distribution. The CCN and AMS Rosemount inlets both have inlet efficiencies greater than one at the lowest Stokes number 0.009; the median values are 1.78 and 1.51 respectively. This Stokes number equates to an optical diameter of  $0.28\ \mu\text{m}$ . Each inlet also has a shoulder in the rising leg of the efficiency curve, this is more pronounced in the data from the AMS inlet where it is at a Stokes number of 0.0078 ( $0.96\ \mu\text{m}$ ), in the CCN inlet it is at the larger diameter of  $1.2\ \mu\text{m}$  and is much less obvious. This pronounced shoulder is present in all of the SLR runs

analysed from this data set and is not apparent in the laboratory comparisons undertaken prior to the project. As such this feature is not considered to be an instrument error. Both inlets have a peak in the median inlet efficiency at a Stokes number of 0.65, which corresponds to an optical diameter of  $2.91\text{ }\mu\text{m}$ , the CCN Rosemount enhances the ambient mixing ratio by 10.24 times compared to the AMS enhancement of 8.15 at this diameter. At larger diameters the traces for both inlets fall back towards zero. This maxima is the tipping point at which the loss functions in the inlet out weighs the enhancements due to its sub-isokinetic nature.

Figure 2.36 demonstrates that in the submicron range the two inlets sample in a similar manner, with a mean difference of  $1.0\% \pm 14\%$  at one standard deviation. The variation in this mean difference is weighted by the pronounced shoulder at a Stokes number of 0.0078 in the AMS data below this shoulder (an optical diameter  $\leq 0.72\text{ }\mu\text{m}$ ) the mean difference is  $3.0\% \pm 9\%$  at  $1\sigma$ . It must be kept in mind that even at these diameters neither inlet is sampling representatively. Above a micron the CCN inlet shows a pattern of greater enhancement driving the comparability of the inlets away from unity. The mean difference between 1.0 and  $10\text{ }\mu\text{m}$  is  $46\% \pm 42\%$  at  $1\sigma$ . The divergence between the two inlet enhancements increases with size. These comparisons suggests that where submicron aerosols are being sampled, data from instruments operated behind these inlets can be compared and those data used to derive secondary products, assuming the sample losses are equal or corrected appropriately.

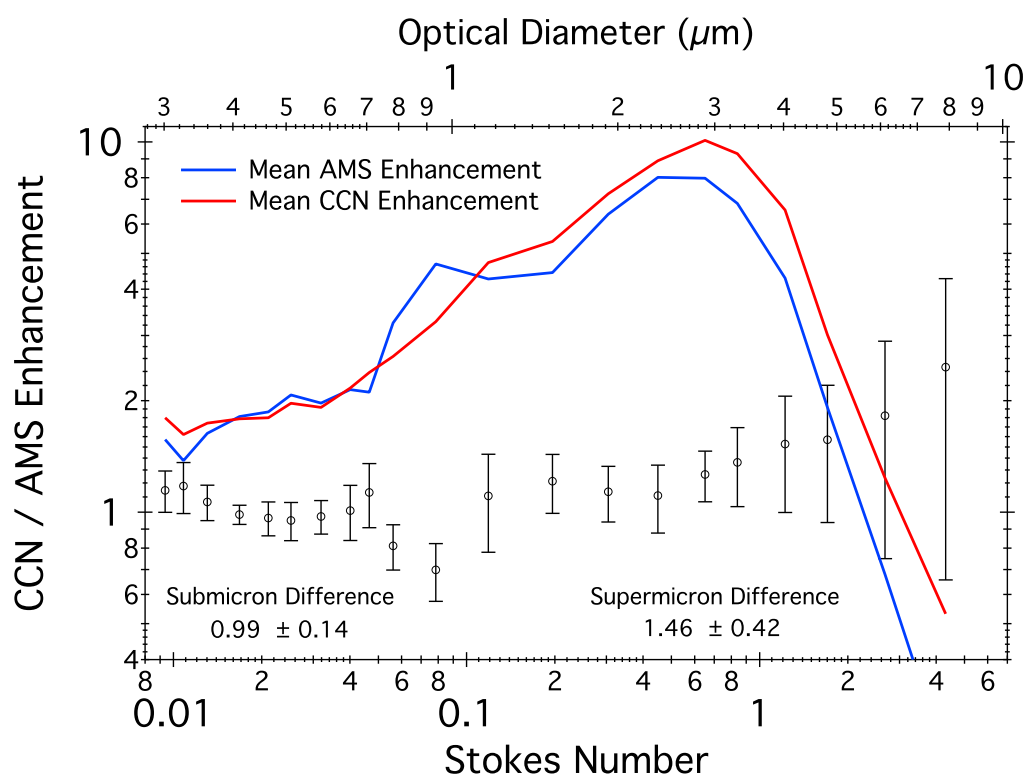


Figure 2.36: The mean inlet enhancements for the two Rosemount inlets (AMS in blue and CCN in red) and the difference between them (open circles) for all flights during the Fennec campaign over the Sahara in 2011 where the LTI was operating isokinetically ( $1.0 \pm 0.25\%$ ).

Figure 2.37 compares the inlet sampling efficiency of the CCN Rosemount from a flight in the North Sea, UK, during the summer of 2011, with those data collected over the northern Sahara. For ease it is assumed that this outflow from the UK is comprised of ammonium sulphate. Therefore a density of  $1769 \text{ kg m}^{-3}$  was used for all calculations and the particles were considered to be aqueous and therefore spherical. The major finding from the N.Sea data is that the inlet efficiency is maintained at approximately one below Stokes numbers of 0.02 (RI corrected optical diameter for the assumed composition of  $0.6 \mu\text{m}$ ) for all altitudes (75 to 1000 m), TAS, between  $107 \text{ ms}^{-1}$  and  $110 \text{ ms}^{-1}$  and angle of attack (AOA) which varied between  $5.8^\circ$  and  $6.3^\circ$ . A second trend is also evident in these data, the N.Sea aerosol inlet efficiency is distinctly bimodal with modes centred at

Stokes numbers of 0.07 and 0.4, RI corrected optical diameters of  $1.17\,\mu\text{m}$  and  $2.8\,\mu\text{m}$ . Compared to dust, the UK outflow distribution has far less contribution from super micron particles. During this test flight the mean mixing ratio above a diameter of  $0.5\,\mu\text{m}$  was below  $1.0\,\text{cm}^{-3}$  even summing the counts for the whole ten minute SLR returns concentrations of only  $1.2\,\text{cm}^{-3}$  from the larger of the two diameter modes. As such these data are dominated by counting statistics errors and therefore only the data in the sub micron size range are considered significant here. The underlying processes that cause divergence in inlet behaviour between the two different aerosol compositions, seen in Figure 2.37, is investigated further using a set of empirical inlet efficiency models.

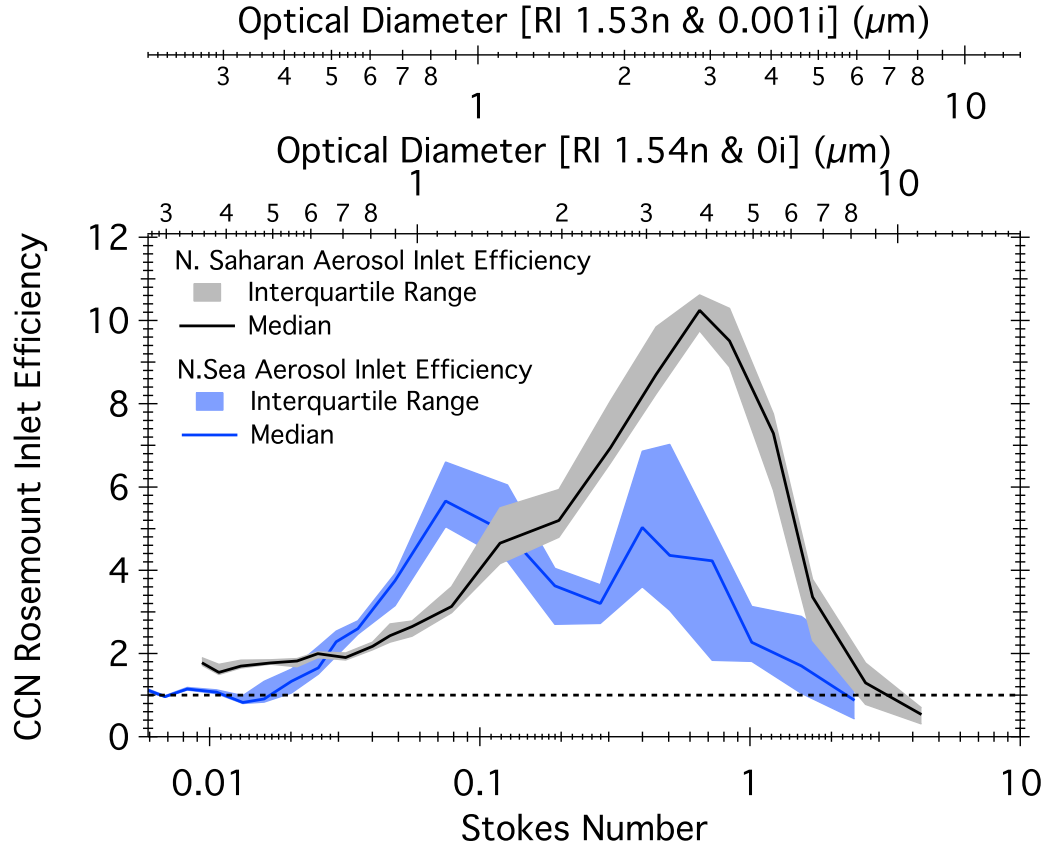


Figure 2.37: Comparison of two different aerosol compositions and the CCN inlet sampling efficiency for each. The black represents the data taken during the Fennec project, the blue represents data taken from one instrument test flight over the North Sea on June 14 2011. Both traces represent the median and the interquartile ranges of the RI corrected data collected. The dashed line represents an inlet operating isokinetically and sampling representatively.

The inlet efficiency ( $\eta_{inlet}$ ) can be modelled in the same manner as the transport losses in Section 2.2.2 and the subsampled losses in this section, where

$$\eta_{inlet} = \eta_{asp}(\eta_{transport} = \eta_{inlet,inert}\eta_{inlet,grav}). \quad (2.40)$$

Under the simplifying assumption that the Rosemount is a thin walled circular inlet. Anisoaxial inlet, referring to an inlet whose incident free stream angle is not zero, aspiration ( $\eta_{asp}$ ) can be estimated using the following equation from

(Hangal and Willike, 1990):

$$\eta_{asp} = 1 + \left[ \left( \frac{U_0}{U} \right) \cos\theta - 1 \right] 1 - \frac{1 - [1 + [2 + 0.617(\frac{U_0}{U})]\overline{Stk}]}{1 - [1 + 2.617\overline{Stk}]^{-1}} [1 - [1 + 0.55\overline{Stk} \exp(0.25\overline{Stk})]^{-1}], \quad (2.41)$$

where

$$\overline{Stk} = Stk \exp(0.022\theta) \quad (2.42)$$

and  $U$  is the velocity in the inlet,  $U_0$  the velocity in the free stream, equal to TAS,  $\theta$  is the incident angle between inlet and the free stream and  $Stk$  is the Stokes number as in Equation 2.23 on page 90. As is the case with the LTI subsampler, itself a form of inlet, described in Equation 2.35 if the ratio  $\frac{U_0}{U}$  increases the inlet becomes more subisokinetic and enhancement increases at smaller Stokes numbers or particle diameters. This model has been tested under the following envelope:  $0.02 \leq Stk \leq 4$  and  $0.5 \leq \frac{U_0}{U} \leq 2$  and  $0^\circ \leq 60^\circ$ . As seen in the Rosemount inlet efficiency curves the aspiration is the process that drives enhancement. This process will not continue unchecked but will asymptote at some particle diameter. However, the process of aspiration alone does not capture all the processes in the inlet head. As in the inlet experiment the loss functions will dominate above a certain diameter, as such they must be estimated. The gravimetric losses in the Rosemount inlet housing can be estimated from the following empirical relationship:

$$\eta_{inlet,grav} = \exp[-4.7K_\theta^{0.75}] \quad (2.43)$$

where

$$K_{\theta} = Z_{grav}^{0.5} Stk^{0.5} Re^{-0.25} \cos\theta \quad (2.44)$$

and

$$Z = \frac{L}{d} \frac{V_{ts}}{U}, \quad (2.45)$$

$Z_{grav}$  is gravitational deposition parameter,  $L$  is the length of the inlet measured as the distance from the front of the inlet to the first right angle as 0.049 m,  $d$  the diameter of the inlet, measured as the smaller of the two rectangular dimensions at 0.013 m,  $V_{ts}$  is the settling velocity from Equation 2.21 on page 90 and  $U$  the sampling velocity (estimated). This model holds under the following criteria:  $0.02 \leq Stk \leq 4$  and  $0.5 \leq \frac{U_0}{U} \leq 2$ . The inertial losses in the Rosemount inlet can be estimated using the empirical relationship in Equation 2.37 on page 105 with the addition of a direct loss impaction term,  $I_w$  to the *vena contracta* losses term,  $I_v$ . The model holds under the following regime:  $0.02 \leq Stk \leq 4$  and  $0.25 \leq \frac{U_0}{U} \leq 4$ , and

$$I_w = Stk \left( \frac{U_o}{U} \right)^{0.5} \sin(\theta + \alpha) \sin\left(\frac{\theta + \alpha}{2}\right) \quad (2.46)$$

and

$$\alpha = 12 \left[ \left( 1 - \frac{\theta}{90} \right) - \exp(-\theta) \right]. \quad (2.47)$$

Equation 2.46 as highlighted is the expression of the direct loss impaction in the inlet. This is the only loss function strongly dependent on the orientation of the inlet. When the inlet faces up, gravitational settling moves particles away

from the walls, reducing impaction. The counter to this is also true. This orientation effect of direct loss impaction is incorporated into the empirical relationship by changing the sign of the ordinator in the final term from a positive to capture processes associated with downwards sampling (upward facing inlet) and negative when the sampling is in the upward direction.

These equations initialised with the parameterisations used here have been pushed beyond the limits of their applicability with regards to the velocity ratio and subsequently Stokes number. Most of these models maintain a modest velocity ratio envelope for physical reasons alone. It is difficult to generate the disproportionate flows required to investigate these relationships whilst generating aerosols in the laboratory. Using these models out of the bounds of their original studies is not unique. Kramer and Afchine (2004) evaluated isoaxial subisokinetic sampling using Equation 2.35 against a computational fluid dynamical model at velocity ratios and Stokes numbers lower than was applicable. Their findings suggested only minor modifications to the original model was needed to capture the behaviour at lower extremes of both Stokes number and velocity ratios. Since these models are being used here to investigate process difference between two sets of measurements and not to create a unified model for Rosemount sampling, pushing the boundaries of their applicability was considered an appropriate assumption. As with previous sections the equations stated here have all been coded into IGOR Pro to create a model. Once initialised with pressure, temperature, velocities and particle diameters the model can be run and will output the total inlet efficiency and the component process as well.

The model outputs in Figure 2.38 are underpinned by a number of assumptions: the inlet is thin walled, the inlet is circular, the small holes in the Rosemount housing to prevent boundary layer development have no effect on any modelled process and the particles are all spherical. These assumptions aside the



models can be used to elucidate the processes that result in the different efficiency curves seen in Figure 2.37 between the dust dominated and the North Sea aerosol.

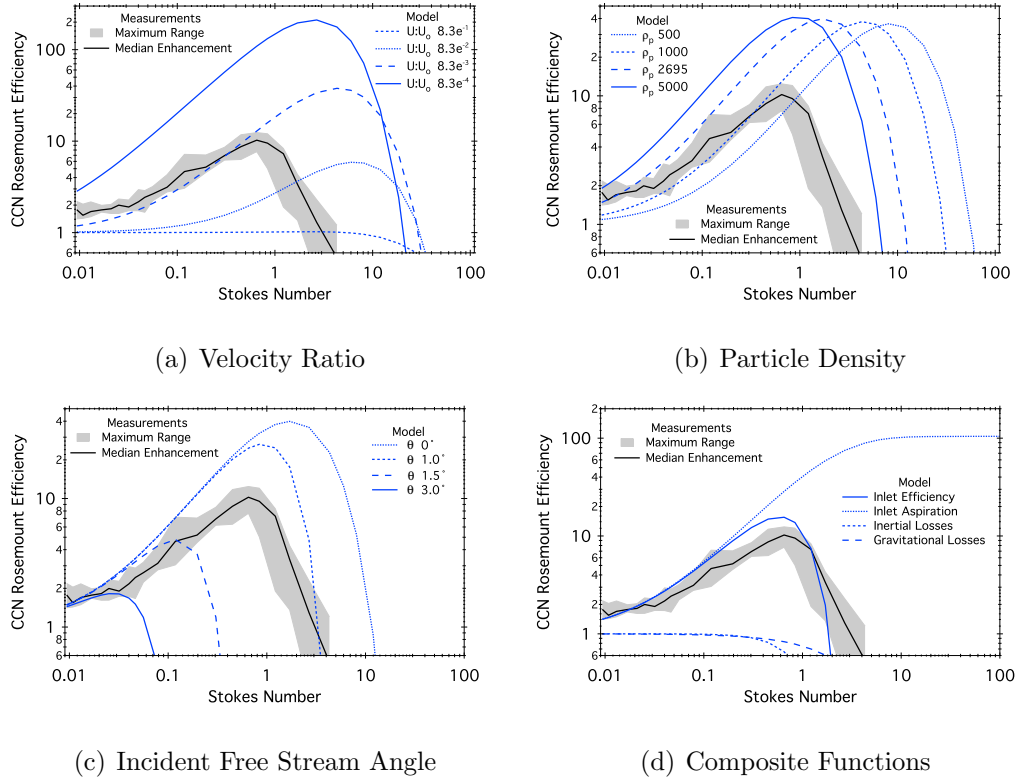


Figure 2.38: CCN Rosemount inlet efficiency measurements and model outputs for inlet aspiration efficiency and loss functions for a circular thin walled inlet as calculated from Equations 2.41, 2.43 and a modified version of Equation 2.37. The initialisation parameters for each graph are different and increase in prescription from left top to bottom right. 2.38(a) is initialised with a pressure of 900 hPa, a temperature of 300 K all the model runs had these values as state parameters, an incident angle ( $\theta$ ) of  $0^\circ$  and particle density ( $\rho_p$ ) of  $1000 \text{ kg m}^{-3}$  and the velocity ratio ( $U : U_0$ ) was varied. 2.38(b) had a  $U : U_0$  of  $8.3 \times 10^{-3}$ , all subsequent parameterisations used this value,  $\theta$  of  $0^\circ$  and a variable  $\rho_p$ . 2.38(c) had a  $U : U_0$  of  $8.3 \times 10^{-3}$ ,  $\rho_p$  of  $2695 \text{ kg m}^{-3}$  and varied  $\theta$ . The final graph 2.38(d) shows all the composite functions at 900 hPa, 300 K,  $U : U_0$  of  $9.6 \times 10^{-3}$ ,  $\theta$  of  $0.7^\circ$  and  $\rho_p$  of  $2695 \text{ kg m}^{-3}$ . These plots should not be compared without noting the ordinates have different scalings.

Figure 2.38(a) shows clearly how the velocity ratio, controlled in these models by assuming greater deceleration in the inlet head and not an increase in the free stream, controls the subisokinetic nature of the inlet and therefore its enhance-

ment (Belyaev and Levin, 1974; Hangal and Willeke, 1990; Hangal and Willike, 1990; Hinds, 1999; Kramer and Afchine, 2004; Willeke and Baron, 2005). Increasing the deceleration in the inlet; increases the maximum enhancement (controlled by the inlet aspiration efficiency Figure 2.38(d)), increases the slope of the aspiration efficiency and subsequently reduces the Stokes number at which the maximum enhancement occurs. The specific deceleration in these Rosemount inlets is unknown but based on these model iterations a value of 0.0083 was taken for subsequent model runs. This value is not unrealistic, Kramer and Afchine (2004) undertook a similar modelling exercise with four aerosol inlets operated on the German Aerospace Centre (DLR) falcon. The velocity ratios of these inlets ranged from 0.2 to 0.007, though these inlets were on a faster platform and the modelling undertaken at a lower pressure they have been specifically designed to sample aerosol and therefore maximising the operational velocity ratio should be one of their primary design criteria.

This chosen velocity ratio produces an inlet efficiency of 1.18 at a Stokes number of 0.009, for particles with the density of  $1000 \text{ kg m}^{-3}$ . This initial enhancement can be modified by changing the density of the aerosol iteratively from half of that of water to a density indicative of a metal oxide (approximately  $5000 \text{ kg m}^{-3}$ ), Figure 2.38(b). An increase in density increases the initial enhancements from 1.09 to 1.9 in the lowest to the highest density models. An increase in density also reduces the Stokes number at which the maximum enhancement occurs, this is because the inertial loss functions as well as the aspiration are density dependent. This density dependence of these models goes some way to explaining how in Figure 2.37 the same inlet can have such different values at low Stokes numbers. This function of the aerosol density is exacerbated at greater values of inlet deceleration. In fact it is possible for inlets on high speed aircraft to operate as virtual inlets where the deceleration is almost complete, Rosemount

inlets on the BAe-146 do not operate in this way, a virtual inlet has a very distinct signal where at low Stokes numbers the sampling efficiency is zero, this rises to a maximum of one in a sigmoidal fashion where the efficiency asymptotes at larger particle diameters (Kramer and Afchine, 2004).

These first two graphs in Figure 2.38 show the inlet system's sensitivity to velocity and particle density, however none of these model iterations capture the onset of the loss functions at small enough Stokes numbers. An anisoaxial inlet would explain this increased rate in the loss functions. Figure 2.38(c) iterates an increasing deviation from isoaxial conditions. This increase in angle away from the horizontal effects all functions, it reduces the maximum aspiration efficiency and increases the number of particles lost at any given Stokes number above 0.03. The loss functions at low Stokes numbers, those particles with minimal inertia are unaffected by a change in  $\theta$  of less than  $3.0^\circ$ . The exact value to which the inlet is misaligned is not known and can't be readily estimated without some exhaustive CFD modelling that includes a 3D model of the aircraft frame. However what this model run does demonstrate is the sensitivity of the Rosemount inlets as defined by these models to aircraft angle of attack (AOA), specifically for those particles with larger Stokes numbers. AOA is constantly varying during flights and is dependent on aircraft weight, altitude and TAS. In any given flight the AOA may vary by up to two degrees during SLRs. Figure 2.38(d) shows a plot of all the functions included in the model, showing the interaction between them. No optimisation procedures have been attempted with the initialisation parameters and yet the shape of the inlet efficiency curve is well matched even in this non-idealised solution, suggesting with a little further work a model of inlet efficiency could be achieved.

In conclusion, these inlets are still not fully characterised, but it has been shown here that in a UK outflow, an aerosol composition commonly sampled,

that they measure in a representative manner below  $0.6\ \mu\text{m}$  and that in the dense dust rich aerosol of the Sahara two different Rosemount inlets measure in a similar manner below  $1\ \mu\text{m}$ . In this dense aerosol the sampling is not representative and aerosol mixing ratios will be enhanced even at the lower end of the measured distribution. The similarity in sampling between the AMS and CCN Rosemount inlets in the submicron regime does show that data from instruments sampling on these two inlets can be compared and used to derive secondary information. It has also been shown using two different aerosol compositions that an inlet has its own specific efficiency curves for each aerosol type, something that is important for future projects. This work suggests that if new 'functional groups' of aerosol are to be sampled with these inlets then an inlet efficiency exercise should be undertaken to fully appreciate any sampling biases.

In summary of Section 2.2. Models of sample line losses have been created before (von der Weiden et al., 2009). The models in the literature, however, are not designed for use on aircraft and as such did not include the high velocity ratio right angle sampling from Brixey et al. (2005). The creation of the loss models and the detailed analysis of the sampling architecture has enabled sample transport losses in the system to be estimated. The losses in the accumulate mode are in between 1 % and 4 % for the whole system at all pressures investigated. These models have recently been verified by laboratory measurements. Without these loss estimates there would be no understanding of any possible bias between the CCNc and CPC measurements. This work has also highlighted that there are no excessive losses associated with the sampling of either instrument that would render the data useless. Rosemount inlet efficiency has been investigated once before. Petzold (2009) highlighted the enhanced inlet efficiencies on a single Rosemount inlet for a different aircraft. This work is the first to assess the Rosemount inlet capabilities on the BAe-146 and the first to investigate the

differences between multiple instances of the same inlet on one aircraft. It is also the first to attempt to model the inlets to gain in understanding in the effects of deceleration, particle density and AOA. The Rosemount inlets used to sample ambient aerosol on the BAe-146 have been found to enhance aerosol sampled in a dust dominated aerosol. It has been shown that two different Rosemount inlets enhance in a similar manner in the submicron regime. Allowing for comparison between instruments on different inlets and data derived from different instrument on different inlets. When operated in UK outflow aerosol the Rosemount inlets sampled representatively up to approximately  $0.6\text{ }\mu\text{m}$ . Models suggest that the discrepancies between the UK outflow and dust dominated aerosol is driven by a particle density dependency of the inlets. These models also suggest the inlet sufficiency is sensitive to incident angle of the free stream to the inlet. These findings are of the upmost importance for nearly all aerosol measurements taken on board the BAe-146. Without having prior knowledge of the initial sampling biases (at the inlets) of any aerosol measurement system then there can be no understanding what proportion of size range the measured data is relevant for.

Sections 2.1.1 to 2.2.3 provide an in-depth answer to the first major science question posed in this work, can an ‘off the shelf’ CCNc be used on a fast research jet, such as the BAe-146, to produce viable data sets? The detailed experimentation undertaken in this Section proves that the instrument can be used to produce viable datasets on the BAe-146.

## **2.3 Flying operations**

The CCNc and CPC instruments are operated in the same manner for all flights investigated in this work. Both instruments were warmed up between two and four hours before each flight. The CCNc water pump flow rate was set to high,

72 ml hr<sup>-1</sup>. The flow rate for each column was set to 0.5 lpm at a sheath to sample flow ratio of ten to one.  $T_{inlet}$  was allowed to drift with cabin temperature ensuring no data are lost if the sample entering the instrument is warmer than the top of the column, a possibility if the temperatures are set too low. The reduced pressure inlet is nominally set to 650 hPa. On certain occasions this was varied to investigate the possibility of higher altitude measurements. The instrument sampled exclusively through the aft inlet on the port aft Rosemount pair. Barring instrument failure the TSI 3786 CPC was always operated in conjunction with the CCNc. Each column supersaturation was set using the proprietary dual column CCN software (DMT inc, Boulder); the set point ranged between 0.1 and 0.5 % across all flights. On profiles where the ambient pressure dropped enough to ensure the sample line pressure dropped below 650 hPa the instrument was left running even though the reduced pressure inlet has no active bleed air to add to the system and maintain the set point pressure. The data from such portions of flights are not used. On descending back into the region of pressure control the data is not used for the following 180 seconds to ensure the column flows have re-stabilised.

Three other ancillary data sets from instruments routinely flown on the BAe-146 are used in Section 3. The Aerosol Mass Spectrometer (AMS) as described in Jayne et al. (2000) uses mass spectrometry to retrieve the mass loadings of non-refractory chemical components of the sub-micron aerosol, so any analysis using this data neglects any contribution from refractory particles; such as sea salt, black carbon or mineral species. This instrument employs thermal vapourisation, electron impaction and ionisation at 70 eV and an orthogonal extraction reflection time of flight-of-flight mass spectrometer (Tofwerk model C-TOF, Thun, Switzerland). Mass concentrations for sulphate, nitrate, ammonium, chloride and organics are reported at 30 second intervals following the procedure of Al-

lan et al. (2003) with relative uncertainties of  $\pm 34\text{-}38\%$  (Bahreini et al., 2009). Component mass size distributions can be derived from the AMS if the aerosol loadings are high enough to ensure a signal to noise ratio greater than 1.5, this is not the case for all the data sets used here (Allen et al., 2011).

The Scanning Mobility Particle Sizer (SMPS) measures submicron aerosol size distributions between  $0.01$  and  $0.6\text{ }\mu\text{m}$  as described by Wang and Flagan (1990). The instrument consists of a long DMA column (TSI, 3081) and a modified low pressure 3786 CPC (TSI) the sheath flow of which is recycled in a loop. The relative humidities of the sheath flow are controlled by the ambient humidity and are usually between  $20$  to  $30\%$  and always less than  $60\%$  (P.Williams personal communication, 2010). Unlike a DMA set up with a constant electric field the SMPS collection rod voltage is varied in a monotonic fashion, creating a scan of particle diameters counted by the CPC. The first scan is a  $45$  second up scan followed by a  $15$  second down scan, giving a total integrated measurement time of  $60$  seconds.

The cloud droplet probe (CDP, DMT inc, Boulder, Co) uses a  $0.66\text{ }\mu\text{m}$  diode laser to count and size individual water droplets with a  $0.24\text{ mm}^2$  sample area, the instrument reports binned droplet size distributions in the range of  $2$  to  $50\text{ }\mu\text{m}$  at  $1\text{ Hz}$  frequency (Lance et al., 2010).

All CCNc data collected during a flight undergo an interactive quality assurance process (QA). Calibrations are applied to the flow, pressure and supersaturation as discussed in this chapter. All CCN concentration data are then density corrected, and flagged appropriately with a binary system of 'good' and 'bad' data. These 'bad' flags are generated from housekeeping data where; the flow deviates by more than  $10\%$  from the set point, the sheath to sample flow ratio deviates by more than  $0.3$ , the supersaturation drops below the minimum threshold of  $0.07\%$ , the ambient pressure is lower than the CCNc pressure or

where sharp pressure spikes and slow insidious pressure increases or decreases occur (symptomatic of leaks), where the inlet temperature changes the following 30 seconds of data are flagged and where the temperature gradient collapses ( $T1 \not\approx T2 \not\approx T3$ ).



## Results and Discussion

### 3.1 Characterisation of Aerosol and Cloud Properties in the South Equatorial Pacific

The VOCALS-Rex project was a 2008 multi-national field experiment, incorporating multiple instrument platforms, ground based, ocean going and airborne, designed to increase the understanding of the Southern Equatorial Pacific (SEP) regional climate system. Interactions between the S.American continent and the SEP are important for both regional and global climate systems. This region has the largest and most persistent subtropical stratocumulus deck on the planet. Stratocumulus decks are a common feature of coastal regions where cold upwelling of water reaches the ocean surface (Wood et al., 2011; Allen et al., 2011; Zheng et al., 2011; Bretherton et al., 2010). These upwellings are driven by a strong coastal jet formed by the blocking of zonal flow by the Andes Cordilla. These strong southerly surface winds drive Ekman transport, resulting in surface flow away from the continent. This divergence draws nutrient rich water up from deeper in the water column to replace the warmer nutrient depleted surface water.

The SEP region is part of the Humbolt current large marine ecosystem (LME).

This ecosystem provided between 16 and 18 % of the worlds marine fish catch, some 12 million tonnes. The fishery is estimated at 2000 prices to be worth US\$10 billion. The UN LME report (XVII-56 Humbolt Current: LME 13) considers climatic variability to be the primary driving force for changes in ocean biomass. Therefore understanding the process that controls this regions climate of economically importance.

The goal of this work is to use the CCNc and other instruments to determine the aerosol and cloud characteristics of the stratocumulus (Sc) deck and its environment. Thus providing parameters to initialise and validate models at all scales and complexities. It is at present a challenge for global and regional scale models to simulate the SEP system because of the sharp horizontal and vertical gradients that persist. Where controlling physical processes are both subgrid and poorly resolved. In general the occurrence, coverage and depth of SEP marine stratocumulus is poorly represented in models.

The IPCC Fourth Assessment Report (Meehl et al., 2007) identified feedbacks associated with the radiative properties of clouds to be one of the larger uncertainties in estimating the effects of increasing green house gases on the current climate. The largest uncertainty highlighted in the same report was the indirect effect of anthropogenic aerosol on cloud microphysical properties and the resultant radiative forcing. Indirect effects of warm clouds also remain poorly treated in models. The CCN data used here provide a bridge between the aerosol and cloud microphysics so can help understand the processes involved in the Sc deck.

It was also deemed to be a perfect atmospheric laboratory to test the CCNc, as the aerosol chemistry can be considered a simple sulphuric acid - ammonia - water system (Seinfeld and Pandis, 2006) with only small contributions from organics, indicating a uniform composition of readily activated particles.

All data used in this study were collected during VOCALS, (Wood et al., 2011;

Allen et al., 2011), between the 26<sup>th</sup> October and the 13<sup>th</sup> November, 2008. 13 missions in total were flown; the flight track for those flights included here can be seen in Figure 3.1 and Figure 3.2. These plots show the latitudinal, longitudinal and vertical extent of the flights conducted during the project. A number of different mission strategies were undertaken in this period, only three of which are used in this analysis. This subset of the data can be seen in Table 3.1. A full description of the VOCALS project can be seen in Wood et al. (2011). All the data used here are collected from the FAAM BAe-146 aircraft. The amount of data available for the analyses was reduced by an OPC laser failure in column A of the CCNc on November 7, 2008.

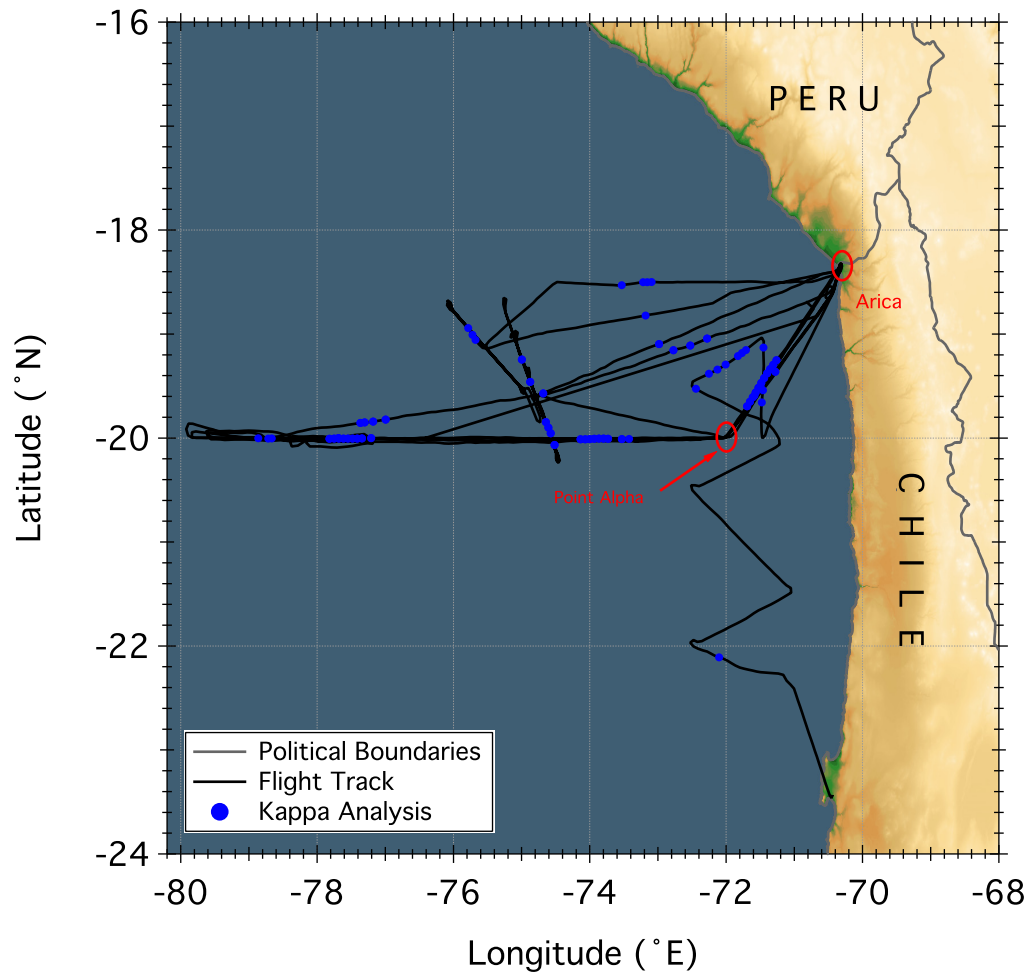


Figure 3.1: VOCALS flight tracks for the sorties in Table 3.1 used in the analysis. The operating base Arica can be seen on the Peru, Chile border. The grey lines are the political boundaries, the black the flight tracks and the blue closed circles those points where data was included in the  $\kappa$  analysis.

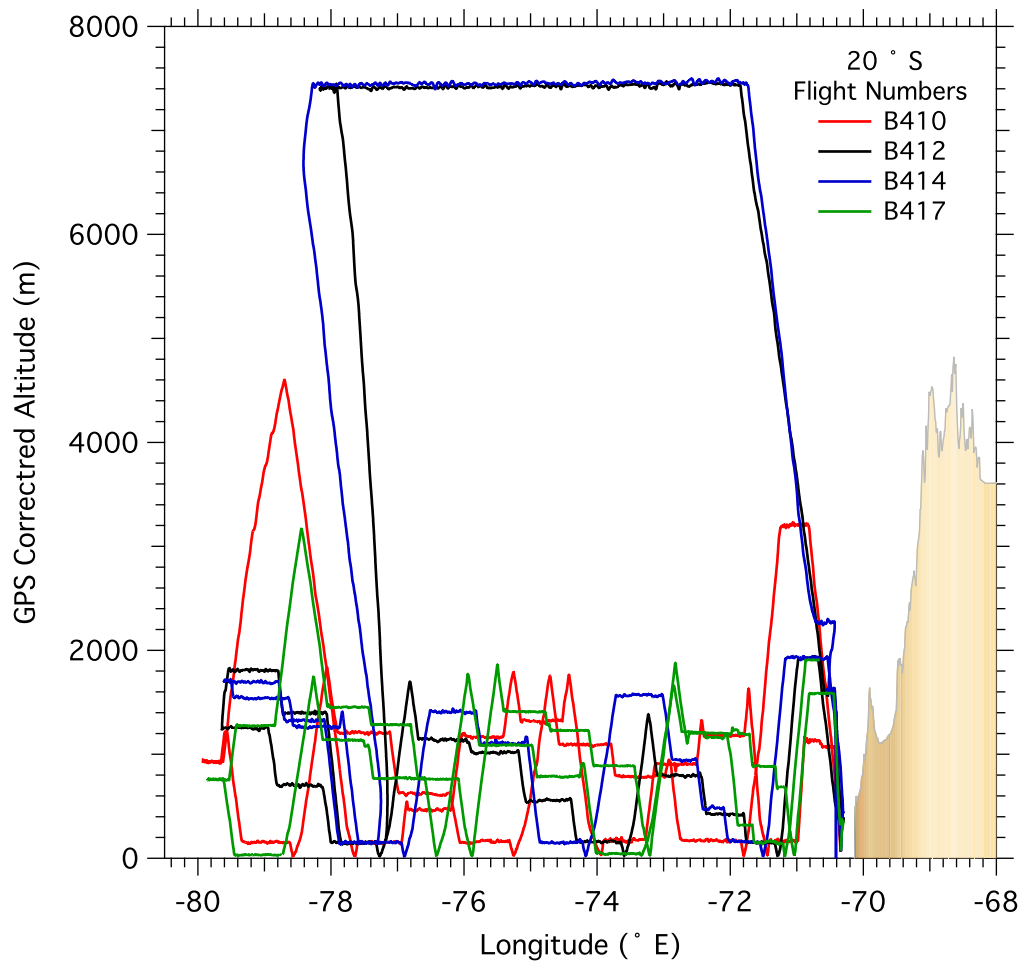


Figure 3.2: A schematic of the vertical and longitudinal extent of each flight from the VOCALS subset of sorties used in this analysis. Data is also shown in Table 3.1 and Figure 3.1. Each flight is given a different coloured line, B410 red, B412 black, B414 blue and B417 green.

Flight	Date	Times	[UTC]	Mission	Comments	Analysis
	2008	T/O	Land	Type		
B408	Oct 26	10:05	15:05	20° S	No SMPS data	N/A
B409	Oct 27	19:58	24:28	POC	Col. A and B	N/A
B410	Oct 29	09:59	15:16	20° S	Col. A and B	Stat/ $\kappa$ /Close/TDGA
B411	Oct 30	10:25	15:48	RHB	Col. A and B	Stat/ $\kappa$ /Close/TDGA
B412	Oct 31	09:47	14:52	20° S	Col. A and B	Stat/ $\kappa$ /Close/TDGA
B413	Nov 3	11:03	16:05	20° S	No CCN Data	N/A
B414	Nov 4	09:44	15:04	20° S	Col. B	Stat/ $\kappa$ /Close/TDGA
B415	Nov 5	09:12	14:33	POC	Col. A	N/A
B416	Nov 7	10:32	15:27	POC	Col. B	N/A
B417	Nov 9	09:58	15:23	20° S	Col. B	Stat/ $\kappa$ /Close/TDGA
B418	Nov 10	11:31	21:17	Pollution	Col. B	$\kappa$ /Close/TDGA
B419	Nov 12	11:29	16:51	RHB	Col. B	Stat/ $\kappa$ /Close/TDGA
B420	Nov 13	11:31	21:17	20° S	No CCN Data	N/A

Table 3.1: Details of the VOCALS sorties as flown by the BAe-146 and the flights whose data are used in this analysis. Comment is given on those flights where data is not included and the reason for exclusion. 'No CCN data' refers to one or more columns being operated below the minimum threshold after pressure corrections.

The three mission types used in this analysis are; *(i)* 20° South (20° S) missions, cross section transects travelling west from point Alpha (72° W 20° S) to 80° W designed to sample longitudinal gradients of cloud microphysics and characterise the aerosol and chemistry of the marine boundary layer (MBL); *(ii)* the Ronald H Brown research ship co-sampling mission (B411 and B419 on 30<sup>th</sup> October and 12<sup>th</sup> November, respectively), the first sector of which was analogous to a 20° S missions and *(iii)* a pollution study (B418 on 10<sup>th</sup> November). B418 has been included in the  $\kappa$ , CCN closure and TDGA analyses only and was excluded from longitudinal and vertical characterisation study.

The MBL in this region is generally deeper offshore (1600 m at 85° W), with

more variability in its properties and a greater decoupling, where the MBL is not well mixed across its entire altitude range, than at longitudes closer to the coast. At the coast the MBL shrinks, typically to an altitude of 1000 m where the mixing is complete (Bretherton et al., 2010; Rahn and Garreaud, 2010; Zheng et al., 2011). Allen et al. (2011); Bretherton et al. (2010); Zheng et al. (2011) showed back trajectories for the MBL with low altitude winds from the South and South West. At  $20^{\circ}$  S  $72^{\circ}$  W these back trajectories had contact exclusively with the Chilean coast at some point in the previous five days. These winds are the primary mechanism for transporting pollutants from the continent. Back trajectories at  $20^{\circ}$  S  $85^{\circ}$  W, however, had no contact with the coast in the previous five days in the FNL model used in Bretherton et al. (2010). The majority of these trajectories at this latitude and longitude in Allen et al. (2011) also missed the coastal sources resulting in lower levels of the pollutants being exported to the more remote longitudes. Diurnal variations are not considered here as Allen et al. (2011) showed there is a greater variability in the data between flights than between the morning and afternoon of any given day.

### **3.1.1 Longitudinal Structure**

The boxplots in Figure 3.3 and the analysis in this section only include data from the flights labelled as ‘Stat’ in Table 3.1. This Section, 3.1.1 Longitudinal Structure and the following Section, 3.1.2 Vertical Structure have been subdivided into three categories; gas and aerosol properties (pages 134 and 160), size distribution characteristics (pages 145 and 166) and cloud properties (pages 156 and 169).

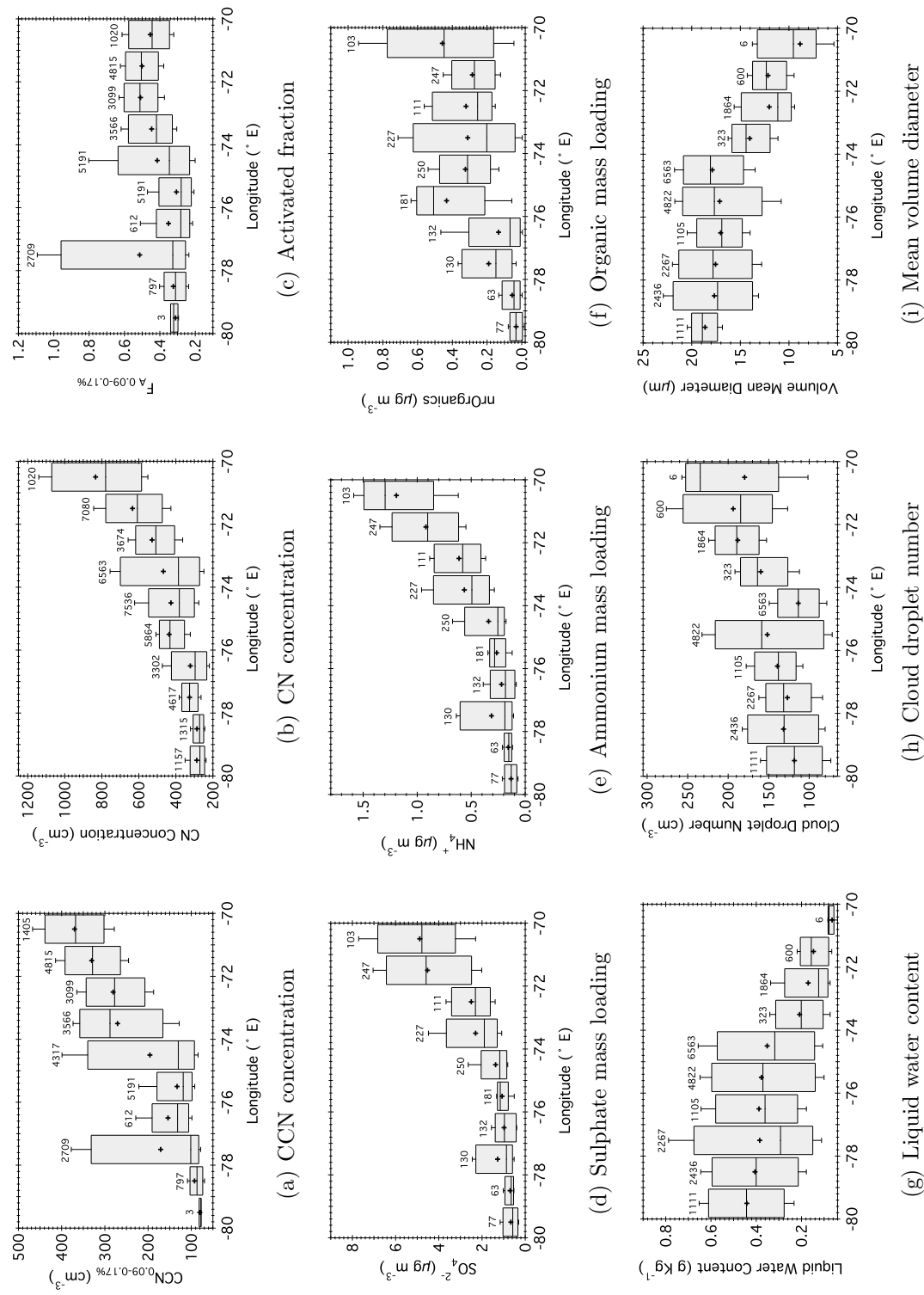


Figure 3.3: Longitudinal gridded descriptive statistics for aerosol and cloud microphysics parameters. Whiskers represent the interdecile range, the box extremities the interquartile range, the middle bar the median and the crosses the mean. The numbers above each box are the number of samples.



## Gas and Aerosol Properties

The top row of Figure 3.3 shows the aerosol measurements sampled from the CCN Rosemount inlet namely CCN and CN concentrations (graphs 3.3(a) and 3.3(b)). Both parameters show an overall decreasing trend with longitude. The source for these higher concentrations is the Chilean coast, as described by the boundary layer back trajectories (Bretherton et al., 2010; Allen et al., 2011). Mean CCN particle concentrations fall from a maximum of  $370 \text{ cm}^{-3}$  down to  $80 \text{ cm}^{-3}$ , the rate of decrease in concentration is greatest between  $70^\circ$  and  $75^\circ \text{ W}$ . This period of greater dilution with longitude is matched in the CN between  $70^\circ$  and  $76^\circ \text{ W}$ , with the maximum mean particle concentration of  $833 \text{ cm}^{-3}$  closest to the South American continent, and a minimum at  $80^\circ \text{ W}$  of  $287 \text{ cm}^{-3}$ .

CN concentrations show an 80 % incidence of negative skew, where the median is lower than the mean suggesting that a few larger concentrations have some effect on mean values and that these populations are not normally distributed. There is a greater prevalence of skew closer to the South American continent, the major source for particulates, a pattern that is also visible in the concentration of carbon monoxide (CO). When correlated to particle number CO can be utilised as a tracer of combustion for both fresh and aged biomass burning and urban plumes. The increased variability in both particle numbers and CO close to the coast is indicative of the variability in the emission strength from coastal sources. Allen et al. (2011); Kleinman et al. (2012) both showed a clear longitudinal gradient in CO similar to that seen here for CN and CCN number concentrations. Both studies also showed a reduced variability and a more normal distribution (in concentration probability density functions) indicating an absence of sources and a stable background level further from the coast. The high variability in coastal longitudes is exemplified in the sulphur dioxide concentrations, where the mean boundary layer values range between 20 and 30 ppt (Allen et al., 2011) and the

upper decile at  $70^\circ$  W exceeds 140 ppt suggest high concentration episodic events. The skew in these  $\text{SO}_2$  data extend out to the westerly edge of the transect though the concentrations decrease. The sporadic nature of these events is indicative of discrete elevated  $\text{SO}_2$  episodes primarily released into the free troposphere (FT) by the coastal smelters in Chile and Peru (Allen et al., 2011; Kleinman et al., 2012). Probability distribution functions of these MBL data suggest that the  $\text{SO}_2$  is dynamically mixed from the FT.

The activated fraction (graph 3.3(c)) has a slightly more complex relationship with longitude where close to shore the median value is lower than in the next two bins. This is because a larger proportion of the aerosol is fresh and therefore of a smaller diameter than the critical diameter for activation to a CCN. This is further evidence that the major aerosol source is correctly attributed to the Chilean coast. This fraction reduces from a maximum of 0.51 at  $73^\circ$  W with some fluctuation to 0.3 at  $80^\circ$  W, showing the potential effect of anthropogenic aerosol sources on cloud microphysics. Both the CCN and activated fraction are subsets of the entire data set used in this work. To enable comparison across latitudes data were only used where the CCNc effective supersaturation was between 0.09 and 0.17 %. To include data with an effective supersaturation of 0.4 % for example would weight those latitudinal bins containing this data to much higher concentrations making them incompatible to those bins that only contained data recorded at 0.17 %. With respect to the activated fraction there appears to be two distinct regions with a threshold somewhere at  $75^\circ$  W; a population with a median value above 0.4 closer to the coast and a second with an average below 0.4 from  $75^\circ$  W to  $80^\circ$  W. The overall trend in these aerosol measurements on the top row of the panel is a reduction in concentration out to a boundary at  $75^\circ$  W west of which are fluctuating lower concentration and activated fractions.

The middle row of the panel show mass loadings of non-refractory aerosol

as measured by the AMS. Of all the parameters measured, sulphate ( $\text{SO}_4^{2-}$ ), graph 3.3(d), shows the strongest response with increased distance from the coast. Again this is due to the proximity of the main source, the South American continent, shown by the correlation with CO concentrations (Allen et al., 2011). The mass loadings drop from a mean of  $4.9$  to  $0.7 \mu\text{g m}^{-3}$  across the whole transect. The rate of this decrease is at its highest between  $72^\circ$  and  $75^\circ$  W with the loadings in the four most remote longitude bins being comparable between  $0.7$  and  $1.0 \mu\text{g m}^{-3}$ . These constant low values and the back trajectories in the remote environment suggest a marine source for the sulphate from the oxidation of dimethyl sulphide (DMS) and methyl sulphonic acid (MSA) (Allen et al., 2011).

The ammonium ( $\text{NH}_4^+$ ) loadings (graph 3.3(e)) show a similar trend decreasing from the median coastal maxima of  $1.3$  to  $0.13 \mu\text{g m}^{-3}$  at  $76^\circ$  W, the rate of decrease collapses in the most remote bins where loadings fluctuate between  $0.13$  and  $0.18 \mu\text{g m}^{-3}$ . There is an overall decreasing trend in the variability of these two inorganic mass loadings with distance from the coast.

There is, however, slightly more variability in the organic (graph 3.3(f)) mass loadings with a distinct lack of trend in the mean values in the first six longitudinal bins to  $76^\circ$  W. Over the entire transect the organic mass falls with increasing longitude West, however, unlike with the inorganic ions this trend is not monotonic in its nature. In the first six longitudinal bins the mass loadings initially fall from a maximum mean value of  $0.46 \mu\text{g m}^{-3}$  at  $70^\circ$  W to  $0.28 \mu\text{g m}^{-3}$  at  $71^\circ$  W. The loadings then fluctuate between  $0.28$  and  $0.32 \mu\text{g m}^{-3}$  out to  $75^\circ$  W where the loadings increase to  $0.43 \mu\text{g m}^{-3}$  at  $76^\circ$  W. Like  $\text{SO}_4^{2-}$  and  $\text{NH}_4^+$ , organic loadings are lowest in the final four degree bins with masses between  $0.19$  and  $0.032 \mu\text{g m}^{-3}$ . Results by Hawkins et al. (2010) show organic concentrations close to the coast to be correlated with radon, sulphate and crustal elements of calcium, iron and potassium and elements associated with heavy industry includ-

ing sulphur, vanadium, bromine, nickel and tin. However, carboxylic acid had a strong negative correlation with sulphate loadings suggesting an external mixture of these two components. These coastal organic sources were mixed with marine sources, almost exclusively west of 74° W, the marine organics were themselves a mixture of biogenic and ship emissions and were characterised by those regions with low mass loadings, as low as  $0.2 \mu\text{g m}^{-3}$ .

It is from these six graphs, and the back trajectory information discussed earlier, that the envelopes for three longitudinal zones used through out this work were set. These zones will be used to contrast aerosol, gas, cloud and aerosol distribution properties.

The high sulphate zone, between 70° and 72° W is the region of high  $\text{SO}_4^{2-}$  loadings and aerosol particle concentrations greater than  $600 \text{ cm}^{-3}$ , defined by O'Dowd et al. (2001) as modified maritime air, where back trajectories come solely from the coast to the South.

The falling sulphate zone between 72° and 76° W, is a region characterised by decreasing  $\text{SO}_4^{2-}$  and  $\text{NH}_4^+$  and aerosol particle concentrations between 600 and  $400 \text{ cm}^{-3}$  but still a relatively high organic loading. This zone incorporates the region at which the coastal influence decreases, at 75° W, as quoted from the back trajectories of Bretherton et al. (2010) and also seen in Figure 3.3.

Finally the low sulphate zone between 76° and 80° W is the most remote from the coast characterised as a region of low aerosol mass and low aerosol number concentration; less than  $330 \text{ cm}^{-3}$ . This is considered to be sufficiently close to the value of  $200 \text{ cm}^{-3}$  in the accumulation mode defined by Twohy et al. (2005) as clean maritime. This most distant of regions is the most disconnected in terms of coastal sources as highlighted by the back trajectories.

The justification for choosing these longitude boundaries is from an aerosol

composition and number perspective only. These are not the same zones used in Allen et al. (2011). Where the Coastal Zone reached from 70° to 75° W, Intermediate Zone from 75° to 80° W and Remote Zone from 80° and 85° W. These zones were chosen with a decidedly more sophisticated logic incorporating specific back trajectories for air mass history. Hawkins et al. (2010) used radon as a tracer for land contact and identified three air mass encountered during the RH Brown cruise; continental air masses (radon concentration  $> 350 \text{ mBq m}^{-3}$ ), none of which travelled west of 78.2° W, maritime air masses (radon concentrations  $< 250 \text{ mBq m}^{-3}$ ) none of which passed east of 74.6° W and mixed air masses (radon  $> 250$  and  $< 350 \text{ mBq m}^{-3}$ ), none of which passed to the east of 74.2° W. The data used here are not the same as is used in the study by Allen et al. (2011) which incorporates data from three aircraft platforms, one ship and two field stations. The data used here were solely measured using the BAe-146.

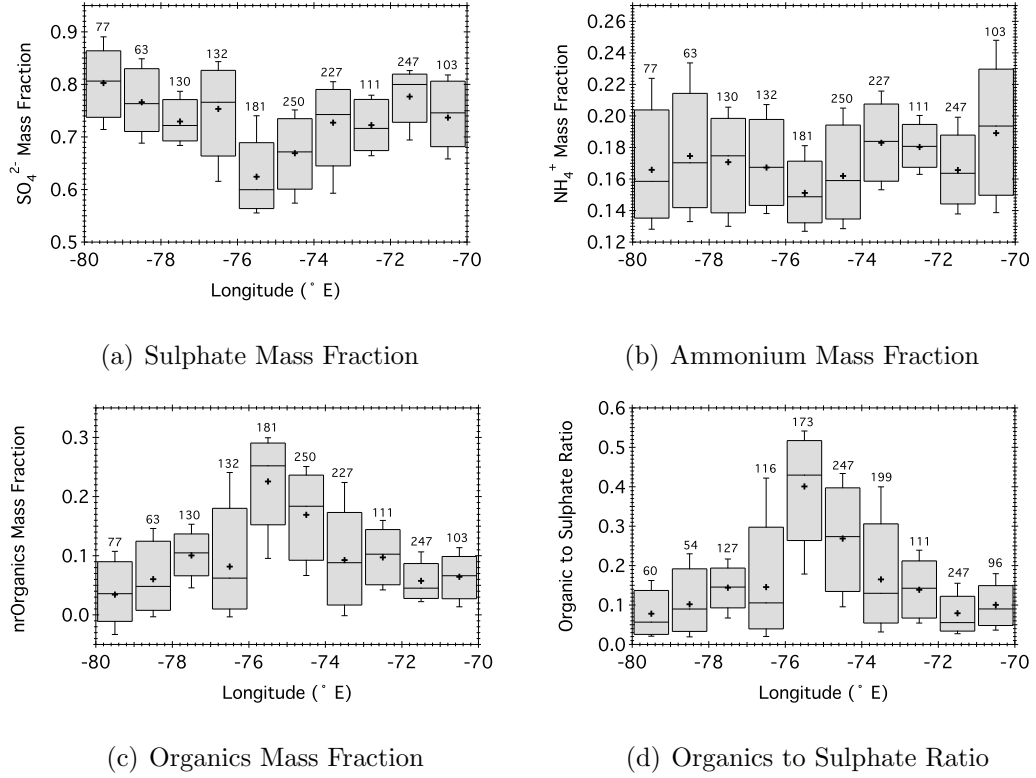


Figure 3.4: Longitudinal gridded descriptive statistics for sulphate and nitrate ions and non-refractory organic mass fractions from the VOCALS data set. These mass fractions ignore any contribution from ammonia, and chloride ions, on average these components make up a mean value of 4.5 % ( $\sigma$  2.8 %) of the total mass fraction. Graph 3.4(d) shows the longitudinal trend in organics to sulphate ratio an aerosol characteristic used to highlight differences in source.

Figure 3.4 shows the longitudinal trends in AMS mass fractions for sulphate, ammonium and organics. Chloride and nitrate ions have not been considered here and on average make up less than 5 % of the total aerosol mass for the entire VOCALS project. In reality nitrate concentrations were never recorded above the detection limit of  $0.05 \mu\text{g m}^{-3}$ .

Sulphate and organic mass fractions, graphs 3.4(a) and 3.4(c), have an inverse relationship to one another with sulphate dipping to a minimum of 0.62 at  $75^\circ \text{ W}$  from 0.74 at  $70^\circ \text{ W}$  recovering to 0.80 at  $80^\circ \text{ W}$ . Where as the mean organic mass fraction is 0.06 at  $70^\circ \text{ W}$  peaking at 0.23 at  $75^\circ \text{ W}$  and falling back to 0.03 at

80° W. This peak in the OMF and the organic to sulphate ratio is also seen in the RH Brown data incorporated in Allen et al. (2011) with a peak in the organic mass loadings between 76° and 79° W that does not correspond to an increase in the sulphate loadings. This mirroring in the two fractions is symptomatic of a negative correlation. Which could occur for two reasons; firstly if the aerosol was externally mixed with respect to the two components or secondly if the source type or balance changes with longitude.

If the aerosol were internally mixed and the source stable in composition and location (assuming a constant wind direction) the correlation between sulphate and organics would be a positive one similar to the relationship between ammonium and sulphate mass fractions. When the mass of a particle increases so does the mass of the constituent parts of that particle, within reason as particles may be quasi-internal mixtures. There is an identified external mixture in the VOCALS region data set, it was identified primarily by a decreased collection efficiency to an organic and dust fraction in the AMS on-board the RH Brown. As such it is unlikely that it would cause this increase in signal in the AMS data due to the refractive core. This negative correlation is more likely to be a function of the aerosol source.

The first possible difference in source is from local shipping, the fact that the two longitudinal bins with enhanced organic to sulphate ratio include the data from the RH Brown co-sampling flights B411 and B419 suggest that these enhanced ratios could be due to the inclusion of ship emissions in the measurements. This can be discounted for a few reasons; both flights had their SLRs orientated into and away from the mean wind direction centred on the ship and there is no difference in this ratio up or down wind of the ship. None of the co-sampling SLRs had any significant correlation between CO as would be expected with a combustion source, the data from B411 had the lowest CO concentrations of the

flights used in this analysis. Both flights also had different organic to sulphate ratios. This is inconsistent with the same fuel being used in the same engines and the same output and finally the same organic to sulphate ratio seen in B419 is also encountered during B412 and to some extent B410 flights separated by 12 days. The final three arguments are represented in Figure 3.5 which shows at least two regions of elevated organic to sulphate ratio associated with two different CO concentrations that appear to not match the remainder of the data, both sampled during RH Brown co-sampling.

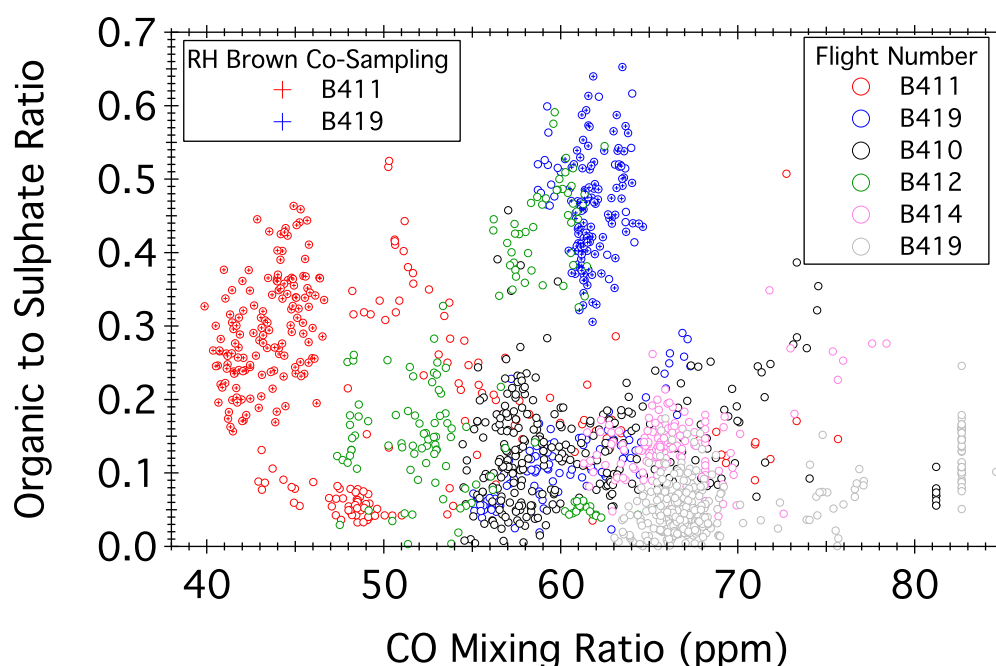


Figure 3.5: Relationship between organic to sulphate ratio and carbon monoxide concentration for all flights included in the longitudinal survey. Flights that co-sampled with the RH Brown are picked out with crosses as well as open circles. Colours of open circles represent individual flights.

Shank et al. (2012) used this organic to sulphate ratio and the association with black carbon measurements from an single particle soot photometer (SP2) instrument on the NCAR C-130 to show how low the contribution of marine organics, as measured by the AMS, is to the submicron organics over the SEP.



Most of the organics in this study correlated well with black carbon suggesting a common combustion source. At the least polluted longitudes, however, there was no correlation between sulphate and black carbon suggesting a marine source for the sulphate. Above the MBL the FT has a higher organics and lower sulphate ratios particularly in the mid longitudes of the transect. Entrainment of this air would increase the organics whilst diluting the sulphate loadings. Component analysis of filters from the RH Brown indicates that much of the organic mass originates from Santiago. The peak in organic mass fraction and organic to sulphate ratio in Figure 3.4(d) is between  $75^{\circ}$  and  $76^{\circ}$  W the back trajectories from Allen et al. (2011) and Hawkins et al. (2010) suggest air masses at this longitude also originate from the Santiago region of Chile. The trajectories further to the east on the  $20^{\circ}$  S transect make contact with the land but further north and those trajectories to the West have little or no contact with the land. In contrast ammonium mean mass loadings have a more subtle trend with their mass fraction falling to a minimum at  $75^{\circ}$  W, beyond this longitude the mass fraction recovers. None of the AMS measured aerosol loadings had high enough signal to noise ratio to size resolve single particle composition.

Figure 3.6 shows the relationship of the mole mass ratio (MMR) between ammonium and sulphate as measured by the AMS. Some understanding of the neutrality of the aerosol can be interpreted from this measurement. The mean CCNc instrument relative humidity during this project was 33 % (with a standard deviation of 4 %), calculated using the Magnus equation by applying the drying associated with warming of the sample on entry to the aircraft. It has been assumed here that this is also true of the AMS data. In a simple system containing sulphuric acid, ammonia and water an MMR value of less than two indicates a lack of ammonium to fully neutralise the sulphate resulting in a potentially acidic aerosol, assuming there is no other species acting to buffer the

system. An MMR of two and the aerosol could be considered to be fully neutralised. If the MMR falls between these two extremes it can be assumed to be partially neutralised. In this simple system these MMR values relate to the dominant species, sulphuric acid ( $\text{H}_2\text{SO}_4$ ), ammonium bisulphate ( $(\text{NH}_4)\text{HSO}_4$ ) and ammonium sulphate ( $(\text{NH}_4)_2\text{SO}_4$ ) as in Table 3.8 on page 199.

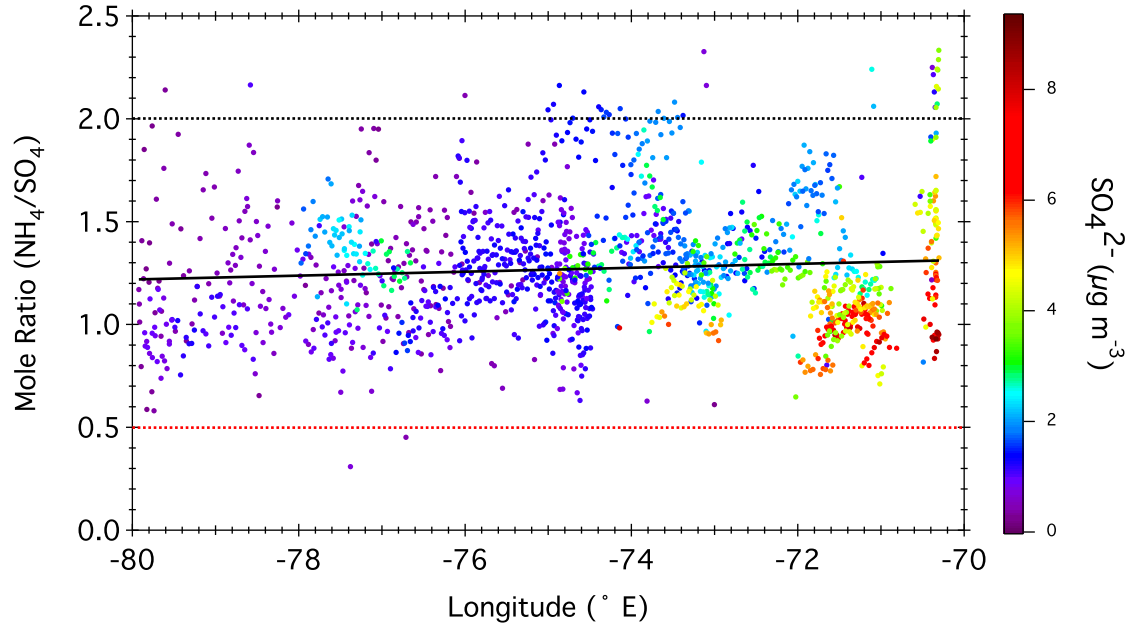


Figure 3.6: Longitudinal plot of the mole mass ratio with a line of best fit denoting an increase in acidification with distance from the coast, the  $y = 0.5$  and  $y = 2.0$  lines showing the ratio at which  $\text{H}_2\text{SO}_4$  and  $(\text{NH}_4)_2\text{SO}_4$  dominate respectively.

Figure 3.6 illustrates how the MMR falls with distance from the coast along the  $20^\circ \text{S}$  transect suggesting that there is a higher contribution of ammonium sulphate in the coastal region compared to a system dominated by ammonium bisulphate in the remote region. The significance of this relationship is tenuous having an  $R^2$  of only 0.01. The colour coding on the plot indicates the sulphate ion loadings. This overall trend agrees with data from the University of Leeds Volatile and Aerosol Concentration and Composition (VACC) system, though the trend is the opposite to that in Allen et al. (2011), whose data also suffered from a

weak correlation. It should be noted that the contribution of MSA to this balance of ammonium and sulphate ions is not considered here, though it has been shown to contribute up to 20 % of the aerosol number between the diameters of 0.1 and  $0.5\ \mu\text{m}$  in the remote region (Allen et al., 2011; Shank et al., 2012). Using this MMR data to derive the relative volumetric fractions of  $\text{H}_2\text{SO}_4$ ,  $\text{NH}_4\text{HSO}_4$  and  $(\text{NH}_4)_2\text{SO}_4$  has been used in polluted atmospheres (Asa-Awuku et al., 2011; Moore et al., 2012) before, however, its use here is limited. The signal to noise ratio in this data set is very low due to the low aerosol burden of the VOCALS environment. This is of particular consequence in the measurement of particulate ammonium. Unlike nitrate or sulphate where peaks in the mass to charge ratio ( $m/z$ ) are normally distinct, ammonium's peak is not. Particulate ammonium vapourises into ammonia ( $\text{NH}_3$ ) which fragments under electron impact in the AMS into the following three ions,  $\text{NH}^+$ ,  $\text{NH}_2^+$  and  $\text{NH}_3^+$ ,  $m/z$  of 15, 16 and 17 respectively. These three peaks all receive significant interference from  $^{15}\text{N}$ ,  $\text{CH}_3^+$ ,  $\text{O}^+$ ,  $\text{O}_2^{2+}$  when operating in positive ion mode,  $\text{OH}^-$  would also contribute to this interference if negative ions were detected. These interferences can be overcome to some extent by using a fragmentation tables technique (Allan et al., 2004) but at such low concentrations even this method is limited and any errors in the ammonium ion mass loadings will propagate into the speciation of the sulphate and ammonium using the MMR method. Relative uncertainties for the AMS mass loadings are estimated to be in the region of  $\pm 34 - 38\%$  (Bahreini et al., 2008).

In summary of the longitudinal gas and aerosol characteristics; there is a strong gradient in the MBL from the coast to the western edge of the  $20^\circ\text{S}$  transect in all particulate and gas concentrations as well as a distinct decrease in the variability of these measurements, this is primarily due to a function of distance from the main anthropogenic sources. The variability in the measurements sug-

gest that these sources are variable in their strength. There is a suggestion that the primary coastal source of sulphate, the most dominant species, is replaced with a marine source at the western end of the transect, the organics however, are nearly exclusively associated with a combustion source, and therefore contribution from marine sources can be considered limited. The OMF and organic to sulphate ratios suggests that there may be differences in the MBL source location with peaks suggesting a source from Santiago or entrainment from the FT and that the further west on the 20° S transect the further south the origin of the coastal influence, to a point at which the air masses lose contact with the land. Due to the clean nature of the environment and the low particle concentrations it will be hard to derive what form the sulphate measured is in and if there is any externally mixed fractions. It is assumed from these data that the aerosol is a mix of acidic sulphate aerosol with some ammonium sulphate and MSA, the presence of an external mixture of mineral dust and organics as measured on-board the RH Brown should also be considered.

### **Size Distribution Characteristics**

The properties of the size distributions are not included in Figure 3.3 on page 133. However, their longitudinal characteristics are considered here. Size distributions in the Aitken and accumulation mode were measured with the SMPS scanning at 45 second intervals. The SMPS measures mobility diameter, not geometric diameter and it is assumed here that a mobility diameter is equivalent to geometric diameter, i.e the particles are spherical. The limitation with this assumption is that neither the SMPS or CCNc actively control the sample RH. Based solely on the heating associated with drawing a sample into the cabin of the BAe-146 the SMPS mean sample RH for the flights analysed is 23.5 % with a standard deviation of  $\pm 9.9$  %. This mean value is similar to the values reported for the SMPS

in the previous section. Since this mean value is at the upper end of the estimate for ammonium sulphate efflorescence (Martin, 2000), and one standard deviation bridges this estimate, it must be considered that some particles measured will be crystalline and some aqueous, some angular and some spherical.

The data from the SMPS were heavily screened prior to analysis. Figure 3.7 and Table 3.2 outline the criteria under which this process was achieved. Data were only included where the total CN concentration number from both the CPC and derived from the SMPS (both modified TSI WCPC model 3786) were within 20 % of one another. Data were rejected where the CDN, as measured by the CDP probe, was greater than  $5 \text{ particles cm}^{-3}$  and the liquid water content was greater than  $0.04 \text{ g kg}^{-1}$ , indicating drizzle or cloud, called inlet shatter here as this is the outcome of a droplet intercepting the inlet. If the distribution had inversion errors, where the reported data for a given bin had a negative concentration, the data were not considered. The SMPS data were provided with a data flag that incorporated a diagnostic of leaks at low pressure and of scans which spanned a profile climb or descent. These flags were also used to reject data. This quality assurance procedure resulted in only 6.9 % of all the possible data being accepted. The possible effect of including these rejected data can be seen in Figure 3.7, the wide ‘shot gun’ pattern would have included distributions with integrated number concentrations in the thousands where complimentary data show only hundreds and *visa versa*. There is the possibility that the rejection criteria used here are too stringent, many yellow markers can be seen on the  $y=x$  line that may have proved useful in the analysis. To understand the effects of this with some level of certainty a threshold analysis would be required to understand the value and the number of occurrences of inversion errors which could be included and what effect this would have on the distribution. This was not investigated here. There is the possibility that the rejection criteria used here has caused a longitudinal

bias as inlet shattering is correlated to drizzle occurrence in the below cloud legs. Bretherton et al. (2010) highlighted that drizzle was measured on 75 % of all remote legs, those beyond 75° W. This increase in drizzle with distance from the coast can also be seen in Figure 3.14(c) on page 169 and in the reduced number of ‘Kappa Analysis’ plotted points to the western end of the transect on the flight tracks in Figure 3.1 on page 129. This increase in rejection naturally skews acceptable SMPS data towards the coastal regions where higher CDN may well actively play a role in pluvial constipation (Hudson, 1993; Andreae and Rosenfeld, 2008).

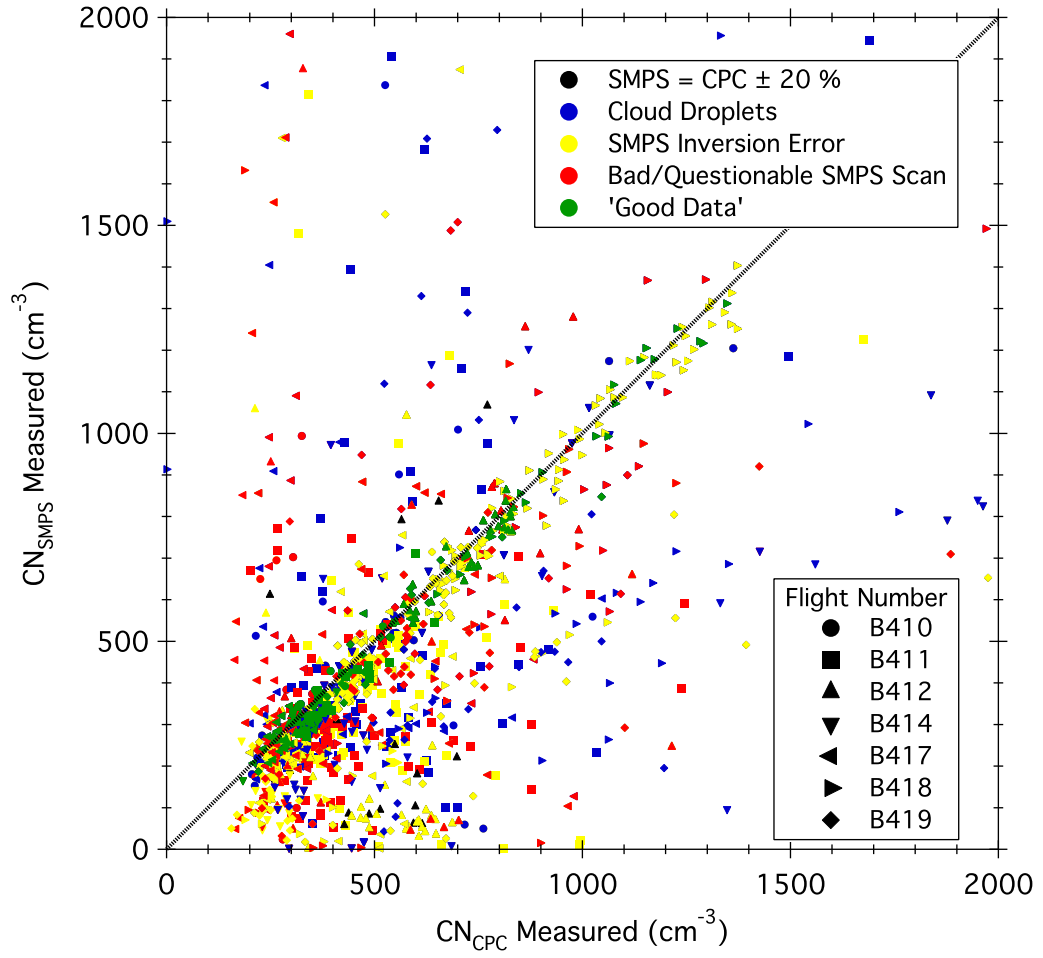


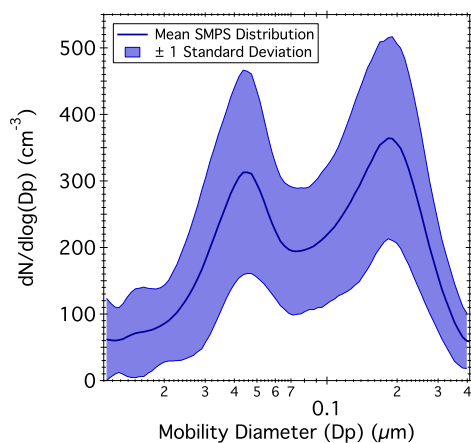
Figure 3.7: Scatter plot of CN as measured by the TSI modified 3786 WCPC against integrated CN as measured by the SMPS, highlighting the rejection criteria used in the SMPS data stratification procedures. Flight numbers are represented by closed shapes and colours represent the failure criteria and 'good data'.

Data Type	B410	B411	B412	B414	B417	B418	B419
$CN_{cpc} = CN_{smgs} \pm 20\%$	64	78	66	54	74	110	139
Inlet Shattering	289	323	203	188	314	205	279
Inversion Error	167	165	111	167	188	124	186
Flagged Data	105	106	70	167	122	52	76
Useable Data	11	20	43	9	25	19	19
Total Data Points	321	345	245	325	333	218	324

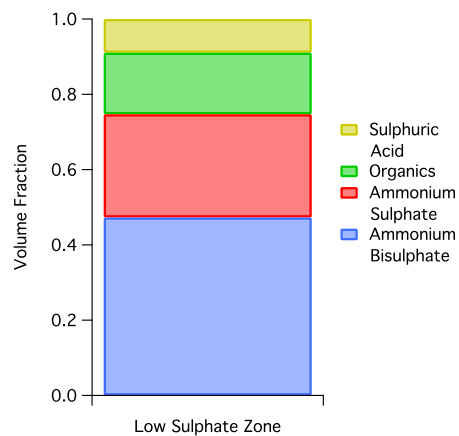
Table 3.2: SMPS data rejection criteria and the number of data points rejected by each or included by each method. It should be noted that the erroneous data are not mutually exclusive, a data point with an inversion error is more than likely to also be rejected on grounds of inlet shattering.

The SMPS distributions, once quality assured, have been categorised into either high sulphate, falling sulphate or low sulphate zones, as discussed and plotted as log-normal distributions, so the area under each curve is equivalent to the concentration, Figure 3.8. All three distributions show a multimodal structure with the high sulphate and low sulphate showing a distinct bimodal structure separated by a minima. This minima is less obvious in the falling sulphate zone.

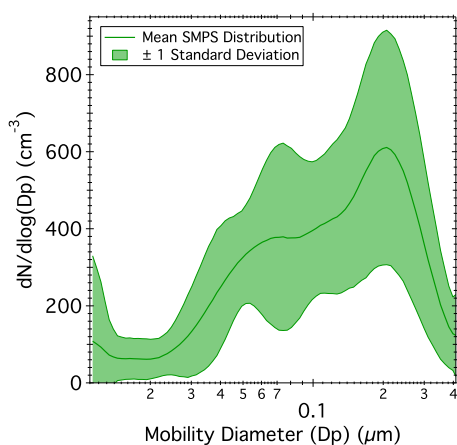




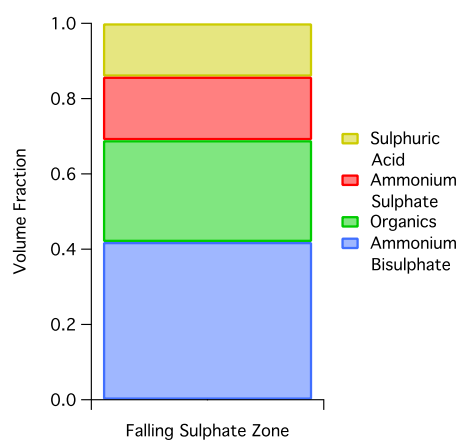
(a) Low Sulphate Zone



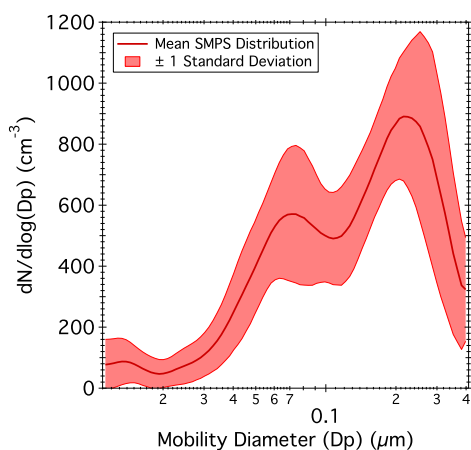
(b) Low Sulphate Zone



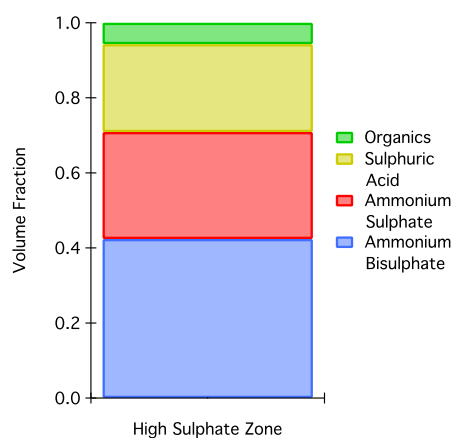
(c) Falling Sulphate Zone



(d) Falling Sulphate Zone



(e) High Sulphate Zone



(f) High Sulphate Zone

Figure 3.8: Mean SMPS distributions for each longitudinal zone with shading representing  $\pm$  one standard deviation of the mean. Average aerosol volume fractions calculated from the AMS mass loadings.

Hoppel et al. (1986) explained that this minimum or 'gap' is a result of the large particles, those with lower and subsequently more atmospherically relevant critical supersaturations, in a distribution being activated to form clouds, whilst those smaller particles remain as interstitial particles. Whilst in the aqueous phase, mass is added to these activated particles primarily by the oxidation of dissolved sulphur dioxide to sulphate, being non-volatile this added mass remains after droplet evaporation. Dissolution of sulphur dioxide ( $S(iv)$ ) in water produces three products under different pH regimes; in solutions with a pH less than 2.0 the product is hydrated  $SO_2$ , a solution with a pH between 2.0 and 7.0 bisulphate ions ( $HSO_3^-$ ) exists and a pH greater than 7.0 the sulphite ion  $SO_3^{2-}$  forms. The mixture of these is pH dependent, and the depletion of any of one in solution will instantaneously re-establish an equilibrium. In cloud, aqueous phase reactions oxidise  $S(iv)$  to form sulphate,  $S(vi)$ . There are multiple oxidation pathways, the three most important in atmospheric conditions being oxidation by dissolved ozone, oxidation by hydrogen peroxide and metal catalysed auto-oxidation. The first and last of this list are directly pH dependent, though the final step, the reduction of peroxymonosulfurous acid, of hydrogen peroxide pathway is also.

The mean pH of the cloud water during the VOCALS project was 4.3 with a maximum and minimum of 2.9 and 7.2 respectively, overall there was an increase in acidity with proximity to the coast, though not all samples collected close to the shoreline were acidic Benedict et al. (2012). In this study  $S(iv)$  oxidation pathways for all three mechanisms were calculated, oxidation by hydrogen peroxide was the fastest 76% of the time and ozone oxidation was fastest 24%. These results were pH dependent and as the  $S(iv)$  speciated into the more reactive forms oxidation by ozone became the more important pathway. Oxidation by hydrogen peroxide was more important where cloud water was below pH 5.5. The metal oxide pathway was never the fastest but was slowest in 37% of all the

samples. Analysis of the samples collected using the cloud water probe, fitted to the NCAR C-130, showed low concentrations of  $S(iv)$  whilst concentrations of hydrogen peroxide were relatively high suggesting that the oxidation is limited by availability of  $SO_2$  not by the availability of oxidising agents. The oxidation process adds mass moving particles from the Aitken to the accumulation mode creating a size differential between the two populations of the distribution over time.

The distribution minima does not fall around the same diameter in all zones. In the two extreme zones it is centred at  $0.107$  and  $0.074\ \mu m$  for the high and low sulphate zones respectively. These values of minima centers fit well with other studies. Twohy et al. (2005) (and references there in) report values of  $0.08\ \mu m$  for the north east Pacific,  $0.09\ \mu m$  and  $0.1\ \mu m$  for measurements on the Washington coast and  $0.12\ \mu m$  off the Oregon coastline. The shift in minima with longitude in this work could be explained by an increase in frequency and magnitude of updraft velocities away from the coast. The mean standard deviations of updraft velocities in the MBL are  $0.34$ ,  $0.39$  and  $0.48\ ms^{-1}$  for the high, falling and low sulphate zones, respectively. This will activate smaller particles in the most remote zone, if the composition in each zone is the same, the difference in minimum diameter could also be explained by a significant alteration in the aerosol chemistry ensuring a more hygroscopic aerosol further from the coast, though there is no evidence for this based on the AMS data. The falling sulphate zone does not appear to have a distinct minima which could be explained by air mass mixing or an arithmetic legacy. In defence of a physical mixing solution if the two extreme distributions were mixed the resultant population should have a distinct mode centred around  $0.2\ \mu m$  with a second very broad mode between  $0.07$  and  $0.04\ \mu m$ , suggesting the zonal boundaries are well defined with little coastal influence air reaching the low sulphate zone. The integrated area of the

SMPS distributions falls with longitude in agreement with the aerosol concentration, see Figures 3.3(a) to 3.3(f) . The high sulphate zone has a further weak mode centred about  $0.014\ \mu\text{m}$  which is indicative of nucleation most likely due to the proximity of this zone to the coastal emission sources, evidence suggests this mode is entrained from the FT (Allen et al., 2011)

Log normal probability distribution functions ( $n_N^o(\log D_p)$ ) of these data are shown in Figure 3.9 and were calculated using Equation 3.1

$$n_N^o(\log D_p) = \frac{N}{(2\pi)^{0.5}\sigma_g} \exp\left(-\frac{(\log D_p - \log D_{pg})^2}{2\log^2\sigma_g}\right), \quad (3.1)$$

where  $N$  is the number of aerosol particles ( $\text{cm}^{-3}$ ).  $D_p$  is the particle diameter. The geometric standard deviation  $\sigma_g$  is the ratio of the diameter below which 84.1 % of the particles lie to the median diameter. Essentially a measure of the width of the mode.  $D_{pg}$  is the number median diameter, that diameter at which exactly half of the particles are larger and half smaller. The fit parameters for these distributions were calculated using IGOR Pro's native optimisation procedure to fit a cumulative (trimodal) log normal PDF. This iterative approach uses the Levenberg-Marquardt algorithm to search for the coefficient values (user defined initial estimates) that minimise the value of a chi-square. These fit parameters are shown in Table 3.3

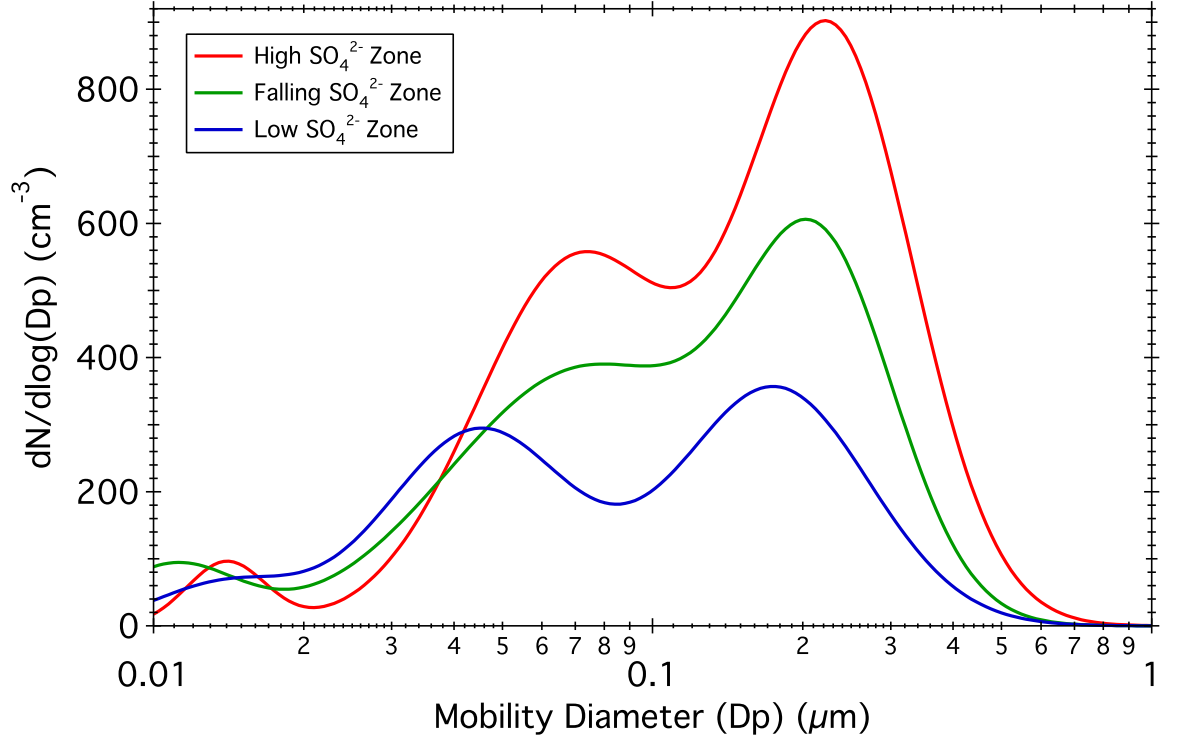


Figure 3.9:  $dN/d\log(D_p)$  log-normal fits for the mean SMPS distribution measured in the MBL between  $70^\circ$  and  $80^\circ$  West. The traces represent the high (red), falling (green) and low (blue) sulphate zones, respectively. The reduction in concentration can be seen along with a shift in dominant mode from the accumulation to the nucleation with distance from the South American continent. The count median diameter ( $D_{pg}$ ) and the geometric standard deviation ( $\sigma_g$ ) for these fits can be found in Table 3.3.

Table 3.3 shows the resultant binning of the descriptive statistics from the boxplot panel into the three longitudinal zones. The major trends of falling particle concentrations, of both CN and CCN and AMS measured mass loadings of sulphate and ammonium ions and organics with longitude is clear. Activated fraction and organic mass loadings do not follow this trend, but have a humpback trend. The log normal fit parameter values for total number,  $N$ , in mode one are comparable to those for sub-cloud Passive Cavity Aerosol Spectrometer Probe (PCASP) (DMT inc, Boulder, Co) measurements from the NCAR C-130, the values published by Bretherton et al. (2010) decrease with distance from the

Table 3.3: Descriptive statistics for aerosol measurements and lognormal parameters for the coarse MBL zonal data stratifications; high, falling and low sulphate regions. It should be noted that the difference between the number of points in each analysis will be different as each instrument has their own criteria for data rejection.

Parameter	Zone		
	High Sulphate	Falling Sulphate	Low Sulphate
Longitude ( $^{\circ}$ )	70-72	72-76	76-80
CN ( $\text{cm}^{-3}$ )	$544.3 \pm 255.4$	$325.1 \pm 92.2$	$298.8 \pm 72.1$
CCN <sub>0.09-0.17%</sub> ( $\text{cm}^{-3}$ )	$339.4 \pm 74.7$	$208.3 \pm 107.6$	$153.9 \pm 108.9$
F <sub>A0.09-0.17%</sub>	$0.494 \pm 0.108$	$0.405 \pm 0.176$	$0.453 \pm 0.311$
SO <sub>4</sub> <sup>2-</sup> ( $\mu\text{g m}^{-3}$ )	$4.642 \pm 1.826$	$1.737 \pm 1.055$	$0.971 \pm 0.656$
NH <sub>4</sub> <sup>+</sup> ( $\mu\text{g m}^{-3}$ )	$1.003 \pm 0.336$	$0.427 \pm 0.240$	$0.223 \pm 0.172$
ORG ( $\mu\text{g m}^{-3}$ )	$0.336 \pm 0.217$	$0.345 \pm 0.223$	$0.120 \pm 0.146$
LogNormal Fits			
Mode 1			
N	$364.6 \pm 4.8$	$191.9 \pm 5.1$	$168.3 \pm 2.8$
D <sub>pg</sub> ( $\mu\text{m}$ )	$0.227 \pm 0.001$	$0.217 \pm 0.001$	$0.175 \pm 0.001$
$\sigma_g$	$1.467 \pm 0.007$	$1.418 \pm 0.006$	$1.545 \pm 0.012$
Mode 2			
N	$281.8 \pm 4.6$	$267.1 \pm 5.6$	$133.7 \pm 4.5$
D <sub>pg</sub> ( $\mu\text{m}$ )	$0.07 \pm 0.001$	$0.074 \pm 0.001$	$0.045 \pm 0.0004$
$\sigma_g$	$1.604 \pm 0.012$	$1.893 \pm 0.023$	$1.522 \pm 0.021$
Mode 3			
N	$18.9 \pm 1.0$	$28.7 \pm 1.6$	$22.9 \pm 5.0$
D <sub>pg</sub> ( $\mu\text{m}$ )	$0.014 \pm 0$	$0.011 \pm 0$	$0.014 \pm 0.001$
$\sigma_g$	$1.2 \pm 0$	$1.340 \pm 0.025$	$1.390 \pm 0.1031$

coast with the first longitudinal grid between 70 and 75 west having a median of  $252 \text{ cm}^{-3}$  and an interquartile range between 222 and 287 particles  $\text{cm}^{-3}$ , the second bin between  $75^{\circ}$  and  $80^{\circ}$  W has a median of 176 particles  $\text{cm}^{-3}$  and an interquartile range between 121 and 251 particles  $\text{cm}^{-3}$ . The measured values for the C-130 would be expected to be lower than the integrated model number concentration as PCASP measurements only extend down to  $0.1 \mu\text{m}$ . Where as the modelled distributions extend below this diameter. The larger sizes measured by the PCASP, the supermicron particles as shown in Allen et al. (2011), add little to the number concentration.

In summary, all the mean distributions are multimodal in structure with accumulation modes between  $0.22$  and  $0.175 \mu\text{m}$  and in the Aitken mode between

0.074 and 0.045  $\mu\text{m}$ , both modes shift to smaller diameters at the western end of the 20° S transect. There is evidence of a nucleation mode in the high sulphate zone binned data centred around 0.01  $\mu\text{m}$ , evidence not available in this data set suggest this mode is entrained from above. The dominance of the accumulation mode decreases with distance from the coast as does the minima in the distributions. This is most likely due to an increase in the frequency and scale of the updraft velocities in the low sulphate compared to the high sulphate zones and not due to a change in aerosol chemistry. Particle concentrations as derived by integrating the SMPS distributions fall with longitude in agreement with data from the previous section. There are no super micron particles included in these distributions due to instrument issue with the wing mounted PCASP on the BAe-146 but comparison with other work suggests that their influence on the number distribution is small.

### **Cloud Properties**

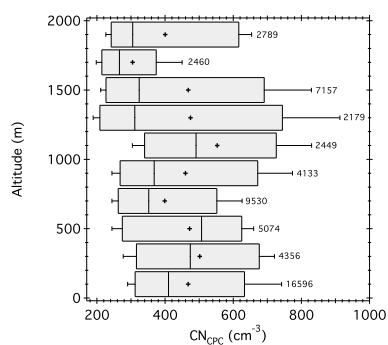
The final row of Figure 3.3 on page 133 describes cloud properties, these data are all taken from the wing-mounted cloud droplet probe (CDP) flown on the BAe-146. Graph 3.3(g) shows the increase in liquid water content (LWC) with distance from the coast with a distinct gradient change at 74° W. Droplet numbers in cloud close to the coast are in excess of 175  $\text{cm}^{-3}$ , West of 74° W this value drops to between 150 and 100  $\text{cm}^{-3}$  and across the entire transect CDN is a corollary of the aerosol concentrations. The CDN converges with the CCN concentration further to the West, suggesting that the local supersaturation maxima is within the range reported by the CCNc, 0.09 to 0.17 % between 74° and 78° W. The volume mean diameter (VMD) is driven by trends in the two previous parameters (graphs 3.3(g) and 3.3(h)), the more cloud droplets there are, the less water is available for each droplet driving the distribution to smaller sizes for a given CCN

concentration. As such the coastal regions has the smallest VMD in the region of  $10\text{ }\mu\text{m}$ , rising to maximum mean diameter of  $19\text{ }\mu\text{m}$  at  $79^\circ\text{ W}$ . These final two graphs represent the underlying process of the indirect effect. The extent of this effect can not be estimated here as the changes in droplet number and sub cloud aerosol occur at the same time as variations in LWC and cloud thickness, this added complexity has also been observed in the north east Pacific region (Twohy et al., 2005) where dynamical processes had more of an effect on the LWC and cloud thickness than simple aerosol cloud interactions.

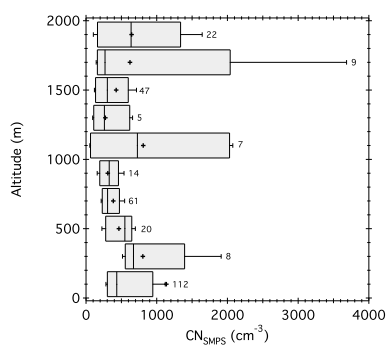


### **3.1.2 Vertical Structure**

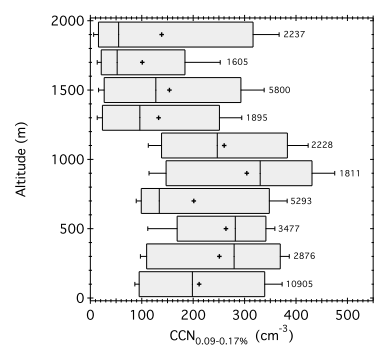
The graphs in Figure 3.10 use the same data as the longitudinal boxplots with the substitution of CDP data with SMPS and AMS derived measurements. All plots extend to the 2000 m, the highest SLR where data are available.



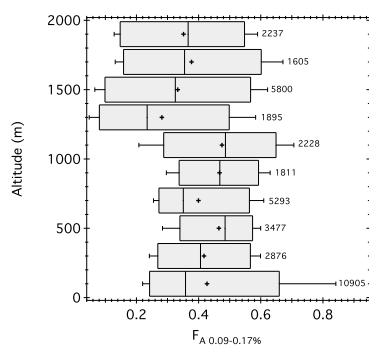
(a) CPC CN Concentration



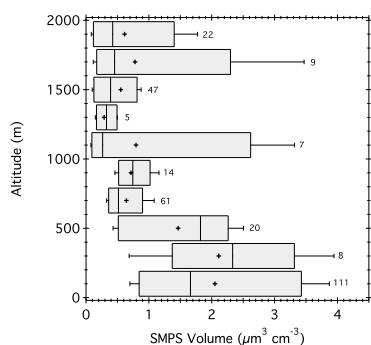
(b) SMPS CN Concentration



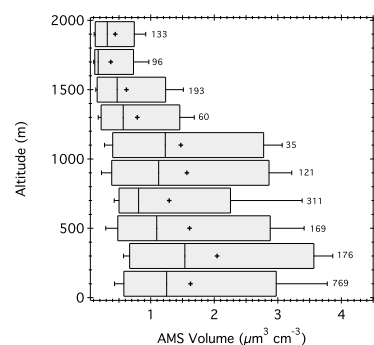
(c) CCN Concentration



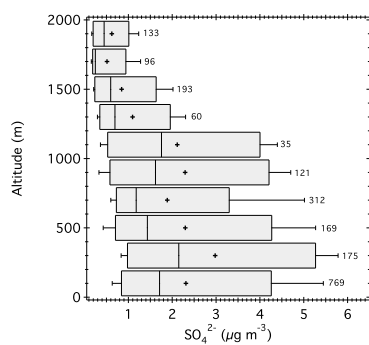
(d) Activated Fraction



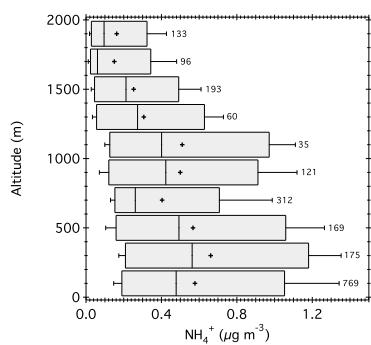
(e) SMPS Volume



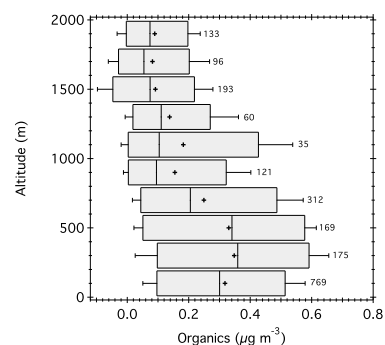
(f) AMS Volume



(g)  $\text{SO}_4^{2-}$  Mass



(h)  $\text{NH}_4^+$  Mass



(i) Organic Mass

Figure 3.10: Describes the altitude response of important aerosol parameters used in this analysis. Whiskers represent the interdecile range and the limits of the box the interquartile range. The median is represented by the line bisecting the box and the mean represented by the black crosses.

## Gas and Aerosol Properties

The CN concentration as measured by the CPC, graph 3.10(a) remains constant with altitude up to 1500 m, with mean concentrations varying between 552 and 398 particles  $\text{cm}^{-3}$  across the vertical extent of the MBL (0 to 1200 m), though there are fluctuations between any two altitude bins. This variation also shows little trend with altitude. All the data are positively skewed to higher concentrations. This is because the high concentrations from this longitudes close to the coast are included in and skew every altitude bin.

The CN concentration integrated from the SMPS distributions, graph 3.10(b), has an overall trend of falling concentrations with altitude within the MBL, this trend appears to have two distinct regions; between 0 and 400 m there is an increase in median concentration, above 400 m up to 1000 m the median value falls from 803 to 308 particles  $\text{cm}^{-3}$ . This is counter to the findings of Kleinman et al. (2012) where on individual flights little difference was found between particle distributions as measured by the SMPS hundreds of meters apart vertically and separated by up to 3 hours. At 70° W Zheng et al. (2011) showed the MBL to be well mixed with a constant mean PCASP concentration of just under 500 particles  $\text{cm}^{-3}$  for all 18 flights undertaken in the CIRPAS twin otter. The variability of the SMPS derived CN also drops with altitude as does the number of points included in each altitude bin, this is a function again of increased instances of drizzle and cloud droplet encounters added to instrument pressure issues which subsequently increases the frequency of data rejection.

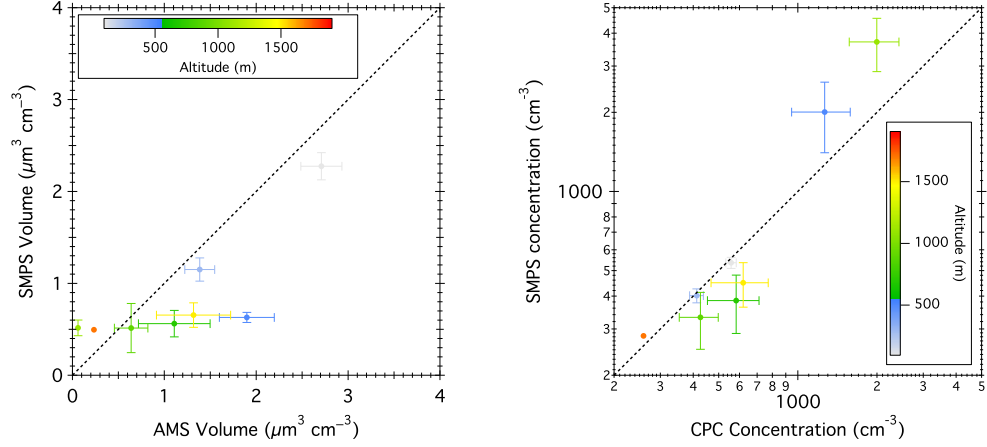
Again only CCN concentrations with a supersaturation between 0.09 and 0.17 % are plotted in graph 3.10(c) to allow for comparison. These data show a weak increasing trend with altitude. The mean concentrations increase from 211 to 260 particles  $\text{cm}^{-3}$  across the MBL.

This slight increase in CCN concentration drives the trend of increasing activated fraction with altitude, graph 3.10(d), from a mean of 0.43 at the surface to 0.48 at 1200 m. This falls back to a value of 0.28 above the MBL.

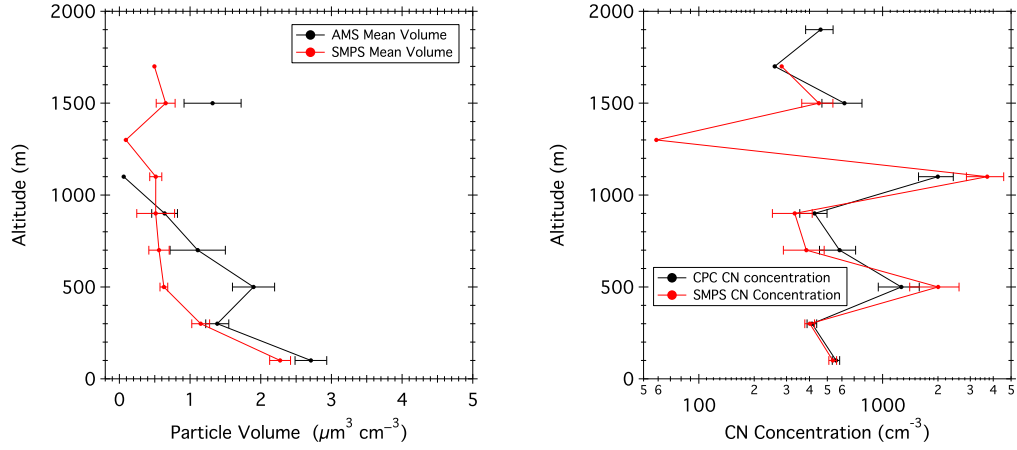
As seen in the SMPS CN concentration, the median SMPS volume (graph 3.10(e)) decreases with altitude from a maximum of  $2.11 \mu\text{m}^3 \text{cm}^{-3}$  at the top of the MBL. As with the SMPS derived CN concentration the variation in this parameter also drops with altitude and the trend is split between an increase between 0 and 400 m and a distinct fall above 400 to 1200 m, suggesting that the variation in SMPS volume is driven by a variation in number and not by a shift in diameter.

The AMS derived volume, graph 3.10(f), does not follow the falling trend seen in the SMPS volume. The behaviour is more akin to the CN concentration as measured by the CPC with a median value that fluctuates between 0.8 and  $1.5 \mu\text{m}^3 \text{cm}^{-3}$  over the depth of the MBL. There is a distinct fall above the MBL as seen in the median values of CN in graph 3.10(a).

The inconsistency between the SMPS derived CN measurements and the other particle number and volume measurements has highlighted possible issues with the SMPS measurements. Figure 3.10 is not suitable to make a detailed assessment as each instrument's data are plotted with their own native measurement frequency and data QA procedures are used. For a true comparison of instrument behaviour co-located measurements are required, Figure 3.11 shows direct comparison of resampled AMS, CPC and SMPS data to directly compare the instrument behaviour.



(a) Scatter plot of SMPS and AMS derived volume (b) Scatter Plot of CPC and SMPS CN concentration



(c) Altitude response of SMPS and AMS derived volume (d) Altitude response of SMPS and CPC CN concentration

Figure 3.11: Co-located measurements for AMS, CPC and SMPS using the same QA procedure for all data which has been averaged to match the same time sequence as the SMPS so data are co-located to the same altitude zone, longitude, flight and time. In Figures 3.11(a) and 3.11(b) the colour array represents altitude. In Figures 3.11(c) and 3.11(d) the red represents the SMPS data whilst the black is AMS and CPC, respectively

No comparison should be made between instruments other than those contained in each plot, so no inference should be taken from the fall in AMS volume with altitude not being concurrent with a fall in number concentration in the CPC measured CN data, these data are more than likely from different parts

of the 20° S transect on different flights. That being said it is clear that the discrepancies hinted at in the altitude box plots are obvious here. In terms of closure of the mass, only three altitude zones get close to the  $y = x$  line at 0 to 200, 200 to 400 and 600 to 800 m in Figure 3.11(a). The altitude trend between the two measurements (Figure 3.11(c)) shows that the closure at 800 m is merely a consequence of two overlapping vertical trends, the AMS reducing in volume with altitude and the SMPS staying invariant between 400 and 1200 m. These discrepancies are also borne out in the SMPS and CPC CN concentration (Figures 3.11(b) and 3.11(d) comparison where it is clearly only the lower two altitude zones that compare favourably. There is obviously some data issues with the SMPS above 400 m in this data set, as such data collected above this altitude will not be used beyond this section.

Sulphate ion loadings as measured by the AMS, graph 3.10(g) have a similar response with altitude to the CPC measured CN. There is little overall trend in the MBL with the median loadings varying from 1.17 to 2.15  $\mu\text{g m}^{-3}$ . The data are heavily skewed due to the contributions of the coastal influenced high sulphate zone.

The organic loadings, graph 3.10(i), have a weak response with altitude, the loadings fall across the altitude range from 0.3 to 0.1  $\mu\text{g m}^{-3}$ . There is little skew in these data compared to that in the sulphate data suggesting that all longitudinal zones have a similar loadings as shown in Figure 3.3.

The mean ammonium loadings, graph 3.10(h), fall with altitude though the median values much like the sulphate ions fluctuate with altitude. Again these data are subjected to a high level of skew due to the longitudinal gradient in aerosol.

All graphs in Figure 3.10 show a reduction in values above 1200 m, defined here as the FT. As such it should be considered that the source for these parameters

is primarily in the boundary layer and that any downwelling does not act as a perpetual or significant source of material at the top of the boundary layer.

The sulphate mass fraction Figure 3.12(a) increases slightly with altitude over the extent of the MBL from a median value of 0.72 to 0.77. Ammonium mass fraction is stable and fluctuates between 0.16 and 0.19 with no distinct vertical gradient. As with the longitudinal transects the organic mass fraction shows the opposite trend to sulphate, falling slightly over the 1200 m of the MBL from a value of 0.1 to 0.06. Above the MBL the variability in the measurements increases though the median fractions fluctuate without any evident trends. However, the organic to sulphate ratio shows that in fact there is a relative increase in organics above the MBL suggesting that the increased organics and organic to sulphate ratios seen in the mid longitudes of the transect could also be as a result of episodic FT subsidence and not localised marine source, though this does not discount localised shipping as a source.

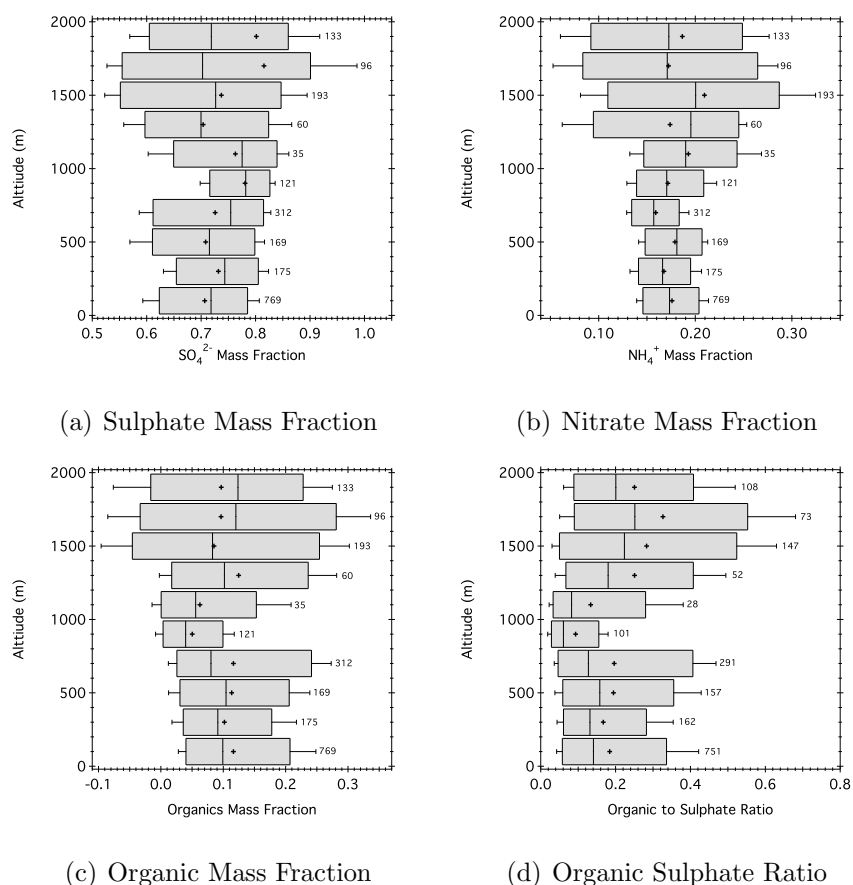


Figure 3.12: Describes the altitude response of AMS mass fractions parameters from the sub set of flights used in this analysis. Again these fractions ignore the contribution from chloride and ammonium ions. Whiskers represent the interdecile range and the limits of the box the interquartile range. The median is represented by the line bisecting the box, the mean is represented by the black crosses.

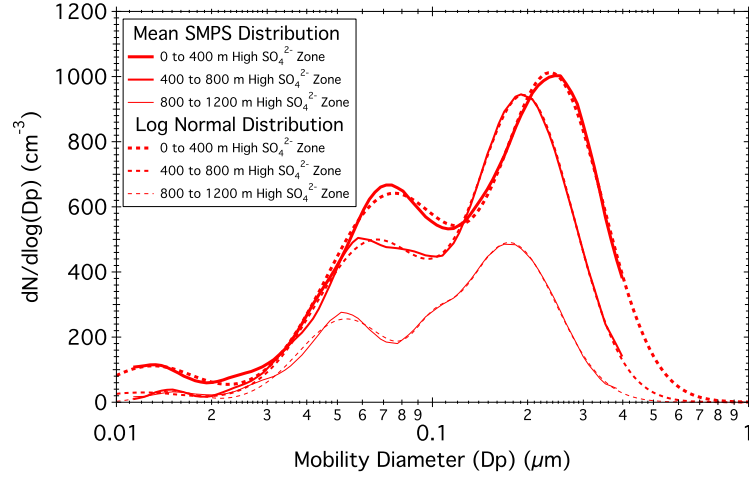
In summary, CPC measured CN, Sulphate, organic and nitrate loadings and mass fractions show little trend with altitude. Excluding organics all the parameters show a positive skew associated with higher concentrations in the coastal longitudes. CCN and activated fraction show slight increases with altitude and SMPS derived measures show a strong decrease with altitude within the MBL. The weak trends are representative of a turbulently well mixed MBL. This can be seen in comparisons between ship and aircraft data where the AMS mass loadings measured at 18 m on the R.H.Brown research vessel are consistent with those



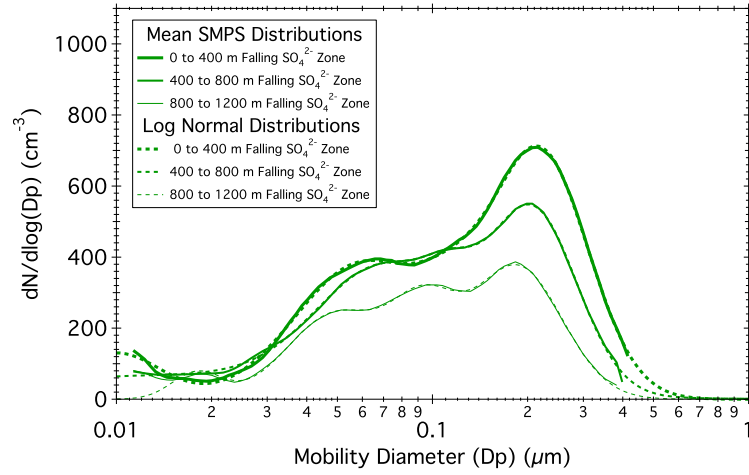
measured on the aircraft some altitude above (Allen et al., 2011).

### **Size Distribution Characteristics**

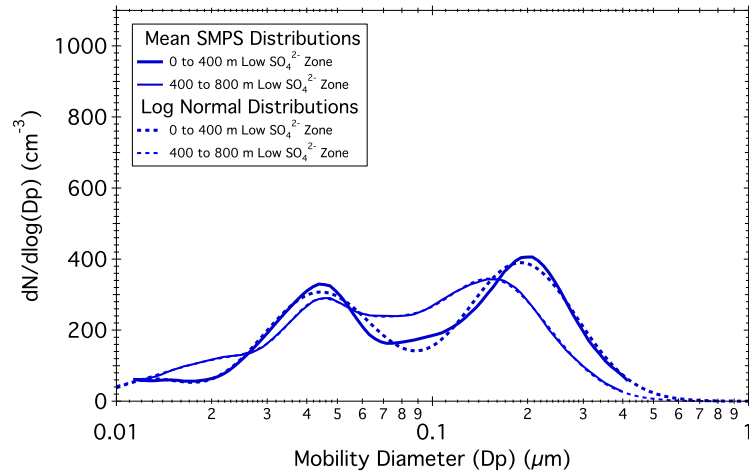
The SMPS data was further binned by both longitude and altitude and means of the distributions calculated. All of these mean SMPS distributions can be seen in Figure 3.13 as solid lines. These are all to some extent open at the larger diameters (the distributions do not continue to zero). When integrating a number concentration for these distributions the open nature will lead to some ‘missing particles’, the number of particles missed can be calculated using the log normal cumulative distribution function (CDF). The most open of these distributions is the lowest altitude of the high sulphate zone where 9 particles are missing from the total number of 397 particles, a loss of 2.5 %. This missing particle proportion decreases with distance from the coast and with distance from the sea surface. In the low sulphate mid level data only two particles in 155.7 are missing, a loss of 1.2 %. The altitude segregated SMPS distributions do show some marked differences from the altitude independent integrated zonal distributions; see Figure 3.8 on page 150. Each zone has been split into three altitude bins, 0 to 400, 400 to 800 and 800 to 1200 m. The altitude levels were chosen in response to the SMPS data in Figure 3.10. Level one, the lowest level in the atmosphere where the SMPS data compares well to other measurements. Level two the altitude zone above this where the concentration and volume of the SMPS fall away and level three the upper most level in the MBL. As would be expected, the lowest level distributions have higher concentrations than the simple longitudinal zoned distributions as they are not diluted by averaging out over the entire vertical extent of the MBL. It can be seen in these plots that the reduction in particle concentration with altitude drives the reduction in SMPS volume with altitude and not a shift in the distribution.



(a) High Sulphate Zone



(b) Falling Sulphate Zone

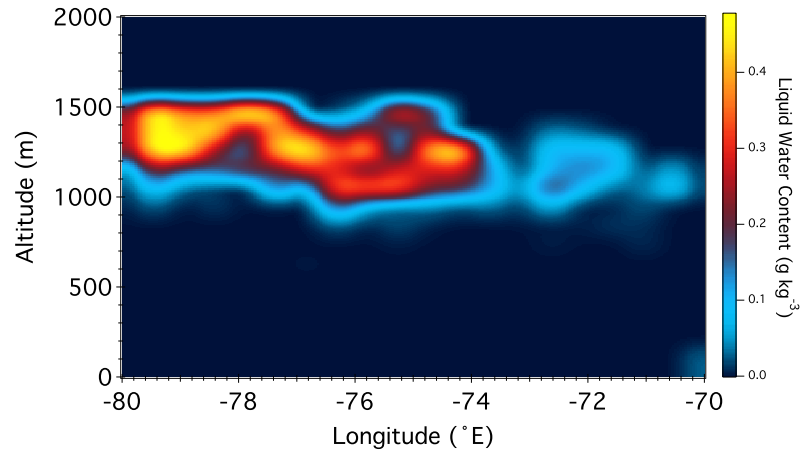


(c) Low Sulphate Zone

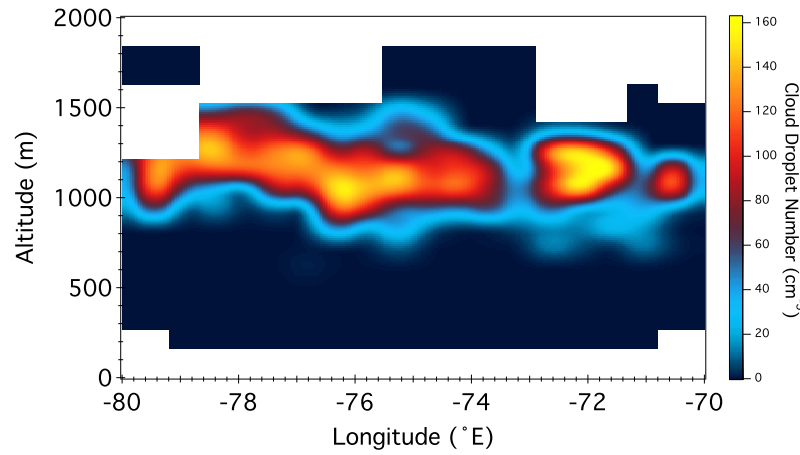
Figure 3.13: Mean SMPS distributions for each longitudinal and altitude zone, solid lines and dashed lines representing the mean measurement and the log normal distribution fit respectively.

Also noticeable is a shift in the count median diameters of the accumulation mode with increasing altitude. Associated with these shifts in mean diameters are reductions in the minima of the distributions with altitude, the process driving this is unidentified due to the questionable quality of the SMPS data above 400 m. The effect of the reduced number concentrations, and to a lesser extent the distribution shift, would have a very small effect on a MBL averaged data sets used in other studies. As discussed and shown in the following section the greater the altitude in the MBL, the lower the pass frequency of the data as the incidences of drizzle and higher LWCs result in data being flagged and removed from the analysis.

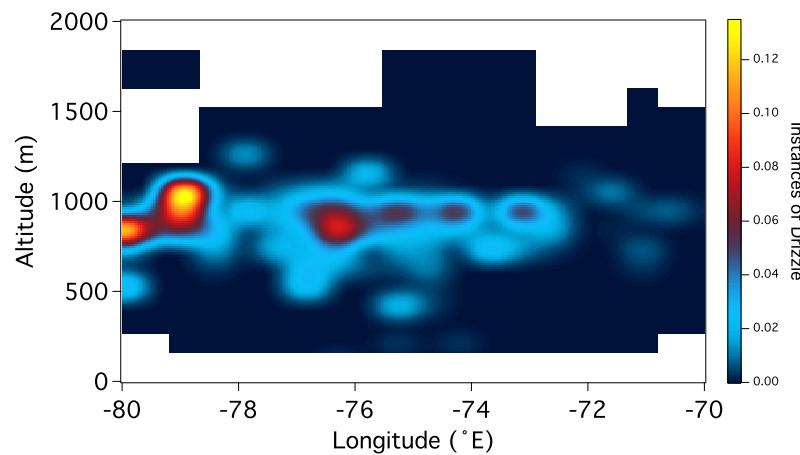
## Cloud Properties



(a) Median LWC for each  $0.5^\circ$  degree by 100 m altitude grid square.



(b) Median CDN for each  $0.5^\circ$  degree by 100 m altitude grid square.



(c) Instances of drizzle for each  $0.5^\circ$  degree by 100 m altitude grid square.

Figure 3.14: (a), (b) and (c) Show the cloud parameters represented in both longitudinal and altitude space. White grids represent bins with no data.

The altitude and longitude characteristics of the cloud properties in the VOCALS experiment can be seen in Figure 3.14. These plots add a vertical dimension to the longitudinal trends in Figure 3.3 on page 133 with this added dimension it is impossible to also include information about the variability of the measurements as such these plots are more qualitative than the box plots. As in Figure 3.3, mean LWC increases with longitude West and median CDN drops along the same transect. Graphs 3.14(a) and 3.14(b) depict the stratus cloud deck deepening and lifting with longitude from  $70^{\circ}$  to  $80^{\circ}$  W. These two graphs also show the paucity of cloud cover in the first two degrees of the transect. This lack of in cloud cover close to the coast can also be seen in the GOES-10 1 km resolution visible satellite images in Figure 3.15 below. This image is from the 9<sup>th</sup> November at 12:28 UTC, some 30 minutes after take off of B419.

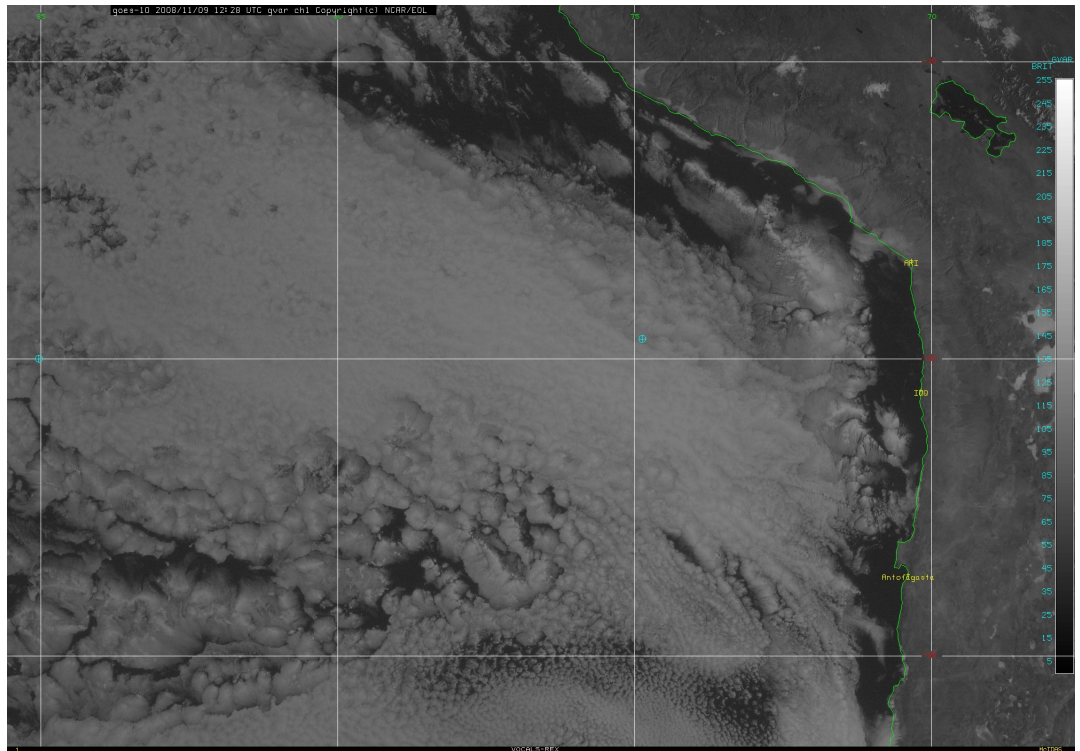


Figure 3.15: GOES 10 1 km resolution. The most northerly and southerly lines of latitude represent  $15^{\circ}$  and  $25^{\circ}$  S. The most easterly line of longitude is  $70^{\circ}$  and westerly  $85^{\circ}$  W. Both longitude and latitude cells are  $5^{\circ}$  by  $5^{\circ}$ .

Graph 3.14(c) represents those instances where drizzle is encountered. The CDP maximum diameter is  $50\text{ }\mu\text{m}$  (assuming a refractive index of 1.59 and 0.0i), as such it cannot be considered a precipitation probe. However, once it falls from the cloud base drizzle will start to evaporate. This evaporation of the droplets reduces their diameter enough to allow measurement by the CDP below cloud base as such it was assumed here that any data point with a VMD greater than  $40\text{ }\mu\text{m}$  (well beyond the maximum droplet diameter measured in cloud) is assumed to be drizzle. These instances of drizzle were further categorised by only including data where the CDN was less than  $40\text{ particles cm}^{-3}$ . These instances were then normalised by the number of data points in each grid square. The occurrence of drizzle can be seen to increase with longitude in accordance with data from other studies (Bretherton et al., 2010; Allen et al., 2011). The peak instances of drizzle are between  $75^\circ$  to  $80^\circ$  W between 800 and 1000 m, lower than this and the drizzle will have evaporated, at least below the lower assumed criterion of drizzle diameter used here, in many cases. Though instances of drizzle, as defined here, have reached as low as 500 m. The MBL in this region increases in height with distance from the coast Figures 3.14(a) and 3.14(b) show this with the lifting cloud base, accompanied by thicker cloud at the MBL top and more decoupling within this layer (Bretherton et al., 2010; Jones et al., 2011; Rahn and Garreaud, 2010; Zheng et al., 2011). This decoupling is driven by a number of processes. Daytime insolation heats the cloud layer more than the underlying sub-cloud layer promoting stratification of the boundary layer. Drizzle coupling occurs as precipitation heats the cloud and cools the sub-cloud layer as it evaporates (Jones et al., 2011). Cloud top radiative cooling leads to a strong turbulence in the cloud layer. This turbulence increases with cloud thickness and distance from the continent (Bretherton et al., 2010). This process also drives entrainment of free tropospheric air into the boundary layer. Near the coast the Andean slope heats the lower free troposphere reducing the long wave cooling

effect but this control does not extend off shore where the air remains cooler maintaining a deeper boundary layer and stronger entrainment.

All of these longitudinal and vertical stratified data have been incorporated into a meta table for comparison. The aerosol parameters have been averaged and the variation in that average is reflected by an estimate of one standard deviation across the three longitudinal and three altitude zones; see Table 3.4.

The data analysed here provides answers to the second major science question posed in Chapter 1 by resolving the characteristics of the SEP with regards to aerosol, gases and cloud microphysics. In summary of the VOCALS transect, the MBL increases in height with distance from the coast as does the amount of drizzle encountered. The SMPS distributions show a shift in the minima to smaller diameters which is possibly due to the more frequent and higher velocity updrafts in the more remote coastal regions. With increasing westerly longitudes the concentrations of gas and particle mixing ratios and mass loadings fall away with distance from the primary coastal source in the MBL. The variability in the gas and particle measurements suggests that these sources are episodic and decreasing influence away from the coast. Peaks in the organic to sulphate ratios, which are associated with low CO mixing ratios in the mid longitudes suggests a different source to that closer to shore and further offshore, this is most likely transport from Santiago (Hawkins et al., 2010). Little of the organics measured in this system are of marine origin, this is not unusual for oligotrophic subtropical waters (Shank et al., 2012). However, the sulphate at the western edge of the transect is most likely of marine origin. The cloud microphysical properties also show marked longitudinal trends with an increase in both VMD and cloud droplet number, these parameters could with a stable liquid water path be used to infer the contribution of the indirect effect, however the LWC on the transects is not stable. In the vertical there appears to be little trend in the particle and gas mixing ratios as would be expected in a well mixed boundary layer though the increase in the organic to sulphate ratio in the mid latitudes could be indicative of entrainment from aloft, though this is not conclusive. These characteristics of the SEP are well known from the literature (Allen et al., 2011; Bretherton et al., 2010; Kleinman et al., 2012). However these literature characteristics are for other aircraft or meta-analyses of all the data from all of the platforms undertaking measurements during VOCALS. This data is of little use to this study as the



Parameter	Zone									
	High Sulphate 70-72			Falling Sulphate 72-76			Low Sulphate 76-80			
Longitude (°)	< 400	400 - 800	800 - 1200	< 400	400 - 800	800 - 1200	< 400	400 - 800	800 - 1200	
Altitude (m)	< 400	400 - 800	800 - 1200	< 400	400 - 800	800 - 1200	< 400	400 - 800	800 - 1200	
CN (cm <sup>-3</sup> )	605.3±186.3	544.7±102.7	424.8±375.1	339.6±76.4	317.9±117.8	303.8±76.9	316.1±64.0	282.4±70.8	325.4±91.2	
CCN <sub>0.09-0.17%</sub> (cm <sup>-3</sup> )	320.4±62.4	351.8±64.8	360.8±99.4	198.0±107.6	204.9±96.0	248.4±121.5	176.2±123.9	102.5±33.7	123.0±39.9	
F <sub>A0.09-0.17%</sub>	0.46±0.09	0.54±0.08	0.50±0.15	0.38±0.20	0.41±0.13	0.47±0.17	0.52±0.35	0.31±0.09	0.37±0.09	
SO <sub>4</sub> <sup>2-</sup> (μg m <sup>-3</sup> )	4.73±1.91	5.17±1.37	3.64±1.68	1.77±1.07	1.64±0.98	1.82±1.89	1.17±0.76	0.84±0.42	0.44±0.45	
NH <sub>4</sub> <sup>+</sup> (μg m <sup>-3</sup> )	1.02±0.34	1.09±0.26	0.81±0.35	0.44±0.25	0.41±0.23	0.41±0.23	0.28±0.20	0.18±0.11	0.10±0.11	
ORG (μg m <sup>-3</sup> )	0.35±0.20	0.36±0.23	0.24±0.24	0.36±0.22	0.37±0.21	0.14±0.16	0.15±0.15	0.09±0.14	0.03±0.09	
Log Normal Fit										
Mode	Param									
1	N	359.2±3.1	184.0±2.7	266.0±4.8	174.6±8.4	133.58.3	172.5±2.8	155.7±2.8	-	
	D <sub>pg</sub>	0.197±0.001	0.175±0.001	0.218±0.002	0.209±0.001	0.185±0.004	0.190±0.001	0.154±0.001	-	
	σ <sub>g</sub>	1.427±0.004	1.412±0.008	1.423±0.007	1.381±0.0114	1.388±0.023	1.502±0.013	1.524±0.069	-	
2	N	-	16.4±2.6	34.5±8.6	19.2±4.2	58.7±16.8	-	37.1±6.6	-	
	D <sub>pg</sub>	-	0.100±0.001	0.116±0.002	0.114±0.002	0.094±0.003	-	0.069±0.002	-	
	σ <sub>g</sub>	-	1.152±0.015	1.281±0.0292	1.208±0.0191	1.269±0.040	-	1.317±0.036	-	
3	N	225.3±3.1	94.0±1.9	208.106.8	182.1±11.05	94.4±12.1	138.7±3.2	37.6±7.1	-	
	D <sub>pg</sub>	0.064±0.0004	0.053±0.0004	0.061±0.001	0.072±0.021	0.050±0.003	0.044±0.0003	0.043±0.001	-	
	σ <sub>g</sub>	1.523±0.009	1.403±0.011	1.645±0.020	1.6408±0.067	1.433±0.048	1.515±0.018	1.243±0.014	-	
4	N	10.9±1.5	6.7±0.7	46.06±1.26	108.636.2	14.91.4	16.45.0	89.8±8.3	-	
	D <sub>pg</sub> <sup>1</sup>	0.012±0	0.015±0	0.006±0	0.016±0	0.018±0	0.013±0.001	0.026±0.002	-	
	σ <sub>g</sub> <sup>1</sup>	1.4±0	1.2±0	1.385±0.017	4.380±2.16	1.2±0	1.293±0.105	1.922±0.085	-	

Table 3.4: Descriptive statistics for aerosol measurements and log-normal parameters for the coarse zonal and altitude data stratifications; high, falling and low sulphate zones in the longitudinal axis, 0-400 m, 400-800 m and 800 -1200 m in the vertical. All data including or derived from the CCN concentration, CCN and  $F_A$  are for instrument measurements when the supersaturations were between 0.09 and 0.13%

<sup>a</sup>These parameters were force fitted in the optimisation procedure for the lognormal fits; as such there is no associated variation. If the code was left to run unforced the distributions fitted were un-realistic with the smallest diameter nucleation mode often extending well into the accumulation mode.

following sections deal with data collected from the BAe-146. If inference about the hygroscopicity of the aerosol are to be made they need to be made with data collected at the same time from the same platform.

The most striking and novel outcome from the vertical analysis is the inability to achieve closure between AMS derived and SMPS derived mass and the subsequent assumption that the SMPS data above 400 m is not of a good enough quality to be used in the remainder of the analyses.

## 3.2 Kappa Analysis

Single variable parameterisations simplify estimates of CCN concentrations in climate models. However, their application to a range of aerosol types is still not well characterised. One such single variable parameterisation widely used in the literature is  $\kappa$ , also known as the hygroscopicity parameter (Petters and Kreidenweis, 2007). This parameter can be estimated from measurements by estimating dry size critical diameter ( $d_c$ ) using Equation 3.2 (Seinfeld and Pandis, 2006). The parameter allows direct comparison of hygroscopicity to other studies, laboratory data and model outputs. The critical diameter of an aerosol population can be estimated from the SMPS distribution using Equation 3.2. Integrating from the largest to smallest diameter for any averaged time period until the mean CCN concentration for that period is equalled, linearly interpolating between bins as in Figure 3.16. Where the number of CCN at any given supersaturation is given as

$$CCN_{ss} = \int_{d_c}^{\infty} n(D_p) dD_p, \quad (3.2)$$

where  $n(D_p)$  is the number distribution of the aerosol population,  $d_c$  the dry size critical diameter for supersaturation  $SS$  % of the particles measured. In this notation,  $CN = CCN(\infty)$ . The underlining assumption here is of an internally mixed aerosol.

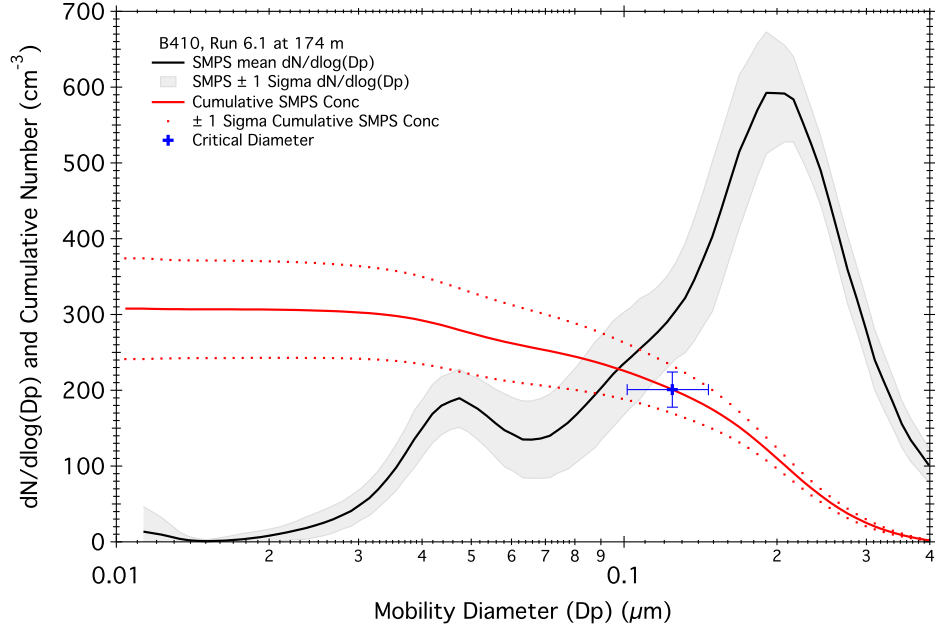


Figure 3.16: Graphical representation of the methodology of Equation 3.2 from data collected during the VOCALS campaign. The cumulative SMPS concentration is cumulated from the large to the small diameters.

$\kappa$  can be calculated from Equations 1.4 and 1.5 on page 40. For ease they are rewritten here (Petters and Kreidenweis, 2007):

$$\kappa = \frac{4A^3}{27d_c^3 \ln^2 S_c}$$

and

$$A = \frac{4\sigma M_w}{RT\rho_w},$$

where  $\kappa$  is the hygroscopicity parameter and  $A$  is the representation of the Kelvin effect. In Equation 1.4  $d_c$  is the critical activation diameter and  $S_c$  the critical supersaturation. It is assumed here that  $d_c$  is the equivalent of the activation diameter in Equation 3.2 and that  $S_c$  is the instrument calibrated supersaturation. In Equation 1.5,  $M_w$  is the molecular weight of water,  $R$  the universal gas

constant,  $T$  the temperature (taken from the instrument OPC),  $\rho_w$  the density of water and  $\sigma$  the surface tension of the solution to air interface.  $\sigma$  can be estimated using the Eötvös rule

$$\sigma V^{2/3} = k(T_c - T), \quad (3.3)$$

where  $k$  the Eötvös constant is equal to  $2.1 \times 10^{-7} \text{ J (K}^1 \text{ mol}^{2/3})$  this holds for all liquids.  $V$  the molar volume and  $T_c$  the critical temperature of 647.1 K, both for water, and  $T$  is the instrument OPC operating temperature.

$\kappa$  was calculated using Equation 1.4 on page 40 with the critical diameter being estimated from the integrated SMPS distributions, only from the lowest 400 m of the MBL, and CCN concentrations. Figure 3.17 represents the relationship between  $\kappa$  and critical diameter for those data collected below 400 m in altitude. The mean values are 0.26, 0.19, 0.11 and 0.08 with mean critical diameters of 0.22, 0.16 0.12 and 0.11  $\mu\text{m}$  for the effective supersaturations, 0.09, 0.17, 0.32 and 0.43 %, respectively. The overall  $\kappa$  for the sub 400 m data is 0.21. This mean is somewhat skewed as there are five times as many measurements at 0.09 % effective supersaturation as there are at 0.32 %. This skew occurs as on each flight one of the channels, when both were operational, was always run at this supersaturation. In Figure 3.17 the CCNc derived data are compared to a  $\kappa$  calculated from the ammonium sulphate critical diameter output from ADDEM. Only the 0.09 % supersaturation  $\kappa$  estimate is within the 50 % error estimate of the theoretical value for ammonium sulphate in the sub 400 m data. There is a falling trend in the mean  $\kappa$  with increasing supersaturation indicative of an external mixture with respect to hygroscopicity or an instrument bias. The values for  $\kappa$  split by longitude and altitude bin can be seen in Figure 3.18 and Table 3.5.

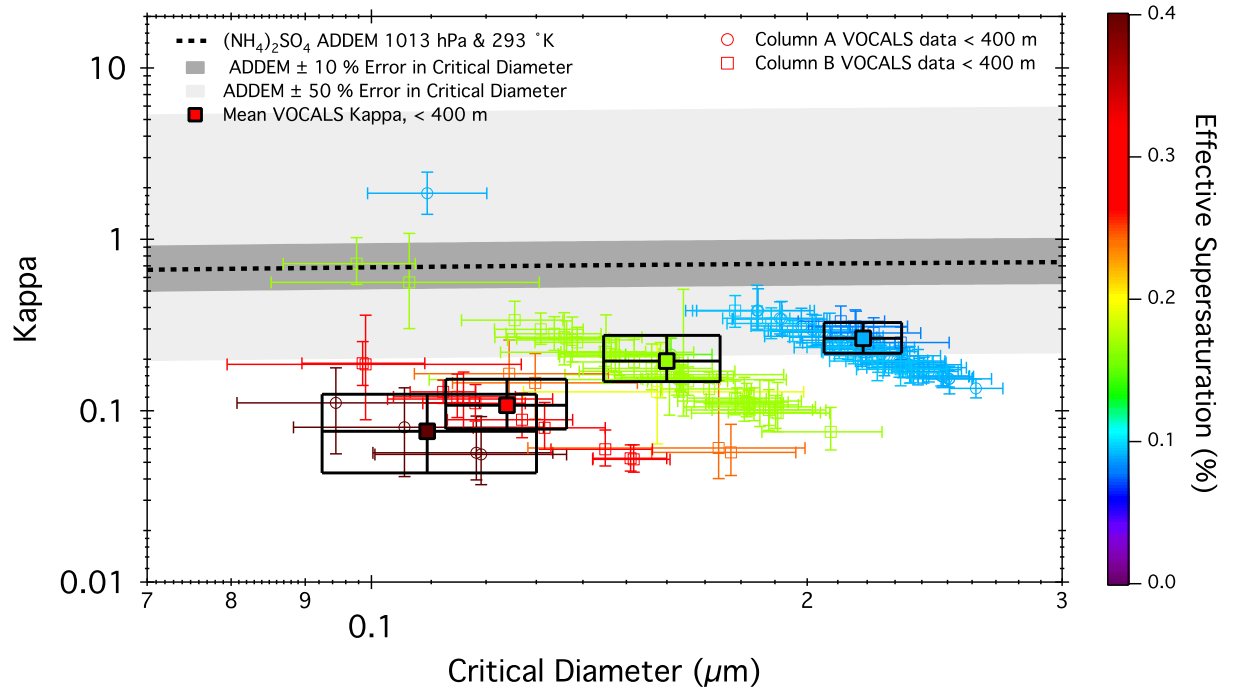


Figure 3.17: Relationship between  $\kappa$  and SMPS derived critical diameter. The error bars express the propagated standard deviation in the averaging of the CCN to match the SMPS measurement frequency. Bound and filled squares represent the mean  $\kappa$  and are colour filled by effective supersaturation. The larger box represents one standard deviation of this mean.

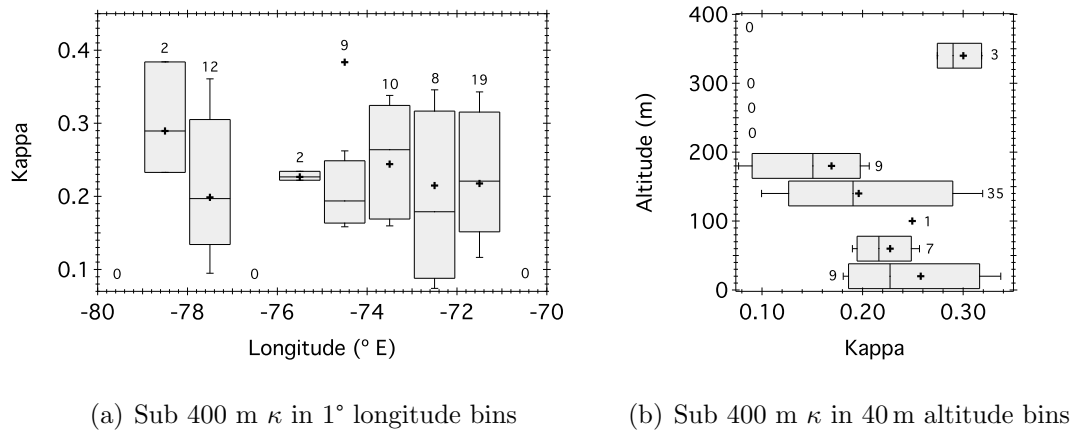


Figure 3.18: Variation in  $\kappa$  with longitude and altitude.

There is little obvious trend in the longitudinal data set of  $\kappa$ . All median values vary between 0.18 and 0.29 and any obvious trends should be considered

insignificant and possibly skewed to specific flights on specific dates because of the very small population numbers of the data set. In particular there is no apparent effect of the increase in organic sulphate ratio, which should be reflected in a decrease of  $\kappa$ , seen at the mid latitudes in Figure 3.4(d). Overall the median values for both latitude bins between 74° and 76° W fall within the interquartile ranges of all the other latitudes. The anomalous mean value between 74° and 75° W is driven by one value of  $\kappa$  above 1. The apparent lack of effect in the increased organic sulphate ratio of the aerosol on  $\kappa$  is not statistically significant. The co-located ratio mean for these two degree boxes is 0.38 close to the maximum latitudinal mean measured on the transect. This would suggest that unlike other studies (Roberts et al., 2010; Asa-Awuku et al., 2011) the organic content is not the primary driver of the hygroscopicity of the aerosol in this environment, at least those organic species which are measured by the AMS. Other recent studies have shown that bulk or even size resolved aerosol composition maybe insufficient to predict an aerosol's bulk hygroscopicity, due to the presence of marginally hygroscopic modes not captured by the AMS (McFiggans et al., 2006; Wex et al., 2010).

The vertical segregated data also has no significant trend with altitude. There is a fall with altitude over the first 200 m from a  $\kappa$  of 0.23 to 0.15 as would be expected in a maritime environment. Though the values are too small to be dominated by sea salt entrainment (Pringle et al., 2010) which is the usual determinant of this altitude function over the ocean. Above this is an increase in  $\kappa$  between 320 to 360 m; though with such small population sizes and no data between 200 and 320 m this trend is weak. A lack of any strong trend in the SEP suggests where data is available that the hygroscopicity of the aerosol is fairly constant in both the horizontal and vertical planes. This suggests the aerosol in this environment is all of a similar composition and mixing state.

Table 3.5: Kappa and critical diameter calculations binned by longitudinal for SPMS scans from the lowest 400 m. The maximum and minimum values are calculated from the propagation of the errors associated with the variability in the CCN measured during each SMPS scan.

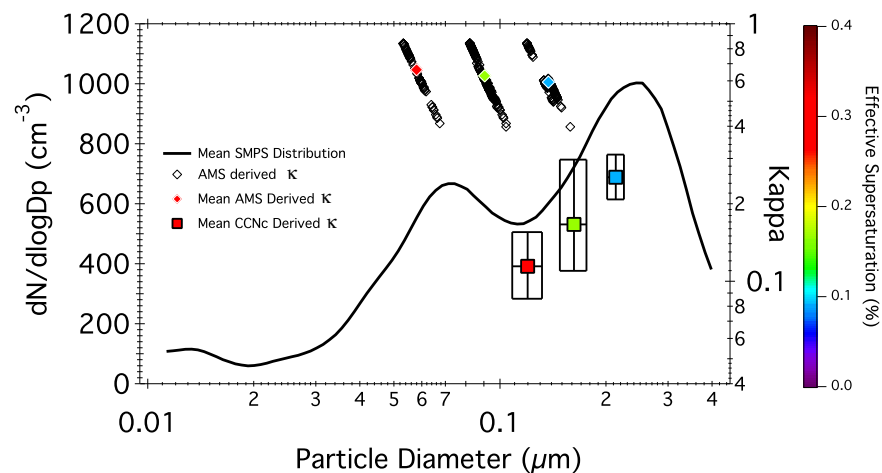
Zone	Altitude (m)	$\kappa$	Critical Diameter ( $\mu\text{m}$ )	N
High Sulphate	0 - 400	$0.210 \pm 0.081$	$0.183 \pm 0.046$	19
Falling Sulphate	0 - 400	$0.260 \pm 0.300$	$0.196 \pm 0.050$	29
Low Sulphate	0 - 400	$0.194 \pm 0.095$	$0.195 \pm 0.052$	14

In binning the  $\kappa$  into larger longitudinal sections, which correspond to the sulphate zones, (see Table 3.3) a humpback pattern emerges with the highest  $\kappa$  values being in the falling sulphate zone. There is little variability in the hygroscopicity of the ambient aerosol with mean values all falling within one standard deviation of one another, a trend borne out in the reported humidigrams from the BAe-146 wet nephelometer system (Allen et al., 2011) where there is little or no variation in growth factor across the 20° S transect.

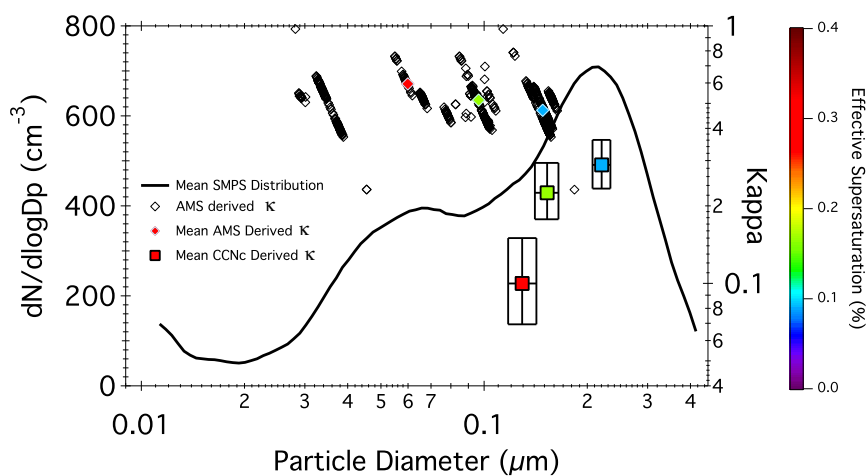
Hygroscopicity, described here using  $\kappa$ , is an intrinsic property of an aerosol's chemical composition and the ability of an aerosol to activate into a cloud droplet is a property of both its size and its composition. The mean CCNc derived  $\kappa$  values split by sulphate loading zone during the VOCALS campaign are plotted against their critical diameters in Figure 3.19. Error bars represent one standard deviation of the means of the CCNc measurements carried through the same calculations. These data are compared to a  $\kappa$  derived using the AMS bulk composition data. Where inorganic speciation under the MMR method and organic mass fractions measured directly by the AMS are used to calculate the critical diameter from Equation 3.5 on page 198 and Equation 3.6 on page 199. The organics are assumed to be insoluble and have a density of  $1270 \text{ kg m}^{-3}$ . Critical



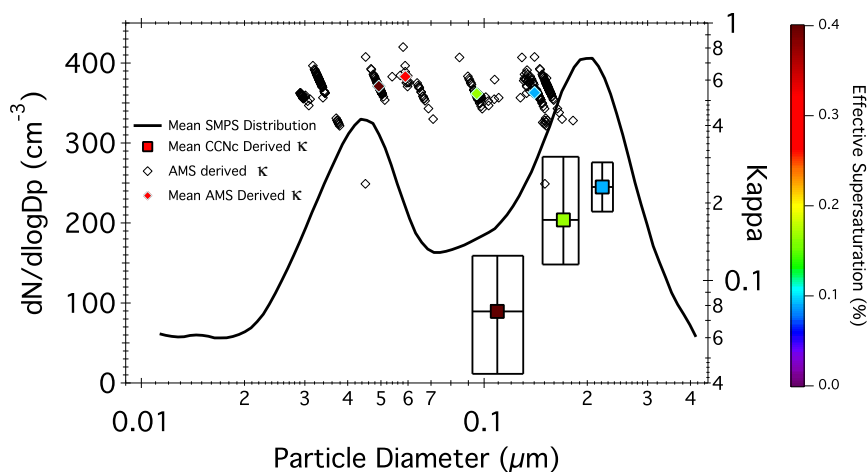
diameters were then fed into Equation 1.4 on page 40 to estimate the mean bulk  $\kappa$  for each data point. The AMS derived values have been averaged over the same periods as the CCNc individual supersaturation data to match the scan time of the SMPS before being plotted against calculated critical diameters. In all zones the CCN derived hygroscopicities are substantially lower than those inferred from the non-refractory bulk aerosol composition. This overestimation of the AMS derived  $\kappa$  is greatest at higher effective supersaturations. With the CCNc derived  $\kappa$  being between 14 and 17 % of the AMS derived value at supersaturations of 0.32 and 0.43 %. This overestimation is reduced at lower supersaturations with CCNc derived  $\kappa$  being on average 49 % at 0.09 % effective supersaturation of the values estimated from the bulk aerosol composition for the whole dataset.



(a) High sulphate zone.



(b) Falling sulphate zone.



(c) Low sulphate zone.

Figure 3.19: AMS and CCNc derived  $\kappa$  compared with mean SMPS distributions for each zone. The data for this figure can also be seen in Table 3.6. Filled squares represent the CCNc derived and filled diamonds represent the AMS derived  $\kappa$ . The colour array for both represent the supersaturation.

Table 3.6: Mean and relative standard deviation measurements for the data plotted in Figure 3.19.

			Supersaturation			
			0.09 %	0.17 %	0.32 %	0.43 %
HSZ	$\kappa$	CCNc	0.25±0.22	0.17±0.29	0.11±0.38	-
		AMS	0.59±0.17	0.63±0.19	0.66±0.18	-
	$d_c$	CCNc	0.21±0.07	0.16±0.10	0.12±0.13	-
		AMS	0.14±0.06	0.09±0.06	0.06±0.06	-
FSZ	$\kappa$	CCNc	0.29±1.18	0.22±0.64	0.10±0.58	-
		AMS	0.47±0.18	0.51±0.18	0.60±0.14	-
	$d_c$	CCNc	0.22±0.15	0.15±0.16	0.13±0.18	-
		AMS	0.15±0.06	0.10±0.05	0.06±0.05	-
LSZ	$\kappa$	CCNc	0.23±0.32	0.17±0.83	-	0.08±0.34
		AMS	0.54±0.30	0.53±0.07	0.62±0.09	0.57±0.07
	$d_c$	CCNc	0.22±0.09	0.17±0.17	-	0.11±0.11
		AMS	0.14±0.06	0.10±0.03	0.06±0.03	0.05±0.02

There are a number of reasons for the AMS derived  $\kappa$  to over predict the CCNc.

(i). Without size resolved data the AMS instrument can only estimate the mean bulk aerosol composition and as such the  $\kappa$  derived by this method will be skewed in favour of larger particles. Larger particles have more mass that inherently contains a higher fraction of soluble material. This characteristic of the AMS is a function of the instrument being sensitive to mass and not number (Wex et al., 2010; McFiggans et al., 2006). However, this would not be expected to lead to such large discrepancies between the two methodologies.

(ii). The composition data from the AMS is of non-refractory components only, those species that will volatilise between 550 and 600° C. This is acceptable when trying to understanding the mass loading budgets of the commonest aerosol

species. However, refractory particles play a disproportionate role in an aerosol's mean hygroscopicity compared to their low mass fractions in the environment. Three functional types of refractory particles are considered here, mineral dust, black carbon (BC) and sea salt. The former two of these can be considered to form a group of marginally hygroscopic particulates. Mineral dust aerosols having values of  $\kappa$  between 0.05 and the kelvin line ( $\kappa = 0.0$ ) (Kumar et al., 2011). Whilst ambient elemental or BC can be considered as non-hygroscopic and therefore won't take up water. However, both these refractory particle types have complex aging pathways which are dependent on many processes that will eventually modify their hygroscopicities through the chemistry of particle coatings (McMeeking et al., 2011). Sea salt, however, is extremely hygroscopic, with a  $\kappa$  of 1.28 (Petters and Kreidenweis, 2007).

During VOCALS sea salt contribution to the submicron aerosol was estimated from ion chromatography to  $9 \pm 6\%$  (Hawkins et al., 2010) on board the RH Brown. The VACC instrument on the BAe-146 estimated the contribution of core aerosol, those aerosols that do not volatilise below  $750^\circ\text{C}$ , namely mineral dust and sea salt, to be in the region of 6.3 to 7.9% in the size range between 0.1 and  $0.5\mu\text{m}$ .

Crustal and metal elements were also measured on board the RH Brown using X-ray fluorescence. Average contributions for the project are  $17.68 \pm 15.63\text{ngm}^{-3}$  to the overall mass of particles measured, only 1.5% of the mass of sulphate and organics averaged over the same period. The contribution of these crustal elements was higher during coastal and mixed coastal and maritime air flow than purely maritime as would be expected. The contribution of elemental carbon to the aerosol burden was not directly measured on any platform in the literature.

Both the DOE G1 and the BAe-146 flew particle soot absorption photome-

ters (PSAP, Radiance Research, Seattle) which measure aerosol absorption from which elemental carbon mass loadings can be inferred. The overall absorption measured from the BAe-146 was, however, too low to quantify with a project median of  $0.9 \text{ Mm}^{-1}$ . This equates to a median loading in the region of  $0.096 \mu\text{g m}^{-3}$  irrespective of any of the limitations of the measurement itself (Bond et al., 1999). This was also the findings from the DOE G-1 (Kleinman et al., 2012).

Neither the sea salt or the crustal material have been added to the AMS bulk composition estimate of  $\kappa$  as no specific information on these components is available for individual SMPS scans, the primary time step used here. The contribution from sea salt can be expected to be very weak, non-existent or highly episodic as shown by the low estimate of CCNc derived  $\kappa$ . Using the simple Equation 3.4 from Wex et al. (2010)

$$\kappa = \chi_{org} * 0.1 + \chi_{inorg} * 0.6 + \chi_{NaCl} * 1.28, \quad (3.4)$$

where  $\chi_{org}$ ,  $\chi_{inorg}$  and  $\chi_{NaCl}$  are mass fractions of organics, inorganics and sea salt, respectively. The mean mass fractions for the whole of the BAe-146 VOCALS data set for inorganics (0.88) and organics (0.12) whilst assuming a zero contribution from sea salt can be used to estimate a theoretical  $\kappa$  value of 0.54. This is some 33 % greater than the mean CCNc derived estimate. If 9 %, the estimate of sea salt contributions by Hawkins et al. (2010), of the aerosol mass is assumed to be sea salt then the calculation of  $\kappa$  becomes 0.66, 45 % more than the mean CCNc estimate. The CCNc and SMPS do not differentiate between refractory and non-refractory particles and as such any sea salt in the aerosol population will be included in the derived estimate of  $\kappa$ . Since the maximum  $\kappa$  estimated by the CCNc is 0.29 the contribution from sea salt for these data must be minimal. This is not to say there is no sea salt in the aerosol fraction.

Cloud water from the VOCALS campaign has on average a volume weighted average  $\text{Na}^+$  content of 37% (Benedict et al., 2012) this contribution to the cloud water could be highly episodic and correlated to periods of high windspeed. The zero sea salt content assumed here fits with the wind speeds correlations to sea salt uplift. Where wind speeds greater than  $10\text{ ms}^{-1}$  on a regional scale are required to entrain sea salt. The highest mean wind speeds encountered during VOCALS were  $9.8\text{ ms}^{-1} \pm 2.2\text{ ms}^{-1}$  at 750 m in the low sulphate zone. The mean winds between the sea surface and 200 m were  $4.4\text{ ms}^{-1} \pm 1.7\text{ ms}^{-1}$ ,  $5.8\text{ ms}^{-1} \pm 1.7\text{ ms}^{-1}$  and  $8.7\text{ ms}^{-1} \pm 2.1\text{ ms}^{-1}$  for the three longitudinal zones high, falling and low sulphate, respectively. It should also be noted that the sea salt measurements, Hawkins et al. (2010) were taken from the 18 m on the RH Brown, some 140 m below the aircraft's most numerous SLR altitude included here. The comparative low values of CCNc derived  $\kappa$  does however, suggest a contribution from a marginally hygroscopic mode not sampled by the AMS.

(iii). The inability of the AMS to sample refractory particles leads to inaccuracies in estimated  $\kappa$ . This is exacerbated in this environment by the presence of an external mixture containing both dust and organics. Hawkins et al. (2010) showed AMS organic mass on board the RH Brown during VOCALS to be 2.4 times that collected on filter substrate and measured by FTIR spectroscopy. This missing organic fraction, carboxylic acid, correlated well to crustal elements and was negatively correlated to sulphate ions suggesting that the dust and organics formed an external mixture not captured by the AMS. This provides another possible reason for the mirroring seen between the organic and sulphate mass fractions with longitude in Figure 3.4(a) and 3.4(c) on page 139. This organic and dust fraction was not captured by the AMS due to its refractory core. It was assumed by Hawkins et al. (2010) that the collection efficiency for this aerosol was too low to capture the organic signal and that the particles simply bounce

off the AMS vaporiser before the organics in the particle had evaporated. Even if this were not the case and the organics were to volatilise on the vaporiser no information would be obtained about the non-refractory core of the particle. The negative correlation seen in the longitudinal mass fractions in the previous section, particularly in the falling sulphate zone indicate that a portion of the organics associated with this possible external dust mixture are being captured or that a second external mixture is present. Given that the SMPS and CCNc instrument have no bias in the sampling of this organic dust aerosol fraction its effects will be included in the estimation of  $\kappa$ . Given that the organics and dust both have lower affinities for water than any of the sulphate species measured the CCNc derived  $\kappa$  would be expected to be lower than that estimated from the bulk AMS methodology, as is the case. The hygroscopicity of this external organic dust mixture would depend on the organic chemistry and the form of the dust organic conglomeration, full film, partial film or inclusion (McFiggans et al., 2006). There is no detailed particle diameter measurements for the two organic mass analysis methods given in Hawkins et al. (2010). Though it is considered in their work that some of the discrepancy in mass maybe due to particles with diameters greater than the 100 % transmission limit of the AMS being collected on to the filters. The AMS particle transmission efficiency is 100 % between particle diameters of 0.1 and 0.6  $\mu\text{m}$  at sea level (Bahreini et al., 2008). These diameters span the particles sizes relevant for activation given by the critical diameters in Figure 3.19.

Credence to the presence of an external mixture, at least with respect to hygroscopicity and possibly composition, is corroborated by the second stand out characteristic of Figure 3.19. That the CCNc derived  $\kappa$  falls with increasing CCNc effective supersaturation. In a perfectly internally mixed aerosol  $\kappa$  would be expected to be insensitive to supersaturation, as seen in the AMS derived  $\kappa$ .

In the interests of scientific rigour the other possible reasons for this trend should be briefly discussed before returning to the effects of an external mixture on  $\kappa$ .

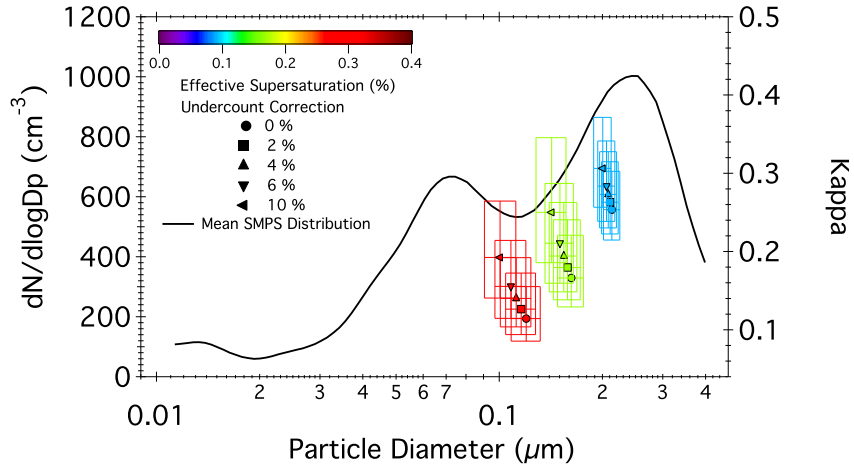
This falling trend in CCNc  $\kappa$  could be explained by a reduction in the CCNc column midline supersaturation that is independent of usual temperature gradient controls. Water vapour competition as discussed in Section 2.1.3 could explain this trend. However, as already discussed this phenomenon effects the midline supersaturation by less than 10 % unless the CCN number concentrations exceed 5,000 particles  $\text{cm}^{-3}$  (Lathem and Nenes, 2011). This process of water vapour competition can be excluded from the discussion as the CCN concentrations rarely exceeded 500 particles  $\text{cm}^{-3}$  during the VOCALS field campaign even at the higher supersaturations where this effect is more prevalent. This mechanism would also be evident in the TDGA, in Section 3.4 on page 239. Evidence of this would be expressed as data that fall solely below the pressure corrected ammonium sulphate mean droplet diameter line. There is no evidence of this being the case.

It is feasible that the fall in CCNc derived  $\kappa$  with effective supersaturation is due to an instrument bias. A systematic undercounting by the CCNc OPC as compared to the CPC used in the SMPS system. If the CCNc only counts 80 % of the particles detected by the SMPS, fewer particles are activated than would be expected from the SMPS distribution resulting in a reduced value of  $\kappa$ . This effect is magnified at higher supersaturations leading to a increasing under estimation with supersaturations. A trend equivalent to that seen in these data.

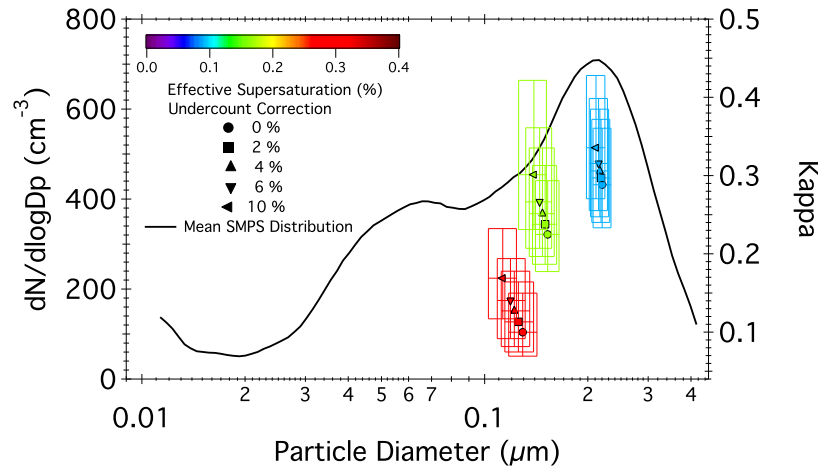
In order to test this theory a direct comparison between the counting efficiency of the SMPS and CCNc would be required in either the field or the laboratory. For logistical reasons this was not done. However, each instrument was operated in tandem with a third cross referenced instrument in either laboratory comparisons or routine CCNc calibrations. The CCNc calibration of column B under-



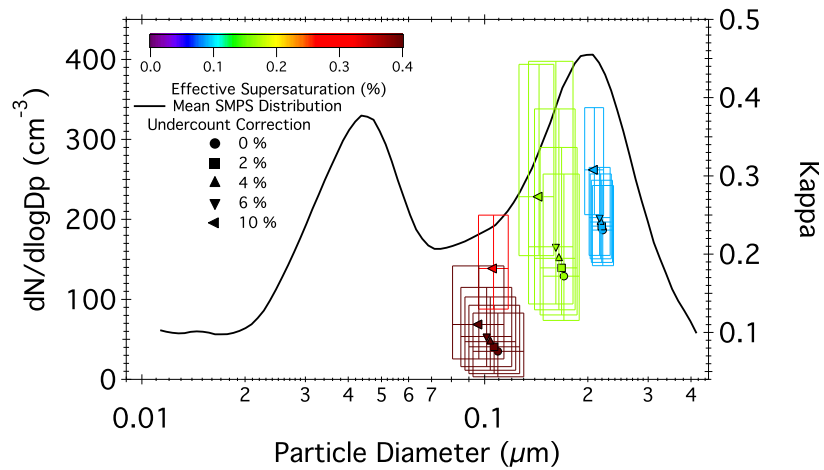
taken post campaign used a lab based TSI 3776 that was also used during the VOCALS project to compare aircraft CPCs. During the post campaign calibration the mean activated fraction of column B was  $0.92 \pm 0.04\%$  for ammonium sulphate aerosol between the diameters of 0.05 and  $0.1\ \mu\text{m}$ . When this TSI 3776 CPC was compared to the modified 3786 used for the SMPS system they agreed to within 2%, with the 3786 under reading, across a range from tens to thousands of particles  $\text{cm}^{-3}$ . This laboratory based 3776 CPC was itself involved in lab based comparison with a CPC whose counting efficiency had been verified in experiments with an electrometer (TSI inc., 3068B). A second line of verification of the counting efficiency was provided by the pre-campaign calibration. This experiment used a third CPC, a TSI 3010, which was also involved in the laboratory based CPC electrometer intercomparison. This 3010 CPC over read the 3776 by 2% in the concentration range applicable to the CCNc calibration. Where mean activated fractions of  $0.95 \pm 0.03$  and  $0.94 \pm 0.04$  were achieved for both columns A and B, respectively. Overall this suggests a maximum CCNc OPCs undercount somewhere in the region of  $6 \pm 4\%$ . Though a more conservative estimate based on the calibration undertaken some months prior to the project suggests a mean undercount closer to  $4 \pm 4\%$ . A 4% systematic undercount has little effect on the overall magnitude of  $\kappa$  and no effect on the underlying trend of falling hygroscopicity with increasing effective supersaturation as can be seen in Figure 3.20.



(a) High sulphate zone.



(b) Falling sulphate zone.



(c) Low sulphate zone.

Figure 3.20: CCNc derived  $\kappa$  of differing levels of instrument undercounting (circle at 0 %, squares 2 %, up triangles 4 %, down triangles 6 % and left triangles 10 %) compared with mean SMPS distributions (solid black line) for each zone. The colour array is the supersaturation.

The effect of a 0 to a 10% undercount in the CCNc OPC on  $\kappa$  can be seen in Figure 3.20. In all instances of undercounting the estimated  $\kappa$  is increased and the critical diameter reduced. Even with a 10 % undercount, where in all cases the CCNc derived  $\kappa$  is brought closer to the AMS derived value. The CCNc derived  $\kappa$  is still on average 28 % lower than the AMS in the falling sulphate zone, that zone where the AMS derived and CCNc derived  $\kappa$  are closest. On average across, all latitudes, the CCNc derived  $\kappa$  is still only 40 % of the AMS derived values even with an assumed 10 % undercount. The fall in  $\kappa$  with increasing effective supersaturation holds across all levels of undercounting corrections and suggests categorically that there is a change in aerosol hygroscopicity and subsequently chemistry with size. This would be expected in an externally mixed aerosol and shows that the effect is not due solely to an instrument counting bias. As there was not an explicit instrument intercomparison during the project itself, a definitive level for any bias can't be carried through the rest of this work. As such no correction for undercounting is used, though it should be recognised in any further discussion that a small undercount somewhere in the region of 4 % is likely.

In returning to the discussion of the external mixture, the form of the mixture needs consideration. With respect to an aerosol population's hygroscopicity an external mixture is where at any given diameter in the distribution there are particles with different compositions and different hygroscopicities. However, an aerosol can also be a quasi-internal mixture where a spread of hygroscopicities are observed around a mean hygroscopicity related to the mean aerosol composition. If the aerosol mix was only quasi-internally mixed the resultant hygroscopicities should result in a spread, typically in the order of 11 % (McFiggans et al., 2006; Wex et al., 2010), around the mean hygroscopicity. This is not the case with these data where there is a distinct falling trend in the region of 44 % in the high sul-

phate zone for example. This large fall in  $\kappa$  with supersaturation is characteristic of a fully externally mixed aerosol. The data in Table 3.6 on page 184 and Figure 3.19 alludes to the fact that there is a larger proportion of a less hygroscopic mode at diameters below than  $0.2\ \mu\text{m}$  than above this diameter. This would give some indication that there is a larger proportion of the more hygroscopic aerosol in the larger diameters measured by the SMPS. Those diameters with the most mass and those that therefore dominate the AMS bulk composition data. There is a trend for smaller particles, nearer  $0.05\ \mu\text{m}$  to have a lower affinity for water than those closer to  $0.2\ \mu\text{m}$  due to the high organic content seen in sub  $0.1\ \mu\text{m}$  particles, especially close to source. Assuming that the largest mode in all these distributions is a product of cloud processing then it would stand to reason that this mode contained more sulphate mass fraction and was more hygroscopic.

Using the  $\kappa$  allows for comparison between aerosol types, from different sources and different environments. Table 3.7 contains  $\kappa$  measurements taken of pure substances in the laboratory, those taken at field stations and from other aircraft around the world and generic values used to parameterise some models. In comparison with the literature these sub 400 m derived  $\kappa$  estimates from this work show good agreements for similar environments using the same technique. The VOCALS project had a  $\kappa$  of  $0.21 \pm 0.18$ . The mean aerosol volume fraction composition was  $0.29 (\pm 0.26)$  for ammonium sulphate,  $0.52 (\pm 0.33)$  for ammonium bisulphate,  $0.01 (\pm 0.03)$  for sulphuric acid and  $0.18 (\pm 0.11)$  for organics respectively. In flights in the northwestern Pacific during the INTEx-B campaign Roberts et al. (2010) estimated the  $\kappa$  to be  $0.21 \pm 2.0$ . This was in an airmass with a mean CN count of  $793\ \text{particles cm}^{-3} (\pm 370)$ . At an effective supersaturation of 0.35 %, with CCN concentrations of  $156\ \text{particles cm}^{-3} (\pm 85)$  and a bimodal aerosol distribution with a median diameter of  $0.136\ \mu\text{m}$ . The mean OMF of this aerosol was  $0.18 (\pm 0.18)$  with similar chemistry consisting primarily

of sulphate and ammonium ions. Moore et al. (2012) inferred  $\kappa$  values between 0.1 and 0.25 for a range of environments. The values for the marine outflow in the Los Angeles basin, measured on the NOAA P3 aircraft, ranged between 0.15 and 0.21 (values digitised from Figure 5 in the publication). The aerosol distribution in this air mass was bimodal with AMS derived volume fraction of 49 % for organics, 21 % ammonium sulphate, 8 % ammonium nitrate, 3 % sulphuric acid and 8 % ammonium bisulphate.  $\kappa$  was estimated from a remote marine background site, Finokalia station, on the island of Crete ( $35^{\circ}32'N$ ,  $25^{\circ}67'E$ ). The mean  $\kappa$  inferred from CCN measurements was 0.24. This value was strongly correlated to the amount of sulphate in the aerosol. The aerosol composition was assumed to be composed of ammonium sulphate and organics where 46 % of the total aerosol mass was ammonium sulphate and the remainder organics. All three of these case studies share similar conditions to the VOCALS data sets in terms of chemistry being primarily a mixture of ammonium sulphate and organics, however the contribution of organics to the overall mass in most of the literature far exceeds the values from this work. Where the mean organic volume fraction in the sub 400 m data set is 0.18 ( $\pm 0.14$ ).

Table 3.7:  $\kappa$  values taken from the literature. It should be noted that all these measurements are made in the boundary layer unless specifically stated otherwise. Again unless otherwise stated these data are derived from CCNc measurements and not other methodologies.

Compound	$\kappa$			Reference
	$\kappa_{\text{low}}$	$\kappa_{\text{mean}}$	$\kappa_{\text{high}}$	
$(\text{NH}_4)_2\text{SO}_4$	-	0.61	-	Petters and Kreidenweis (2007)
$\text{H}_2\text{SO}_4$	-	0.90	-	Petters and Kreidenweis (2007)
NaCl	-	1.28	-	Petters and Kreidenweis (2007)
levoglucosan	0.19	0.21	0.22	Petters and Kreidenweis (2007)

Environment	Field Data			Reference
	$\kappa_{\text{low}}$	$\kappa_{\text{mean}}$	$\kappa_{\text{high}}$	
Urban <sup>1</sup>	-	0.30	-	Wex et al. (2010)
Rural <sup>1</sup>	-	0.24	-	Wex et al. (2010)
Maritime <sup>1</sup>	-	0.45	-	Wex et al. (2010)
Continental/Maritime, USA	0.08	-	0.88	Asa-Awuku et al. (2011)
Continental, USA	-	0.25	-	Roberts et al. (2010)
Continental/Maritime, USA	-	0.21	-	Roberts et al. (2010)
Pristine Rainforest, BR	0.12	0.16	0.20	Gunthe et al. (2009)
Continental, CH	-	0.34	-	Juranyi et al. (2010)
Continental/Maritime, GR	0.15	0.24	0.43	Bougiatioti et al. (2009)
Maritime, Arctic	0.10	-	0.30	Moore et al. (2011)
Continental, USA	0.11	-	0.25	Moore et al. (2012)
Continental, Asia	0.10	0.30	0.50	Rose et al. (2010)
Maritime, Caribbean	-	$0.60 \pm 0.2$	-	Allan et al. (2008) <sup>2</sup>
Maritime, Caribbean	-	$0.87 \pm 0.24$	-	Hudson (2007) <sup>2</sup>
Continental/Maritime, SEP	0.05	$0.21 \pm 0.18$	0.73	This study

Environment	Model Data			Reference
	$\kappa_{\text{low}}$	$\kappa_{\text{mean}}$	$\kappa_{\text{high}}$	
Global, Continental <sup>3</sup>	-	$0.27 \pm 0.21$	-	Pringle et al. (2010)
Global, Maritime <sup>3</sup>	-	$0.72 \pm 0.24$	-	Pringle et al. (2010)

<sup>1</sup> Data derived from HTDMA data not CCNc data

<sup>2</sup> These data are taken from Table 2 in Pringle et al. (2010)

<sup>3</sup> The  $\kappa$  values are estimates at the surface

In summary and in partial answer to question three and four posed in Chapter 1. Measurements of hygroscopicity from the SEP have not been made before. The CCNc derived  $\kappa$  for the VOCALS region compares well to similar environments in the literature. However, they are somewhat lower than mean global maritime  $\kappa$ ,  $0.72 \pm 0.24$  and much closer to the mean global continental value of  $0.27 \pm 0.21$  used in modelling studies (Pringle et al., 2010). This may be a function of the proximity of this study, and those considered in the paragraph above, to continental aerosol sources and the local synoptic southerly winds encountered during the project. As well as low or non-existent contributions from sea salt. There appears to be no significant difference between the hygroscopicity of the aerosol measured between zones of longitude. The aerosol is, with respect to hygroscopicity, an external mixture. Whether this extends to the composition as inferred by Hawkins et al. (2010) is impossible to qualify with the data used here. However, the dust organic mixture identified in their work is likely to have more influence at larger diameters. Where as in this study It is clearly shown that the marginally hygroscopic mode has more pronounced effect at smaller diameters, Figure 3.19 on page 183. As such it is unlikely that the dust organic mixture is the controlling factor in this study. Other sources for marginally hygroscopic modes not captured by the AMS are; marine organics, local shipping and long range transport. The former in this list has been shown to have minimal contribution. Even at low levels of pollution in the SEP Shank et al. (2012) has shown that organics were correlated to BC and therefore not of a primary biological origin. It is not uncommon in oligotrophic waters, such as the SEP, where naturally there is little marine productivity to have little or no contribution to the aerosol burden from marine organics. There is little evidence of local shipping having been the major source. Figure 3.5 on page 141 shows no distinct correlation between CO and organic sulphate ratio which would be indicative of a local combustion source from shipping. Long range transport from the region to the south of the SEP is

the most likely source of the marginally hygroscopic mode identified from the  $\kappa$  analysis.

It is important to be able to derive the value of  $\kappa$  using the CCNc method as it is less discriminatory than the value derived from the AMS. The inability of the AMS to probe the intricacies in the aerosol composition in the SEP has implications for modelling studies. The issues surrounding the use of these data in isolation are discussed in the following section.



### 3.3 CCN Closure

The activation properties of an atmospheric aerosol determine to a large part the extent of cloud formation and propagation. Comparing measurements of CCN concentrations to predictions based on activation theory, a CCN closure study, can serve as both a gross validation of the measurements and a more detailed validation of the theory (VanReken et al., 2003). These closures also provide a mechanisms for quantifying how well the models or to what extent simplifications in the models can be used without jeopardising their predictive ability in an effort to understand aerosol cloud interactions. This is important for parameterising sub-grid processes in climate models (Wood et al., 2011).

The data used for the CCN closure studies was heavily stratified. Data were used only where the following caveats were met; the aircraft was in straight and level flight, the SMPS data passed the screening procedure (including being below 400m), the AMS recorded two or more data points for the period and CCN data had passed all the diagnostic and QA tests routinely applied. Once these data were defined all parameters were averaged to the same time resolution as the SMPS. This gives this analysis a spatial scale of approximately 6 km over which the aerosol is assumed to be distributed uniformly.

The AMS data can be used to calculate the critical diameter ( $d_c$ ) of the sampled aerosol using simplified Köhler theory. Assuming that the aerosol is composed of a mixture of soluble and insoluble fractions (Seinfeld and Pandis, 2006; Asa-Awuku et al., 2011; Moore et al., 2012)

$$d_c = \left( s^2 \frac{27}{256} \left( \frac{\rho_w RT}{M_w \sigma} \right)^3 \left( \frac{M_w}{\rho_w} \right) \frac{\rho_s}{M_s} \sum_s v_s \varepsilon_s \right), \quad (3.5)$$

where  $R$  is the universal gas constant.  $T$  is the average temperature across the

CCNc flow column.  $\sigma$  is the droplet surface tension at the point of activation (calculated at the temperature of the CCNc OPC using the Eötvös Rule).  $M_s$  is the molar mass of each solute.  $M_w$  is the molar mass of water.  $\rho_w$  is the density of water and  $v_s$  the the effective van't Hoffs factor of the solute. For which values of 2.31, 2.5 and 2.0 were used for ammonium sulphate, ammonium bisulphate and sulphuric acid, respectively (Wise et al., 2003). The more complex Pitzer water activity correlations were not used here (Clegg and Brimblecombe, 1988).  $\varepsilon_s$  is the volume fraction of each solute, estimated assuming an additive function as

$$\varepsilon_s = \frac{\frac{m_s}{\rho_s}}{\sum_j \frac{m_j}{\rho_j}}, \quad (3.6)$$

where  $m_j$  and  $\rho_j$  are the mass fraction and density, respectively, of an aerosol component ‘ $j$ ’. The density of the organic fraction was assumed to be  $1270 \text{ kg m}^{-3}$  (Asa-Awuku et al., 2011). Where ammonium and sulphate dominate the inorganic mass the speciation of ammonium sulphate salts depends on the molar ratio of ammonium to sulphate ions,  $R_{so4}$  (Nenes et al., 1998), this relationship can be seen in Table 3.8.

$R_{so4}$	Species One				Species Two		
	Form	$M_s$	$\rho_s$	Form	$M_s$	$\rho_s$	
<1	sulfuric acid	0.098	1841	ammonium bisulphate	0.115	1780	
$1 < 2$	ammonium bisulphate	0.115	1780	ammonium sulphate	0.132	1760	
> 2	ammonium sulphate	0.132	1760	N/A	N/A	N/A	

**Table 3.8:** Table showing the speciation of ammonium and sulphate ions referenced to the value of  $R_{so4}$ .

This model is one of a range of models that could be used to generate critical

diameters for comparison to the measurements. An exhaustive list is given in Topping et al. (2005a). The simplified Köhler model was chosen due to its wide use in the literature and its simplicity, in that there is no complicated thermodynamic model architecture to learn and that it can be coded and run quickly and simply. In choosing any model there are necessarily biases in the output. Biases in this model can occur via the parameterisation of the various composition related terms and in the simplification of the processes effecting multicomponent aerosol activation. In comparing this simplified model to the thermodynamic modelling framework, ADDEM (Topping et al., 2005a) for ammonium sulphate activation at 293.15 K. The simplified Köhler predicted a critical supersaturation 9 % higher at the mean critical diameter for the VOCALS project,  $0.182\text{ }\mu\text{m}$  than ADDEM. The source of this bias stems from the parameterisation of surface tension, molecular weight, solubility and van't Hoff factor. Generic biases are considered briefly here but studied quantitatively later in this chapter by running the simplified model across a wide parameter space bookended by extremes from the literature and this work.

Surface tension is assumed in this basic model to be that of bulk water and to be invariant with droplet size and solution strength. This is a simplification as the surface tension of a droplet can be affected by many processes. It can be reduced by the action of surfactants such as water soluble organic compounds (WSOC). Or increased by the effects of solute concentration in nascent droplets and ion associations between the surface and the bulk of these drops (Ervens et al., 2005). Neither does this model capture any surface bulk partitioning of organics that can effect both the Kelvin term via the surface tension and the solute term by reducing the availability of solute in the bulk solution (Topping et al., 2005a; McFiggans et al., 2006; Prisle et al., 2008).

Molecular weight of the aerosol components are well known for the inorganic

salts. Values for organics, however, can vary by an order of magnitude (Ervens et al., 2005). Since the volume fractions of organics are relatively low, less than 20 % of total aerosol volume in this study, then the effect on bulk solute term is considered to be negligible. This has been shown experimentally where the addition of adipic acid, a soluble organic salt, to a pure ammonium sulphate aerosol does not significantly increase the activation diameter until the mole fraction is upwards of 90 % (McFiggans et al. (2006) and references therein). The effect of having an inclusion of marginally soluble material will also effect the solute term of the equation by reducing the number of molecules of solute in the droplet solution. This addition of limited solubility necessarily leads to an increase in the critical supersaturation and critical diameter. The maximum effect via this process is achieved when there is an inclusion of an insoluble component (McFiggans et al., 2006; Seinfeld and Pandis, 2006). This simple model also ignores effect of soluble gases, such as nitric acid, on the activation of droplets. The presence of such gases act in opposition to the inclusion of lower solubility components in reducing the critical diameter and the critical supersaturation of the droplets if the gas is in limited supply. If the supply of gas is limitless it only acts to reduce the critical supersaturation (McFiggans et al., 2006; Seinfeld and Pandis, 2006).

Variability in the van't Hoff factor is negligible for organics as is often considered to be equal to one (Ervens et al., 2005) and the sensitivity of the model to variability in this parameter is assessed later in the work. The use of unity for organics is a possible source of bias. Wise et al. (2003) showed variability in this parameter between 0.64 and 1.37 for four different organic compounds. The effect of this in this study will be of limited relevance due to the low organic contribution. Solutions in this model are expected to behave ideally as showed by the sum of the product of the volume fraction of each solute in final term of Equation 3.5 and the van't Hoff factor. This is not necessarily always true and the

number of ions in solution is not always independent of solution concentration.

The sources of bias are complex and act on the model in opposing directions to both enhance and reduce the critical diameter. Ervens et al. (2005) investigated the effects of composition on cloud droplet formation by investigating the effects of surface tension, van't Hoff factor, molecular weight and solubility not just in isolation but as an ensemble. The authors used the simplified Köhler equation coupled with an adiabatic cloud parcel model set at a range of constant updraft velocities between 10 and 300  $\text{cm s}^{-1}$ . Though the study was designed to understand the compositional effects of organics on activation, it is a useful insight into other species that share the parameter space explored. All results were compared to an ammonium sulphate base line and the model run for a polydisperse population at two different concentrations, 100 and 5000  $\text{cm}^{-3}$ . The total deviation in droplet number for variation in any one parameter in isolation is  $-70$  to  $+140\%$  for reduced solubility and reduced surface tension, respectively. This was true in the polluted model environment at low updraft velocities. However, when the parameter combinations are representative of real organic compounds, and not one dimensional unrealistic stretching of parameter space, absolute differences to the base line model are reduced. This suggests there is interplay between the terms in the model that preclude any overall bias. The simple Köhler model does not capture the dynamic nature of many of the processes or many of the complexities in multi-component aerosol activation. However, it is the most relevant to use in this work particularly since the majority of information on any one of these more complex parameters, such as Nitric acid concentrations, presence of complex salts or their structure and location of organics in the droplets are unknown.

The measured CCN are compared to five separate models: *(i)* an idealised aerosol made entirely of ammonium sulphate (AS), *(ii)* an internal mixture whose composition is estimated using the bulk inorganic chemistry mass loadings from

the AMS (INORG), (*iii*) an external mixture (EXMIX) of ideally non-hygroscopic organics and internal mixture of inorganics both determined by the AMS bulk composition, (*iv*) an internal mixture of insoluble organics and inorganic salts (INTMIX) as determined by the AMS, (*iv*) an internal mixture of water soluble organics, insoluble organics and inorganics (INTMIX\_WSOC).

AS and INORG models represent the upper limit of the CCN activity as the organic fraction is assumed to have the same physical properties as the inorganic fraction (Lance et al., 2009; Roberts et al., 2010; Asa-Awuku et al., 2011). In the third model, EXMIX, the bulk inorganic and external organics scheme, the aerosol is made up of externally mixed inorganic and organic populations. Where the organic partition is perfectly non-hygroscopic and does not contribute to the CCN number. The relative amount of this proportion and the and inorganic hygroscopic population is again determined by the AMS composition. INTMIX is an internal mixture of insoluble organics and inorganic salts as determined by the AMS composition. This scheme assumes uniformity of composition across the size distribution. The final scheme, INTMIX\_WSOC, is an internal mixture as in the previous model except the organic fraction is now split into water soluble organic compounds (WSOC) and perfectly non-hygroscopic organics. Again the composition is assumed to be uniform across the size distribution. The proportion of organics that are water soluble is assumed to be equal to the mass fraction of  $m/z$  44 taken from Hawkins et al. (2010). Estimated to be  $0.085 \pm 0.057\%$  of  $0.23 \pm 0.1 \mu\text{g m}^{-3}$ . The  $m/z$  44 peak on the spectrum is associated with oxygenated organic material, assumed here to be the equivalent of WSOC (Roberts et al., 2010; Asa-Awuku et al., 2011). The data from Hawkins et al. (2010) used here was collected during the VOCALS-Rex project with an AMS aboard the NOAA R/V Ronald H. Brown Research Vessel.

The model predictions are compared to the observed CCN. The slope and

correlation coefficient were used to summarise the level of agreement. Where a slope of one is perfect agreement, a slope of less than one the model under predicts the observations and a slope greater than one the model over predict the measurements.  $R^2$  values close to one suggest errors from unaccounted compositional data, size distribution variation, random errors and spatiotemporal fluctuations below the averaging period are small. The data was also subjected to two asymmetric relative difference metrics, the normalised mean error (NME) and normal mean bias (NMB), Equations 3.7 and 3.8. The NME indicates the degree of scatter between predictions and observations, the lower the values the less scatter. The NMB reflects the degree of systematic bias between the modelled and measured value; a negative value is consistent with an underestimation by the model and *visa versa*. Large values for both of these indicates that the parameterisations were poorly assumed, or that the correlation is not strong. As such the model with the best fit to measurements is that model with values for both parameters close to zero.

$$NME = \frac{\sum_i^n |P_i - O_i|}{\sum_i^n O_i} \quad (3.7)$$

$$NMB = \frac{\sum_i^n (P_i - O_i)}{\sum_i^n O_i} \quad (3.8)$$

This analysis asks the question, how well can the CCN concentration be estimated using the simplified Köhler equation? it also attempts to quantify the uncertainties associated with using the assumptions of the simplified Köhler equation. These uncertainties are important as the simplifications used here are commonly used in typical large scale models. This CCN closure experiment is not an estimate of cloud droplet number. Though that is a logical extension to this work. There is no attempt to model the disequilibrium in real updrafts required

to model droplet number. However, given a measurement of the aerosol size distribution and an estimate of the bulk aerosol composition how well can the CCN concentration be estimated under certain assumptions of mixing state and organic solubility? The results from the lowest 400 m of the MBL are plotted in Figure 3.21. The difference metrics used to describe the level of prediction accuracy and scatter are in Table 3.9.  $N_p/N_o$  in this table refers to quotient of the number of predicted CCN to observed.



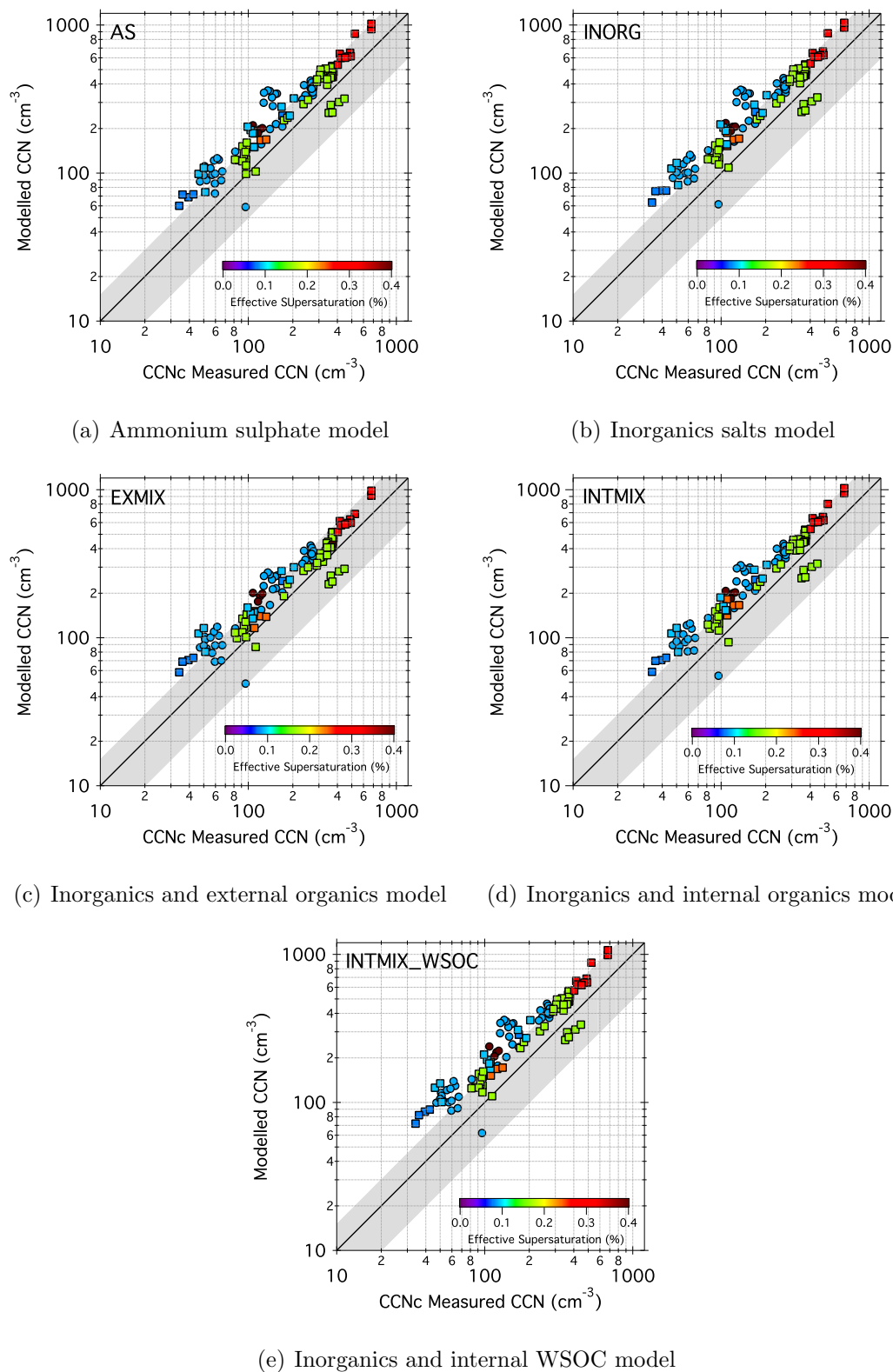


Figure 3.21: Five physiochemical schemes of the simplified Köhler equation compared to CCN measurements from the VOCALS campaign. Only data from the lowest 400 m are used. The shaded area is the  $y = x \pm 50\%$ . The colour array represents the supersaturation, circles column A and squares column B of the CCNc.

Parameter	Model AS	INORG	EXMIX	INTMIX	INTMIX_WSOC
Sub 400 m (N=118)					
Slope ( $R^2$ )	1.22 (0.87)	1.24 (0.87)	1.16 (0.89)	1.23 (0.89)	1.27 (0.88)
NME (NMB)	44.5 (40.1)	47.5 (43.3)	33.4 (27.9)	42.0 (27.9)	43.6 (47.9)
Mean ( $1\sigma$ ) $N_p/N_o$	1.52 (0.38)	1.56 (0.40)	1.37 (0.32)	1.48 (0.33)	1.62 (0.41)
Min (max) $N_p/N_o$	2.74 (0.62)	2.75 (0.64)	2.32 (0.51)	2.33 (0.58)	2.72 (0.65)

**Table 3.9:** Closure analysis for the VOCALS CCN data set and the five particle physio-chemical models. The table shows the slope of the fit of the data, and the correlation coefficient,  $R^2$ . The normal mean error, NME, indicates the degree of scatter, and normal mean bias, NMB, reflects the degree of systematic errors from perfect closure. The mean, standard deviation, minimum and maximum predicted to observed ratio ( $N_p/N_o$ ) are also shown.

The model in the top left, Figure 3.21(a), is a simple ammonium sulphate (AS) model. This could be considered the least representative of the true aerosol measured, a bench mark and an upper limit to the activation potential of the aerosol. In the majority of instances the model overestimated the measured ( $N_p/N_o = 1.52$ ), as would be expected for this simple idealised population. The large coefficient of determination,  $R^2$  of 0.87, suggest a good fit which is most probably due to the low sensitivity of the system to the chemistry of the observed aerosol. Any variation in the measured composition has little effect on modelled CCN number. This is because the composition is dominated by the amount of ammonium sulphate and bisulphate both salts which are readily activated and have near identical hygroscopicities (see Figure 3.12 on page 165 for inorganic and organic mass fractions). This tenet of a stable chemistry, or a system that is insensitive to variation in the AMS bulk composition, holds for all models used here.

Figure 3.21(b) tests the INORG model, which incorporates the inorganic chemistry of the observed aerosol using the MMR technique to calculate the contribution from sulphuric acid, ammonium sulphate and ammonium bisulphate. Again this model overestimates the measurements, but to a greater extent than

the simple ammonium sulphate model. The fact that this closure has a greater scatter (NME) and has a greater overestimate (Slope of 1.24 and larger NMB) than the simple ammonium sulphate model may be an indication of inaccuracies in the determination of the MMR as previously discussed. The increased  $N_p/N_o$  is driven by the inclusion of sulphuric acid which is more hygroscopic than the either of the other sulphate species ( $\kappa = 0.9$  (Petters and Kreidenweis, 2007)).

In the EXMIX model, Figure 3.21(c), the aerosol is assumed to be an external mixture of inorganic salts and idealised non-hygroscopic organic components. This model has the best fit to the measurements and the least over prediction of all the models, with an  $N_p/N_o$  of 1.37 and a NME value of 33.4. The scatter, NMB of 27.9, is also reduced when compared to the previous two models at 40.1 and 43.3. This model fits the data well as it essentially renders a proportion of the aerosol distribution, equal to the mass fraction of organics as measured by the AMS, unavailable for activation to CCN. This reduces the number of particles greater than the modelled critical diameter.

The internal mixture, INTMIX Figure 3.21(d), again assumes a perfectly non-hygroscopic organic fraction. However, this fraction is incorporated into the aerosol using the additive function for aerosol volume fraction. This model does not fit the data as well as the EXMIX model but it is better than the two simple inorganic models, with less over prediction ( $N_p/N_o$  of 1.48 and an NME of 42.0) and less scatter, NMB of 27.9. These two models, INTMIX and EXMIX, show that organics need to be included to better capture the complexities of activation.

The internally mixed aerosol of inorganic salts, non-hygroscopic organics and WSOC over predicts CCN concentrations more than any other model, with an NME of 43.6 and  $N_p/N_o$  of 1.62 and has more scatter with an NMB of 47.9. This is a function of the 10 % reduction in surface tension as parameterised here and in Asa-Awuku et al. (2011) where it is used to account for the effect of WSOC acting

as a surfactant. This increased over estimation in this model provides evidence to suggest that none of the organics measured are acting to reduce surface tension.

Overall there is little difference between all the models used here, they all over predict the measured CCN concentration with a constantly high coefficient of determination. Including organics in the parameterisation of the models increases the ‘goodness of fit’ using the  $N_p/N_o$  metric and reduces the resultant scatter, ignoring WSOC. However, inferring that these organics modify the surface tension reduces the level of the fit. This adds weight to the assumption that the surface tension is equal to that of pure water. The exclusive over prediction of the models does suggest there is an error in some assumptions or some systematic bias in the data. Obvious candidates are; counting and sizing errors in the SMPS data (possibly due to deliquescence and efflorescence hysteresis), poor parameterisation of; the aerosol composition, the CCNc effective supersaturation, droplet surface tension, the level of ionic dissociation, the possible size independent chemistry or the exclusion of a less CCN active mode in the aerosol that is not captured by the AMS. All bar the latter two of these factors will be assessed in the following sensitivity analysis.

In summary, all models overestimate the predicted CCN concentrations when parameterised with AMS composition. This suggests that these data should not be routinely used in this parameterisation as the sole source of information for modelling activation of ambient aerosols in this environment. Overall the EXMIX parameterisation shows the greatest level of closure.

There are numerous CCN closure studies in the literature, see Table 3.10 with which to compare these findings. However, few are concerned with maritime air masses and aircraft measurements. Moore et al. (2012), using the  $\kappa$  model of Petters and Kreidenweis (2007) and AMS derived bulk chemistry as described in the previous section, over predicted CCN number between 21 and 50 percent for

internally mixed aerosols with both soluble and insoluble organics respectively over a supersaturation range of 0.33 to 0.63 % in a marine outflow off the Californian coast. A simple ammonium sulphate model over predicted by 53 to 81 percent for the same supersaturation range and an external mixture with insoluble organics underestimated by 8 to 26 percent. These over predictions are of a similar magnitude to those of this study. However, the level of underestimation in the external mixture is not matched here. This is most likely a function of the lack of size resolved aerosol composition data. Even with this information the predictions may not be improved, as the fraction of interest may be refractory and therefore not sampled by the AMS. Such as the organic dust external mixture described in Hawkins et al. (2010). This suggests that using the organic mass fraction to apportion the magnitude of the external mixture is not an accurate assumption. This is clearly shown by falling  $\kappa$  with increasing effective supersaturation in the previous Section. Where a marginally hygroscopic mode, responsible for the drawing down the bulk aerosol hygroscopicity, is more effective at  $0.1\ \mu\text{m}$  than  $0.2\ \mu\text{m}$ . Moore et al. (2012) used size resolved AMS derived volume fractions and as such did not assume the external organic fraction was spread equally across the size distribution as was the case in this work.

Table 3.10: CCN closure experiments from the literature.

$SS_{eff}$ %	$N_p/N_o$	Closure		Model Type	Environment	Reference
		Slope	$R^2$			
0.2 & 0.85		1.05 & 1.2	0.91 & 0.84	AS	Airborne, Florida	VanReken et al. (2003)
0.4	$2.06 \pm 0.65$	-	-	AS	Airborne, N.E. Pacific	Roberts et al. (2006)
2.1 to 2.8	$1.92 \pm 1.29$	-	-	AS	Airborne, Oklahoma	Rissman et al. (2006)
0.2	-	0.94	0.9	INTMIX	Airborne, California	Wang et al. (2008)
0.3 to 1.0	-	$1.026 \pm 0.006$	0.91	INTMIX	Airborne, Houtson	Lance et al. (2009)
0.21 to 0.73	-	0.95 to 1.01	0.9 to 0.93	INTMIX.WSOC	Ground, Finikola, Gr.	Bougiatioti et al. (2009)
0.1 to 0.32	-	1.16	-	INTMIX <sup>1</sup>	Airborne, California	Murphy et al. (2009)
0.12 to 1.18	-	0.93 to 1.05	0.98 to 0.99	INTMIX	Ground, JungFraujoch, Ch.	Juranyi et al. (2010)
0.43 to 0.71	-	$0.96 \pm 0.07$	-	INTMIX.WSOC	Airborne, Houston	Asa-Awuku et al. (2011)
0.33 to 0.63	1.09 to 1.2	-	-	INTMIX.WSOC <sup>1</sup>	Airborne, California	Moore et al. (2012)
0.09 to 0.4	$1.37 \pm 0.32$	1.16	0.89	EXMIX	Airborne, S.E. Pacific	This Study

<sup>1</sup> These closure experiments use size resolved chemistry

Roberts et al. (2006) reported an over prediction of 2.06 with a standard deviation of 0.65, using a simple ammonium sulphate model compared to CCN data collected off the Californian coast at 0.4 % supersaturation. Assuming an internal mixture with water insoluble organic fraction Wang et al. (2008) achieved closure with a slope of 0.94 and a coefficient of determination of 0.9 for the MBL off Monterey Bay, California, at 0.2 % supersaturation. Assuming a constant composition derived from AMS data. At the remote ground based station of Finokalia, Greece, closure  $N_p/N_o$  values ranged between 0.84 and 0.96. With coefficient of determinations between 0.88 and 0.92. This was achieved for supersaturations between 0.21 and 0.73 % assuming insoluble organic material. When 70 % of that organic material was considered water soluble ( $\kappa = 0.158$ ) the values increase slightly ranging from 0.95 to 1.01 with coefficients of determination between 0.9 and 0.92. Similar closures can be seen in Juranyi et al. (2010) where slopes ranged between 0.934 and 1.013 with coefficients for determinations ranging from 0.99 to 0.98. These results were for data collected from the high alpine site on the Jungfrauoch, using the same methodology employed here. These data suggest that an accurate closure is possible if the ambient aerosol is aged,

internally mixed or if some level of knowledge of the size resolved composition is known and there is not a significant contribution from refractory particulates.

All five models here have different treatments for their aerosol compositions. This appears to have little effect on the predicted numbers of CCN and subsequently the CCN closure. The extent to which this statement is true can be seen in Figure 3.22. This shows the results of the EXMIX model's comparison to measured CCN under two diagnostic regimes. In Figure 3.22(a) the model inputs were constrained to a project mean aerosol chemistry. In comparison with the unconstrained model in Table 3.9 fixing the chemistry results in a slight increase in slope to 1.2 from 1.16, and a one percent reduction in the level of fit with the  $R^2$  dropping from 0.89 to 0.88. This shows how an invariant chemical scheme with moderately hygroscopic components has negligible effect on the number of particles activated (Dusek et al., 2006; McFiggans et al., 2006; Juranyi et al., 2010), suggesting aerosol chemistry is not the primary driver of CCN number in this environment. In contrast to this is the effect of homogenising the aerosol distribution. The outcome of using a project wide mean SMPS distribution is a collapse of the slope, increase in the intercept and a coefficient of determination below 1 percent; see Figure 3.22(b). Essentially the model loses all sensitivity and thus the ability to predict any of the variability seen in the concentration of activated particles. In summary this analysis shows that the ability of a particle to act as a CCN is controlled primarily by the particles size and not its chemistry. However, this is not to say that composition is of no importance. Even though the CCN predictions here show that number concentrations are most sensitive to the size distributions, closure has still not been achieved with size alone, an accurate chemical scheme is needed to fine tune this modelled system.

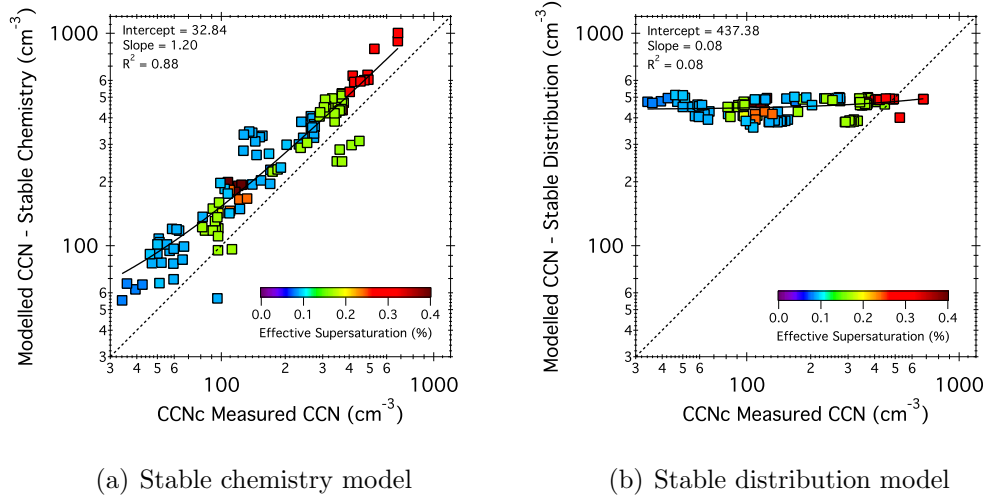


Figure 3.22: Effects on the EXMIX model of stabilising both the chemistry and the particle size distributions to investigate which of the aerosol characteristics have a first order effect on CCN concentrations. The colour array represents supersaturation and the dotted line the  $x = y$  line.

In summary of the CCN closure, the EXMIX scheme shows the best closure though this model scheme still overestimates the measured data by some 37%. It appears as if adding information on the organics composition increases the accuracy of the closure. However, the overestimation in the model seen in this study does not compare favourably to similar studies in the literature. Data from the literature does suggest that size resolved composition can increase closure between model estimates and measurements. This analysis also shows that size is the primary driver in the ability of an aerosol to act as a CCN in the SEP.

### 3.3.1 Sensitivity Analysis of Externally Mixed Model

The sensitivity of the EXMIX system was examined in an effort to glean information on the possible sources of uncertainties in the simplifying assumptions of the EXMIX scheme. In an effort to better answer the questions posed in the introduction. The output from this analysis can be seen in Figures 3.23 to 3.25. Table 3.12 incorporates the goodness of fit metrics for all model runs. Each input



parameter to Equation 3.5 was nudged to investigate the effect on the level of closure in an attempt to understand the model overestimation and sensitivities of the models. Table 3.11 gives possible values of error in these parameters from both this work and the literature, creating a maximum possible parameter space to work in. To reduce the computational effort of nudging each parameter by the exact amount three values were chosen to covering all possible variation, they were 10, 30 and 50 %. Each resultant plot shows the sensitivity data in two different forms, an absolute difference from the base line model run on the left hand side of each figure and normalised difference approach on the right. The data for both presentation methods has been sorted in  $x,y$  pairs using the CCNc measured data to reduce scatter and increase clarity.

Parameter or Measurement	Parameter Values or Error Estimates	Reference
AMS	$\pm 34$ to $38$ %	Bahreini et al. (2009)
$SS_{eff}$	$\pm 7$ %	This Work
	$\pm 10$ %	Roberts et al. (2010)
	$\pm 30$ %	Roberts et al. (2010)
van't Hoff	$(\text{NH}_4)_2\text{SO}_4 = 2.52$	Roberts et al. (2010)
	$(\text{NH}_4)_2\text{SO}_4 = 2.5$	Wang et al. (2008)
	$(\text{NH}_4)_2\text{SO}_4 = 2.0$ to $2.5$	Wise et al. (2003)
	$(\text{NH}_4)\text{HSO}_4$ and $\text{H}_2\text{SO}_4 = 3.0$	Roberts et al. (2010)
Surface Tension ( $\sigma$ )	$-10$ %	Asa-Awuku et al. (2011)
	$0.085 \text{ Nm}^{-1}$ ( $\sigma_{\text{H}_2\text{O}} = 0.073 \text{ Nm}^{-1}$ )	Ervens et al. (2005)
	$0.03 \text{ Nm}^{-1}$	Ervens et al. (2005)
SMPS Particle Concentration	$\pm 2$ %	This Work
SMPS Particle Diameter	$-15$ to $-28$ %	Murphy et al. (2009)

**Table 3.11: Various parameterisations and measurement errors from this work and the literature for the initialisation parameters used in Equation 3.5 under the EXMIX scheme.**

## Aerosol Chemistry

The sensitivity of the simplified Köhler model running the EXMIX scheme to aerosol chemistry is investigated in Figure 3.23. Of the three aerosol components the model is most sensitive to a decrease in organic mass loadings; see Figures 3.23(e) and 3.23(f). Increasing the organic mass increases the predicted number and *vice versa*. The effect of modifying the organic loadings however, is non linear. Decreasing the mass has more of an effect on total number than increasing by the same value. This non linearity in changing composition is best reflected in the metrics of Table 3.12 on page 225. Where a 50 % increase in the sulphate loadings increases the over prediction of the model by 4 % and a decrease by the same factor results in a 6 % decrease in the over prediction. This response is a reflection of the simple external mixture parameterisation where the organic mass fraction is equated to a proportion of the aerosol distribution made unavailable for activation. This proportion is applied linearly across the distribution. Depending on where the critical diameter is calculated to be the nudging of this parameter can have a variable effect. For example if it is at a mode centre then the effect will be more than if it is at the distribution minima.

The model is more sensitive to variability in the sulphate ion loadings (Figures 3.23(a) and 3.23(b)) than the ammonium (Figure 3.23(c) and 3.23(d)). This can be seen by simply comparing the maximum number of added activated particles with a 50 % perturbation. When nudged 50 % upwards the resultant number of maximum particles added is 58 and 10 for sulphate and ammonium ions respectively.

However, ammonium has a more complex relationship with the sign of the resulting effect after a perturbation. A reduction in mass of ammonium can both reduce and increase the number of activated particles. It is the ammonium in the MMR methodology that controls the neutrality of the aerosol. The ammonium

measured during the project was often on or around the detection limit of the AMS, therefore small in comparison with the sulphate loadings making the MMR sensitive to alterations in the ammonium concentration. This sensitivity causes the non-linearity in the model. A small change in ammonium, where the MMR is above 1.0, has little effect on the system but a small change around 1.0 can introduce sulphuric acid. This more hygroscopic component when added to the system has a larger effect on the outcome of the model estimate. A relative drop in the ratio of sulphate to ammonium results in a less acidic and less hygroscopic aerosol. The reverse is also true.

So in summary the model is relatively insensitive to variations in the AMS measured mass loadings when the aerosol external mixture is assumed to be evenly spread across the distribution. Suggesting that perturbing the parameterisation of this specific composition does not account for the model over prediction. As a byproduct it also shows that errors in the MMR technique could not account for all of the overestimation seen in the model. As even at an unrealistic level of error, 50 %, in AMS measurements the discrepancy in the model estimates can not be accounted for. This still leaves open the possibility that the overestimation is due to an unrealised size dependent chemistry of a marginally hygroscopic fraction. The influence of varying the the physical parameters on the modelled CCN concentration is investigated next.

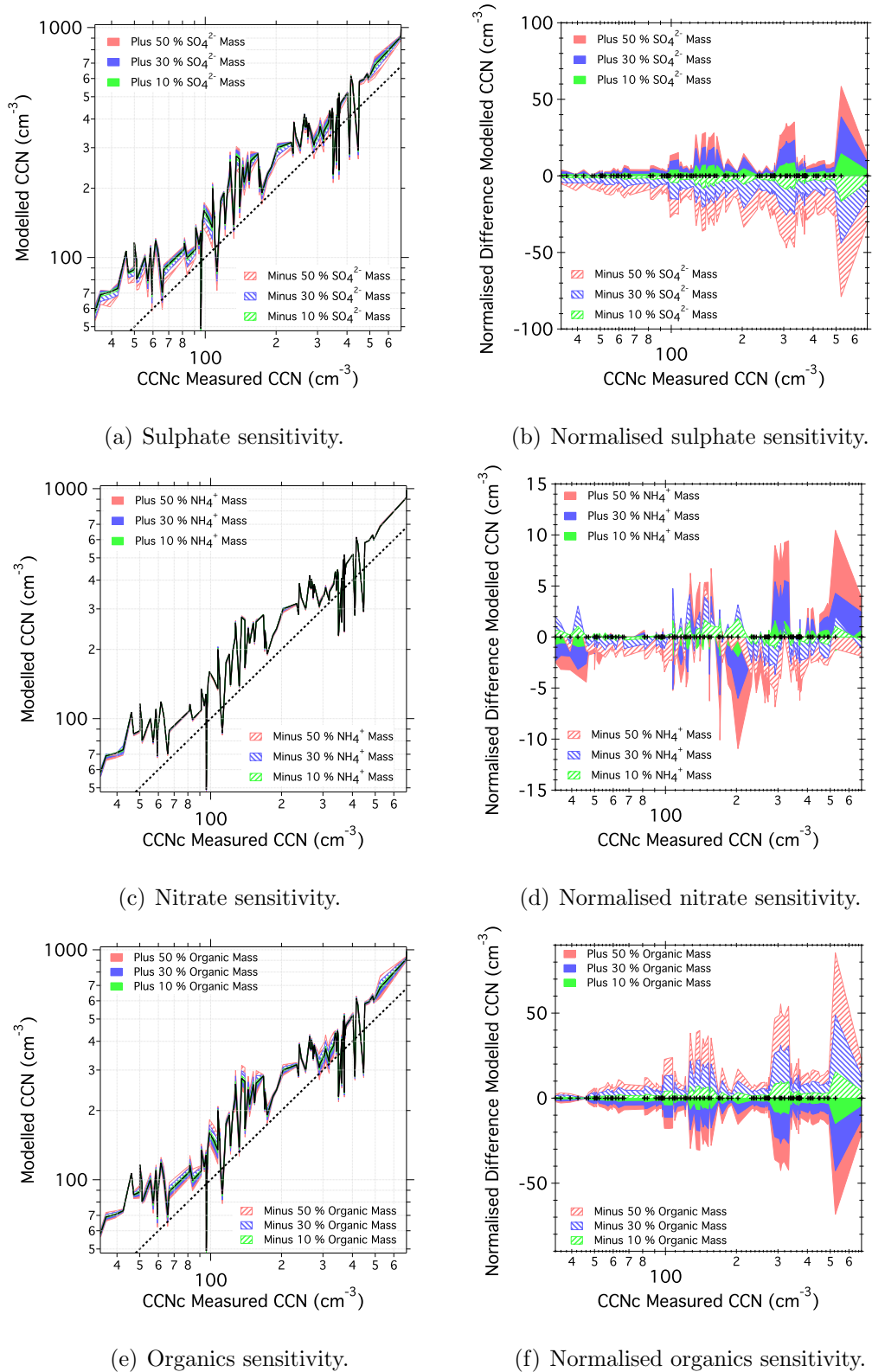


Figure 3.23: Sensitivity of the EXMIX Köhler model to an increase and decrease of 50%, 30% and 10% in sulphate, nitrate and organic mass loadings. This analysis was conducted only on data from the lowest 400 m of the MBL. Right hand side panels show the  $y = x$  as a dashed line. All data have been sorted in ascending order with respect to CCNc measured CCN concentrations.

## Environment and Droplet Properties

The outcome of nudging the physical parameters of the aerosol and its environment can be seen in Figure 3.24, including surface tension, the level of ionic disassociation as captured by the van't Hoffs number and the critical supersaturation. These parameters have a much greater effect on the predicted CCN number than modifying the aerosol chemistry.

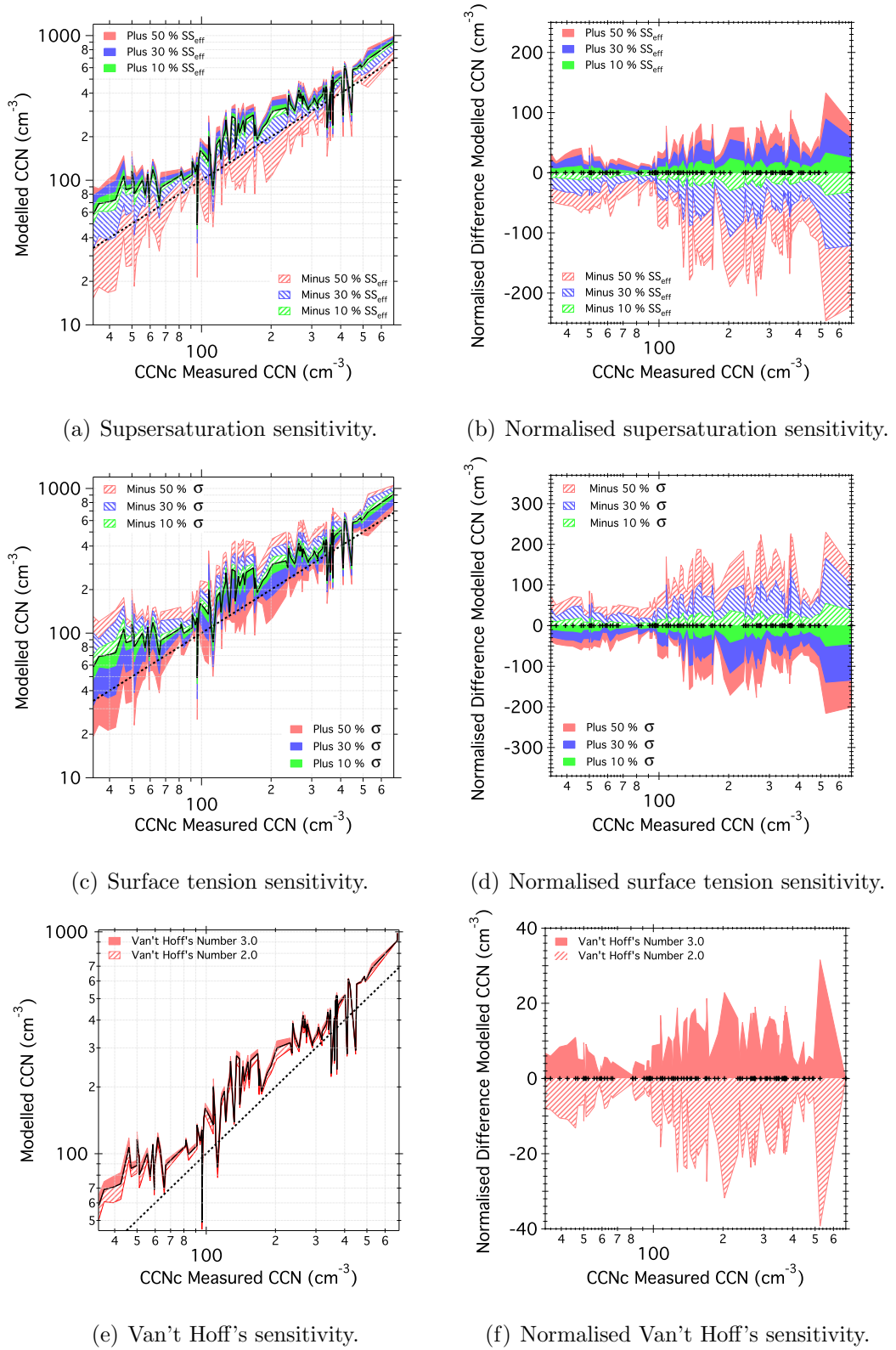


Figure 3.24: Sensitivity of the EXMIX Köhler model to an increase and decrease of 50%, 30% and 10% in critical supersaturation, surface tension and van't Hoff's number, this analysis was conducted only on data from the lowest 400 m of the MBL. All right hand side panels show the  $y = x$  as a dashed line. All data have been sorted in ascending order with respect to CCNc measured CCN concentrations.

Figures 3.24(a) and 3.24(b) show the non linear effects of varying the critical supersaturation (assumed to be CCNc effective supersaturation in the model) on the predicted CCN concentration. A decrease of 10 % results in a reduction in over prediction from 1.37 to 1.29 using the  $N_p/N_o$  metric, a 5 % reduction. The scatter is also reduced by reducing the supersaturation in this simulation. Though unlikely, if pushed to the 50 % reduction limit the model will under predicts the measured data. An increase of the same magnitude in effective supersaturation results in an increase in  $N_p/N_o$  to 1.64 and an associated increase in the scatter.

Modification of surface tension, Figures 3.24(c) and 3.24(d), is another non linear process though the variability in this parameter under different simulations has more symmetry than the effective supersaturation. A reduction in surface tension, as shown in the INTMIX WSOC model, increases the estimate of the CCN number. The suppression of the surface tension allows smaller particles to reach a critical nature under a stable supersaturation. Ervens et al. (2005) discuss that in ionic solutions enrichment of anions at the surface and their interaction with the cations in the bulk solution can slightly increase the surface tension, to  $0.085 \text{ Nm}^{-1}$  an increase of approximately 18 %. Nudging surface tension has an effect of a similar magnitude to the effective supersaturation, a 10 % increase, causes a reduction of 8 % in the  $N_p/N_o$ . A decrease of the same order effects a 9 % increase in over prediction and a decrease in the scatter. Both the critical supersaturation and surface tension can modify the predicted CCN number by hundreds of particles but more frequently by tens of particles  $\text{cm}^{-3}$  within realistic measurement errors.

Alteration of the van't Hoff's number has the least effect on the CCN number of this triplet of parameters. Again the sensitivity analysis alludes to the non linear effect of varying this parameter. Increasing the value from the baseline used in the EXMIX model from 2.5 to 3.0 increases modelled CCN concentrations up to

30 particles  $\text{cm}^{-3}$ . A reduction in this value to 2.0 induces a fall in concentration at the same point of 40 particles  $\text{cm}^{-3}$ .

In summary modification of this set of parameters can have more effect than modification within known error estimates of the aerosol composition. The most likely error in this parameterisation group is the effective supersaturation of the CCNc which at  $\pm 10\%$  will account for a maximum swing of  $12\%$  around the baseline  $N_p/N_o$ . The surface tension is unlikely to be incorrectly parameterised. As previously discussed there is no reason for it to be any different to the value for pure water. Even if the van't Hoff number was only two thirds of the correct value it will not account for the level of overestimation seen in the model.



## Particle Distribution Measurements

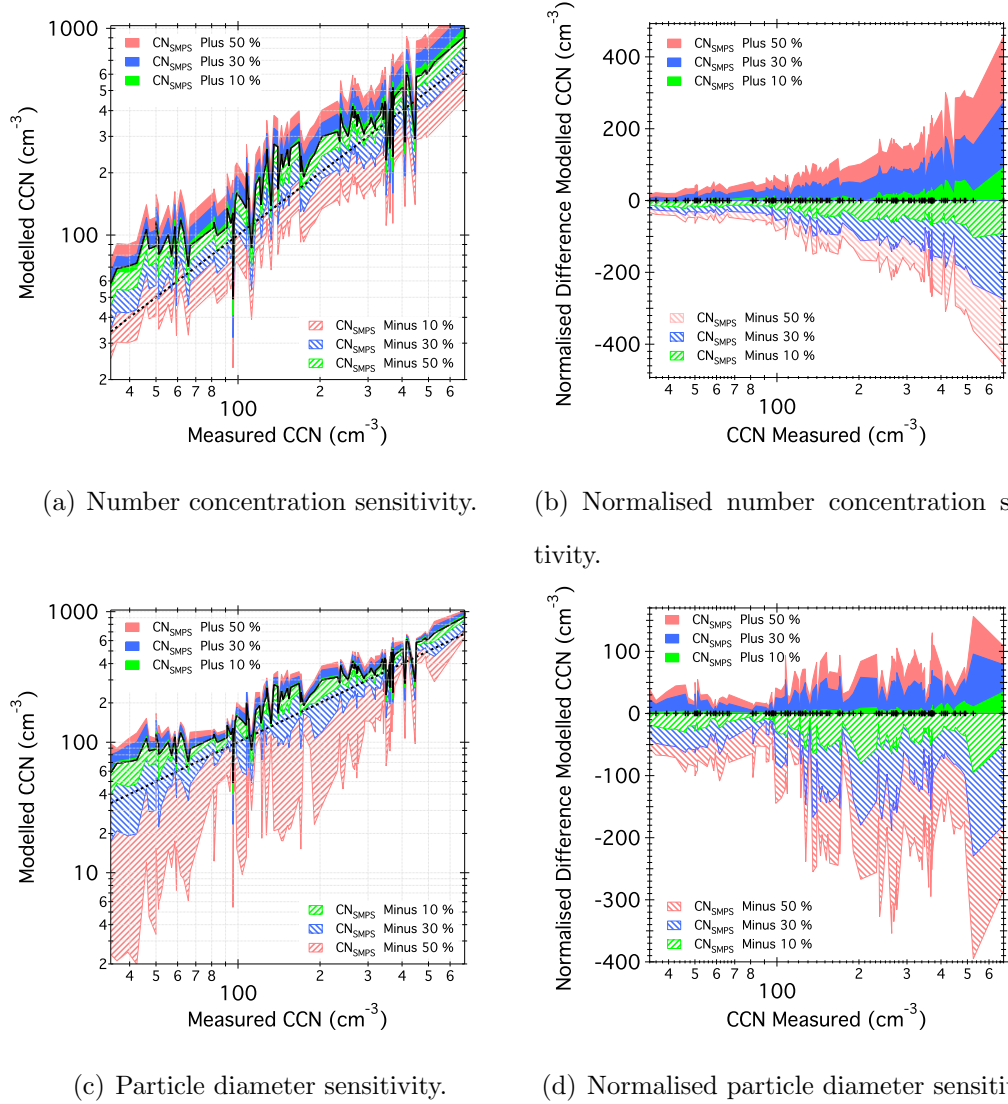


Figure 3.25: Sensitivity of the EXMIX Köhler model to an increase and decrease of 50%, 30% and 10% in aerosol number concentration and particle diameter, this analysis was conducted only on data from the lowest 400 m of the MBL. All right hand side panels show the  $y = x$  as a dashed line. All data have been sorted in ascending order with respect to CCNc measured CCN concentrations.

As shown previously the CCN concentration as modelled by the EXMIX parameterisation is sensitive to particle number and distribution shape, Figure 3.22. However, that analysis doesn't untangle the two parameters. Figure 3.25 shows the effect on the model of modifying the particle number and the shifting of the

size distribution in isolation from one another. Modifying the particle number has a perfectly linear and monotonically increasing effect on the estimated activated particle number. An increase in SMPS number concentration increases the number of estimated CCN and *visa versa*. At the highest concentrations and maximum perturbation this can account for a differential of 400 particles  $\text{cm}^{-3}$ . Though at a more realistic level of SMPS bias,  $\pm 10\%$ , the differential is reduced to 90 particles  $\text{cm}^{-3}$ . The perturbation of adding 10 % easily covers the largest instance of ‘missing particles’ due to open distributions as discussed previously, this measurement bias makes the closure worse. It is not until an unrealistic 30 % reduction in particle number that the gap in the closure is reduced and predicted against measured reaches unity.

Due to the multimodal characteristics of the VOCALS SMPS distributions the effect of shifting the distribution around the critical diameter estimated by the EXMIX parameterisation is non linear. A shift in the distribution to smaller diameters results in a reduction in the estimated activated particle concentrations. A shift to larger diameters an increase in concentrations. The former of these shifts has a greater effect on the overall numbers. A 30 % reduction in particle diameter (Murphy et al., 2009) can lead to a reduction in estimated CCN concentrations of up to 230 particles  $\text{cm}^{-3}$ . Where as an equal increase in particle diameters leads only to an additional 96 particles  $\text{cm}^{-3}$ . This is due to the relationship between critical diameter and the two modes either side of it. The Aitken and droplet modes. The modelled critical diameter falls between these two modes, below 400 m. The droplet mode has more particles in it than the Aitken mode (see Table 3.4) and in the majority of cases the droplet mode is the narrower of the two modes. Firstly consider two modes of equal width, in shifting the distribution by a constant percentage a constant fraction of particles are no longer, or are, now added to those activated. In the mode with the most number,

here the droplet mode, this results in a larger differential when the distribution is shifted to smaller diameters than to larger ones. This proportion removed for activation is increased further in most of the SMPS distributions as the droplet mode is narrower than the Aitken mode as well as being more populous. Counter to this, when the distribution is shifted to larger diameters fewer particles are added than are lost due to the lower number and greater width of the Aitken mode.

Parameter	Metric	Minus				Plus		
		50%	30%	10%	0 %	10%	30%	50%
Sulphate	Slope	1.12	1.14	1.16	1.16	1.17	1.18	1.18
	$R^2$	0.88	0.88	0.89	0.89	0.89	0.89	0.89
	NME	25.54	29.16	32.12	33.34	34.38	36.19	37.36
	NMB	18.07	22.91	26.44	27.88	29.07	30.88	32.22
	$N_p/N_o$ Mean	1.25	1.31	1.35	1.37	1.39	1.41	1.43
	$N_p/N_o$ $\sigma$	0.30	0.31	0.32	0.32	0.33	0.34	0.34
Nitrate	Slope	1.16	1.16	1.16	1.16	1.17	1.17	1.17
	$R^2$	0.88	0.89	0.88	0.89	0.89	0.89	0.89
	NME	32.70	33.20	33.42	33.34	33.32	33.23	33.12
	NMB	27.06	27.64	27.91	27.88	27.78	27.65	27.5
	$N_p/N_o$ Mean	1.36	1.37	1.37	1.37	1.37	1.37	1.36
	$N_p/N_o$ $\sigma$	0.33	0.33	0.33	0.32	0.32	0.32	0.32
Organics	Slope	1.20	1.19	1.17	1.16	1.16	1.15	1.13
	$R^2$	0.89	0.89	0.89	0.89	0.89	0.88	0.88
	NME	39.75	37.08	34.59	33.34	32.28	30.30	28.66
	NMB	34.86	31.92	29.18	27.88	26.62	24.23	21.97
	$N_p/N_o$ Mean	1.46	1.42	1.39	1.37	1.36	1.33	1.30
	$N_p/N_o$ $\sigma$	0.35	0.34	0.33	0.32	0.32	0.32	0.32
Critical	Slope	0.96	1.07	1.14	1.16	1.19	1.24	1.28
Supersaturation	$R^2$	0.87	0.90	0.89	0.89	0.88	0.87	0.87
	NME	21.75	16.42	27.96	33.34	38.23	46.35	53.02
	NMB	-16.61	6.51	21.9	27.88	33.06	41.73	48.81
	$N_p/N_o$ Mean	0.79	1.09	1.29	1.37	1.44	1.55	1.64
	$N_p/N_o$ $\sigma$	0.22	0.21	0.29	0.32	0.36	0.42	0.47
Surface	Slope	1.36	1.31	1.21	1.16	1.13	1.07	0.99
Tension	$R^2$	0.81	0.86	0.88	0.89	0.89	0.90	0.88
	NME	81.03	58.9	41.33	33.34	26.00	15.59	17.88
	NMB	77.90	55.00	36.38	27.88	19.70	4.12	-10.54
	$N_p/N_o$ Mean	2.23	1.72	1.48	1.37	1.26	1.06	0.86
	$N_p/N_o$ $\sigma$	0.63	0.50	0.38	0.32	0.27	0.21	0.21
Particle	Slope	0.58	0.81	1.04	1.16	1.27	1.50	1.73
Number	$R^2$	0.89	0.89	0.89	0.89	0.89	0.89	0.89
	NME	38.90	28.35	18.72	33.34	39.38	61.66	84.15
	NMB	-38.87	22.26	10.30	27.88	34.48	58.93	83.38
	$N_p/N_o$ Mean	0.65	1.29	1.16	1.37	1.42	1.68	1.94
	$N_p/N_o$ $\sigma$	0.14	0.29	0.26	0.32	0.31	0.37	0.43
Particle	Slope	0.78	1.00	1.11	1.16	1.19	1.26	1.31
Diameter	$R^2$	0.73	0.88	0.89	0.89	0.88	0.87	0.86
	NME	49.34	19.83	20.32	33.34	35.68	47.81	57.55
	NMB	-48.63	-12.56	12.78	27.88	30.27	43.25	53.55
	$N_p/N_o$ Mean	0.42	0.83	1.17	1.37	1.40	1.57	1.70
	$N_p/N_o$ $\sigma$	0.29	0.22	0.24	0.32	0.34	0.43	0.49
van't Hoffs Number								
		2.0		2.5		3.0		
van't Hoffs	Slope	1.15		1.16		1.17		
	$R^2$	0.89		0.89		0.88		
	NME	22.34		33.34		37.49		
	NMB	22.26		27.88		32.31		
	$N_p/N_o$ Mean	1.29		1.37		1.43		
	$N_p/N_o$ $\sigma$	0.29		0.32		0.36		

Table 3.12: Sensitivity analysis metrics of the EXMIX model.

It should be noted that this CCN closure and the subsequent sensitivity analysis can not be used as a validation of the measurements. This exercise, however, can use the models to explain the findings in the measurement when there are no supporting data. The sensitivity analysis shows the order of the effects of each of the functional groups of parameters input into the EXMIX model. Within the bounds of the physically reasonable, as set by Table 3.11, the chemistry of the aerosol and modification of the environmental, droplet and solute properties has an effect in the order of tens of particles. The aerosol number and distribution characteristics have an effect an order of magnitude greater, with a maximum modification of over 200 particles  $\text{cm}^{-3}$ , if the distribution were shifted by 30 % to smaller diameters. Of all the different simulations examined here this is the only parameter shift that can cause the model to under estimate the measurements.

The data in Table 3.12 can be compared to known sources of error in the measurements to quantify the effects on the accuracy of the CCN closure, beyond the initial limits and errors given in Table 3.11. It would appear that just increasing the organics and therefore the proportion of the distribution that is unavailable for activation, even by up to 50 %. Which is close to the factor of 2.4 estimated by Hawkins et al. (2010) to be the level of underestimation in organics loading during VOCALS, still does not bring the  $N_p/N_o$  estimate down to 1.0. This suggests, as does the results from the  $\kappa$  analysis, that the external mixture is not evenly spread across the distribution, as is assumed here. Or that its characteristics are not captured by the AMS measured organics. Accurate size resolved data is needed to understand the effects of any potentially less hygroscopic mode on the modelled CCN. No amount of modification of the chemistry has an order of effect great enough to bring the model measure ratio down to unity.

As discussed using the surface tension of pure water is an adequate assump-

tion. The van't Hoff's number has such a small effect that the accurate parameterisation in this field's data is almost irrelevant. The 10 % error in the pressure correction of the CCNc, supersaturation using Equation 2.15 on page 71 from Roberts et al. (2010), also has little effect on the modelled CCN data using the EXMIX Köhler model. Maximum perturbations from the base line model being are the region of 50 particles  $\text{cm}^{-3}$  at a CCNc concentration of 500 particles  $\text{cm}^{-3}$ . If the surface tension were not that of pure water variation in the parameter has an effect in the same order of magnitude as the deviations caused by variation in the effective supersaturation.

Characteristics of the aerosol distribution, as has already been highlighted, has the greatest control over the predicted CCN number concentration in this environment. Comparing Figure 3.26(a) to 3.25(c) on page 222, a 10 % reduction in both the CN concentration and in particle diameter brings the CCN to within 17 % of the measured data. However, a 10 % reduction in the particle concentration as measured by the SMPS is an overestimate, as discussed previously in laboratory comparisons the SMPS CPC undercounts in somewhere in the region of 2 %. The accuracy of the SMPS distribution is harder to quantify with no overlapping distribution measurement available for comparison. The most plausible source of error in this measurement is a result of the uncontrolled relative humidity of the sample. For the sub 400m data the mean CCNc sample line RH is  $36.2 \pm 4.0\%$ . This value falls between the estimates of the efflorescence point of ammonium sulphate of 33 to 48 % and is very close to the deliquescence point of ammonium bisulphate between 39 and 40 % ((Martin, 2000), and references therein). These theoretical values would be expected upper limits as the addition of organics to the particles will lower the critical RH values (Parsons et al., 2004). The formation of aqueous particles and their subsequent recrystallisation creates step changes in the particle diameter, in the region of 45 % and

15 % increase and decrease, respectively, for ammonium sulphate (Seinfeld and Pandis, 2006). These changes in particle diameter however, are not an issue if the aerosol is not vertically mixed above 500 m. This is the altitude above which the ambient RH exceeds the deliquescence point of ammonium sulphate at 80 % (Martin, 2000; Parsons et al., 2004; Seinfeld and Pandis, 2006), or if the instrument RH subsequently never drops below the efflorescence point. Assuming the MBL is vertically well mixed and previous plots suggest that it is, any instrument RH estimates below 33 % could possibly cause SMPS distribution shifts. In all of the left hand graphs shown in this CCN closure sensitivity analysis section there are seven anomalous points where the estimated CCN under predict the measurements. Four of these points occur at anomalously low instrument RH values, between 28.3 and 29.7 % suggesting a possible shift to smaller diameters due to recrystallisation of a proportion of the aerosol. This, however, is not the case. These four points, and the others below the  $y=x$  line, do not show any shift away from the SMPS distribution modal statistics of Table 3.4 on page 174 for the dominant droplet mode, suggesting there is no diameter shifts due to particle efflorescence. This sensitivity study highlights how critical accurate distribution measurements are taken in the diameters relevant to particle activation and how important it is to understand their growth with respect to RH.

The model here has been used as the independent variable, as is customary in model measurement comparisons. In the interests of a full investigation and since there is no explicit measure of error associated with the CCNc OPC measurements the baseline EXMIX model has been compared to CCNc concentration nudged by the same percentage points as all the other parameters. Therefore investigating the effect of a CCNc bias on the closure; see Figure 3.26. Ten percent is a likely upper limit for this bias, both the discussion on instrument under reading in Section 3.2 and the calibrations in Section 2.1 suggest this is the case. The pos-

sibility of the model overestimation being a function of the CCNc undercounting bias should be discounted. At a maximum realistic level of 10 % undercounting the model still significantly overestimates the measured CCN concentrations.

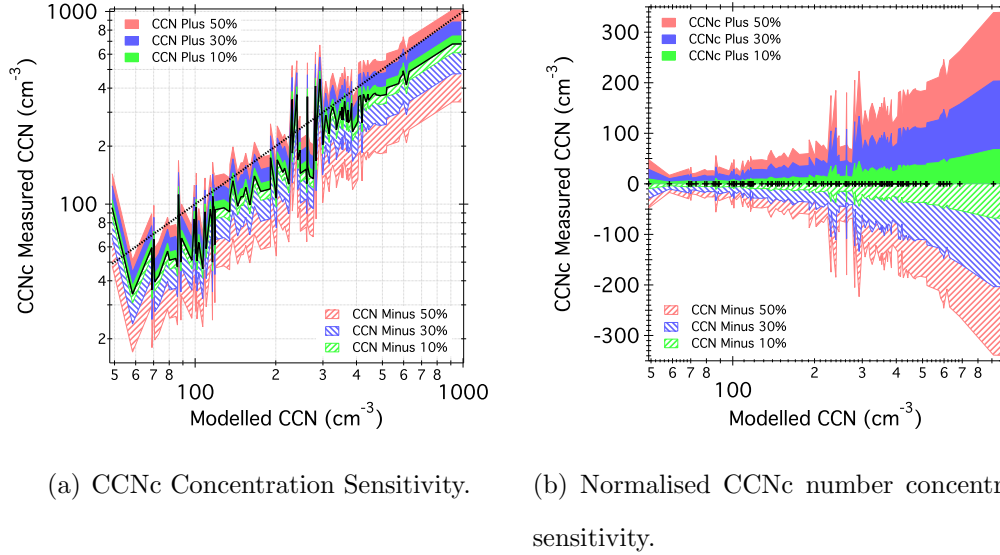


Figure 3.26: Sensitivity of the CCNc instrument to an increase and decrease of 50%, 30% and 10% in CCN number concentration to the baseline EXMIX Köhler model, this analysis was conducted only on data from the lowest 400 m of the MBL. All right hand side panels show the  $y = x$  as a dashed line. All data have been sorted in ascending order with respect to the model.

In summary, none of the parameterisations in the sensitivity analysis have highlighted a possible route to closure, even biases in the CCNc measurements themselves. The only possible explanation is the presence of an external mixture of limited hygroscopicity. A mixture that is not measured or whose full characteristics is not elucidated by the AMS, as proposed by the measurements of Hawkins et al. (2010). Modes of limited hygroscopicity have also been discussed in McFiggans et al. (2006) and Wex et al. (2010) and have been shown in these studies to cause discrepancies between AMS derived and HTDMA  $\kappa$ . The results of the  $\kappa$  analysis in the previous Section also allude to the presence of this mode of limited hygroscopicity. The analysis of an external mixture with a less hygro-



scopic nature than the AMS mass loadings suggest is investigated here with the INTMIX model.

### **Externally Mixed Hygroscopicity Model**

Firstly an estimation of the magnitude and the nature of the distribution of the less hygroscopic external mixture is needed. In comparing AMS to HTDMA derived  $\kappa$ , Wex et al. (2010) derived a model for the maximum fraction of a less hygroscopic mode based on the overestimation of the AMS derived  $\kappa$  compared to that derived from HTDMA measurements. Using their findings an assessment of the maximum fraction of the less hygroscopic mode at any diameter could be estimated using the data in Table 3.6. Figure 3.27 shows this data, the results compare well with the data from McFiggans et al. (2006) where estimates of the fractions of the total aerosol that is made up of these external less hygroscopic fractions in specific air mass types are published. This study split aerosol by environment, the fractions estimated here fit best with urban aerosol at their upper range but also cover the range of continental polluted. At all supersaturations the less hygroscopic fraction is greater than the maximum estimated for remote maritime environments. This plot also reflects the findings from the previous Section, showing an increase in the fraction of less hygroscopic data with decreasing particle diameter. The linear model was fitted to allow extrapolation of this low hygroscopicity fraction beyond the diameters available as calculated from the CCN concentration and SMPS distributions.

This second less hygroscopic mode was constructed by calculating the fraction of the total aerosol number at any given diameter from the linear relationship in Figure 3.27 for each SMSP distribution included in the CCN closure study. A log normal fit was applied to this data to achieve a maximum contribution (Max  $f_{less}$  in Figure 3.28) of the less hygroscopic mode, two further modes were

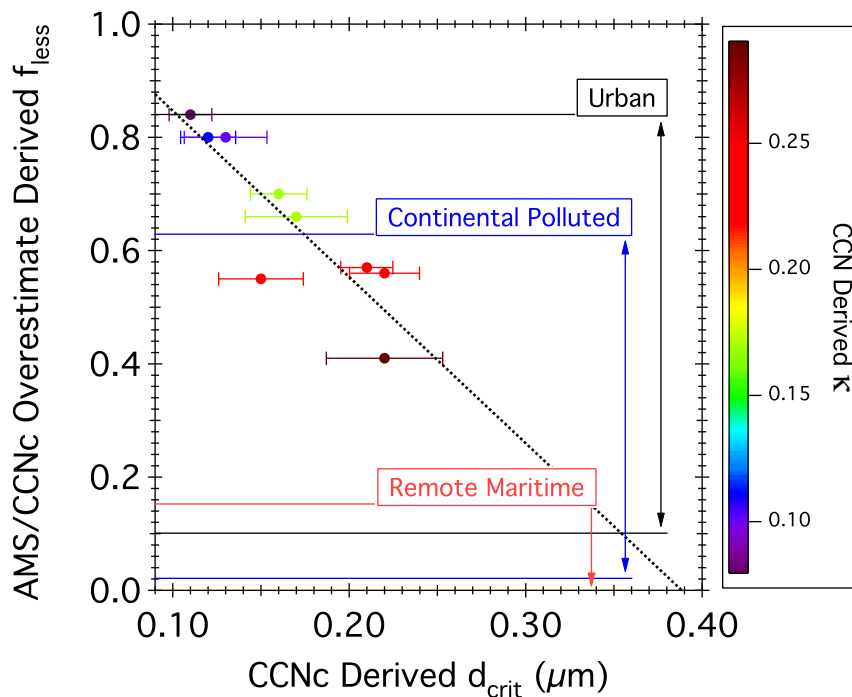
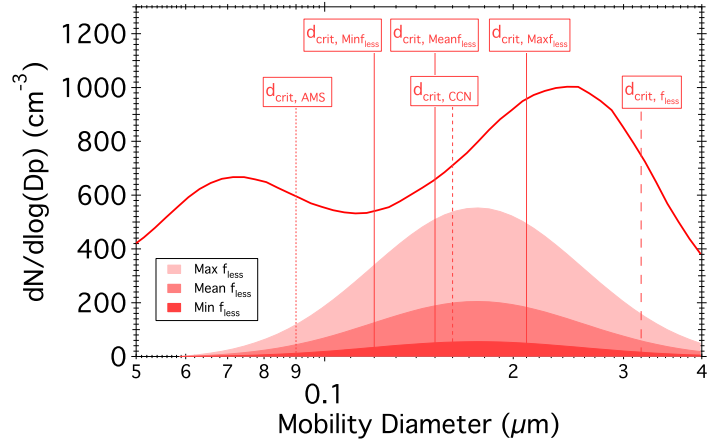
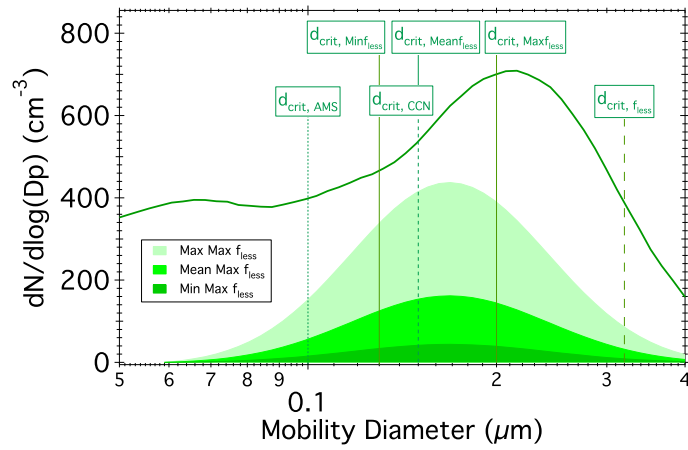


Figure 3.27: The fraction of less hygroscopic aerosol as a function of particle diameter as calculated from the maximum overestimation model shown in Wex et al. (2010). Data points are coloured by CCNc derived  $\kappa$  for all effective supersaturations, the error bars represent one standard deviation of the critical diameter mean values. The linear model fit used to extrapolate to larger diameters is also shown as are the estimated ranges for three environment types from McFiggans et al. (2006).

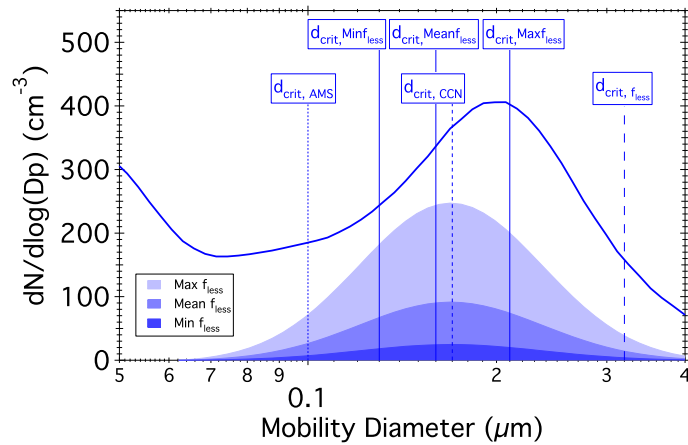
created; a minimum fraction at 10% of the maximum reflecting the minimum contribution of this mode in the urban environment and a mean fraction simply being the difference between the maximum, an 84% fraction, and the minimum (Figure 3.27 and (McFiggans et al., 2006)). A schematic of these modes and a zoomed in section of the mean SMPS distributions for each of the longitudinal sulphate loading zones can be seen in Figure 3.28



(a) High sulphate zone.



(b) Falling sulphate zone.



(c) Low sulphate zone.

Figure 3.28: Mean SMPS distributions and less hygroscopic modes for each sulphate zone. The  $f_{less}$  model critical diameter estimates have solid bisecting lines, the AMS, the CCNc and the critical diameter of the less hygroscopic mode itself use dashed lines. All measurements are for an effective supersaturation of 0.17 %

These secondary less hygroscopic modes were added to the information for each SMPS scan that met the QA procedures and the INTMIX model was used to assess the effect on the estimated concentration of CCN. A  $\kappa$  of 0.02, a value associated with this less hygroscopic fraction in urban environments (Wex et al., 2010), was used for the less hygroscopic mode. This resulted in a critical diameter of  $0.32\ \mu\text{m}$  for this mode as can be seen in Figure 3.28. In essence like the EXMIX model these less hygroscopic modes were removed from the number distributions and the number of CCN for the remainder calculated using AMS data, under the INTMIX assumptions and Equation 3.5 on page 198. The CCN contributions from each of the three less hygroscopic modes were then calculated and added to the concentrations from the dominant mode. The scatter plots of these new modelled CCN estimates and the measured CCN concentrations are shown in Figure 3.29. These modelled CCN were then used to back out a population mean critical diameter, seen as the upper estimates in the Figure 3.28 with the solid lines. The fit statistics for these new models that incorporate a less hygroscopic modes can be seen in Table 3.13.

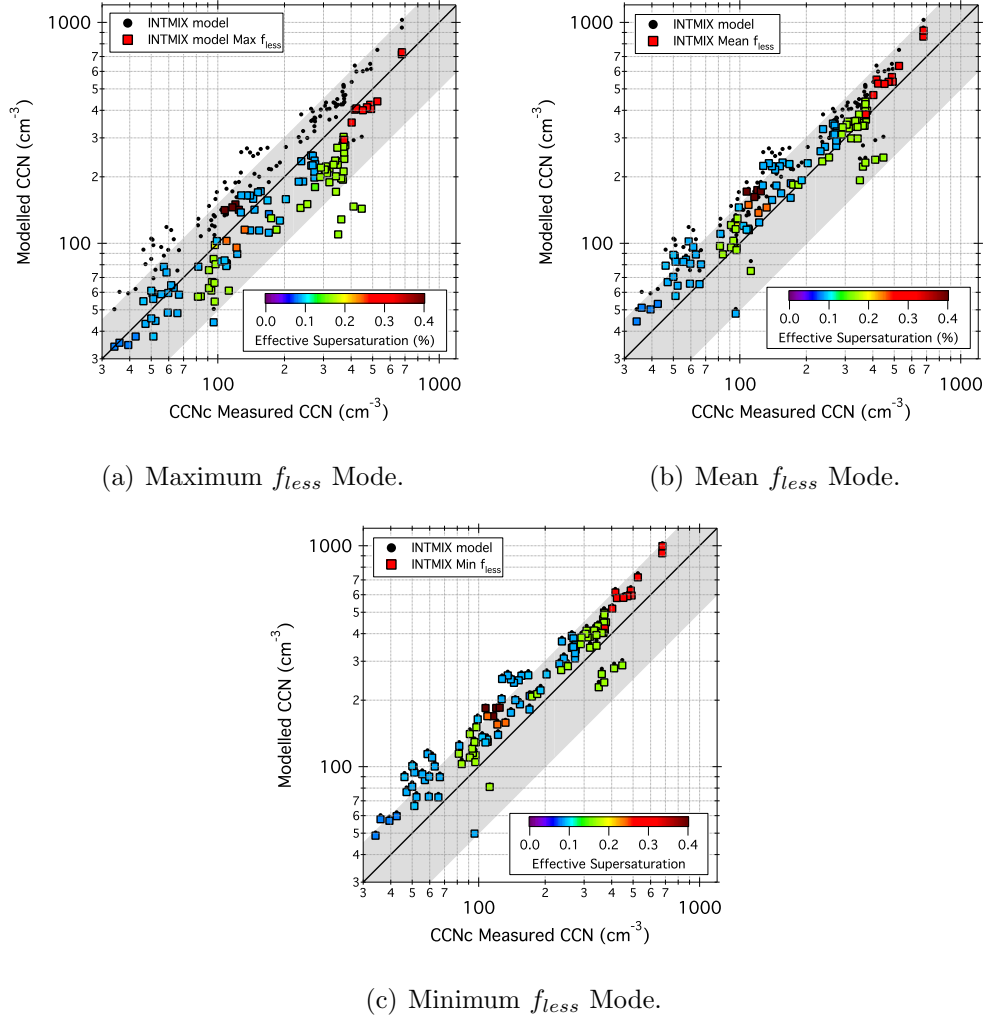


Figure 3.29:  $f_{less}$  models compared to CCNc measured CCN concentrations, colour coded by effective supersaturation. The black closed circles represent the EXMIX baseline model.

Metric	Model			
	EXMIX	Max $f_{less}$	Mean $f_{less}$	Min $f_{less}$
Slope	1.16	0.76	1.05	1.17
$R^2$	0.89	0.82	0.88	0.90
NME	33.34	24.99	19.53	31.08
NMB	27.88	-21.56	11.34	25.45
$N_p/N_o$ Mean	1.37	0.83	1.18	1.36
$N_p/N_o$ $\sigma$	0.32	0.22	0.25	0.28

Table 3.13: Fit statistics for  $f_{less}$  models compared to the simple EXMIX model.

It must be noted that this is a thought experiment used to test the hypothesis that there is a less hygroscopic aerosol mode encountered during the VOCALS

experiment. There is no data collected on the BAe-146 to prove the existence of or the magnitude of this less hygroscopic mode or its hygroscopicity either. However, it is clearly shown that the presence of such a secondary mode can account for the shortfall in the CCNc estimated value of  $\kappa$  compared to the AMS composition based estimates. It also accounts for the overestimate of the AMS parameterised model estimates of CCN. In all three sulphate zones the Mean  $f_{less}$  model only deviates by a maximum of  $0.01\ \mu\text{m}$  from the CCNc derived critical diameter at an effective supersaturation of 0.17 %. The suitability of this model is shown by the closeness of fit to the 1:1 line in Figure 3.29(b) and in the statistics that describe the relationship between the modelled and measured data in Table 3.13. The Mean  $f_{less}$  reduces both the slope and the model overestimation, shifting it closer to 1.0. It also reduces the scatter in the data with an NME closer to zero. These fit parameters are more in keeping with other values taken from the literature in Table 3.10. Obviously the size of the less hygroscopic mode interacts, in this model, with the hygroscopicity parameterisation. An increase in the hygroscopicity would increase the modelled CCNc contribution from this mode as would an increase in the mode's number assuming a stable hygroscopicity. Since there is no measurement of these factors it can only be proposed here that there is second less hygroscopic mode. The structure of which is not elucidated by the AMS and that this mode can explain the discrepancy between AMS derived and CCNc measured CCN concentrations as well as the difference in derived  $\kappa$  estimates for the two methods.

The exact composition and source of this marginally hygroscopic mode is unknown as is its exact contribution to the aerosol number concentration. It may not even be a 'missing' mode, just that there is not complete information about the aerosol's mixing state. When this information is substituted, as is assumed, by the hygroscopicity as defined by the bulk composition the models

understandably fail to replicate the reality of the CCN concentration.

To remove the possible sampling biases associated with the AMS one can compare the data from the  $\kappa$  analysis in this study to the literature. The bulk  $\kappa$  itself is too low to suggest a marine source even if the marginally hygroscopic mode was explicitly identified. Wex et al. (2010) show from literature sources of HTDMA measurements that in the marine environment the bulk  $\kappa$  should be in the region of 0.4, a more realistic measure than that of Andreae (2009) or Pringle et al. (2010) who estimate it to be 0.7 and 0.72, respectively. The SEP average of  $0.21 \pm 0.18$  is more akin to a rural or urban source as defined by Wex et al. (2010).

If marine sources are discounted as being the primary source of the accumulation mode aerosol then that leaves continental and long range transport via FT mixing as other sources for the marginally hygroscopic mode.

Entrainment of FT air into the MBL via subsidence is by its nature episodic and not uniform across the entire transect (Allen et al., 2011; Bretherton et al., 2010) and can therefore be discounted as the dominant source of accumulation mode aerosol. As suggested previously in this work the aerosol gradients in the offshore MBL are driven by coastal sources (Wood et al., 2011; Bretherton et al., 2010; Allen et al., 2011; Kleinman et al., 2012; Chand et al., 2010) and back trajectories show that the further west along the 20° S transect travelled the further south the five day back trajectory sources originate (Allen et al., 2011). On the line of these back trajectories is a field station at Paposo (25 0.4° S, 70 27.01° W and 690 m asl). This station took measurements of submicron aerosol composition (using a filter technique), light scattering and size distributions during the VOCALS campaign. The site is considered to be representative of the natural and anthropogenic regional scale sources along the coast that drive the gradients seen in the SEP (Chand et al., 2010). Using positive matrix factorisation four

source category solutions were obtained for the aerosol measured, marine, biomass burning, smelter output/soils and urban/biofuels. Aerosol mass contributions for each source show the dominant source to be urban and biofuels (>50 %) with biomass burning (>20 %), smelter output and soils being the next with marine source contributing the least to aerosol mass (<10 %). To test this PMF, a cluster analysis was conducted using back trajectories, a four cluster solution was found. Approximately 90 % of trajectories, 3 clusters, indicated flow from the south, the main difference between these clusters was northward wind speed. All three of these northerly clusters indicated flow that passed the Santiago area. This adds weight to the dominance of the urban biofuels as the dominant source type in the SEP. This fits with the estimates of CCNc derived  $\kappa$ . Sulphate was the most dominant species resolved in this study with a dry mass equivalent to 40 %. The filter analysis used water as the solute, as such, only water soluble anolytes were measured. Of the total mass 50 % was not speciated, most of which the authors purport to be organics (Chand et al., 2010). This analysis fits with that of Hawkins et al. (2010) in suggesting a substantial proportion of the organic aerosol is not captured using an AMS and that this aerosol originates from continental sources, Santiago in particular. The inclusion of these missing organics will necessarily reduce the modelled CCN concentrations and could easily form a marginally hygroscopic mode that could increase the compatibility of the two instrument derived estimates of  $\kappa$  and the closure analysis.

To summarise these discussion points concur with the findings of the  $\kappa$  analysis that the use of the AMS bulk chemical composition does not capture all the characteristics of the ambient aerosol in the VOCALS environment. If these data are carried through as parameterisations for Köhler modelling in large scale models then the critical diameters will be grossly underestimated. Consequently any inferences gleaned from the estimation of CCN number to droplet number,



size and ultimately indirect aerosol effects via this method will be biased to greater values. Therefore CCNc data must be considered to be invaluable in estimating and understanding the hygroscopic nature of the ambient aerosol. It is with hygroscopicities derived from these CCNc instrument's data that further modelling studies should be parameterised.

### 3.4 Threshold Droplet Growth Analysis

The growth kinetics of an atmospheric aerosol sampled with the CCNc can be investigated using ‘Threshold Droplet Growth Analysis’, TDGA. This analysis can make inferences into the water vapour up take rate of growing droplets. It can also be utilised to highlight any possible retardation or enhancement in an aerosol activated growth rates when compared to an ideal calibration salt model (Asa-Awuku et al., 2009; Bougiatioti et al., 2009; Lance et al., 2009; Asa-Awuku et al., 2011). The size of an activated particle exiting the CCNc growth column is a function of time, instrument supersaturation and the hygroscopicity of the particle. Particles with a low  $S_c$  will activate before those with a higher  $S_c$ , closer to the instrument set point, and as such exit the column as larger droplets. Under this assumption the mean droplet diameter exiting the CCNc growth column can be used as a measure of growth kinetics. A model for a standard ‘rapid growth’ can be estimated using a calibration salt,  $(\text{NH}_4)_2\text{SO}_4$ , where the water vapour uptake is uninhibited during activation and growth. This model can then be compared to atmospheric samples.

During operation the OPC at the end of the CCNc flow path measures the number and optical diameter of activated droplets between 0.75 and 20  $\mu\text{m}$  in 20 bins. The CCN concentration reported by the CCNc is simply an integration of all these binned data. Five  $(\text{NH}_4)_2\text{SO}_4$  aerosol diameters, 0.04, 0.05, 0.065, 0.085 and 0.1  $\mu\text{m}$  were subjected to 27 different instrument supersaturations. The supersaturations were chosen to be close to the  $S_c$  for each particle size sampled. The final minute of a ten minute sample of OPC droplet distributions were averaged to give a mean OPC distributions for each size and supersaturation. An example of three of these distributions can be seen in Figure 3.31. A normal probability distribution function was fitted to these distributions and the mean droplet diameter and its standard deviation extracted. The distributions measured were tested

by comparing the geometric mean diameter (GMD) as calculated in Equation 3.9 to the output from the PDF fits. The results of this test are in Figure 3.30. A discrepancy between these two methods would have highlighted any deviations from normality such as a bimodal distribution. All the distributions in this analysis were, based on agreement of the methods described, assumed to be normally distributed.

$$GMD = \frac{\sum n_i d_i}{\sum n_i}, \quad (3.9)$$

where  $n_i$  is the number of particles in bin  $i$ , having the midpoint of diameter  $d_i$  and  $\sum n_i$  is the total number of particles.

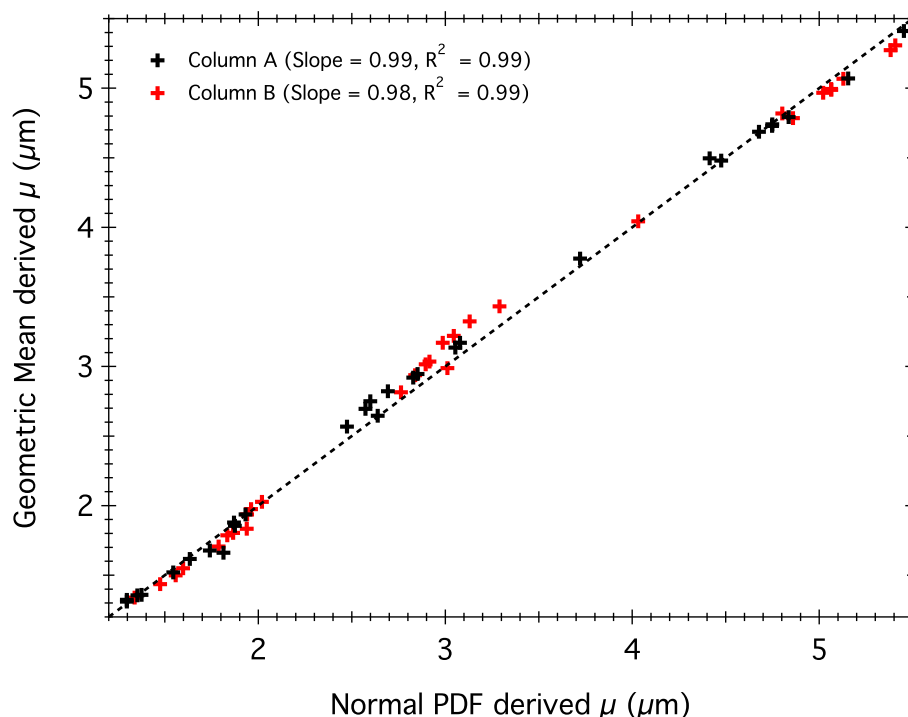


Figure 3.30: Example of the output distribution from the CCNc OPC and model estimates of the Normal probability distribution function for each, used to estimate mean droplet diameter and the standard deviation of that mean in Figures 3.32 and 3.33. The dotted line represents the  $x = y$  and the red and black crosses the column A and column B of the CCNc respectively.

The mean droplet diameter data was used to create a number of different standard ‘rapid growth’ pressure models for ambient pressure (1014 hPa), 700 and 650 hPa for both columns. The effective supersaturations on the abscissa are calculated from CCNc measured  $\Delta T$ , the pressure and Equation 2.15. These models can be seen in Figures 3.32 and 3.33 with the associated standard deviation represented on the measured data. The power laws fitted here are compared to the measured data from the VOCALS project to assess the level of inhibition or enhancement in droplet growth. This can be used to infer supersaturation retardation or highlight effects of organics on the activation dynamics of the aerosol

(Bougiatioti et al., 2009; Lance et al., 2009).

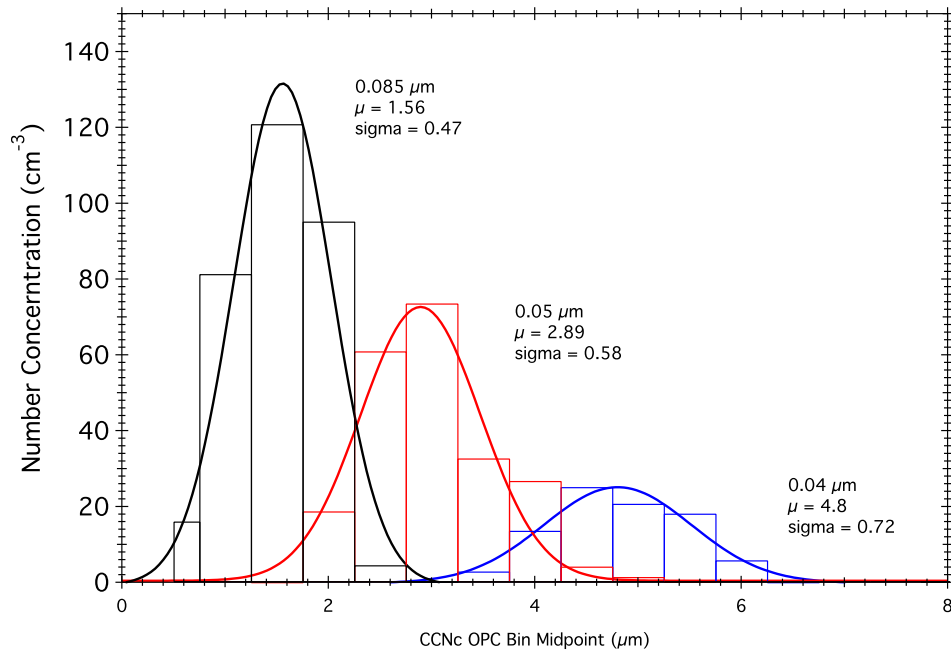


Figure 3.31: Example of the output distribution from the CCNc OPC and model estimates of the normal probability distribution function for each, used to estimate mean droplet diameter and the standard deviation of that mean in Figures 3.32 and 3.33. Black represents 0.085, red 0.05 and blue 0.04  $\mu\text{m}$   $(\text{NH}_4)_2\text{SO}_4$  dry particle diameters.

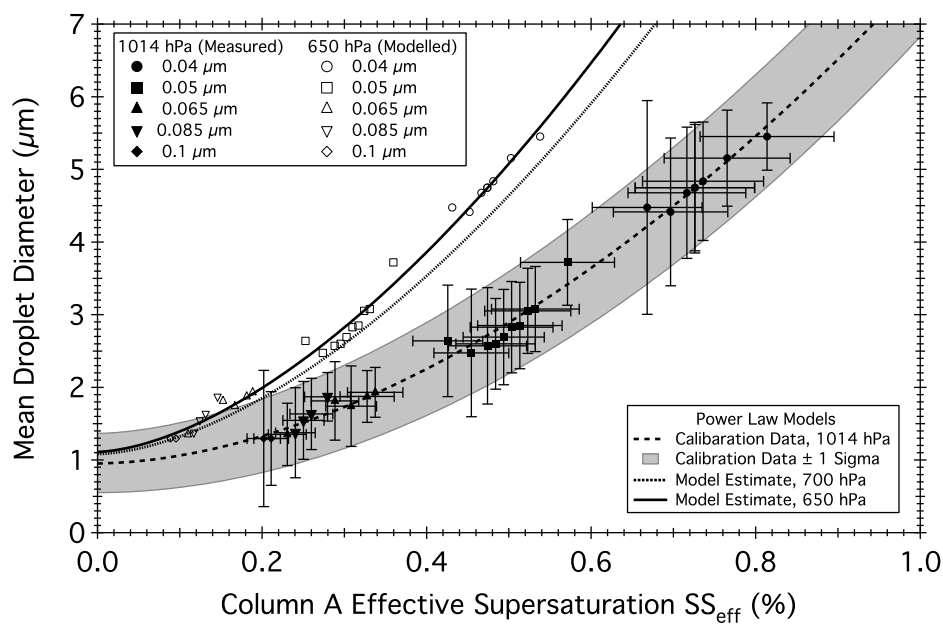


Figure 3.32: Calibration salt TDG analysis for column A. The closed symbols are calibration salt diameters. The open symbols represent the modelled data at 650 hPa. The lines represent different power laws, dashed for measured, dotted for 700 and solid for 650 hPa, respectively.

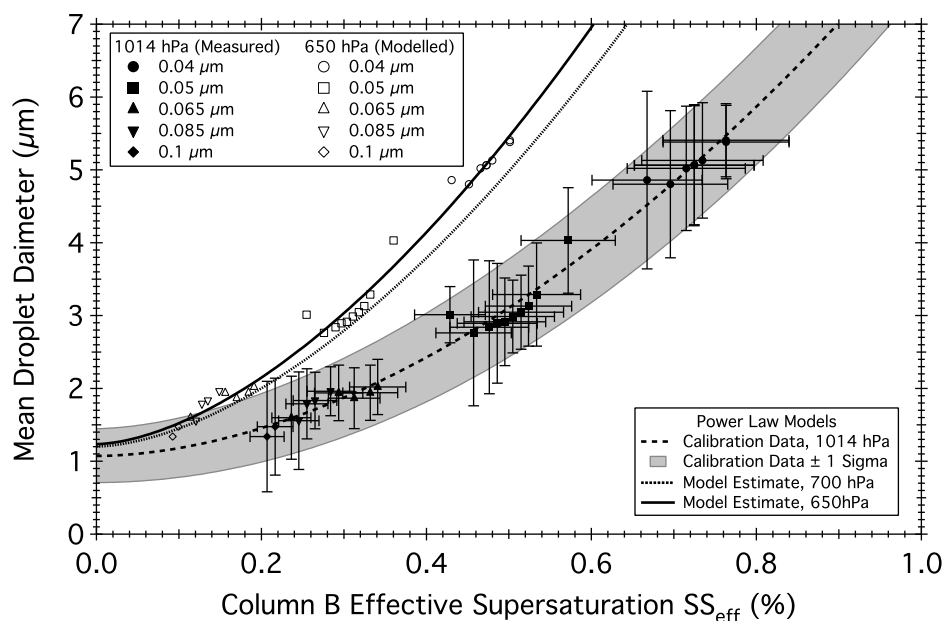
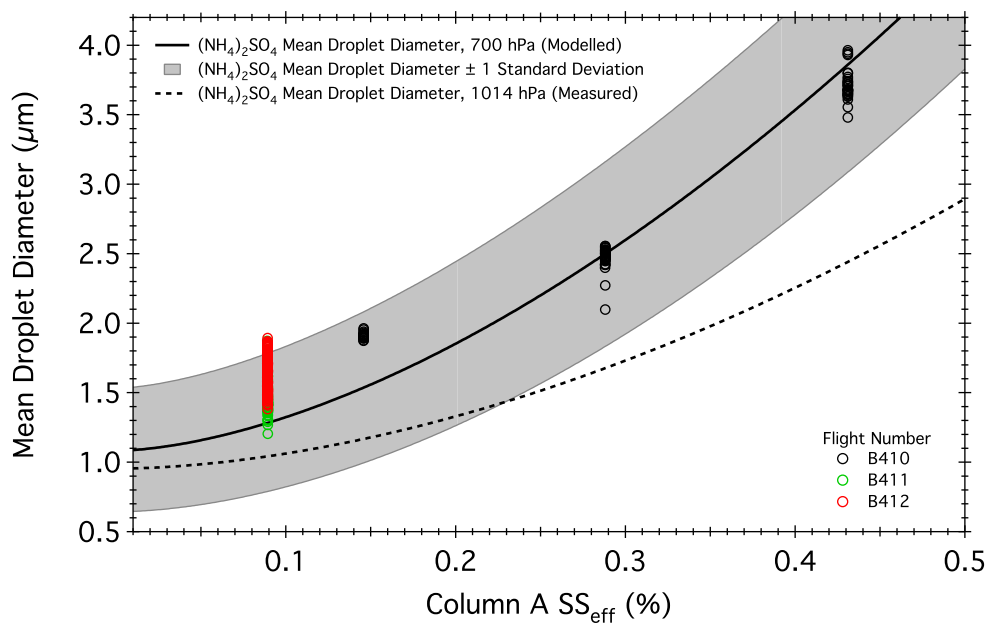
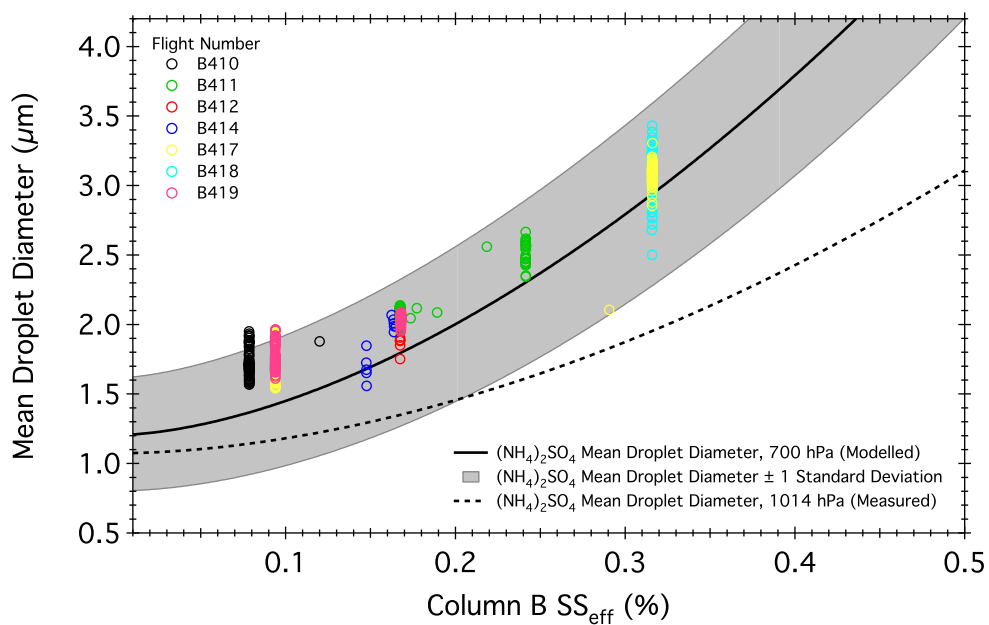


Figure 3.33: Calibration salt TDG analysis for column B. The closed symbols are calibration salt diameters. The open symbols represent the modelled data at 650 hPa. The lines represent different power laws, dashed for measured, dotted for 700 and solid for 650 hPa, respectively.

Both columns, Figures 3.34(a) and 3.34(b), show that the majority of all droplets formed from the ambient aerosol population are within one standard deviation of the mean droplet diameter expected from an ammonium sulphate calibrant. This analysis also shows that there is no water depletion in the instrument, which should not be expected at such low aerosol concentrations (Lathem and Nenes, 2011; Lance et al., 2009), but should not be assumed. The majority of data fall above the growth kinetics line defined by ammonium sulphate. Suggesting that the organics present in the ambient aerosol sample do not inhibit the activation of the CCN to droplets and their growth in the CCNc. The effect of the ambient polydisperse size distribution, compared to a monodisperse calibration salt, is not discussed here and as such the relationships in these plots are simply qualitative.



(a) TDGA for column A during VOCALS.



(b) TDGA for column B during VOCALS

Figure 3.34: Threshold droplet growth analysis for the data collected throughout the VOCALS campaign with both columns compared to ammonium sulphate calibration salts. Shaded area represents the standard deviation of the calibrated model as estimated in the previous section of this work.

In summary and in answer to the final question posed in Chapter 1 there are



no limitations on water uptake in the aerosol of the SEP. Suggesting that any organics in the system do don't create a barrier to activation that could affect the activation of aerosol to cloud droplets or any associated cloud processes.

## Further Work

This section can be split simply into further work with regards to the instrument and measurement infrastructure and those advancements that can be made with the methodologies.

The CCNc calibrations need to be undertaken at reduced pressure to build up a instrument specific model in the form of Equations 2.15. This would reduce any error in estimating effective supersaturation at multiple pressures. The pressure range of the reduced pressure inlet is not large enough to cover the entire altitude range of the aircraft without operator interaction. The BAe-146 is operated by a skeleton crew not all of whom have knowledge of the system so increasing the range would enable more data to be collected over a larger vertical range. In a similar manner the CCNc instrument built and operated by the Desert Research Institute which is run at a nominal 300 hPa (J.Hudson, personal communication, 2010). In the current set up the instrument is only really set up to take boundary layer measurements. It has been shown in this work that measuring at more instrument supersaturation set points adds more information on the mixing state of an ambient aerosol. If the instrument measured at only one effective supersaturation no information on the less hygroscopic mode would be available in

this work. If ten supersaturations had been available then this mode of marginal hygroscopicity could have been completely mapped in relation to the aerosol size distribution. Currently there is no commercial way of doing this with the DMT CCNc.

Work by Moore and Nenes (2009) has show in the laboratory how scanning the flow between 0.2 and 1.0 lpm whilst maintaining different stable thermal gradients the instrument can produce a scan of effective supersaturation between 0.08 and 2.6 %. This can be achieved in a time frame relevant to aircraft work, between 10 and 60 s. There is a trade off with longer time periods producing larger supersaturation scans and therefore capturing more information about the size dependent nature of the aerosol hygroscopicity. Moore et al. (2012) used this methodology in an airborne field campaign producing good results. There is also the possibility of investigating and exploiting the relationship between pressure and supersaturation to the same effect using the constant pressure inlet. As a rule of thumb the supersaturation changes by 0.03 % with every 100 hPa. With the two channel instrument used in this work operated at a relatively high and a relatively low starting supersaturation a stepwise scan could cover a range of approximately 0.3 % with the current constant pressure inlet, with an increased pressure range this could be extended.

Planning and undertaking future work on an aircraft platform is not as simple as undertaking laboratory experiments and simply effecting changes in measurement systems accordingly. Simply certifying a change of pump can run to ten times the cost of the pump itself. Testing is also expensive as the aircraft cost many thousands of pounds per hour to fly. However, more flights are planned to attempt to close some of the unknowns with respect to the Rosemount inlet work. Particularly incident angle with respect to the free stream and deceleration measurements. It is of paramount importance for all aerosol measurements that the

inlets used are well characterised and since the inlet enhancements appear to be aerosol specific then understanding the unknowns in their operation may enable us to model enhancements prior to undertaking a program of inlet replacement. Ideally in future these Rosemount inlets will be replaced with an inlet design fit for purpose and that is well characterised across a suitable aerosol size range. However, this does not absolve the need to characterise the Rosemount inlets fully. These inlets have been used to sample aerosol for 8 years to date with this aircraft. To simply switch inlets and not complete this characterisation would be to leave doubt in the veracity of the data collected thus far. In the future there are plans to attempt to co-sample air masses with ground stations in an attempt to provide a final validating data set that does not require an aircraft system measuring behind an inlet as a control. As conducted during the DC-8 Inlet Characterisation Experiment (DICE) (McNaughton et al., 2007). The first flight of this kind was planned for the summer of 2012 where co-located flying with the Izana mountain research station on the island of Tenerife was cancelled because there was none of the required Saharan outflow in the region at the time.

It is also of interest to fit thermal denuders on the inlet to both the SMPS and the CCNc. Their temperatures should be set to that of the AMS vaporiser. With this system data collected will represent the refractory part of the aerosol population. If these denuders can be switched so ambient air can be sampled between denuded air then the difference between these two data sets represent the non-refractory aerosol. The AMS data can then be used to attempt a closure on the number difference between the denuded residuals and ambient CCN. This would be a more accurate test of the methodology outlined in this work as one is comparing like with like.

Similar data sets to that collected for the VOCALS project exist for: polluted European air masses: pristine Asiatic and Amazonian rainforest and London in

and outflow. It is the plan based on the successful methods used here to produce a data set of aerosol hygroscopicities for all these environments.

## Conclusions

It has been shown here for the first time that the DMT dual column CFTGC CCNc is suitable for use on the BAe-146, the calibrations of the instrument effective supersaturation are repeatable, and that variation seen in calibration exercises is a function of instrument behaviour not of experimental design and that this variation is less than 10 %. Though no specific model relating effective supersaturation to pressure was derived in this work, experiments show that the CCNc columns behaved as theory suggests and compared well to other data in the literature. As such a generic correction can be used for all instrument supersaturations, this model has a maximum error of 10 %, however neither column exceeded 6 % deviation from the model across multiple test points. Novel work has shown that the bespoke reduced pressure inlet designed for operation here and used to stabilise the instrument supersaturation is fit for purpose. Modelled losses do not exceed 0.9 up to  $1.2\text{ }\mu\text{m}$  in diameter, measurements show that losses are kept below 10 % below  $0.6\text{ }\mu\text{m}$ . Again, no data is available in the literature but it is shown here that the instrument is well suited to short warm up times associated with airborne operations. Nominally the BAe-146 instrumentation is powered up two hours before flight. After 2 hours the maximum variation in

effective supersaturation is less than 2.5 %. It has also been shown that the specific losses associated with aerosol sampling to the CCNc are acceptable and for the first time that the models compare well to measured losses. However, the assumption used in the sampling losses methodology that the velocity ratio between the inlet head to the first right angle is the same as TAS to sample velocity is an over simplification. In fact the work from the inlet characterisation experiments show that there is substantial deceleration in Rosemount inlet head. This discrepancy will in reality reduce the losses associated with sampling around this right angle and should be propagated into any further loss modelling work.

Rosemount inlets, whose sampling efficiency on the BAe-146 has never been assessed prior to this work, have been shown to compare well across a distribution from 0.03 to 1  $\mu\text{m}$ . This suggests that deriving secondary and tertiary data products from instruments sampling behind different inlets is a viable technique. In aerosol of moderate density these inlets appear to sample representatively below 0.6  $\mu\text{m}$ , though in denser aerosol even at diameters of 0.3  $\mu\text{m}$  samples are enhanced by a factor of 1.8. This enhancement peaks between 10.2 and 8.2 times for two different inlets both at a diameter of 2.91  $\mu\text{m}$ . It was shown here that if all operating parameters of the aircraft are equal the discrepancy in inlet efficiency between the different aerosol types is a function of aerosol density. The models, compiled for this work, used to investigate this also suggest these inlets are also sensitive to changes in aircraft pitch. Without the work undertaken in Chapter 2 no CCN measurements could be made from the BAe-146 limiting our possible understanding of cloud-aerosol interactions. On a less grand scale none of the following analyses could have been achieved without the work undertaken in response to the first question posed in the Introduction.

The aerosol, gas phase and cloud microphysical characteristics of the SEP MBL have been well characterised. Though much of this data is not new, it is

the only source made up solely of BAe-146 data. The VOCALS data shows a well mixed boundary layer across the entire MBL and little evidence of the decoupling seen in other studies, this maybe a function of the limited range of the BAe-146 (80° W) when compared to the NCAR C-130 (85° W) as this decoupling occurs in the more remote maritime environment. There is evidence that the source strengths and locations are variable in time and space with transport of particulates from as far away as Santiago to the south west of the operating region and local marine sources of sulphate to the western end of the transect. The low organic to sulphate ratios suggest that there is little contribution locally from marine organics. The correlation between organics and black carbon suggest a combustion and therefore continental source. The MBL increases with height and the cloud deck thickness increases with distance from the continent as does the LWC and VMD. The cloud droplet number is well correlated to the particle number particularly to the western end of the transect with highest concentrations in the east close to source. The source regions for the majority of particulate matter originate on the South American continent. Consequently there is a strong gradient in aerosol mixing ratios with distance from source with a more polluted and variable environment close to the coast. The dominant component of the aerosol is sulphate and the single longitude binned CN and CCN range between, 833 to 287 and 370 to 80 particles  $\text{cm}^{-3}$  respectively. The dominant aerosol mode is in the accumulation mode between 0.175 and 0.227  $\mu\text{m}$ . In the falling sulphate zone at the western end of the transect this mode is nearly matched by an Atiken mode centred at 0.045  $\mu\text{m}$ . These gradients are driven primarily by air mass history with coastal regions being in greater contact with air masses which have passed over or close to coastal source to the south of the operating area in the previous few days and the more remote regions having had little or no contact in the same time period. The analysis of the vertically stratified data lead to the discrediting of the SMSP data above 400 m. This fact should be taken into account during



any further analysis of these data sets. The characteristics shown here are invaluable for validating, and in the case of the CCN, aerosol composition and aerosol distributions, parameterising regional scale models. On a smaller scale they are important for the discussion centred around the third and four questions posed at the start of this study about the hygroscopicity of the SEP aerosol.

This work is the first to derive the  $\kappa$  of the SEP MBL aerosol, by any method. In comparing the CCNc derived value to the values from the literature and assessing any possible instrumental biases it is concluded here that where there is viable aerosol distribution information, the method is robust. This methodology could only be attempted after the in-depth testing of the CCNc and its associated sampling architecture. The project mean value of  $\kappa$  is 0.21. This value corroborates the SEP characterisation work that even in the low sulphate zone the aerosol is dominated by continental sources as opposed to maritime, even though the low particle numbers at the western end of the transect are representative of a remote marine environment. The horizontal variability in the  $\kappa$  is low across all longitudinal zones suggesting all longitudes have a similar chemistry stretching from the coast to 78° W. There is however, not enough data from the MBL to define any significant trends in either the horizontal or vertical. The  $\kappa$  values derived from CCNc data do not compare well to those derived from the AMS bulk composition. On average the AMS derived values are 51 % larger, with a mean value of 0.53 at instrument supersaturation of 0.09 %. This overestimation increases to 86 % at an instrument supersaturation of 0.43 %. It is of the utmost importance to understand this discrepancy as many large scale models used the composition data to parameterise simplified Köhler models. Errors in this composition will skew the CCN and CDN and therefore any modelled cloud albedo. The verified CCNc and the robust nature of the CCNc derived  $\kappa$  have shown in the SEP the discrepancy between the two techniques.

The hygroscopicity data suggest that there is a less hygroscopic mode in the aerosol population and that this mode is not spread evenly across the distribution. This is indicative of an externally mixed aerosol, at least with respect to hygroscopicity, if not composition. This mode occupies more of the number at smaller diameters between  $0.25\ \mu\text{m}$  and  $0.08\ \mu\text{m}$  than larger diameters. There is no size resolved composition data from the AMS to validate this. The discrepancy seen between the hygroscopicity of the AMS and CCNc based methods, as would be expected, was also seen in the CCN closure experiment. All of the possible sources of uncertainty in the Köhler model schemes, to predict CCN number from AMS composition were investigated in a sensitivity analysis. None of which could account for the discrepancies between the two methods. It is proposed here that the only an external mixture can lead to such an overestimation in hygroscopicity derived from the bulk composition. It was proved here that by manipulating the distributions to include a mode of limited hygroscopicity, based on literature values, could account for the discrepancy borne out of the AMS data. It was also shown that this mode was of an urban source, most possibly associated with long range transport from Santiago. The major consequence of these findings is that the bulk composition does not capture the complexities of the SEP aerosol and as such should not be used as the sole determinant of hygroscopicities in any modelling exercises. The CCNc derived  $\kappa$  should be used in its place.

The activation kinetics of the SEP aerosol are similar to that of laboratory grade ammonium sulphate suggesting there are no delays in activity from the organics present in the system. Consequently there can be no limitations in droplet activation and any associated cloud processes in the SEP.

# Bibliography

- Albrecht BA, 1989: Aerosols, cloud microphysics, and fractional cloudiness. *Science*, 245, 1227–1230.
- Allan JD, Baumgardner D, Raga GB, Mayol-Bracero OL, Morales-García F, García-García F, Montero-Martínez G, Borrmann S, Schneider J, Mertes S, Walter S, Gysel M, Dusek U, Frank GP, and Krämer M, 2008: Clouds and aerosols in puerto rico – a new evaluation. *Atmospheric Chemistry and Physics*, 8, 1293–1309.
- Allan JD, Delia AE, Coe H, Bower KN, Alfarra MR, Jimenez JL, Middlebrook AM, Drewnick F, Onasch TB, Canagaratna MR, Jayne JT, and Worsnop DR, 2004: A generalised method for the extraction of chemically resolved mass spectra from aerodyne aerosol mass spectrometer data rid b-1160-2010 rid a-5294-2008 rid e-4831-2011 rid d-2817-2009. *Journal of Aerosol Science*, 35, 909–922.
- Allan JD, Jimenez JL, Williams PI, Alfarra MR, Bower KN, Jayne JT, Coe H, and Worsnop DR, 2003: Quantitative sampling using an aerodyne aerosol mass spectrometer 1. techniques of data interpretation and error analysis. *Journal of Geophysical Research*, 108, 4090–.
- Allen G, Coe H, Clarke A, Bretherton C, Wood R, Abel SJ, Barrett P, Brown P, George R, Freitag S, McNaughton C, Howell S, Shank L, Kapustin V, Brekhovskikh V, Kleinman L, Lee YN, Springston S, Toniazzo T, Krejci R, Fochesatto J, Shaw G, Krecl P, Brooks B, McMeeking G, Bower KN, Williams PI, Crosier J, Crawford I, Connolly P, Allan JD, Covert D, Bandy AR, Russell LM, Trembath J, Bart M, McQuaid JB, Wang J, and Chand D, 2011: South east pacific atmospheric composition and variability sampled along 20 degrees s during vocals-rex rid a-7679-2008 rid b-1160-2010. *Atmospheric Chemistry and Physics*, 11, 5237–5262.
- Andreae MO, 2009: A New Look at Aging Aerosols. *Science*, 326, 1493-1494.
- Andreae MO and Rosenfeld D, 2008: Aerosol-cloud-precipitation interactions.

- Part 1. The nature and sources of cloud-active aerosols. *Earth-Science Reviews*, 89, 13-41.
- Asa-Awuku A, Engelhart GJ, Lee BH, Pandis SN, and Nenes A, 2009: Relating ccn activity, volatility, and droplet growth kinetics of beta-caryophyllene secondary organic aerosol. *Atmospheric Chemistry and Physics*, 9, 795–812.
- Asa-Awuku A, Moore RH, Nenes A, Bahreini R, Holloway JS, Brock CA, Middlebrook AM, Ryerson TB, Jimenez JL, DeCarlo PF, Hecobian A, Weber RJ, Stickel R, Tanner DJ, and Huey LG, 2011: Airborne cloud condensation nuclei measurements during the 2006 texas air quality study rid e-9653-2010 rid e-4831-2011 rid c-9611-2009 rid a-5294-2008. *Journal of Geophysical Research-atmospheres*, 116, D11201.
- Bahreini R, Dunlea EJ, Matthew BM, Simons C, Docherty KS, DeCarlo PF, Jimenez JL, Brock CA, and Middlebrook AM, 2008: Design and operation of a pressure-controlled inlet for airborne sampling with an aerodynamic aerosol lens. *Aerosol Science and Technology*, 42, 465-471.
- Bahreini R, Ervens B, Middlebrook AM, Warneke C, de Gouw JA, DeCarlo PF, Jimenez JL, Brock CA, Neuman JA, Ryerson TB, Stark H, Atlas E, Brioude J, Fried A, Holloway JS, Peischl J, Richter D, Walega J, Weibring P, Wollny AG, and Fehsenfeld FC, 2009: Organic aerosol formation in urban and industrial plumes near houston and dallas, texas. *Journal of Geophysical Research-atmospheres*, 114, D00F16.
- Belyaev S and Levin L, 1974: Techniques for collection of representative aerosol samples. *Journal of Aerosol Science*, 5, 325 - 338.
- Benedict KB, Lee T, and Collett JL, 2012: Cloud water composition over the southeastern pacific ocean during the vocals regional experiment. *Atmospheric Environment*, 46, 104–114.
- Bond T, Anderson T, and Campbell D, 1999: Calibration and intercomparison of filter-based measurements of visible light absorption by aerosols. *Aerosol Science and Technology*, 30, 582-600.
- Bougiatioti A, Fountoukis C, Kalivitis N, Pandis SN, Nenes A, and Mihalopoulos N, 2009: Cloud condensation nuclei measurements in the marine boundary layer of the eastern Mediterranean: CCN closure and droplet growth kinetics. *Atmospheric Chemistry and Physics*, 9, 7053-7066.
- Bretherton CS, Wood R, George RC, Leon D, Allen G, and Zheng X, 2010: Southeast pacific stratocumulus clouds, precipitation and boundary layer structure sampled along 20° s during vocals-rex. *Atmos. Chem. Phys.*, 10, 10639–10654.
- Brixey L, Evans D, and Vincent J, 2005: Aspiration efficiency of a thin-walled probe at right angles to the wind. *Journal of Aerosol Science*, 36, 1144-1156.

- Chand D, Hegg DA, Wood R, Shaw GE, Wallace D, and Covert DS, 2010: Source attribution of climatically important aerosol properties measured at paposo (chile) during vocals. *Atmospheric Chemistry and Physics*, 10, 10789–10801.
- Chen SC, Tsai CJ, Wu CH, Pui DYH, Onischuk AA, and Karasev VV, 2007: Particle loss in a critical orifice. *Journal of Aerosol Science*, 38, 935–949.
- Clegg SL and Brimblecombe P, 1988: Equilibrium partial pressures of strong acids over concentrated saline solutions .1. hno<sub>3</sub>. *Atmospheric Environment*, 22, 91–100.
- Cotton W, Zhang H, McFarquhar G, and Saleeby S, 2007: Should we consider polluting hurricanes to reduce their intensity. *J. Wea. Mod*, 39, 70–73.
- Dusek U, Frank GP, Hildebrandt L, Curtius J, Schneider J, Walter S, Chand D, Drewnick F, Hings S, Jung D, Borrmann S, and Andreae MO, 2006: Size matters more than chemistry for cloud-nucleating ability of aerosol particles. *Science*, 312, 1375–1378.
- Ervens B, Feingold G, and Kreidenweis SM, 2005: Influence of water-soluble organic carbon on cloud drop number concentration rid e-5993-2011. *Journal of Geophysical Research-atmospheres*, 110, D18211.
- Foltescu V, SELIN E, and BELOW M, 1995: Corrections for particle losses and sizing errors during aircraft aerosol sampling using a Rosemount inlet and the PMS LAS-X. *Atmospheric Environment*, 29, 449–453.
- Forster P, Ramaswamy V, Artaxo P, Berntsen T, Betts R, Fahey D, Haywood J, Lean J, Lowe D, Myhre G, Nganga J, Prinn R, Raga G, Schulz M, and Dorland RV, 2007: *Changes in Atmospheric Constituents and in Radiative Forcing. In: Climate Change 2007: The Physical Science Basis. Contribution of Working Group I to the Fourth Assessment Report of the Intergovernmental Panel on Climate Change*. Cambridge University Press, Cambridge, United Kingdom and New York, NY, USA.
- Fuchs N, 1964: *The Mechanics Of Aerosol*. Pergamon.
- Good N, Coe H, and McFiggans G, 2010: Instrumentational operation and analytical methodology for the reconciliation of aerosol water uptake under sub- and supersaturated conditions. *Atmospheric Measurement Techniques*, 3, 1241–1254.
- Gunthe SS, King SM, Rose D, Chen Q, Roldin P, Farmer DK, Jimenez JL, Artaxo P, Andreae MO, Martin ST, and Poeschl U, 2009: Cloud condensation nuclei in pristine tropical rainforest air of Amazonia: size-resolved measurements and modeling of atmospheric aerosol composition and CCN activity. *Atmospheric Chemistry and Physics*, 9, 7551–7575.

- Hangal S and Willeke K, 1990: Aspiration efficiency - unified model for all forward sampling angles. *Environmental Science & Technology*, 24, 688–691.
- Hangal S and Willike K, 1990: Overall efficiency of tubular inlets sampling at 0-90 degrees from horizontal aerosol flows. *Atmospheric Environment Part A-general Topics*, 24, 2379–2386.
- Hawkins LN, Russell LM, Covert DS, Quinn PK, and Bates TS, 2010: Carboxylic acids, sulfates, and organosulfates in processed continental organic aerosol over the southeast pacific ocean during vocals-rex 2008. *Journal of Geophysical Research-atmospheres*, 115, D13201.
- Haywood J and Boucher O, 2000: Estimates of the direct and indirect radiative forcing due to tropospheric aerosols: A review. *Reviews of Geophysics*, 38, 513–543.
- Haywood J, Francis P, Dubovik O, Glew M, and Holben B, 2003: Comparison of aerosol size distributions, radiative properties, and optical depths determined by aircraft observations and sun photometers during safari 2000 rid a-8235-2009. *Journal of Geophysical Research-atmospheres*, 108, 8471.
- Heim M, Mullins BJ, Umhauer H, and Kasper G, 2008: Performance evaluation of three optical particle counters with an efficient "multimodal" calibration method. *Journal of Aerosol Science*, 39, 1019–1031.
- Heyder J and Gebhart J, 1977: Gravitational deposition of particles from laminar aerosol flow through inclined circular tubes. *Journal of Aerosol Science*, 8, 289–295.
- Hinds W, 1999: *Aerosol technology: properties, behavior, and measurement of airborne particles*. Wiley.
- Hoppel WA, Frick GM, and Larson RE, 1986: Effect of nonprecipitating clouds on the aerosol size distribution in the marine boundary-layer. *Geophysical Research Letters*, 13, 125–128.
- Hudson J, 1993: Cloud condensation nuclei. *Journal of Applied Meteorology*, 32, 596–607.
- Hudson JG, 2007: Variability of the relationship between particle size and cloud-nucleating ability. *Geophysical Research Letters*, 34, L08801–.
- James A, 2003: Location of inlets and sensors in relation to the boundary layer. *Technical Note*, pp. 1–12.
- Jayne JT, Leard DC, Zhang XF, Davidovits P, Smith KA, Kolb CE, and Worsnop DR, 2000: Development of an aerosol mass spectrometer for size and composition analysis of submicron particles rid a-8596-2009 rid d-2817-2009. *Aerosol Science and Technology*, 33, 49–70.

- Johnson G, Ristovski Z, and Morawska L, 2004: Method for measuring the hygroscopic behaviour of lower volatility fractions in an internally mixed aerosol. *Journal of Aerosol Science*, 35, 443-455.
- Jones CR, Bretherton CS, and Leon D, 2011: Coupled vs. decoupled boundary layers in vocals-rex. *Atmospheric Chemistry and Physics*, 11, 7143-7153.
- Juranyi Z, Gysel M, Weingartner E, DeCarlo PF, Kammermann L, and Baltensperger U, 2010: Measured and modelled cloud condensation nuclei number concentration at the high alpine site jungfrau-joch. *Atmospheric Chemistry and Physics*, 10, 7891-7906.
- Kaaden N, Massling A, Schladitz A, Muller T, Kandler K, Schutz L, Weinzierl B, Petzold A, Tesche M, Leinert S, Deutscher C, Ebert M, Weinbruch S, and Wiedensohler A, 2009: State of mixing, shape factor, number size distribution, and hygroscopic growth of the saharan anthropogenic and mineral dust aerosol at tinfou, morocco. *Tellus Series B-chemical and Physical Meteorology*, 61, 51-63.
- Kleinman LI, Daum PH, Lee YN, Lewis ER, Sedlacek III AJ, Senum GI, Springston SR, Wang J, Hubbe J, Jayne J, Min Q, Yum SS, and Allen G, 2012: Aerosol concentration and size distribution measured below, in, and above cloud from the doe g-1 during vocals-rex. *Atmospheric Chemistry and Physics*, 12, 207-223.
- Kramer M and Afchine A, 2004: Sampling characteristics of inlets operated at low U/U-0 ratios: new insights from computational fluid dynamics (CFX) modeling. *Journal of Aerosol Science*, 35, 683-694.
- Kumar P, Sokolik IN, and Nenes A, 2011: Measurements of cloud condensation nuclei activity and droplet activation kinetics of fresh unprocessed regional dust samples and minerals. *Atmospheric Chemistry and Physics*, 11, 3527-3541.
- Lance S, Brock CA, Rogers D, and Gordon JA, 2010: Water droplet calibration of the cloud droplet probe (cdp) and in-flight performance in liquid, ice and mixed-phase clouds during arcpac rid a-4834-2011 rid g-3406-2011. *Atmospheric Measurement Techniques*, 3, 1683-1706.
- Lance S, Medina J, Smith J, and Nenes A, 2006: Mapping the operation of the DMT Continuous Flow CCN counter. *Aerosol Science and Technology*, 40, 242-254.
- Lance S, Nenes A, Mazzoleni C, Dubey MK, Gates H, Varutbangkul V, Rissman TA, Murphy SM, Sorooshian A, Flagan RC, Seinfeld JH, Feingold G, and Jonsson HH, 2009: Cloud condensation nuclei activity, closure, and droplet growth kinetics of houston aerosol during the gulf of mexico atmospheric composition and climate study (gomaccs) rid a-4834-2011 rid e-5615-2011 rid e-3949-2010. *Journal of Geophysical Research-atmospheres*, 114, D00F15.

- Lathem TL and Nenes A, 2011: Water vapor depletion in the dmt continuous-flow ccn chamber: Effects on supersaturation and droplet growth. *Aerosol Science and Technology*, 45, 604–615.
- Lee J, Rubow K, Pui D, and Liu B, 1993: Design and performance evaluation of a pressure-reducing device for aerosol sampling from high purity gases. *Aerosol Science and Technology*, 19, 215–226.
- Liu BYH, Zhang ZQ, and Kuehn TH, 1989: A numerical study of inertial errors in anisokinetic sampling. *Journal of Aerosol Science*, 20, 367–380.
- Martin S, 2000: Phase transition of aqueous atmospheric particles. *Chemical Reviews*, 100, 3403–3453.
- McFiggans G, Artaxo P, Baltensperger U, Coe H, Facchini MC, Feingold G, Fuzzi S, Gysel M, Laaksonen A, Lohmann U, Mentel TF, Murphy DM, O’Dowd CD, Snider JR, and Weingartner E, 2006: The effect of physical and chemical aerosol properties on warm cloud droplet activation. *Atmospheric Chemistry and Physics*, 6, 2593–2649.
- McMeeking GR, Good N, Petters MD, McFiggans G, and Coe H, 2011: Influences on the fraction of hydrophobic and hydrophilic black carbon in the atmosphere. *Atmospheric Chemistry and Physics*, 11, 5099–5112.
- McNaughton CS, Clarke AD, Howell SG, Pinkerton M, Anderson B, Thornhill L, Hudgins C, Winstead E, Dibb JE, Scheuer E, and Maring H, 2007: Results from the DC-8 Inlet Characterization Experiment (DICE): Airborne versus surface sampling of mineral dust and sea salt aerosols. *AEROSOL SCIENCE AND TECHNOLOGY*, 41, 136–159.
- Meehl GA, Stocker TF, Collins WD, Friedlingstein P, Gaye AT, Gregory JM, Kitoh A, Knutti R, Murphy JM, Noda A, Raper SCB, Watterson IG, Weaver AJ, and Zhao ZC, 2007: Global climate projections, in: Climate change 2007: The physical science basis. contribution of working group i to the fourth assessment report of the intergovernmental panel on climate change.
- Moore RH, Bahreini R, Brock CA, Froyd KD, Cozic J, Holloway JS, Middlebrook AM, Murphy DM, and Nenes A, 2011: Hygroscopicity and composition of alaskan arctic ccn during april 2008. *Atmospheric Chemistry and Physics*, 11, 11807–11825.
- Moore RH, Cerully K, Bahreini R, Brock CA, Middlebrook AM, and Nenes A, 2012: Hygroscopicity and composition of california ccn during summer 2010. *Journal of Geophysical Research-atmospheres*, 117, D00V12.
- Moore RH and Nenes A, 2009: Scanning Flow CCN Analysis-A Method for Fast Measurements of CCN Spectra. *Aerosol Science and Technology*, 43, 1192–1207.



- Murphy SM, Agrawal H, Sorooshian A, Padro L, Gates H, Hersey S, Welch WA, Jung H, Miller JW, Cocker DR, Nenes A, Jonsson HH, Flagan RC, and Seinfeld JH, 2009: Comprehensive simultaneous shipboard and airborne characterization of exhaust from a modern container ship at sea. *Environmental Science and Technology*, 43, 4626–4640.
- Muyshondt A A McFarland and Anand A, 1996: Deposition of aerosol particles in contraction fittings. *Aerosol Science and Technology*, 24, 205–216.
- Nenes A, Pandis SN, and Pilinis C, 1998: Isorropia: A new thermodynamic equilibrium model for multiphase multicomponent inorganic aerosols. *Aquatic Geochemistry*, 4, 123–152.
- O’Dowd CD, Becker E, and Kulmala M, 2001: Mid-latitude north-atlantic aerosol characteristics in clean and polluted air. *Atmospheric Research*, 58, 167–185.
- Osborne SR, Johnson DW, Wood R, Bandy BJ, Andreae MO, O’Dowd CD, Glantz P, Noone KJ, Gerbig C, Rudolph J, Bates TS, and Quinn P, 2000: Evolution of the aerosol, cloud and boundary-layer dynamic and thermodynamic characteristics during the 2nd lagrangian experiment of ace-2. *Tellus B*, 52, 375–400.
- Parsons MT, Knopf DA, and Bertram AK, 2004: Deliquescence and crystallization of ammonium sulfate particles internally mixed with water-soluble organic compounds. *Journal of Physical Chemistry A*, 108, 11600–11608.
- Petters MD and Kreidenweis SM, 2007: A single parameter representation of hygroscopic growth and cloud condensation nucleus activity. *Atmospheric Chemistry and Physics*, 7, 1961–1971.
- Petzold A, 2009: Characterisation of a rosemount inlet for airborne aerosol measurement. *ASGOS Interim Report to Sub-task 4.1*.
- Pich, 1964: Impaction of aerosol particles in the neighbourhood of a circular hole. *Collection of Czechoslovakia Chemical Communications*, 29, 2223–2227.
- Pringle KJ, Tost H, Pozzer A, Poeschl U, and Lelieveld J, 2010: Global distribution of the effective aerosol hygroscopicity parameter for CCN activation. *Atmospheric Chemistry and Physics*, 10, 5241–5255.
- Prisle N, Raatikainen T SR, Svenningsson B LA, and M B, 2008: Surfactant partitioning in cloud droplet activation: a study of c8, c10, c12 and c14 normal fatty acid sodium salts. *Tellus B*, 60, 416–431.
- Prisle NL, Dal Maso M, and Kokkola H, 2011: A simple representation of surface active organic aerosol in cloud droplet formation. *Atmospheric Chemistry and Physics*, 11, 4073–4083.

- Pui D, Rubow K, Lee J, and Lui B, 1990: Design of pressure reducing devices for high purity gas sampling. *Proceedings 10th International Symposium of Contamination Control, Zurich, Switzerland*, September 10-14th, 408-412.
- Pui F DYH Romnay-Novas and Liu B, 1987: Experimental study of particle deposition in bends of circular cross section. *Aerosol Science and Technology*, 7, 310-315.
- Pui Y, Ye Y, and Liu B, 1988: Sampling, transport and deposition of particles in high purity gas supply system. *Proceedings 9th International Symposium of Contamination Control, Zurich, Switzerland*, September 26th-30th, 287-292.
- Rahn DA and Garreaud R, 2010: Marine boundary layer over the subtropical southeast pacific during vocals-rex part 1: Mean structure and diurnal cycle. *Atmospheric Chemistry and Physics*, 10, 4491-4506.
- Reeves JM, Wilson JC, Brock CA, and Bui TP, 2008: Comparison of aerosol extinction coefficients, surface area density, and volume density from SAGE II and in situ aircraft measurements. *Journal of Geophysical Research-Atmospheres*, 113.
- Rissman TA, VanReken TM, Wang J, Gasparini R, Collins DR, Jonsson HH, Brechtel FJ, Flagan RC, and Seinfeld JH, 2006: Characterization of ambient aerosol from measurements of cloud condensation nuclei during the 2003 atmospheric radiation measurement aerosol intensive observational period at the southern great plains site in oklahoma. *Journal of Geophysical Research-atmospheres*, 111, D05S11.
- Roberts G, Mauger G, Hadley O, and Ramanathan V, 2006: North american and asian aerosols over the eastern pacific ocean and their role in regulating cloud condensation nuclei. *Journal of Geophysical Research-atmospheres*, 111, D13205.
- Roberts G and Nenes A, 2005: A continuous-flow streamwise thermal-gradient CCN chamber for atmospheric measurements. *Aerosol Science and Technology*, 39, 206-221.
- Roberts GC, Day DA, Russell LM, Dunlea EJ, Jimenez JL, Tomlinson JM, Collins DR, Shinozuka Y, and Clarke AD, 2010: Characterization of particle cloud droplet activity and composition in the free troposphere and the boundary layer during intex-b. *Atmospheric Chemistry and Physics*, 10, 6627-6644.
- Rogers R and Yau M, 1996: *A short Course in Cloud Physics*. Butterworth-Heinemann.
- Rose D, Gunthe SS, Mikhailov E, Frank GP, Dusek U, Andreae MO, and Poeschl U, 2008: Calibration and measurement uncertainties of a continuous-flow cloud

- condensation nuclei counter (DMT-CCNC): CCN activation of ammonium sulfate and sodium chloride aerosol particles in theory and experiment. *Atmospheric Chemistry and Physics*, 8, 1153–1179.
- Rose D, Nowak A, Achtert P, Wiedensohler A, Hu M, Shao M, Zhang Y, Andreae M, and Pöschl U, 2010: Cloud condensation nuclei in polluted air and biomass burning smoke near the mega-city guangzhou, china—part 1: Size-resolved measurements and implications for the modeling of aerosol particle hygroscopicity and ccn activity. *Atmospheric Chemistry and Physics*, 10, 3365–3383.
- Rosenberg PD, Dean AR, Williams PI, Dorsey JR, Minikin A, Pickering MA, and Petzold A, 2012: Particle sizing calibration with refractive index correction for light scattering optical particle counters and impacts upon pcasp and cdp data collected during the fennec campaign. *Atmospheric Measurement Techniques*, 5, 1147–1163.
- Ryder CL, Highwood EJ, Rosenberg PD, Trembath J, Brooke JK, Bart M, Dean A, Crosier J, Dorsey J, Brindley H, Banks J, Marsham JH, McQuaid JB, Sodemann H, and Washington R, 2013: Optical properties of saharan dust aerosol and contribution from the coarse mode as measured during the fennec 2011 aircraft campaign. *Atmos. Chem. Phys.*, 13, 303–325.
- Seinfeld J and Pandis S, 2006: *Atmospheric Chemistry and Physics: From Air Pollution to Climate Change*. John Wiley.
- Shank LM, Howell S, Clarke AD, Freitag S, Brekhovskikh V, Kapustin V, McNaughton C, Campos T, and Wood R, 2012: Organic matter and non-refractory aerosol over the remote southeast pacific: oceanic and combustion sources. *Atmospheric Chemistry and Physics*, 12, 557–576.
- Snider JR, Guibert S, Brenguier JL, and Putaud JP, 2003: Aerosol activation in marine stratocumulus clouds: 2. kohler and parcel theory closure studies. *Journal of Geophysical Research-atmospheres*, 108, 8629.
- Squires P, 1958: The microstructure and colloidal stability of warm clouds. *Tellus*, 10, 262–271.
- Topping D, McFiggans G, and Coe H, 2005a: A curved multi-component aerosol hygroscopicity model framework: Part 1 - Inorganic compounds. *Atmospheric Chemistry and Physics*, 5, 1205–1222.
- Topping D, McFiggans G, and Coe H, 2005b: A curved multi-component aerosol hygroscopicity model framework: Part 2 - Including organic compounds. *Atmospheric Chemistry and Physics*, 5, 1223–1242.
- Twohy CH, Petters MD, Snider JR, Stevens B, Tahnk W, Wetzal M, Russell L, and Burnet F, 2005: Evaluation of the aerosol indirect effect in marine stratocumulus clouds: Droplet number, size, liquid water path, and radiative impact. *Journal of Geophysical Research-atmospheres*, 110, D08203.

- Twomey S, 1974: Pollution and the planetary albedo. *Atmospheric Environment* (1967), 8, 1251–1256.
- VanReken TM, Rissman TA, Roberts GC, Varutbangkul V, Jonsson HH, Flagan RC, and Seinfeld JH, 2003: Toward aerosol/cloud condensation nuclei (ccn) closure during crystal-face. *Journal of Geophysical Research-atmospheres*, 108, 4633.
- Wang J, Lee YN, Daum PH, Jayne J, and Alexander ML, 2008: Effects of aerosol organics on cloud condensation nucleus (ccn) concentration and first indirect aerosol effect rid g-9344-2011. *Atmospheric Chemistry and Physics*, 8, 6325–6339.
- Wang SC and Flagan RC, 1990: Scanning electrical mobility spectrometer. *Aerosol Science and Technology*, 13, 230–240.
- von der Weiden SL, Drewnick F, and Borrmann S, 2009: Particle Loss Calculator - a new software tool for the assessment of the performance of aerosol inlet systems. *Atmospheric Measurement Techniques*, 2, 479-494.
- Wex H, McFiggans G, Henning S, and Stratmann F, 2010: Influence of the external mixing state of atmospheric aerosol on derived ccn number concentrations. *Geophysical Research Letters*, 37, L10805.
- Willeke K and Baron P, 2005: *Aerosol Measurement: Principles, Techniques and Applications*. Van Nostrand Reinhold, New York.
- Wilson J, Lafleur B, Hilbert H, Seebaugh W, Fox J, Gesler D, Brock C, Huebert B, and Mullen J, 2004: Function and performance of a low turbulence inlet for sampling supermicron particles from aircraft platforms. *Aerosol Science and Technology*, 38, 790-802.
- Wise ME, Surratt JD, Curtis DB, Shilling JE, and Tolbert MA, 2003: Hygroscopic growth of ammonium sulfate/dicarboxylic acids rid d-3611-2009. *Journal of Geophysical Research-atmospheres*, 108, 4638.
- Wood R, 2012: Stratocumulus clouds. *Monthly Weather Review*, 140, 2373–2423.
- Wood R, Mechoso CR, Bretherton CS, Weller RA, Huebert B, Straneo F, Albrecht BA, Coe H, Allen G, Vaughan G, Daum P, Fairall C, Chand D, Gallardo Klenner L, Garreaud R, Grados C, Covert DS, Bates TS, Krejci R, Russell LM, de Szoeke S, Brewer A, Yuter SE, Springston SR, Chaigneau A, Toniazzo T, Minnis P, Palikonda R, Abel SJ, Brown WOJ, Williams S, Fochesatto J, Brioude J, and Bower KN, 2011: The vamos ocean-cloud-atmosphere-land study regional experiment (vocals-rex): goals, platforms, and field operations. *Atmospheric Chemistry and Physics*, 11, 627–654.
- Zheng X, Albrecht B, Jonsson HH, Khelif D, Feingold G, Minnis P, Ayers K, Chuang P, Donaher S, Rossiter D, Ghate V, Ruiz-Plancarte J, and Sun-Mack

S, 2011: Observations of the boundary layer, cloud, and aerosol variability in the southeast pacific near-coastal marine stratocumulus during vocals-rex. *Atmospheric Chemistry and Physics*, 11, 9943–9959.

# Chapter 6

## Appendices

Table 6.1: List of principle symbols

Symbol	Definition
$\alpha$	diffusivity of heat
$A$	cross sectional area
$C_c$	Cunningham slip correction factor
$C_p$	heat capacity for air
$C_v$	flow coefficient
$d$	diameter
$D$	particle diffusion coefficient
$D_v$	diffusivity of water vapour
$d_c$	dry size critical diameter
$D_e$	internal diameter of pipework
$D_o$	DMA size selected particle diameter
$D_{or}$	internal diameter of orifice
$D_p$	particle diameter
$D_{pg}$	median diameter
$D_t$	internal diameter of expansion chamber
$D_s$	internal diameter of extraction tube
$\delta T$	CCNc temperature gradient
$F_A$	activated fraction
$g$	gravitational acceleration
$k$	specific heat ratio
$\kappa$	kappa, hygroscopicity parameter
$L$	length
$M$	molar mass of air
$M_s$	molar mass of solute
$M_w$	molar mass of water
$N_{CCN}$	cloud condensation nuclei concentration

Table 6.2: List of principle symbols cont.

$N_{CN}$	condensation nuclei Concentration
$\eta$	gas absolute viscosity
$P$	pressure
$p_w(D_p)$	equilibrium vapour pressure of water over a droplet of diameter $D_p$
$P^o$	equilibrium vapour pressure of water over a flat surface
$\rho$	air density
$\rho_p$	particle density
$\rho_s$	density of solute
$\rho_w$	density of water
$Q$	flow rate
$R$	universal gas constant
$R_{can}$	radius of CCN column
$Re$	Reynolds number
$R_{sp}$	specific gas constant for air
$\sigma$	surface tension
$\sigma_g$	geometric standard deviation
$S$	instrument supersaturation
$S_c$	critical supersaturation
$S_{eff}$	effective supersaturation
$Stk$	Stokes number
$Stk', Stk_0, \overline{Stk}$	modified Stokes numbers
$T_{1,2,3}$	TEC plate temperatures
$T$	temperature
$\tau$	particle relaxation time
$\tau_c$	timescale for mass transfer in CCN column
$\tau_T$	timescale for heat transfer in CCN column
$\theta$	angle with respect to gravity
$\theta_{cont}$	angle of contraction
$\theta_e$	equivalent potential temperature
$U$	free stream velocity
$U_i$	inlet velocity
$U_o$	sampling velocity
$U_{or}$	orifice velocity
$\mu$	dynamic viscosity
$v$	velocity
$v_s$	effective van't Hoffs factor
$V_{ts}$	particle terminal settling velocity
$\theta_{cont}$	angle of contraction
$Z$	mean gas compressibility factor
$Z_{grav}$	gravitational deposition parameter

---